

**Homodyne Spin Noise Spectroscopy
and
Noise Spectroscopy of a Single Quantum Dot**

Von der Fakultät für Mathematik und Physik
der Gottfried Wilhelm Leibniz Universität Hannover

zur Erlangung des akademischen Grades

Doktor der Naturwissenschaften

Dr. rer. nat.

genehmigte Dissertation

von

M.Sc. Pavel Sterin

2023

Referent: Prof. Dr. rer. nat. Michael Oestreich
Korreferent: Prof. Dr. rer. nat. Ilja Gerhardt
Korreferent: Prof. Dr. rer. nat. Daniel Hägele

Tag der Disputation: 25.08.2023

Abstract

The steady-state fluctuations of a spin system are closely interlinked with its dynamics in linear response to external perturbations. Spin noise spectroscopy exploits this link to extract parameters characterizing the dynamics without needing an intricate spin polarization scheme. In samples with an accessible optical resonance, the spin fluctuations are imprinted onto a transmitted linearly polarized quasi-resonant probe laser beam according to the optical selection rules, making an all-optical observation of spin dynamics possible. The beam's detuning and intensity determine whether the system is probed at thermal equilibrium or under optical driving. The technique is uniquely applicable for studying single quantum dots, where a charge carrier's spin and occupancy dynamics can be observed simultaneously.

This thesis presents a step-by-step derivation of the shape and statistical properties of experimental spectra and highlights the experimental limitations faced by the technique at very low probe intensities through uncorrelated broadband technical noise contributions. Optical homodyne amplification is evaluated in a proof-of-principle experiment to determine whether this limitation can be overcome at low frequencies < 5 MHz. Unlike previous attempts, the presented proof-of-principle experiment demonstrates that shot-noise limited spin noise measurements are possible in low-frequency ranges down to $\gtrsim 100$ kHz. For even lower frequencies, the suppression of laser intensity noise by the limited common-mode rejection of conventional balanced detectors is found to be the limiting contribution.

In the second part of the thesis, optical spin noise spectroscopy is used to conduct a long-term study of spin and occupancy dynamics of an individual hole spin confined in an (In,Ga)As quantum dot with high radial symmetry in the high magnetic fields regime. For magnetic fields $\gtrsim 250$ mT, the splitting of the Zeeman branches with an effective g -factor of $2.159(2)$ exceeds the quantum dot's trion resonance's homogeneous line width of $6.3(2)$ μeV , revealing a rich spectral structure of spin and occupancy dynamics. This structure reveals a so far ne-

glected contribution of an internal photoeffect to the charge dynamics between the quantum dot and its environment. Previously developed theoretical modeling is extended to incorporate the photoeffect and successfully achieves excellent qualitative correspondence with experimental spectra for almost all detuning ranges. The photoeffect shuffles the charge from and into the quantum dot with two distinct rates. Within the model, the previously required Auger process is unnecessary to describe the experimental data. The rates of discharging and recharging the quantum dot are determined to be on the order of $12(7) \text{ kHz } \mu\text{m}^2 \text{ nW}^{-1}$ and $6(2) \text{ kHz } \mu\text{m}^2 \text{ nW}^{-1}$, respectively.

For magnetic fields $< 500 \text{ mT}$, very long $T_1^{(h)}$ hole spin relaxation times $\gg 1 \text{ ms}$ are observed, while above 500 mT , $T_1^{(h)}$ falls to $5(2) \mu\text{s}$ at 2.5 T , qualitatively confirming the theoretical prediction of a single-phonon mediated relaxation process. Furthermore, the electron spin relaxation time $T_1^{(e)}$ in the trion state shows no pronounced dependence on magnetic fields above 500 mT and stays at a constant value of $101(2) \text{ ns}$. The saturation intensity of the transition also does not depend on the magnetic field and stays at a constant value of $4.8(7) \text{ nW } \mu\text{m}^{-2}$.

Keywords: quantum dot, laser spectroscopy, spin dynamics, spin noise

Contents

Introduction	1
I Noise Spectroscopy	11
1 Basic Concepts	13
1.1 Continuous Fourier Transform and Autocorrelation	14
1.1.1 Coherent Signals	14
1.1.2 Incoherent Signals	17
1.2 Discrete-Time Fourier Transform	18
1.2.1 Discrete Sampling	18
1.2.2 Power Spectrum and Aliasing	20
1.3 Discrete Fourier Transform	22
1.3.1 Sampling the Discrete Time Fourier Transform	22
1.3.2 Fast Fourier Transform	23
1.3.3 Real-valued Discrete Fourier Transform	24
1.3.4 Finite Power	25
1.3.5 Aliasing and Spectral Leakage	27
1.3.6 Other Window Functions	32
1.3.7 Coherent Artifacts	37
1.3.8 Mitigation of Artifacts	38
1.3.9 One-Sided Spectra	38
1.3.10 Processing of Realistic Signals	39
2 Power Spectral Density Estimation	41
2.1 Bias and Variance of the Periodogram	41
2.2 Broadband Spectra	44
2.2.1 Simulating Spin Noise	44
2.2.2 White and Colored Noise	48

2.3	The Modified Welch Method	50
2.3.1	Welford Summation	51
2.3.2	Chan's Merging Formula	52
2.3.3	Partial Average Statistics	53
2.3.4	Variance Estimate Criterion	54
3	Optical Noise Spectroscopy	57
3.1	Noise Signals in Photodetectors	57
3.2	Balanced Photo-Detection	61
3.3	PSD Estimate Variance and Limits	62
II	Homodyne Spin Noise Spectroscopy on Rubidium	67
4	Theory	69
4.1	Jones Formalism	70
4.1.1	Classical Field Amplitudes	70
4.1.2	State Vectors	71
4.2	Spin Noise Spectroscopy	72
4.2.1	Spin Dynamics	73
4.2.2	Spin Noise	77
4.2.3	Optical Spin Noise Spectroscopy	79
4.2.4	(Spin-Flip) Raman Scattering Picture	83
4.3	Homodyne Detection	85
4.3.1	Self-Homodyne Scheme	86
4.3.2	Mach-Zehnder Interferometer	88
4.3.3	Balanced Scheme	89
4.3.4	Balanced Phase Stabilization	90
4.3.5	Unbalanced Scheme	91
5	Experimental Aspects	95
5.1	The Rubidium D2 Line	95
5.2	Proof-of-Principle Rubidium Setup	98
5.2.1	Laser Source	98
5.2.2	Probe Path	100
5.2.3	Local Oscillator Path	101
5.2.4	Control Port	103

5.2.5	Measurement Port	105
6	Superiority and Limits of Homodyne Spin Noise Spectroscopy	107
6.1	Spin Noise Spectrum	107
6.2	Homodyne Amplification	108
6.2.1	Signal-to-Noise Ratio	110
6.2.2	Shot Noise Variance Ratio	113
6.3	Conclusion	115
III	Measurement Infrastructure	117
7	Parameter Estimation	119
7.1	The Real-Time Histogram Algorithms	122
8	Cryogenic Optics Setup	127
8.1	Cryostat	127
8.1.1	Joule-Thomson Circuit	128
8.2	Cryostat Control Software	132
8.2.1	Control Server	132
8.2.2	Graphical User Interface	137
8.3	Confocal Microscope and SNS Setup	139
8.3.1	Sample Insert	139
8.3.2	Optical Setup	143
8.3.3	Balanced Photo-Detector	150
8.4	Other Control Servers	153
8.4.1	Power and Balance Regulation	153
8.4.2	Matisse Controller: Ring Laser Control	154
IV	Non-equilibrium noise spectroscopy of a single QD	155
9	Preliminary Remarks	157
9.1	(In,Ga)As Quantum Dots	157
9.1.1	Manufacturing	157
9.1.2	The Quantum Dot <i>s</i> -Shell	158
9.1.3	Excitonic Resonances	160
9.1.4	Fine Structure of Excitons	161

9.1.5	Spin Relaxation	163
9.1.6	Incoherent Charge Dynamics	167
9.2	QD Sample	169
9.2.1	QD Selection	170
9.2.2	Photoluminescence Spectroscopy	172
10	Theoretical Model	177
10.1	Model System	179
10.2	Density Matrix	181
10.2.1	Coherent Part	183
10.2.2	Incoherent Part	184
10.3	Stationary Solution	188
10.3.1	Quasi-Stationary Solution	190
10.3.2	True Stationary Solution	194
10.4	Quantum Regression	196
10.4.1	Fluctuation Operators	197
10.4.2	Initial Conditions	198
10.4.3	Separation of Time Scales	200
10.4.4	Exact Solution	203
10.4.5	Model Units and Scaling	207
10.5	Regression Breakdown	208
10.5.1	Regression Parameters	208
10.5.2	Breakdown	209
10.5.3	General Case	215
10.6	Model Parameterizations	216
10.6.1	Fixed Model	216
10.6.2	Simple Intensity Dependences	218
10.6.3	Dual Intensity Dependence	220
11	Limitations of the Results	223
11.1	Frost Degradation of Cryogenic Optics	224
11.2	Degraded Microcavity Performance	224
11.3	Evaluation of Noise Spectra	225
11.3.1	Preprocessing	227
11.3.2	Spectral Distortion Compensation	228
11.3.3	Multi-Range Regression	230

11.3.4	Detuning Dependent Hyperspectra	233
12	Quasi-Resonant Regime	239
12.1	Non-Resonant Dynamics	240
12.1.1	Baseline Dependence	240
12.1.2	Line Shape	244
12.1.3	Noise Powers	246
12.2	Qualitative Correspondence	249
12.3	High Longitudinal Magnetic Fields	251
13	Conclusion and Outlook	257
V	Appendix	263
A	Derivations	265
A.1	Mathematical derivations	265
A.1.1	Welford’s sum of squares	265
B	Technical Drawings	267
C	Additional Figures	269
	Curriculum Vitae	315
	Mentored Bachelor and Master Projects	317
	Acknowledgements	319

List of Figures

1.1	Result of sampling a broadband signal.	20
1.2	Coefficients of a real-valued DFT.	24
1.3	Interpretation of the DFT spectrum as power and magnitude spectrum.	25
1.4	Comparison between the spectra of the continuous and the discretely sampled rectangular window	28
1.5	What the DFT actually computes (square window).	30
1.6	Comparison between the Dirichlet and Hanning windows.	34
1.7	What the DFT actually computes (Hanning window).	36
1.8	Sketch of the safety margin of the Hanning window for broadband signals.	37
2.1	Sketch of the Welch method using Hanning window.	43
2.2	The simplified model of the polarization random walk.	44
2.3	Typical shape of a SN spectrum.	46
2.4	Sketch for the limit of the white noise ACF.	48
2.5	Sketch of the spectra of white and colored noise.	50
2.6	Sketch of a coherent signal violating the variance criterion.	54
3.1	RIN in spectra for two different laser sources.	59
3.2	Possible balanced detection schemes.	60
3.3	Variance and mean of various PSD estimates.	64
4.1	The convention for the inputs and outputs of the beam splitter.	71
4.2	Evolution of the electron spin expectation value in different conditions.	74
4.3	Dielectric functions of a simple four-level resonance and the corresponding ellipticity of a transmitted beam.	81
4.4	The sensitivity of SNS determined by the change in the dielectric response.	82

4.5	Variance of Kerr signal fluctuations for different phase mismatch.	83
4.6	Possible homodyne schemes.	85
5.1	Relative transmission of the rubidium vapor cell.	96
5.2	Term scheme of the D2 hyperfine levels of the rubidium isotopes.	97
5.3	Schematic drawing of the proof-of-principle setup.	99
5.4	Simulation of two-beam interference patterns during interferometer alignment.	103
6.1	Composite spin noise spectrum at the rubidium-85 D2 transition.	108
6.2	Exemplary spectra decomposed into their effective contributions.	109
6.3	Estimates characterizing the homodyne amplification of SN at the foreground Larmor frequency.	112
6.4	Relative variance of samples in the frequency bins around the foreground Larmor frequency.	114
8.1	Sketch of the complete modified JT circuit.	129
8.2	Example vector magnet sweeps.	134
8.3	The main screen of the cryostat control GUI.	136
8.4	The tabs of the control panel in the cryostat control GUI.	138
8.5	Sample insert for confocal microscopy.	140
8.6	Technical drawing of the optical setup.	144
8.7	Laser photon energy dependence of power transmission curves. .	147
8.8	Amplified noise floor of the insufficiently grounded balanced photo detector.	151
8.9	Decomposition of raw difference spectrum for two probe laser powers.	152
9.1	Construction of the QD s-shell.	159
9.2	Possible exciton states in the QD s-shell.	160
9.3	Fine structure of the QD exciton states.	162
9.4	Incoherent charge loss channels.	167
9.5	Simulated intensity distribution within the micro cavity.	169
9.6	Stitched map of sample P911.	171
9.7	Polarization resolved photoluminescence spectroscopy of the investigated QD.	173

9.8	Excerpt from the recorded magneto-luminescence spectra for the investigated QD.	174
10.1	Main steps needed to derive the ACF of Kerr fluctuations.	178
10.2	Energy level diagram for a positively charged QD.	179
10.3	Coherent evolution of the QD states.	183
10.4	Trion decay of the excited QD states.	184
10.5	Spin relaxation of the QD states.	185
10.6	The QD charge dynamics.	186
10.7	Sketch of the dipole term shape functions as defined for the quasi-stationary solution.	193
10.8	Sketch of the decay of the Kerr fluctuations ACF.	201
10.9	Comparison of the spectrum parameters for the SCTS approximation and the exact solution without an Auger relaxation channel.	210
10.10	Comparison of the spectrum parameters for the SCTS approximation and the exact solution with an Auger relaxation channel.	211
10.11	Comparison of the decomposition of the exact solution with the SCTS predictions for the specified model parameters.	214
10.12	SCTS predictions for a model with fixed rates.	217
10.13	SCTS predictions for models with a single internal probe intensity dependence.	219
10.14	SCTS predictions for models with a dual internal probe intensity dependence.	220
11.1	Measured cavity reflectivity at 1.8K.	225
11.2	Evaluation pipeline for PSD spectra.	226
11.3	The correction step of the evaluation pipeline.	229
11.4	Iterations of the fitting strategy.	231
11.5	Iterations of the fitting strategy for a low magnetic field of 250mT.	234
11.6	Iterations of the fitting strategy for a high magnetic field of 2T.	235
11.7	Extracted correlation rates and noise powers for two contributions at 2T, 5K.	236
12.1	Extracted correlation rates and noise powers according to the SCTS approximation at 1.8K, 750mT.	241

12.2	Coefficients of the linear dependence on probe power for correlation rate baselines.	243
12.3	Saturation broadened line width and area probe power dependence.	245
12.4	Results of single spectrum regression of detuning hyper-spectra at 1.8K, 750mT.	247
12.5	Spin noise power dependence models for two different probe powers.	248
12.6	Comparison of experimental detuning hyperspectra and the exact model at 1.8K, 750mT.	250
12.7	Experimental detuning hyperspectra at 1.8K, 2.5T.	252
12.8	Results of single spectrum regression of detuning hyper-spectra at 1.8K, 2.5T.	254
B.1	Technical drawing of the strain free wedge beam splitter holder.	268
C.1	Extracted single spectrum correlation rates according to the SCTS approximation at 1.8K, 30mT.	270
C.2	Extracted single spectrum correlation rates according to the SCTS approximation at 1.8K, 125mT.	271
C.3	Extracted single spectrum correlation rates according to the SCTS approximation at 1.8K, 250mT.	272
C.4	Extracted single spectrum correlation rates according to the SCTS approximation at 1.8K, 500mT.	273
C.5	Extracted single spectrum correlation rates according to the SCTS approximation at 1.8K, 750mT.	274
C.6	Extracted single spectrum correlation rates according to the SCTS approximation at 1.8K, 1T.	275
C.7	Extracted single spectrum correlation rates according to the SCTS approximation at 1.8K, 1.5T.	276
C.8	Extracted single spectrum correlation rates according to the SCTS approximation at 1.8K, 2T.	277
C.9	Extracted single spectrum correlation rates according to the SCTS approximation at 1.8K, 2.5T.	278
C.10	Comparison of experimental detuning hyperspectra and the exact model at 1.8K, 125mT.	279

C.11	Comparison of experimental detuning hyperspectra and the exact model at 1.8K, 250mT.	280
C.12	Comparison of experimental detuning hyperspectra and the exact model at 1.8K, 500mT.	281
C.13	Comparison of experimental detuning hyperspectra and the exact model at 1.8K, 750mT.	282
C.14	Comparison of experimental detuning hyperspectra and the exact model at 1.8K, 1T.	283
C.15	Comparison of experimental detuning hyperspectra and the exact model at 1.8K, 1.5T.	284
C.16	Experimental detuning hyperspectra at 1.8K, 2T.	285
C.17	Experimental detuning hyperspectra at 1.8K, 2.5T.	286
C.18	Results of single spectrum regression of detuning hyper-spectra at 1.8K, 125mT.	287
C.19	Results of single spectrum regression of detuning hyper-spectra at 1.8K, 250mT.	288
C.20	Results of single spectrum regression of detuning hyper-spectra at 1.8K, 500mT.	289
C.21	Results of single spectrum regression of detuning hyper-spectra at 1.8K, 750mT.	290
C.22	Results of single spectrum regression of detuning hyper-spectra at 1.8K, 1T.	291
C.23	Results of single spectrum regression of detuning hyper-spectra at 1.8K, 1.5T.	292
C.24	Results of single spectrum regression of detuning hyper-spectra at 1.8K, 2T.	293
C.25	Results of single spectrum regression of detuning hyper-spectra at 1.8K, 2.5T.	294

List of Tables

8.1	Devices handled by the control server and their respective communication protocols.	133
9.1	Zeeman splitting and fine structure splitting. The specified uncertainties are fit errors.	175
10.1	Possible single-spectra regressions and their interpretation in various detuning regions.	215
12.1	Linear dependence of SCTS correlation rate baselines on probe power.	243
12.2	Line shape parameters.	245
12.3	Results of the global regression of the remaining model parameter using the exact model.	251

Publications

The following list contains authored and co-authored scientific publications submitted during the work on this thesis, which contain some of the topics expanded on here. (In the following list, the italicized word *author* highlights the contributions of the author of this thesis.)

- **P. Sterin**, J. Wiegand, J. Hübner, and M. Oestreich, “Optical Amplification of Spin Noise Spectroscopy via Homodyne Detection”, *Physical Review Applied* **9**, 034003 (2018), doi:10.1103/PhysRevApplied.9.034003.

This publication presents a successful experimental demonstration of optically amplified spin noise spectroscopy utilizing the homodyne detection technique on a rubidium sample. Alongside [2, 3, 4] our study represents important progress in overcoming the electrical noise, typically limiting traditional optical noise spectroscopy. While previous publications have predominantly focused on the high-frequency regime, this study explores the technique’s limits below one megahertz.

The *author* devised this publication’s homodyne experiment and conducted all the measurements. The second author contributed the example quantum dot spectrum. The *author* organized scientific discussions, created the manuscript draft and subsequently edited and finalized it with the co-authors.

- L. Abaspour, **P. Sterin**, E. P. Rugeramigabo, J. Hübner, and M. Oestreich, “Doping and temperature dependence of nuclear spin relaxation in n-type GaAs”, *Physical Review B* **102**, 235205 (2020), doi:10.1103/PhysRevB.102.235205.

This publication investigates the nuclear spin relaxation rate in n-type GaAs across various doping densities near the metal-to-insulator transition. Our study reveals that the density-dependent behavior of the rate is accurately captured by considering nuclear spin diffusion to localized donor electrons

and its interaction with free electrons using the Korringa mechanism. Only for the lowest-doped sample is a deviation observed, likely caused by a nuclear spin heating process through the localized electrons.

The *author's* contributions include developing a portion of the experimental setup and control software, conducting some of the evaluations, discussing the results, and assisting in editing and finalizing the manuscript alongside the co-authors.

- T.-J. Sun, **P. Sterin**, L. Lengert, C. Nawrath, M. Jetter, P. Michler, Y. Ji, J. Hübner, and M. Oestreich, “Non-equilibrium spin noise spectroscopy of a single quantum dot operating at fiber telecommunication wavelengths”, *Journal of Applied Physics* **131**, 065703 (2022), doi : 10.1063/5.0078910.

This publication investigates the spin and occupation noise properties of a single, positively charged (In,Ga)As quantum dot emitting photons in the telecommunication C-band. Our study applies spin noise spectroscopy at a low temperature in a quasi-resonant non-equilibrium regime and provides insights into the hole-spin relaxation time, Auger recombination, and electron-spin relaxation time of the trion state.

The *author* created a part of the experimental setup and control software and recorded and evaluated some of the measurements in this publication. The first author did the bulk of the measurements and created the manuscript. The *author* provided help editing and finalizing the manuscript together with the other co-authors.

- **P. Sterin**, L. Abaspour, J. G. Lonnemann, E. P. Rugeramigabo, J. Hübner, and M. Oestreich, “Temperature-dependent electron spin relaxation at the metal-to-insulator transition in n-type GaAs”, *Physical Review B* **106**, 125202 (2022), doi : 10.1103/PhysRevB.106.125202.

This publication presents a detailed study on the temperature-dependent electron spin relaxation rate in n-type bulk GaAs near the metal-to-insulator transition. Our study reveals that the longest spin relaxation time occurs slightly below the transition region at a temperature of ≈ 7 K. We propose a multi-mechanism theoretical model that successfully explains the experimental data and predicts the maximum possible spin relaxation time of around $\approx 1 \mu\text{s}$ in n-doped, bulk GaAs with negligible external magnetic

fields.

The *author* created a part of the experimental setup and control software. The second author recorded the experimental data. The *author* made substantial contributions to the evaluation and the simulation discussed in the publication and participated in the scientific discussions. Additionally, the *author* collaborated with the co-authors to edit, refine, and finalize the manuscript, initially drafted by the second author.

- **P. Sterin**, K. Hühn, M. M. Glazov, J. Hübner, and M. Oestreich, “Two-way photoeffect-like occupancy dynamics in a single (InGa)As quantum dot”, *Physical Review B* **108**, 125301 (2023), doi : 10.1103/PhysRevB.108.125301.

This publication discusses the extension of optical spin noise spectroscopy of (In,Ga)As quantum dots to high magnetic fields. It highlights the limitations of standard theoretical approximations that can no longer be used to decouple spin and charge dynamics in these conditions. The study suggests that Auger recombination can be neglected at high magnetic fields in favor of a two-way probe-laser-induced photoeffect. The findings have implications for quantum photonic devices and highlight the importance of understanding charging and recharging processes.

The *author* created the experimental setup and control software in collaboration with the second author. The *author* organized scientific discussions, did a significant portion of the evaluation, and took the lead in writing the manuscript, particularly the theory part. During the review, we also gained M. Glazov as a co-author, who improved the mathematical representation of the theory part and co-authored the reply to the referees. Lastly, the *author* edited and finalized the manuscript together with the other co-authors.

Contributions to Scientific Conferences

- **P. Sterin**, J. Hübner, and M. Oestreich, “Interferometrically Enhanced Spin Noise Spectroscopy of ^{87}Rb ”, 2016, Talk, International Workshop of the School for Contacts in Nanosystems.
- **P. Sterin**, J. Hübner, and M. Oestreich, “Interferometrically Enhanced Spin Noise Spectroscopy of Rubidium”, 2017, Poster, Workshop of the School for Contacts in Nanosystems.
- **P. Sterin**, J. Wiegand, J. Hübner, and M. Oestreich, “Optical amplification of spin noise spectroscopy via homodyne detection”, 2019, Poster, DPG Spring Meeting of the Condensed Matter Section in Regensburg.
- **P. Sterin**, J. Wiegand, J. Hübner, and M. Oestreich, “Beating the Electric Limit: Homodyne Detection for Spin Noise Spectroscopy”, 2017, Talk, International Workshop of the School for Contacts in Nanosystems.
- **P. Sterin**, J. Wiegand, J. Hübner, and M. Oestreich, “Optical amplification of spin noise spectroscopy via homodyne detection”, 2018, Talk/Poster, Workshop of the School for Contacts in Nanosystems.
- L. Abaspour, **P. Sterin**, J. G. Lonnemann, E.-P. Rugeramigabo, J. Hübner, and M. Oestreich, “Towards a Complete Model of Spin Relaxation in n-GaAs”, 2018, Talk, Workshop of the School for Contacts in Nanosystems.
- **P. Sterin**, M. Baron, J. Wiegand, J. Hübner, and M. Oestreich, “Spin Noise Spectroscopy via Phase Modulated Homodyne Detection”, 2019, Talk, International Workshop of the School for Contacts in Nanosystems.
- **P. Sterin**, J. Hübner, and M. Oestreich, “Interferometrically Enhanced Spin Noise Spectroscopy of Rubidium”, 2017, Poster, DPG Spring Meeting of the Condensed Matter Section in Dresden.

List of Used Acronyms

FT	Fourier transform
DTFT	discrete-time Fourier transform
DFT	discrete Fourier transform
FFT	fast Fourier transform
SP	stationary process
PSD	power spectral density
MS	magnitude squared
SN	spin noise
NS	noise spectroscopy
SNS	spin noise spectroscopy
ON	occupancy noise
ACF	autocorrelation function
WKT	Wiener-Khinchin theorem
QD	quantum dot
VTI	variable temperature inset
JT	Joule-Thomson
DC	direct current
ADC	analog-to-digital converter
FWHM	full width at half maximum
HWHM	half width at half maximum
DBR	distributed Bragg reflector
MZI	Mach-Zehnder interferometer
HSNS	homodyne spin noise spectroscopy
ECDL	external cavity laser diode
BS	beam splitter
PBS	polarizing beam splitter

EOM	electro-optic phase modulator
LO	local oscillator
ND	neutral density
RIN	relative intensity noise
NEP	noise equivalent power
SCTS	separation of correlator time scales
OVC	outer vacuum chamber
GUI	graphical user interface
API	application programmin interface
PL	photoluminescence
RF	resonance fluorescence
LCR	liquid crystal retarder
MBE	molecular beam epitaxy
(In,Ga)As	indium gallium arsenide

List of Used Symbols

\mathfrak{V} variance

Part I

\mathcal{F}	continuous Fourier transform
\mathcal{F}_z	discrete time Fourier transform
\mathcal{F}_N	discrete Fourier transform
\mathfrak{S}_f	periodogram estimate of signal f
\mathfrak{M}_f	magnitude squared (MS) spectrum of signal f
III_{τ_s}	time domain dirac comb (the sha function)
III_{ν_s}	frequency domain dirac comb (the sha function)
\mathfrak{S}_f	power spectral density (PSD) of signal f
c_f	autocorrelation function (ACF) of signal f

\tilde{c}_f	Fourier transform (FT) of autocorrelation function (ACF) of signal f
ν_s	sampling frequency
t_k	sampling time $t_k = k/\nu_s$
w_{\square}	rectangular (Dirichlet) window function
w_{\odot}	quadratic Hanning window function
η_Q	detector quantum efficiency
η_D	detector responsivity
P_D^*	mean optical power on the detector
i_D^*	mean photocurrent
i_D	photocurrent
ν_p	photon frequency
h	Planck constant

Part II

ν_L	Larmor frequency
$\underline{\mathcal{S}}_s$	spin noise periodogram
$\underline{\mathcal{S}}_t$	thermal (electrical) noise periodogram
$\underline{\mathcal{S}}_p$	photon shot noise periodogram
$\underline{\mathcal{S}}_{fg}$	foregorund periodogram
$\underline{\mathcal{S}}_{bg}$	background periodogram

Part IV

g_e^*	effective electron g factor
g_h^*	effective heavy hole g factor
γ_r	QD reoccupation rate
γ_p	QD hole loss rate due to photoeffect
γ_a	QD hole loss rate due to Auger effect
γ_e	electron spin relaxation rate

γ_h	hole pseudo-spin relaxation rate
γ_0	decay rate of the optical trion transition
γ_1	decay rate given by the saturation broadened trion line width
γ_{extra}	additional dephasing rate of the optical trion transition
γ_d	effective dephasing rate of the optical trion transition
\mathcal{E}	magnitude of the dipole matrix elements of the optical trion transition
Δ	detuning of laser photon energy relative to the center between Zeeman branches
φ	background phase of the Kerr signal
Ω	total Zeeman splitting
Ω_e	electron Zeeman splitting
Ω_h	hole Zeeman splitting
κ_{\pm}	population ratios and line shape functions
Ω_O	Overhauser field
Δ_{\pm}	locations of the Zeeman branches
\mathcal{H}	system Hamiltonian operator
\hat{d}_{\pm}	dipole operators in the circular basis
\hat{n}_o	outer state population operator
\hat{n}_e	excited state (electron) population operator
\hat{n}_h	ground state (hole) population operator
$\hat{n}_{\pm 1/2}$	populations of the electron spin states
$\hat{n}_{\pm 3/2}$	populations of the hole pseudo-spin states
$\hat{\sigma}_e$	excited state (electron) spin polarization operator
$\hat{\sigma}_h$	ground state (hole) spin polarization operator
\hat{n}	QD occupancy operator
$\hat{\rho}$	system density matrix operator
$\hat{\rho}_{\text{QD}}$	QD density matrix operator
$\hat{\rho}_o$	outer state density matrix operator

$\hat{\rho}_{\text{qs}}$	quasi-stationary system density matrix operator
$\hat{\rho}_{\text{ss}}$	steady-state system density matrix operator
\hat{S}_z	total pseudo-spin operator
d_{\pm}	expectation values of the dipole operators in the circular basis
$d_{x,y}$	expectation values of the dipole operators in the linear basis
n	expectation value of the QD occupancy operator
n_o	expectation value of the outer state occupancy operator
$n_{\pm 1/2}$	expectation values of the populations of the electron spin states
$n_{\pm 3/2}$	expectation values of the populations of the hole pseudo-spin states
S_z	expectation value of the pseudo-spin operator
$C_{s,n}^{i,r}$	dipole term shape functions of the quasi-stationary solution
$\delta\hat{K}$	Kerr signal fluctuation operator
$\delta\hat{S}_z$	pseudo-spin fluctuation operator
$\delta\hat{n}$	occupancy fluctuation operator
δS_z	expectation value of the pseudo-spin fluctuation operator
δn	expectation value of the occupancy fluctuation operator
γ_s	kinetic coefficient and correlation rate of spin fluctuations
γ_n	kinetic coefficient and correlation rate of occupancy fluctuations
λ_s	spin-referred kinetic coefficient
λ_n	occupancy-referred kinetic coefficient
\bar{n}	steady-state QD occupancy expectation value
\bar{n}_o	steady-state outer state occupancy expectation value
\bar{S}_z	steady-state total pseudo-spin expectation value
A_{SN}	SCTS noise power of spin noise
A_{ON}	SCTS noise power of occupancy noise
γ_{n_1}	SCTS correlation rate of occupancy fluctuations
P_{SCTS}	set of parameters predicted by the SCTS
γ_s^*	estimated correlation rate of spin noise

$\gamma_{n_1}^*$	estimated correlation rate of occupancy noise
$A_{br.}^*$	estimated noise power of the broad contribution
$A_{nr.}^*$	estimated noise power of the narrow contribution
$\gamma_{br.}^*$	estimated correlation rate of the broad contribution
$\gamma_{nr.}^*$	estimated correlation rate of the narrow contribution
P_{LL}^*	estimated set of regression parameters
$\gamma_{eff.}^*$	estimated correlation rate of a single contribution
$A_{eff.}^*$	estimated noise power of a single contribution
γ_r^*	intrinsic (thermal) reoccupation rate
γ_h^*	intrinsic hole pseudo-spin relaxation rate
γ_1^*	estimated saturation broadened trion line width
γ_d^*	estimated trion homogeneous width
γ_e^*	estimated electron spin relaxation rate
γ_h^\bullet	baseline intercept of spin correlation rate
γ_r^\bullet	baseline intercept of occupancy correlation rate
$\gamma_{n_1}^\bullet$	baseline of the occupancy correlation rate
γ_s^\bullet	baseline of the spin correlation rate
η_p	photoeffect coefficient
η_r	inverse photoeffect coefficient
η_{n_1}	occupancy rate baseline coefficient
P_M	set of underlying model parameters
γ_{c_\pm}	roots or correlations rates of the exact solution
A_\pm	noise powers of the exact solution
P_{LL}	set of parameters from the exact decomposition
c_K	ACF of Kerr fluctuations
\tilde{c}_K	FT of the ACF of Kerr fluctuations
$\tilde{c}_{K,sep}$	FT of the SCTS ACF of Kerr fluctuations
P_{probe}^*	laser probe power

P_{block}^* laser reference power
 $P_{\text{sat.}}^*$ transition saturation power

Introduction

[...] Thus the duty of the man who investigates the writings of scientists, if learning the truth is his goal, is to make himself an enemy of all that he reads, and, applying his mind to the core and margins of its content, attack it from every side. He should also suspect himself as he performs his critical examination of it, so that he may avoid falling into either prejudice or leniency. [...]

Hasan Ibn al-Haytham (965-1040)

Scientific Environment

Qubits

Decoupling a quantum-mechanical system from its environment reveals its internal degrees of freedom. These fundamental properties of matter, like spin, polarization, or internal energy states, define the multitude of states in which the decoupled system coherently evolves. Usually, for a sufficiently good description of the system's dynamics, only a subset of all possible states has to be considered. For example, considering only the lowest two energy states reduces the description to a two-level system. Addressing these two states allows controlling the system's quantum-mechanical state, encoding information within it, and retrieving information back again. Therefore, in analogy to a classical bit, such a system is called a qubit.

For example, a qubit can be realized from a photon and its polarization degree of freedom. Such a flying photon can be effectively decoupled from its environment. However, keeping photons of light localized in a small volume is challenging. Moreover, deliberate interactions between photon qubits are difficult to realize due to their bosonic nature [17, 18]. Another way to realize a qubit is to use a charge carrier's spin degree of freedom, for example, an electron's spin. Such spin qubits may be more suitable for situations requiring many qubits integrated within a small volume.

Logical qubits have attracted significant attention in modern physics due to their numerous potential applications. In quantum metrology, qubits can serve as highly sensitive probes for exploring other quantum systems. These experiments leverage the quantum-mechanical properties of the qubits and the system under investigation to unveil otherwise inaccessible characteristics, surpassing the capabilities of classical probes [19]. Quantum cryptography takes advantage of entangled pairs of photon qubits to distribute cryptographic keys securely. By encoding the potential key information within the entangled polarization state of the qubits, it becomes virtually impossible for an eavesdropper to intercept without destroying the entanglement, thereby revealing their presence [20]. In quantum simulations, deliberately coupled systems of many qubits are used to investigate the behavior and properties of many-body quantum-mechanical systems in a controlled way [21].

Spin Qubits

Electromagnetic fields can be used to control spin qubits, and modern physics developed many different techniques to initialize [22, 23, 24, 25, 26, 27], manipulate [28, 29, 30, 31, 32] and read out [33, 34] the state of the spin. While this ease of manipulation is advantageous, it also introduces a challenge as the influence of the surrounding environment can impose limitations on the maximum duration for which the spin qubit can retain its quantum-mechanical information. Depending on the environment, different relaxation processes can quickly destroy the spin information [35]. To strike a balance between accessibility and spin lifetime, various fields of applied physics employ diverse approaches. In the solid-state domain, one possibility is to use a material system composed of isotopes without a nuclear spin, like artificially enriched silicon 28. Ideally, in an experimental setting, the qubit should be addressable either optically or electrically while preserving its state for durations longer than the time required to manipulate and read out the spin.

Atomic Qubits

A good balance between accessibility and spin lifetime is obtained in systems where the spin qubit serves as the ground state of an optical transition that preserves the spin state. An (ionized) atom in a low external magnetic field is the most prominent example of such a system. An outer-shell electron of the atom

can absorb a photon of appropriate energy and transition to an excited state. At the same time, the excited state's spin represents the absorbed light's polarization state. Such a system is called a spin-photon interface. These systems are advantageous, as they can be used to convert the spin state of a stationary qubit into a flying photon qubit and capture and store the initial information in a stationary qubit that may be on the other side of the Earth. Optical techniques [36, 37, 38, 39, 21, 40] can quickly manipulate an atomic spin qubit. At the same time, an atomic qubit can have very long spin coherence times, as an isolated atom is primarily sensitive only to light resonating with its optical transitions. Unfortunately, single atoms are quite volatile. Much effort is necessary to keep them trapped for an indefinite time. Moreover, it can be prohibitively expensive to integrate significant quantities of isolated atoms while still keeping them individually controllable. Realizing large-scale quantum-logical circuits in quantum simulation is an even more significant challenge. These circuits require a deliberate and controlled one-to-one coupling between each qubit of the circuit and all other qubits.

Solid-State Qubits

An alternative approach is to use charge carriers in solid-state systems like semiconductors. Here, established fabrication techniques from the semiconductor industry can be used to almost arbitrarily tune the solid-state environment. Various solid-state systems use different artificial or self-organized structures to trap individual charges. For example, nitrogen-vacancy color centers in diamond trap pairs of electrons that can be optically addressed. Another approach involves III/V semiconductors with a direct band gap and hence an optical transition with a large oscillator strength. Almost perfect lattices with very few impurities can be grown using molecular beam epitaxy. Such samples have few free charges at cryogenic temperatures. Deliberately doping the lattice with donor atoms creates states just below the band gap, where the dopant charge is localized at low temperatures. Even greater confinement is achieved by allowing self-organized heterostructures to grow using droplet etching or strain-driven growth techniques [41]. For example, the latter technique can be used to create nanometer-scale islands of indium arsenide (InAs) in a matrix of gallium arsenide (GaAs). The equilibrium charge state of these islands is tunable by the environment, as these islands trap the charge carriers of neighboring dopants. At the same time, they constrain the trapped carriers in an effectively zero-dimensional structure, a quantum dot (QD). The con-

finement of charges makes their allowed energy levels discrete. Excitonic excited states of QDs are also bound to the heterostructure. Having localized ground and excited states makes QDs somewhat similar to atoms [42]. Furthermore, QDs can potentially be integrated into more complicated devices, as their position is fixed in the surrounding lattice. However, the proximity of the environment may negatively influence the spin lifetimes of the localized charge carriers in such structures.

Spins in Solid-State Systems

Spin lifetimes of free carriers in a semiconductor are usually quite short. For example, free electrons in semiconductors without inversion symmetry experience an effective momentum-dependent magnetic field through the Dyakonov-Perel mechanism. This mechanism effectively dephases the electron spin on a time scale of nanoseconds. Localizing the charge carriers [43, 44] can suppress such momentum-dependent dephasing mechanisms. Therefore, the spin lifetime of a localized charge carrier in a QD can greatly exceed the corresponding lifetime of a free carrier. The remaining dominant relaxation channel for localized charge carriers is through hyperfine interaction with the surrounding bath of nuclear spins [45, 46]. Such an interaction of a single charge carrier spin with many nuclear spins within the volume of its wave function is usually called the central spin problem. The bath of nuclear spin acts as an effective fluctuating magnetic field, the Overhauser field [47], that dephases the spin. Unlike the *s*-type Bloch wave function of electrons, holes have a *p*-type wave function that falls to zero at the sites of the surrounding lattice atoms [48]. Therefore, the hole spins are protected from a significant part of the hyperfine interaction through the shape of their hole wave function. The relative influence of the Overhauser field can be reduced even further by applying an additional external magnetic field. In such experiments, long spin lifetimes on the order of up to several 100 μs have been reported [25, 31].

III/V Quantum Dots

All in all, quantum dots provide an atom-like platform that can be used to realize qubits with potentially very long coherence times [42]. This allowed many quantum-optical experiments to be transferred from atomic systems to the solid-state domain. The most notable are single-photon emission [49, 50], observations of Rabi oscillations [51, 52, 53], and generation of entangled photon pairs [54]. However, the isolation of the so-realized qubits from their environment is not

perfect. In particular, the solid-state environment can induce specific detrimental effects not present in other domains.

One example of these detrimental effects is a fluctuating residual charge distribution near the QD. The accompanying fluctuation of the electric field experienced by the QD can cause a corresponding undesired fluctuation in the resonance frequency of the optical transition [55]. Another example is the asymmetric shape of the randomly self-organized QD. The ground and excited QD states strongly depend on the shape of the QD [56]. Therefore, matching the emission energies of two qubits may constitute a problem. For some QD samples, this asymmetry can be removed by the recently introduced strain tuning technique. The idea is to mechanically deform the sample to effectively make a single QD from the sample perfectly symmetrical [57, 58]. However, this tuning can usually only optimize just one of the QD states.

Even for a perfectly symmetrical QD, the ground and excited states can be isolated quite poorly from the environment. This remaining coupling can lead to some rather peculiar spin relaxation channels. For example, poor isolation of the excited state can lead to a non-radiative decay through a process similar to Auger recombination in atoms [59, 60, 61, 62]. In this process, the charge carrier is ejected from the QD instead of returning to the ground state by emitting a photon. Alternatively, poor ground state isolation can lead to the direct ejection of the charge carrier through an internal photoeffect [63, 64]. When the charge carrier cools down and returns to the QD, its spin has lost all coherence with its past self due to the much faster spin relaxation mechanisms for free carriers. Therefore, these two processes effectively create a measurement-induced spin relaxation mechanism [65]. Depending on the impact of these relaxation channels, they might restrict the applicability of QDs as qubits.

All possible spin relaxation channels must be considered when designing future QD devices. Furthermore, knowledge about the magnitude of these relaxation channels in the regime when the device is operated is essential. Preferably, techniques that allow the QD system to remain in a steady state close to the thermal equilibrium or the potential operation point of the future device should be used. An example of such a technique is spin noise spectroscopy (SNS). This kind of spectroscopy can be used to investigate the spin and charge dynamics of a QD system in the quasi-resonant driving regime necessary for most quantum-optical experiments [66, 67].

Spin Noise Spectroscopy

Spin noise spectroscopy is a technique that probes the steady state of the investigated spin system. SNS was initially developed to study the spin dynamics of metal vapors [68, 69, 70]. Then it was adapted to the solid-state environment [71] and further enhanced for the spectroscopy of single charges trapped in quantum dots [72].

Many investigation techniques in the solid-state domain require experiments to produce non-equilibrium states. For example, for (polarization resolved) photoluminescence, free charge carriers or higher excited states must be created. Pump-probe spectroscopy usually involves large probe intensities necessary to keep the integration times short. Results gained from spectroscopy of these non-equilibrium states do not necessarily have to represent the dynamics of the unperturbed system. In contrast, SNS does not require non-equilibrium states [73, 74]. In fact, the perturbation exerted by a SNS experiment on a probed system can be made almost negligible.

A spin system at a finite temperature experiences small random fluctuations in spin polarization. Macroscopically, these spin fluctuations become apparent as fluctuations of the sample's dielectric response. Linearly polarized laser light passing through the sample experiences these instantaneous changes in optical activity that get translated into a corresponding rotation of the polarization plane or increased ellipticity of the resulting polarization state [75]. SNS resolves and analyzes these polarization fluctuations in the frequency domain to recover the underlying spin dynamics [76].

Depending on the investigated system, the intensity, and the detuning regime, spin noise spectroscopy can be used to probe spin relaxation and dephasing times, the spin precession frequency, the strength of the hyperfine interaction, and the charge dynamics [73, 77, 67]. In the simplest case, the probe laser cannot influence the system's charge state and is detuned far from the optical resonance. Here, the steady state is equal to the thermal equilibrium. Then, the observed spin fluctuations are representative only of the spin system, as can be derived from the fluctuation-dissipation theorem [78]. If the laser is close to the resonance or can change the system's charge state, then the spin fluctuations represent the steady state to which the laser drives the spin system. In the latter case, the fluctuations include a contribution of the charge dynamics [79]. A detuning dependence and an effective model of possible dynamics are usually necessary to interpret these

results [67].

Homodyne SNS

Measurements on a single hole spin in an (In,Ga)As quantum dot revealed a strong intensity dependence of the spin relaxation even at very low probe intensities [72]. In this interesting but challenging regime, the signal of spin fluctuations becomes so weak that detection becomes difficult due to technical noise sources that are extrinsic to the investigated system [1]. In quantum optics, such challenging situations are usually countered by employing homodyne detection schemes that amplify the signal optically. The demand for such an “optical amplifier” quickly led to several fundamental experiments. A working amplification scheme was demonstrated in Refs. [80, 81] for conceptually similar pump-probe Faraday rotation experiments. Subsequently, a modified heterodyne scheme was implemented to detect spin noise at high radio frequencies that are difficult to access with photodiode detectors [2]. Another scheme increased the sensitivity of an experiment detecting the spin noise of donor-bound electrons in GaAs [3]. Finally, a scheme that detects only light scattered by the spin system was implemented to confirm the microscopical mechanism underlying spin noise spectroscopy [4].

Scope of the Thesis

The scope of this thesis focuses on two main topics: the development of a low-frequency homodyne spin noise spectroscopy experiment and measurements of spin and charge occupancy dynamics in a single quantum dot at high magnetic fields.

Low-frequency Homodyne SNS

Most homodyne and heterodyne amplification schemes are less challenging at high radio frequencies on the order of $\gtrsim 100$ MHz. Due to the high frequencies, the relative contribution of low-frequency noise sources within the laboratory can be managed more easily. However, at low probe intensities, the dynamics of a single localized hole spin are contained within a narrow sideband of less than a megahertz. Therefore, for this thesis, a proof-of-principle low-frequency (< 5 MHz) homodyne spin noise spectroscopy experiment was developed and evaluated using rubidium metal vapor as a sample system. The experiment was used to confirm

that the technical noise source can be overcome using the homodyne scheme, and the sensitivity of the spin noise experiment can be enhanced to the point of the standard quantum limit given by the photon shot noise.

Development of a Long-Term Cryogenic Optics Setup

Studies of quantum dots usually neglect the long-term stability of the sample and its cryogenic environment. Nevertheless, these considerations are crucial for future devices based on this platform. For this thesis, a cryogenic optics setup was constructed, and its performance was evaluated over more than a year using an (In,Ga)As quantum dot system. Investigated regions of the sample were precisely mapped, allowing repeated and reproducible focusing of the experiment onto a specific quantum dot. External control parameters like laser intensity were carefully characterized to prevent skews and drifts during long-term measurements. Finally, the cryogenic system was enhanced to be able to operate for extended periods of time. All these steps allowed the experiment to run on the same quantum dot for over six months. The challenges encountered along the way represent potential challenges that future quantum dot devices will have to overcome.

Spin and Charge Dynamics in (In,Ga)As QDs

During the long-term measurement, various aspects of the spin and occupancy dynamics of the selected quantum dot were observed using spin noise spectroscopy. This thesis concentrates on the quasi-resonant, non-equilibrium regime, where the probe laser strongly influences the steady state of the quantum dot system. In particular, the incoherent, measurement-induced spin relaxation mechanisms due to Auger recombination and photoeffect were investigated in depth at various probe intensity levels, detunings, and magnetic fields. The investigation revealed a so far underestimated influence of the photoeffect that is effective even at rather large detunings. At the same time, the influence of Auger recombination at high magnetic fields was observed to be negligible when compared with previous studies at lower magnetic fields.

Content of the Thesis

This thesis is structured as follows. Part I serves as an introduction to modern optical spin noise spectroscopy. Chapter 1 provides the important concept of PSD

and its relation to stochastic processes and their corresponding broadband signals. Properties of coherent and broadband incoherent signals are discussed, as well as how these properties can be estimated from finite data using the discrete Fourier transform (DFT). In chapter 2, important properties of the PSD estimates are discussed, and an estimation method for streamed data is proposed, which can be used to assess the quality of the estimate. Chapter 3 discusses noise spectroscopy in optically probed systems. This chapter introduces common technical and fundamental noise sources and explains their implications for PSD estimation of spin noise signals.

Part II presents the low-frequency spin noise spectroscopy experiment that was developed for this thesis. First, chapter 4 provides theoretical background information about the rubidium vapor spin system, the possible homodyne detection schemes, and their application to spin noise spectroscopy. Then, chapter 5 summarizes the experimental considerations necessary for the implemented homodyne scheme. Finally, chapter 6 discusses experimental results that confirm the theoretical predictions and highlights the remaining limitations of the experiment.

Part III documents the measurement infrastructure that was developed for the long-term cryogenic setup created for this thesis. Chapter 7 presents the estimation framework for external parameters like temperature and laser intensity. Chapter 8 covers the most important technical aspects of the cryostat, the confocal microscope, and other central components of the setup.

The final Part IV studies the non-equilibrium dynamics of a single quantum dot. In chapter 9, the main properties of the investigated quantum dot sample are summarized, and preliminary results are discussed. Then in chapter 10, an effective spin and charge dynamics model is developed, an extension of previous work in Refs. [74, 65, 67]. Chapter 11 addresses some limitations of the following measurements that directly resulted from the challenges encountered during the long-term experiment. Finally, in chapter 12, the experimental results are compared to theoretical predictions at various magnetic fields.

Part I

Noise Spectroscopy

1 Basic Concepts

Subsequent or parallel measurements of many natural processes inherently fluctuate, commonly known as noise. For classical systems, a measurable quantity describes the average macroscopic state. The system's microscopic constituents are unresolved, but their internal state contributes to the result and introduces a fluctuating uncertainty into the instantaneous measurement. For quantum-mechanical systems, the uncertainty of the outcome of a measurement is a much more fundamental property. In both cases, the noise *appears* completely random in the time domain. However, it follows a fixed distribution determined by the specifics of the measured system. Given an infinite amount of time, this statistical distribution could be measured exactly. This asymptotic limit is, of course, not achievable for a realistic measurement. Instead, the noise spectroscopy (NS) techniques aim to estimate the statistical distribution in the frequency domain from a data recording with finite length. The magnitude and shape of this distribution then reveal the system's properties that were previously hidden behind the noise and not directly accessible.

This chapter serves as a brief reminder of the most important theoretical ideas necessary to explain the concepts of noise spectroscopy (NS). First, section §1.1 discusses the Fourier transform (FT) and its properties for continuous signals, and the idea of power spectral density (PSD) is introduced for coherent and incoherent signals. Then, section §1.2 explains the implications imposed by the discrete sampling of signals modifying the continuous FT into the discrete-time Fourier transform (DTFT). Section §1.3 introduces the discrete Fourier transform (DFT) by further restricting the transform to a window, i.e., a finite amount of experimental data samples, and discusses the effects of this implied windowing of the initial signals on the estimated spectra for both signal classes.

1.1 Continuous Fourier Transform and Autocorrelation

The FT of a real signal $f(t)$ has the meaning of a spectrum, i.e., the decomposition of the signal into complex oscillations that can be put back together using the inverse FT. For signal analysis, it is helpful to define the FT in the following way¹:

$$\tilde{f}(\nu) := \mathcal{F}[f](\nu) = \int_{-\infty}^{\infty} f(t) e^{-i2\pi\nu t} dt, \quad (1.1)$$

$$f(t) := \mathcal{F}^{-1}[\tilde{f}](t) = \int_{-\infty}^{\infty} \tilde{f}(\nu) e^{i2\pi\nu t} d\nu, \quad (1.2)$$

where $f(t)$ is some continuous-time signal. This definition has the benefit of not having a normalization factor before the integral; hence the inverse transform is exactly the conjugate of the forward transform. For example, if the unit of $f(t)$ is V, then the unit of $\tilde{f}(\nu)$ is V Hz^{-1} , i.e., a magnitude density. The existence of these integrals strongly depends on what class of signals f belongs to. Even the treatment of the simplest signal that stays at a constant level for all times ($f = 1$) requires the math to be extended to generalized functions or distributions. Using the employed FT convention, the Fourier spectrum of $f = 1$ is:

$$\mathcal{F}[f](\nu) = \int_{-\infty}^{\infty} e^{-i2\pi\nu t} dt = \delta(\nu).$$

Here, $\delta(\nu)$ is the Dirac distribution that is centered at $\nu = 0$, which is the limit of an increasingly narrow peak (of *any* shape) whose area is constant and equal to 1. Therefore, the unit of $\delta(\nu)$ is reciprocal to the unit of its argument, i.e., Hz^{-1} in this example.

1.1.1 Coherent Signals

The $f = 1$ signal belongs to the class of coherent signals or pure tones. Oscillations like $f(t) = a_0 \cos(2\pi\xi_0 t + \varphi_0)$ continue for all times and therefore have infinite *total power*. Here, the term power is used in a generalized sense of signal analysis and means the integrated *square of the magnitude*. The power in a finite time interval $(-\tau, \tau)$ is finite, i.e., by multiplying the signal f with a window function $w_\tau(t)$ that is 1 inside the interval and 0 otherwise:

¹This corresponds to Mathematica option `FourierParameters->\{0,-2Pi\}` to `FourierTransform`

$$\mathfrak{P}_\tau = \int_{-\infty}^{\infty} |f_\tau(t)|^2 dt = \int_{-\tau}^{+\tau} |f(t)|^2 dt < \infty,$$

where $f_\tau(t) = f(t) \cdot w(t)$. Using Parseval's theorem, it can be shown that this finite power is spread over the spectrum of $f_\tau(t)$ [82]:

$$\mathfrak{P}_\tau = \int_{-\infty}^{\infty} |f_\tau(t)|^2 dt = \int_{-\infty}^{+\infty} |\tilde{f}_\tau(\nu)|^2 d\nu. \quad (1.3)$$

Now, when the limit $\tau \rightarrow \infty$ is approached, both sides of the equation must stay equal. However, while either side of the equation grows toward ∞ , they do so in a reciprocal way. The time domain signal broadens while the frequency domain power distribution narrows. This explains why the limit of $\tau \rightarrow \infty$ results in infinitely large and narrow peaks at $\pm \xi_0$, as the initial real oscillation consists of two complex oscillations with inverse frequencies.

Because the signal is defined for all times, its total power is usually of little interest. Therefore, a better quantity is the average power, which is defined as:

$$\mathfrak{P} = \lim_{\tau \rightarrow \infty} \frac{1}{2\tau} \int_{-\tau}^{+\tau} |f(t)|^2 dt = \lim_{\tau \rightarrow \infty} \frac{1}{2\tau} \int_{-\infty}^{+\infty} |f_\tau(t)|^2 dt.$$

As f is a cosine oscillation, its average power is $\mathfrak{P} = a_0^2/2$ (given in units of V^2). From Eq. (1.3), it is then easy to see why the spectrum of average power is finite, as shown below.

The Fourier spectrum of the windowed signal $f_\tau(t)$ can be expressed using the convolution theorem as a product of the FTs of the window and the FTs of the initial signal. Generally, the convolution theorem has the form:

$$\begin{aligned} \mathcal{F}[f * g](\nu) &= \mathcal{F}\left[\int_{-\infty}^{\infty} f(u)g(t-u) du\right] = \mathcal{F}[f] \mathcal{F}[g] \\ \mathcal{F}[f \cdot g](\nu) &= \mathcal{F}\left[\int_{-\infty}^{\infty} \tilde{f}(\mu)\tilde{g}(\nu-\mu) d\mu\right] = \mathcal{F}[f] * \mathcal{F}[g]. \end{aligned} \quad (1.4)$$

The FTs of the *symmetric* window w_τ and f are (assuming $\varphi_0 = 0$):

$$\begin{aligned} \tilde{w}_\tau(\nu) &= \frac{\sin(2\pi\nu\tau)}{\pi\nu} \\ f(t) &= a_0 \cos(2\pi\xi_0 t) = \frac{a_0}{2} (\exp(-i2\pi\xi_0 t) + \exp(+i2\pi\xi_0 t)) \\ \tilde{f}(\nu) &= \frac{a_0}{2} (\delta(\nu - \xi_0) + \delta(\nu + \xi_0)) \end{aligned} \quad (1.5)$$

1 Basic Concepts

and the $1/2\tau$ limit of the average power is then just another expression of the δ distribution:

$$\begin{aligned} \lim_{\tau \rightarrow \infty} \frac{1}{2\tau} \int_{-\infty}^{+\infty} |\tilde{f}_\tau(\nu)|^2 d\nu &= \int_{-\infty}^{+\infty} \lim_{\tau \rightarrow \infty} \frac{1}{2\tau} |(\tilde{f} * \tilde{w}_\tau)(\nu)|^2 d\nu \\ &= \int_{-\infty}^{+\infty} \frac{a_0^2}{4} (\delta(\nu - \xi_0) + \delta(\nu + \xi_0)) d\nu \\ &= \frac{a_0^2}{2} = \mathfrak{P}. \end{aligned}$$

In other words, even though the average power is finite, the average power spectrum is still a δ distribution like the initial Fourier amplitude spectrum. This is the distinguishing feature of the class of *coherent* signals. Arbitrary *countable* superpositions of pure tones remain coherent: they can be decomposed into their constituent pure tones by the FT, as seen above. The spectrum of the superposition is just a sum of δ distributions.

The power spectrum of the cosine oscillation can also be acquired differently using the convolution theorem and choosing $g(t) = f^*(-t) = f(-t)$. First of all, the Fourier transform of g becomes the complex conjugate of the transform of f :

$$\begin{aligned} \mathcal{F}[g] &= \mathcal{F}[f^*(-t)] = \int_{-\infty}^{\infty} f^*(-t) e^{-i2\pi\nu t} dt && (t \rightarrow -t) \\ &= \int_{-\infty}^{\infty} f^*(t) e^{i2\pi\nu t} dt \\ &= \mathcal{F}^{-1}[f^*] = (\mathcal{F}[f])^*. \end{aligned}$$

With that in mind, the integrand of Eq. (1.3) can be expressed as the FT of the convolution of f with itself:

$$\begin{aligned} |\mathcal{F}[f]|^2 &= \mathcal{F}[f] \mathcal{F}[g] = \mathcal{F}[f * g] = \mathcal{F}\left[\int_{-\infty}^{\infty} f(u)g^*(t-u) du\right] && (u \rightarrow u+t) \\ &= \mathcal{F}\left[\int_{-\infty}^{\infty} f^*(u)f(t+u) du\right] \\ &= \mathcal{F}[c_f(t)](\nu) =: \tilde{c}_f(\nu). \end{aligned}$$

Here, $c_f(t)$ is the autocorrelation function (ACF) of f . Because of the infinite power of f , only the average of $c_f(t)$ is meaningful:

$$\begin{aligned}
 \lim_{\tau \rightarrow \infty} \frac{1}{2\tau} \int_{-\infty}^{+\infty} \mathcal{F}[c_{f,\tau}(t)](\nu)^2 d\nu &= \int_{-\infty}^{+\infty} \mathcal{F} \left[\lim_{\tau \rightarrow \infty} \frac{1}{2\tau} \int_{-\tau}^{+\tau} f(t')f(t'+t) dt' \right] (\nu) d\nu \\
 &= \int_{-\infty}^{+\infty} \mathcal{F} \left[\frac{a_0^2}{2} \cos(2\pi\xi_0 t) \right] (\nu) d\nu \\
 &= \int_{-\infty}^{+\infty} \frac{a_0^2}{4} (\delta(\nu - \xi_0) + \delta(\nu + \xi_0)) d\nu \\
 &= \frac{a_0^2}{2} = \mathfrak{P}.
 \end{aligned}$$

The FT of the ACF of f , $\tilde{c}_f(\nu)$, yields the average power spectrum of f . It can be thought of as the distribution of power in the frequency domain, the PSD of f (in units of V^2/Hz):

$$\mathfrak{S}_f(\nu) := \lim_{\tau \rightarrow \infty} \frac{1}{2\tau} \mathcal{F}[c_{f,\tau}(t)](\nu).$$

Even though this identity looks formally quite similar to the statement of the Wiener–Khinchin theorem (WKT), as discussed below, this identity is a simple consequence of the convolution theorem, and the two should not be confused [83].

1.1.2 Incoherent Signals

Incoherent signals are signals that have a smooth spectrum within their bandwidth and are the subject of NS, i.e., broadband noise signals. A noise signal can be mathematically modeled as a *stochastic process* $X(t)$ that describes the statistical properties of the signal. To limit the scope of this introduction, for the most part, only “well-behaved” random processes are considered, whose statistical properties do not depend on time (wide-sense stationary random processes). Of course, the experimental signals or realizations of the stochastic process are still random. While each recorded realization follows the underlying statistics, it is a priori not clear why this results (in any sense) in a reproducible “constant” spectrum. For the sake of argument, it is useful to take a step back and consider a single realization of a noise signal and treat it as a deterministic signal.

Because f is a realization of a stochastic process, its ACF can be expressed in a more appropriate way using the statistical properties of the *stationary* process itself:

$$c_X(\tau) = \langle X(t)X(t+\tau) \rangle \quad \text{for all } t,$$

1 Basic Concepts

where the *finite* expected value (ensemble average) $\langle \dots \rangle$ over all realizations of X depends only on the time delay τ and not on the particular value of t . Now, the WKT states that the power, i.e., the variance of X if $\langle X(t) \rangle = 0$, of a stationary process X in a frequency band (ν_1, ν_2) is given by the integral over the FT of $c_X(\tau)$:

$$\mathfrak{P}_{(\nu_1, \nu_2)} = \int_{\nu_1}^{\nu_2} \tilde{c}_X(\nu) d\nu,$$

that is, the PSD of any given realization of $X(t)$ is $\mathfrak{S}_f(\nu) = \mathfrak{S}_X(\nu) = \tilde{c}_X(\nu)$. For many wide sense stationary processes, the power distribution of any sufficiently long realization f of the process X over the time window τ_w eventually converges toward the expected value over all realizations and:

$$c_X(\tau) = \lim_{\tau_w \rightarrow \infty} \frac{1}{\tau_w} \int_0^{\tau_w} f(t)f(t + \tau) dt.$$

These kinds of processes are called *ergodic*. The link between their two correlation functions explains why the observed power spectrum of any realization eventually becomes stationary for many realistic processes [83].

1.2 Discrete-Time Fourier Transform

While the continuous FT is a useful theoretical tool, real experiments can neither “sample” a continuous function nor record an unbounded, infinite spectrum. For the time domain, this usually means that the signal f can only be sampled at discrete time points $t_k = k/\nu_s$ with a fixed sampling frequency ν_s . This sampling operation is not unique: two signals that coincide at the sampling points but differ between two samples, i.e., during the sample period $\tau_s = 1/\nu_s$, will have the same sampled spectrum. For this reason, this kind of FT, the DTFT, necessarily has to sacrifice some universality regarding what signals it can be applied to while yielding uniquely different results.

1.2.1 Discrete Sampling

More formally, the sampling operation can be expressed by multiplying the initial signal f with an infinite impulse train that consists of δ functions spaced τ_s apart in the time domain (the sha function, given in units of Hz):

$$\text{III}_{\tau_s}(t) = \sum_{k \in \mathbb{Z}} \delta(t - k\tau_s) = \sum_{k \in \mathbb{Z}} \delta\left(t - \frac{k}{\nu_s}\right).$$

The spectrum of the sampled signal $f_\delta(t) = f(t) \cdot \text{III}_{\tau_s}(t)$ can then be calculated using the convolution theorem of the regular, continuous FT:

$$\begin{aligned} \mathcal{F}[f_\delta](\nu) &= \mathcal{F}[f \cdot \text{III}_{\tau_s}](\nu) = (\mathcal{F}[f] * \text{III}_{\tau_s})(\nu) \\ &= (\tilde{f} * \nu_s \text{III}_{\nu_s})(\nu) = \nu_s \sum_{k \in \mathbb{Z}} \tilde{f}(\nu - k\nu_s). \end{aligned}$$

The result is a spectrum of the initial signal f multiplied by the sample rate ν_s , shifted by integer multiples of the sample rate ν_s , and superimposed onto itself. The units of $\mathcal{F}[f_\delta](\nu)$ are V, i.e., the DTFT no longer yields an amplitude density. Alternatively, the spectrum of the sampled signal f_δ can also be calculated directly:

$$\begin{aligned} \tilde{f}_\delta(\nu) &= \mathcal{F}[f_\delta](\nu) = \int_{\mathbb{R}} f_\delta(t) e^{-i2\pi\nu t} dt \\ &= \int_{\mathbb{R}} \sum_{k \in \mathbb{Z}} f(t) \delta(t - t_k) e^{-i2\pi\nu t} dt \\ &= \sum_{k \in \mathbb{Z}} f_k e^{-i2\pi\nu t_k} =: \mathcal{F}_{\mathbb{Z}}[f](\nu), \end{aligned} \quad (1.6)$$

where $f_k = f(k\tau_s) = f(k/\nu_s)$. The last line in Eq. (1.6) is the usual definition of the DTFT $\mathcal{F}_{\mathbb{Z}}$ of f . In this form, it is easy to see that while the spectrum \tilde{f} is arbitrary, the spectrum \tilde{f}_δ is a periodic function with the period ν_s , as can be easily seen from a straight-forward calculation:

$$\tilde{f}_\delta(\nu + \nu_s) = \sum_{k \in \mathbb{Z}} f_k e^{-i2\pi(\nu + \nu_s) \frac{k}{\nu_s}} = \sum_{k \in \mathbb{Z}} f_k e^{-i2\pi\nu \frac{k}{\nu_s}} \underbrace{e^{-i2\pi k}}_{=1} = \tilde{f}_\delta(\nu).$$

1 Basic Concepts

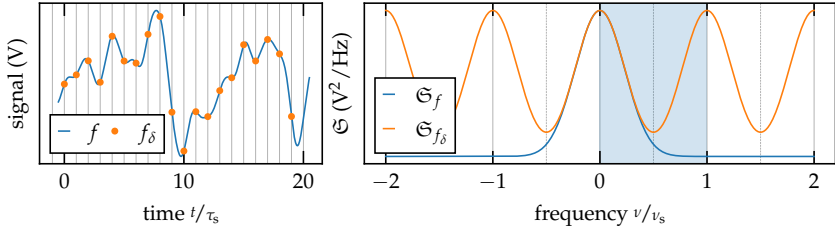


Figure 1.1: Left panel: sketch of a small part of a continuous signal f and its sampled version f_δ . Right panel: spectrum of \tilde{f} and its sampled version \tilde{f}_δ .

The coefficients f_k at each time t_k can be recovered by integrating over a single period of ν_s because \tilde{f}_δ is periodic:

$$\begin{aligned}
 f_l &= \frac{1}{\nu_s} \int_0^{\nu_s} \tilde{f}_\delta(\nu) e^{i2\pi\nu \frac{l}{\nu_s}} d\nu & (1.7) \\
 &= \frac{1}{\nu_s} \int_0^{\nu_s} \sum_{k \in \mathbb{Z}} f_k e^{-i2\pi\nu \frac{k}{\nu_s}} e^{i2\pi\nu \frac{l}{\nu_s}} d\nu = \sum_{k \in \mathbb{Z}} f_k \frac{1}{\nu_s} \int_0^{\nu_s} e^{-i2\pi\nu \frac{k-l}{\nu_s}} d\nu \\
 &= \sum_{k \in \mathbb{Z}} f_k \delta_{k,l},
 \end{aligned}$$

where both sides of Eq. (1.6) have been multiplied by $e^{i2\pi\nu \frac{l}{\nu_s}}$ before integrating over a single period of ν_s and using the orthogonality relation:

$$\frac{1}{\nu_s} \int_0^{\nu_s} e^{-i2\pi\nu \frac{k-l}{\nu_s}} d\nu = \delta_{k,l}.$$

Equation (1.7) is usually taken as the definition of the inverse DTFT, i.e., the actual sampling is taken as implied:

$$f_l = f\left(\frac{l}{\nu_s}\right) = \int_{t_l-\epsilon}^{t_l+\epsilon} \mathcal{F}_{\mathbb{Z}}^{-1}[\tilde{f}_\delta](t) = \frac{1}{\nu_s} \int_0^{\nu_s} \tilde{f}_\delta(\nu) e^{i2\pi\nu \frac{l}{\nu_s}} d\nu. \quad (1.8)$$

1.2.2 Power Spectrum and Aliasing

The power spectrum of sampled signals can be expressed using the DTFT by accounting for the sampling bandwidth and taking the limit using a window w_N that is 1 only in a *symmetric* interval of $\pm N$ samples:

$$w_N \left(\frac{n}{v_s} \right) = \begin{cases} 1 & n \in [-N, \dots, +N] \\ 0 & \text{else} \end{cases}.$$

Similarly to the continuous case, the PSD is then just the limit:

$$\begin{aligned} \mathfrak{S}_{f_\delta}(v) &= \lim_{N \rightarrow \infty} v_s \frac{1}{2N+1} \left| \frac{1}{v_s} \sum_{n=-N}^N f_n e^{-i2\pi v t_n} \right|^2 \\ &= \frac{1}{v_s} \lim_{N \rightarrow \infty} \frac{1}{2N+1} |\mathcal{F}_{\mathbb{Z}} [f w_N](v)|^2. \end{aligned} \quad (1.9)$$

Two PSD spectra of f and f_δ are sketched in Fig. 1.1 for an example broadband signal: the spectrum of f_δ is periodic with a period of v_s and faithfully reproduces the spectrum of f only around the peaks at $v_s \cdot \mathbb{Z}$ while it bends away from the true spectrum at $v_s \cdot \mathbb{Z} \pm v_s/2$. The discrete sampling of an *arbitrary* function f forces its corresponding spectrum \tilde{f}_δ to be periodic. This result is quite striking, as the transform stops being unique: all frequency components that are larger than $v_s/2$ do not appear in their right place in the spectrum of \tilde{f}_δ . Instead, the power of these components appears somewhere else in the periodic spectrum, and it is impossible to determine from the spectrum alone what the initial signal f looked like. The frequency components get *aliased* to a different frequency. A unique mapping is only possible when the initial signal f contains no components at frequencies larger than $v_s/2$ to begin with, and the Nyquist–Shannon sampling theorem formalizes this limitation [82].

The DTFT remains a theoretical object that requires knowledge of the analyzed signal for all times t_k . However, introducing sampling results in the aliasing phenomenon, a practical consequence imposed on the acquisition of experimental signals. Aliasing can potentially contaminate *all* frequency components of a spectrum to some degree with the power of the high-frequency components. The input signal must be low-pass filtered, removing these components to prevent aliasing. This filtering must happen before the DTFT is applied and *before the signal is sampled*, i.e., at the analog recording stage. Aliasing is not an effect of the DTFT itself but a consequence of the signal being sampled in the time domain.

1.3 Discrete Fourier Transform

Going from continuous FT to DTFT, the signal “data” amount is limited from an uncountable amount to a countable but still infinite set. The next step is to limit the number of frequencies analyzed. The choice is usually N equidistantly spaced frequencies that cover the frequency span $[0, \nu_s)$, which is a period of \tilde{f}_δ (the shaded area in the right panel of Fig. 1.1):

$$\nu_k = \nu_s \frac{k}{N}, \quad k = 0, \dots, N - 1.$$

1.3.1 Sampling the Discrete Time Fourier Transform

The DTFT can be evaluated just for the frequency components at the selected frequencies to yield:

$$\begin{aligned} \tilde{f}_\delta(\nu_k) &= \sum_{n \in \mathbb{Z}} f_n e^{-i2\pi\nu_k t_n} = \sum_{n \in \mathbb{Z}} f_n e^{-i2\pi\nu_s \frac{k}{N} \frac{n}{\nu_s}} \\ &= \sum_{n \in \mathbb{Z}} f_n e^{-i\frac{2\pi}{N}kn} = \sum_{l \in \mathbb{Z}} \sum_{n=0}^{N-1} f_{n-IN} e^{-i\frac{2\pi}{N}(n-IN)k} \\ &= \sum_{n=0}^{N-1} \left(\sum_{l \in \mathbb{Z}} f_{n-IN} \right) e^{-i\frac{2\pi}{N}nk} \\ &= \sum_{n=0}^{N-1} g[f]_n e^{-i\frac{2\pi}{N}nk} =: \mathcal{F}_N[g[f]]_k, \end{aligned} \tag{1.10}$$

where the infinite summation over $n \in \mathbb{Z}$ is replaced by a finite summation over $n \in 0, \dots, N - 1$ and an infinite summation over $l \in \mathbb{Z}$. This replacement is always possible, and the second summation yields a new sequence $g[f]_n = \sum_{l \in \mathbb{Z}} f_{n-IN}$. Then, Eq. (1.10) yields the usual definition for the DFT \mathcal{F}_N of a corresponding function $g[f](t)$, which is the periodization of f . This new function $g[f](t)$ is related to but is, in general, not equal to f : it is an infinite sum of the initial signal $f(t)$ shifted by integer multiples of the sampling interval $N\tau_s$.

The DTFT sampling in the time domain restricted the signal’s frequency content. Similarly, sampling in the frequency domain restricts the signal’s shape in the time domain. For $g[f]_n$ to be equal to f_n for all sampled points, $f(t)$ has to be zero for all times outside of the sampling interval. For an arbitrary signal f , this can be achieved by multiplying it with a rectangular (Dirichlet) window function $w_\square(t)$

[84]:

$$w_{\square}(t) = \begin{cases} 1 & t \in [0, N\tau_s) \\ 0 & \text{else.} \end{cases}$$

Then, the periodization $g[f \cdot w_{\square}](t)$ is equal to the initial signal $f(t)$ inside the sampling interval $t \in [0, N\tau_s)$, and the value of its DFT at frequency ν_k is equal to:

$$\begin{aligned} G[f \cdot w_{\square}]_k &= \mathcal{F}_N [g[f \cdot w_{\square}]]_k \\ &= \sum_{n=0}^{N-1} g[f \cdot w_{\square}]_n e^{-i \frac{2\pi}{N} nk} = \sum_{n \in \mathbb{Z}} f_n w_n e^{-i 2\pi \nu_k t_n} \\ &= \mathcal{F}_{\mathbb{Z}} [f \cdot w_{\square}](\nu_k) \\ &= \mathcal{F} [f \cdot w_{\square} \cdot \text{III}_{\tau_s}](\nu_k). \end{aligned} \quad (1.11)$$

Putting in arbitrary N samples of some signal *implies* using the rectangular window w_{\square} because this is what is necessary to make f and $g[f \cdot w_{\square}]$ equal. However, using any window will alter the spectrum in some way, and using w_{\square} as defined above is not always the optimal choice, as is discussed below in section §1.3.6.

Because of the symmetry of the FT, from Eq. (1.7), it is easy to see that the inverse FT of a discretely sampled spectrum in the *frequency* domain leads to a periodic function in the *time* domain. Consequently, the time domain samples can be reconstructed from the DFT:

$$f_l = g[f \cdot w_{\square}]_l = \frac{1}{N} \sum_{n=0}^{N-1} G[f \cdot w_{\square}]_n e^{i \frac{2\pi}{N} nl} =: \mathcal{F}_N^{-1} [G]_l, \quad (1.12)$$

and the δ sampling in *both* the frequency and time domains is implied.

1.3.2 Fast Fourier Transform

In Eq. (1.10), the sampling δ distributions are hidden away, and only a mapping between the two kinds of coefficients remains. In fact, the DFT has become just a matrix operation [85]:

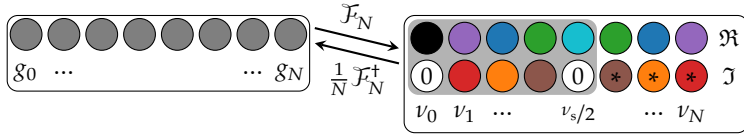


Figure 1.2: Coefficients of a real-valued discrete Fourier transform (DFT). Only the complex coefficients in the shaded region are unique and are returned by fast Fourier transform (FFT) libraries. Neither the ν_0 nor the $\nu_{N/2} = \nu_s/2$ coefficients carry any phase information. The N inputs are uniquely mapped to $N/2 + 1$ outputs, however only N independent real and imaginary parts exist.

$$G_k = \sum_{l=0}^{N-1} (\mathcal{F}_N)_{k,l} g_l \iff \mathbf{G} = \mathcal{F}_N \cdot \mathbf{g} \quad (1.13)$$

$$g_l = \frac{1}{N} \sum_{k=0}^{N-1} (\mathcal{F}_N^+)_{k,l} G_k \iff \mathbf{g} = \frac{1}{N} \mathcal{F}_N^+ \cdot \mathbf{G}, \quad (1.14)$$

where $(\mathcal{F}_N)_{k,l} = e^{-i \frac{2\pi}{N} kl}$. That is, to compute the DFT using Eq. (1.13), N^2 multiplication and addition operations are necessary. However, the matrix \mathcal{F}_N has internal symmetries that can be exploited to reduce the number of operations to about $\approx N \log(N)$. The algorithms that compute G_k using less than N^2 operations are called fast Fourier transform (FFT) algorithms. One of the most famous FFT algorithms is the radix-2 algorithm [82], which is applicable when N is a power of two, $N = 2^m, m \in \mathbb{N}_+$. For this reason, the usual advice is to choose N accordingly. Modern libraries like `FFTW`² contain algorithms that have comparable performance to that of the radix-2 algorithm even when N is not a power of two. Whenever the DFT is mentioned in the rest of this text, it is implied that it is calculated using one of these FFT algorithms.

1.3.3 Real-valued Discrete Fourier Transform

In the context of NS, the analyzed signals are usually real-valued, and for such inputs, the DFT has yet another symmetry. The matrix \mathcal{F}_N has full rank, and it preserves the dimension of the input and output vector spaces. A real-valued in-

²Fastest Fourier Transform in the West, <https://www.fftw.org/>

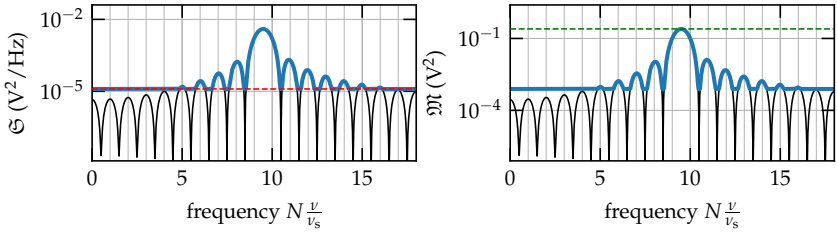


Figure 1.3: Sketch of the two ways to interpret the discrete Fourier transform (DFT) spectrum of $|G|^2$ ($N = 64$). The pure cosine spectrum is depicted in black. Both panels show the corresponding discrete-time Fourier transform (DTFT) spectra of a cosine oscillation on top of a broadband background. The left panel is scaled as a periodogram \underline{S}_f so that the broadband noise level (red) can be estimated correctly, while the right panel is scaled as the magnitude squared spectrum \underline{M}_f so that the average power of the cosine (green) can be estimated. Both quantities cannot be estimated simultaneously.

put g_l has N degrees of freedom, but the output consists of N complex values G_k , i.e., $2N$ degrees of freedom. Therefore, not all of the real and imaginary parts can be independent. The relations between these parts are illustrated in Fig. 1.2 for $N = 8$. Only the first $N/2 + 1$ complex coefficients are unique and complex conjugates of the same coefficients repeat above the Nyquist frequency $\nu_n = \nu_{N/2} = \nu_s/2$ in inverted order. The zero frequency coefficient ν_0 cannot carry any phase information since $\sin(2\pi\nu_0 t) = 0$ when $\nu_0 = 0$, and therefore its imaginary part vanishes. A similar argument is valid for the “highest” frequency component $\nu_{N/2}$ at the Nyquist frequency. Therefore, N real numbers of the input in the time domain are uniquely mapped to N real numbers in the frequency domain. Consequently, libraries like FFTW usually output this unique set of values (the gray-shaded area in 1.2) and drop the redundant values to reduce computation time and memory consumption.

1.3.4 Finite Power

The physical interpretation of the implied window w_{\square} is as follows. All physical signals have a finite power. However, this initial power might appear virtually infinite compared to the power restricted within a sufficiently short window. The

measured finite number of data points within the window can only represent the power contained within it – not the large power distribution outside of it. How the power distribution inside of the window relates to the power distribution outside of it depends on the class of the signal considered and is quite different for coherent and incoherent signals. Furthermore, realistic signals almost always consist of a superposition of coherent and incoherent parts, and this can constitute a challenge when interpreting PSD spectra derived from finite sampled data. The scaling of the two signal classes is sketched in Fig. 1.3 for a signal that consists of the sum of a broadband noise source and a cosine oscillation.

Incoherent Signals

For broadband signals, the limit in Eq. (1.9) cannot be taken anymore, as the data is finite (limited by the implied window). Without the limit, the expression

$$\left(\underline{\mathfrak{S}}_f\right)_k = \frac{1}{\nu_s} \frac{1}{N} |G[f w_{\square}]_k|^2 \quad (1.15)$$

is called a *periodogram* estimate [82]. As only N points contribute to the periodogram, the estimate's variance should be quite high. The properties of $\underline{\mathfrak{S}}_f$ and methods for reducing this variance are discussed in more detail in chapter 2. Nevertheless, intuitively it is clear that sampling the smooth power spectrum of a broadband signal using only N points will produce a spectrum that has a finite spectral resolution but is otherwise an accurate representation of power distribution in the initial spectrum.

Coherent Signals

As explained in section §1.1.1, special math is necessary to express the infinite power properties of coherent signals. This math breaks down when the window limits the power. For example, the FT spectrum of the cosine in Eq. (1.5) consists of two δ distributions. The DTFT limits the maximal frequency content of the signal but still reproduces the δ spectrum through infinite sums in the time domain to retain the infinite power. It is not possible to express infinitely narrow (and infinitely tall) δ distributions using finite sums of finite values. As the DFT is a matrix multiplication, all that is available to it are finite points of finite value in both time and frequency domains. This means that even under theoretically perfect conditions, the DFT of coherent signals reproduces the impulse response of the acquisition

system, i.e., the window w_{\square} , and not the initial signal. The window's response is finite, so it maps the initial spectrum to a spectrum of finite *total* power.

The consequences of this mapping are discussed in more detail in section §1.3.5. The mapping itself can be observed using the cosine signal example $f(t) = a_0 \cos(2\pi\zeta_0 t)$, where the oscillation frequency is fixed to $\zeta_0 = m \frac{\nu_s}{N} < \nu_s$. The squared magnitude of the DFT (and not \mathfrak{S}_f) is equal to the average power of the cosine at its fundamental frequency:

$$\left(\underline{\mathfrak{M}}_f\right)_{\pm m} = \frac{1}{N^2} |G[f w_{\square}]_{\pm m}|^2 = \frac{|a_0|^2}{4} = \int_{\zeta_0 - \epsilon}^{\zeta_0 + \epsilon} \mathfrak{S}_f(\nu) d\nu. \quad (1.16)$$

The magnitude squared (MS) spectrum $\underline{\mathfrak{M}}_f$ (expressed in units of V^2) in Eq. (1.16) is sometimes confusingly called³ the “power spectrum” of f even though it yields the proper average power value only for coherent signals [86]. This mapping is helpful because it allows measuring the average power (i.e., the root mean square value) of coherent signals using a sufficiently fast sampling of the signal and minimal samples N .

Superpositions

The periodogram of a superposition of coherent and incoherent parts is a sum of the constituent's finite periodograms. Therefore, the power of the two dissimilar parts is *ambiguously* mapped to finite values of the superposition's periodogram estimate. This situation is particularly dire when the estimated PSD spectrum \mathfrak{S}_f is in a mean total power sense much weaker than the additional coherent part, see section §1.3.7 below. The MS spectrum of the oscillation is subject to the *spectral leakage* phenomenon that redistributes a part of the oscillation's power to *all* frequencies of the spectrum. In this case, these leaked parts can mask parts of the sought broadband spectrum. The response of the DFT has to be inspected in more detail to understand the source of the spectral leakage phenomenon.

1.3.5 Aliasing and Spectral Leakage

Unlike the theoretical FT, the DFT can be directly applied to empirical data, but several caveats must be considered that arise from the discrete sampling of both the time and frequency domains. Section §1.2 established that aliasing could be

³For example, MatLab and the Python package scipy use this terminology.

1 Basic Concepts

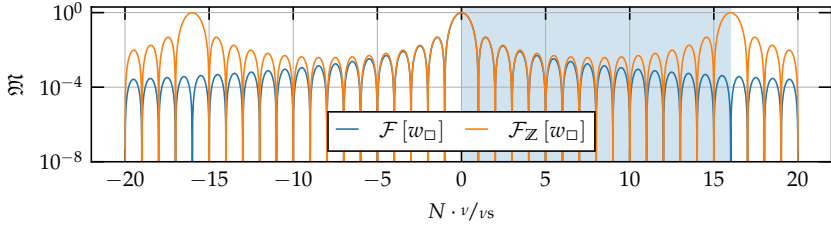


Figure 1.4: Comparison between the spectra of the continuous and the discretely sampled rectangular window w_{\square} .

prevented by restricting the frequency content of the input signal to lie below the Nyquist frequency $\nu_s/2$. However, because the derivation of the DFT required a periodization window like w_{\square} , the frequency content of *the window* also greatly matters, as seen from the identity in Eq. (1.11). Crucially, the step-like response in w_{\square} has *infinite* bandwidth, and therefore aliasing reappears and gravely changes the spectrum that the DFT actually computes.

The Spectrum of the Rectangular Window

From Eq. (1.11), it is easy to see that the DFT spectrum of the periodized version of f using the w_{\square} window, $G[f \cdot w_{\square}]_k$, is the convolution between the initial spectrum of f and the DTFT spectrum of the window:

$$\begin{aligned} G[f \cdot w_{\square}]_k &= \mathcal{F}[f \cdot w_{\square} \cdot \text{III}_{\tau_s}](\nu_k) \\ &= (\mathcal{F}[f] * \mathcal{F}[w_{\square} \cdot \text{III}_{\tau_s}])(\nu_k) \\ &= (\tilde{f} * \mathcal{F}_{\mathbb{Z}}[w_{\square}]). \end{aligned} \quad (1.17)$$

Therefore, the Dirichlet window's DTFT has to be calculated to get its impulse response. Once again, it is useful to start with the continuous FT spectrum of the window:

$$\mathcal{F}[w_{\square}](\nu) = \frac{\sin\left(2\pi \frac{\nu}{\nu_s} N \tau_s\right)}{2\pi \frac{\nu}{\nu_s}} - \mathbf{i} \frac{\sin^2\left(\pi \frac{\nu}{\nu_s} N\right)}{\pi \frac{\nu}{\nu_s}}.$$

The first term of $\mathcal{F}[w_{\square}](\nu)$ is a scaled sinc function, and the second term is a complex phase term that is a consequence of the asymmetry of the window at $t = 0$. A part of the corresponding MS spectrum is plotted in Fig. 1.4 in blue. Note

that the spectrum is plotted over relative frequencies that are multiplied by N . Plotting it this way highlights that the locations of the chosen DFT frequency bins coincide with that of the zeros in the spectrum. The spectrum consists of a main lobe at bin 0 and an infinite number of side lobes that are separated by zeros at all integer bin spacings except for 0, where the limit value of the spectrum is 1.

The DTFT transform of w_{\square} is [84]:

$$\mathcal{F}_{\mathbb{Z}}[w_{\square}](\nu) = \exp\left(-\pi \frac{\nu}{\nu_s} (N-1)\right) \frac{\sin(\pi \frac{\nu}{\nu_s} N)}{\sin(\pi \frac{\nu}{\nu_s})}.$$

A plot of the corresponding MS spectrum is plotted in orange in Fig. 1.4. Both spectra share the location of the zeros. Moreover, the main lobes of both spectra look almost exactly the same. Nevertheless, as expected, $\mathcal{F}_{\mathbb{Z}}[w_{\square}]$ is periodic with a period ν_s (shaded region, $N = 16$ for this example). This spectrum is called a periodic (aliased) sinc or Dirichlet kernel. The phase factor is a consequence of the finite number of bins that fit inside the window and therefore is one less than N : the N -th point already lies outside of the window [84].

Another way to calculate $\mathcal{F}_{\mathbb{Z}}[w_{\square}]$ is using the DFT identity in Eq. (1.11). The right-hand side of the equation is evaluated at the fixed DFT frequencies to obtain the DFT spectrum. Instead, any frequency can be put into the right-hand side to get the generalized or interpolated DFT spectrum:

$$\begin{aligned} \mathcal{G}_N[g](\nu) &:= \sum_{n=0}^{N-1} g_n e^{-i \frac{2\pi}{N} \nu n} = \sum_{n \in \mathbb{Z}} f_n w_n e^{-i 2\pi \nu_k t_n} \\ &= \mathcal{F}_{\mathbb{Z}}[f \cdot w_{\square}](\nu). \end{aligned}$$

Consequently, choosing $f = 1$ results in $\mathcal{G}_N[g[w_{\square}]] = \mathcal{F}_{\mathbb{Z}}[w_{\square}]$. The generalized DFT is much easier to calculate numerically for windows that are more complicated than w_{\square} , as it involves only a finite sum of the window weights $w_n = w(t_n)$.

What the DFT Actually Computes

A new aliasing effect gets reintroduced into the spectrum by violating the Nyquist criterion with the periodization window w_{\square} . This effect appears even though the analyzed signal contains no frequencies above $\nu_s/2$. Therefore, the window changes the spectrum that the DFT computes. The DFT spectrum of the general cosine os-

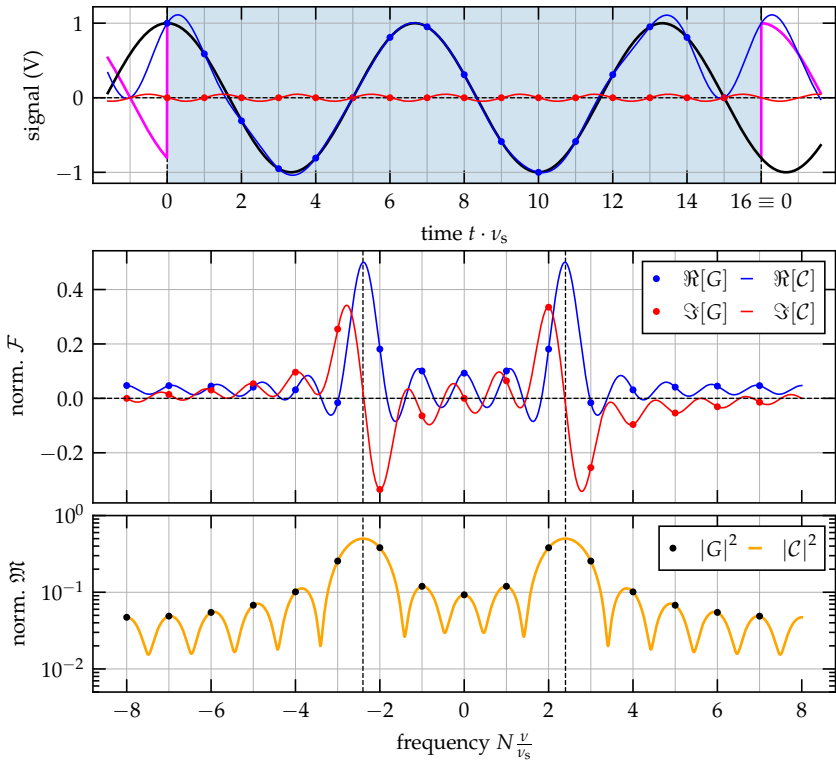


Figure 1.5: Top panel: the discrete Fourier transform (DFT) computes the spectrum of a periodic complex function h that coincides with the f (black) at the sampling points t_k in its real (blue) and imaginary (red) parts but looks quite different between the sampling points at the beginning and end of the interval. The function h is continuous at either end of the interval as opposed to the periodization (magenta) $g[f \cdot w_{\square}]$ of f . Middle and bottom panels: the DFT spectrum (dots) is a discrete sampling of N frequencies taken from the convolution of the Fourier transform (FT) of f and the discrete-time Fourier transform (DTFT) of w_{\square} , $\hat{f} * \mathcal{F}_{\mathbb{Z}}[w_{\square}]$, (solid lines).

cillation $f(t) = \cos(2\pi\xi_0 t)$ can be analyzed using Eq. (1.17). This time, the fundamental frequency $\xi_0 < \nu_s/2$ does not have to be one of the DFT frequencies. The DFT spectrum is:

$$\begin{aligned} \mathcal{G}_N [f \cdot w_{\square}] (\nu_k) &= (\tilde{f} * \mathcal{F}_{\mathbb{Z}} [w_{\square}]) (\nu) \\ &= (\mathcal{F}_{\mathbb{Z}} [w_{\square}] (\nu - \xi_0) + \mathcal{F}_{\mathbb{Z}} [w_{\square}] (\nu + \xi_0)) \Big|_{\nu=\nu_k} \quad (1.18) \\ &=: C(\nu_k). \end{aligned}$$

The spectrum is the sum of two copies of the w_{\square} window function's DTFT, shifted toward the positive and negative frequencies $\pm\xi_0$ of the oscillation, and sampled at the DFT frequencies. The situation is depicted in Fig. 1.5. The initial signal f is depicted in black in the top panel. Black dots designate the samples of f at times t_k . The periodization $g[f \cdot w_{\square}]_k$ of f is plotted in magenta and has an obvious discontinuity (infinite bandwidth jump) at both ends of the interval. The normalized real and imaginary parts of the DFT $G[f \cdot w_{\square}]_k$ are depicted as dots in the middle panel using blue and red colors, respectively, and the normalized MS spectrum is plotted in the lower panel. Moreover, the spectrum given by the convolution in Eq. (1.18) is plotted in the middle and lower panels.

The DFT samples the convolution spectrum $C(\nu_k)$ as intended and reveals the source of spectral leakage in the DFT spectrum. Because the choice of ξ_0 is arbitrary, so is also the location of the central lobe and zeros of $\mathcal{F}[w_{\square}]$ in the convolution spectrum $C(\nu_k)$. If the zeros do not align with the DFT frequencies, the power contained in the oscillation gets *redistributed* to all frequencies of the spectrum. The window's aliasing effect is masked away only when the zeros of $\mathcal{F}[w_{\square}]$ align with the DFT frequencies. This is the case when the oscillation perfectly fits into the sampled interval without a discontinuity (ξ_0 is divisible by ν_s/N).

In general, the DFT does not faithfully reproduce the frequency content of f . Instead, the spectrum belongs to a different function h . This can be easily seen by synthesizing h back from the DFT spectrum:

$$h(t) := \sum_{n=0}^{N-1} \frac{G[f \cdot w_{\square}]_k}{N} \exp(i2\pi \nu_k t).$$

This new function $h(t)$ is *complex*, and its real and imaginary parts are plotted in the top panel of Fig. 1.5 in blue and red, respectively. The function coincides in its real and imaginary parts with f at the sampling points and mostly follows the shape

1 Basic Concepts

of f except at the start and end of the interval. Because h consists only of a finite number of frequencies, it cannot reproduce the discontinuity of the periodization of $g [f \cdot w_{\square}]$. However, unlike f , the new function is periodic within the interval the window covers.

In summary, for any oscillation f in the time domain whose fundamental frequency $\tilde{\zeta}_0$ lies below half the sampling rate ν_s , there exists a complex periodic function h that, when sampled at the sampling points, coincides with the initial oscillation in its real and imaginary parts. The two functions f and h coincide only when $\tilde{\zeta}_0$ is divisible by ν_s/N . This new function h is periodic; hence its spectrum is discrete. These discrete frequencies by construction are situated at the DFT sampling frequencies. Again, the complex amplitudes at these frequencies are samples of another periodic function, whose discrete “spectrum” in the time domain consists of the initial sampling points. This function in the frequency domain is the link between the DFT and the continuous FT, as it is equal to the convolution of the spectrum of the initial oscillation f and the sampled spectrum of the window function. The DFT effectively just translates between the weights that define either function in the frequency or the time domains, and spectral leakage is a consequence of the mismatch between h and f .

1.3.6 Other Window Functions

The DFT does not reproduce spectra of signals with sharp or impulse-like spectra particularly well, as explained in section §1.3.5. Incoherent signals usually have a sufficiently smooth power spectrum, so spectral leakage is not a major challenge [82]. However, spectral leakage of additional oscillating components can mask the broadband spectrum. The spectral leakage depends only on the response of the employed window. Therefore, the damage caused by the coherent parts of the signal can be reduced by shaping this response using a window function that is not w_{\square} . It is important to note that the implied Dirichlet window w_{\square} cannot be “replaced” by another window. Therefore, any other window is realized just by shaping w_{\square} in a particular way.

Window Gains

For coherent signals, the unmodified DFT has an effective gain of N , as follows from Eq. (1.16). This value is the gain of the Dirichlet window w_{\square} , as $N =$

$\sum_{n=0}^{N-1} (w_{\square})_n$. This gain is altered for differently shaped windows, and Eq. (1.16) must be modified [86]:

$$\left(\underline{\mathfrak{M}}_f \right)_k = \frac{1}{\eta_M^2} |G [fw_{\circ}]_k|^2, \quad (1.19)$$

$$\eta_M = \sum_{n=0}^{N-1} (w_{\circ})_n,$$

where η_M is the magnitude gain of some window w_{\circ} .

Incoherent signals are mapped differently to the DFT spectrum. Their corresponding window gain is not described by η_M but by the power gain η_P instead. The Eq. (1.15) for the PSD of a windowed signal needs to be modified correspondingly to:

$$\left(\underline{\mathfrak{S}}_f \right)_k = \frac{1}{\nu_s} \frac{1}{\eta_P} |G [fw_{\circ}]_k|^2, \quad (1.20)$$

$$\eta_P = \sum_{n=0}^{N-1} (w_{\circ})_n^2,$$

The quantities

$$\hat{\nu}_{\Delta} = \nu_s \frac{\eta_P}{\eta_M^2} \quad \text{and} \quad \hat{N}_{\Delta} = N \frac{\eta_P}{\eta_M^2}$$

are the effective noise bandwidth and the normalized effective noise bandwidth, respectively. The DFT can be interpreted as a filter bank that consists of N band-pass filters. These filters are centered at the DFT frequencies, and the DTFT of the window gives the individual filter response. In this interpretation, $\hat{\nu}_{\Delta}$ and \hat{N}_{Δ} quantify the effective frequency span from which the major part of the power in the frequency bins is drawn. For the Dirichlet window $\hat{N}_{\Delta} = 1$ and therefore each frequency bin collects power only from its own frequency span (right panel of Fig. 1.6) [85, 86].

Hanning Window

The most used window functions are the von Hann windows, commonly called the *Hanning* windows. This is a whole class of window functions that are derived from a half-period cosine oscillation raised to some integer power. The most com-

1 Basic Concepts

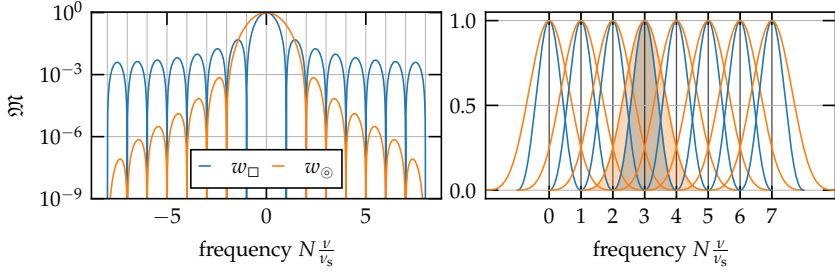


Figure 1.6: Comparison between the Dirichlet (w_{\square}) and Hanning (w_{\circ}) windows for $N = 16$. The left panel shows the MS of both windows using a logarithmic scale: The right panel is a sketch of the corresponding filter bank interpretation of the DFT.

mon variant is the quadratic Hanning window:

$$w_{\circ} = w_{\square} \cdot \cos\left(\frac{z - \pi}{2}\right)^2, \quad z = \frac{2\pi}{N}l = \frac{2\pi\nu_s}{N}t.$$

The DTFT of the Hanning window can be calculated from the convolution of the DTFT of the Dirichlet window and the cosine term of the Hanning window:

$$\begin{aligned} \mathcal{F}_{\mathbb{Z}}[w_{\circ}](\nu) &= \left(\mathcal{F}_{\mathbb{Z}}[w_{\square}] * \mathcal{F}\left[\frac{w_{\circ}}{w_{\square}}\right] \right)(\nu) \\ &= \left(\mathcal{F}_{\mathbb{Z}}[w_{\square}] * \left(-\frac{1}{4}\delta\left(\frac{\nu_s}{N} - \nu\right) + \frac{\delta(\nu)}{2} - \frac{1}{4}\delta\left(\frac{\nu_s}{N} + \nu\right) \right) \right)(\nu) \end{aligned} \quad (1.21)$$

$$= -\frac{1}{2} \exp\left(-\frac{i\pi\nu N}{\nu_s}\right) \frac{\sin^2\left(\frac{\pi}{N}\right) \sin\left(\frac{\pi\nu N}{\nu_s}\right)}{\sin\left(\pi\left(\frac{\nu}{\nu_s} - \frac{1}{N}\right)\right) \tan\left(\frac{\pi\nu}{\nu_s}\right) \sin\left(\pi\left(\frac{\nu}{\nu_s} + \frac{1}{N}\right)\right)}. \quad (1.22)$$

From line (1.21), it is easy to see that the final simplified expression consists of three terms that redistribute the power of any impulse to three Dirichlet kernels that are spaced one frequency bin apart. Effectively, this makes the central lobe of the Hanning window so wide that it swallows the first frequency bin to each side of 0. The benefit of this redistribution is visible in the left panel of Fig. 1.6: the sinc contributions of the Hanning window sum up in a way that makes the magnitude

of the side lobes decay significantly faster. Two bins away from the fundamental frequency of an oscillation, the leaked power is already several orders of magnitude smaller than in the Dirichlet case.

For the Hanning window, $N_{\Delta}^{\circ} = 1.5$ and consequently some part of the estimated spectral density value of each bin comes from its neighboring bins as seen in the right panel of Fig. 1.6. The effective bin width is not a problem for smooth spectra, but for very steep and narrow spectral peaks, it reduces the minimal frequency resolution [82]. Therefore, any window choice is a compromise between spectral leakage and effective frequency resolution.

Of course, the interpretation of section §1.3.5 can be used to determine how the Hanning window function shapes the spectrum and the signal perceived by the DFT. The result of repeating the steps from before and using Eq. (1.19) for the MS is depicted in Fig. 1.7 for the same cosine example. The Hanning window is periodic and does not jump at the beginning or end of the sampling interval. Therefore, by multiplying the signal by the window, the periodization of the input to the DFT is forced to be periodic as well. The signal $h(t)$ perceived by the DFT (blue and red curves) corresponds well to this periodized input inside the sampling interval but deviates from it outside. The amplitude and MS spectra are again described by the convolution of Eq. (1.22) and the impulses of the oscillation at $\pm\zeta_0$. In the frequency domain (middle and bottom panels), the increased drop of the window is seen, and the oscillations are mostly contained inside the first two bins around ζ_0 .

Other Windows Choices

The Hanning window is a good starting point for many spectroscopy applications, but some fields might demand more special windows that shape the response of the DFT in some particular way. A reference of various windows and their performance data can be found in Refs. [84, 86, 87]. Of course, the estimates of the windows DFT in Eq. (1.19) and Eq. (1.20) remain valid for any window choice. Note that to allow for a later interpretation of the data, the window choice w_{\circ} , the sample rate ν_s , the DFT size N , and the kind of spectrum ($G[fw_{\circ}]$, $\underline{\mathfrak{S}}_f$, or $\underline{\mathfrak{M}}_f$) must be saved *along* with the spectrum data, as without this crucial information it is no longer possible to convert between $\underline{\mathfrak{S}}_f$ and $\underline{\mathfrak{M}}_f$.

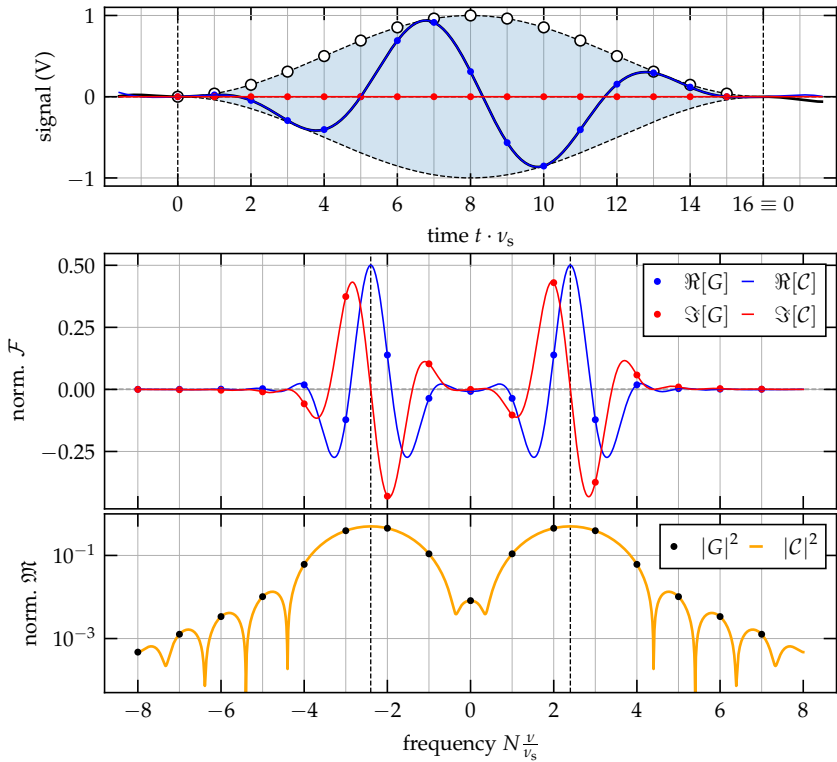


Figure 1.7: Top panel: the discrete Fourier transform (DFT) spectrum of a Hanning weighted cosine oscillation f . Again, the DFT computes the spectrum of a periodic complex function h that coincides with the f (black) at the sampling points t_k in its real (blue) and imaginary (red) parts but this time the Hanning window makes both functions similar at the beginning and end of the interval. Middle and bottom panels: the DFT spectrum (dots) is a discrete sampling of N frequencies taken from the convolution of the Fourier transform (FT) of f and the discrete-time Fourier transform (DTFT) of $w_{\otimes}, \tilde{f} * \mathcal{F}_Z[w_{\otimes}]$, (solid lines).

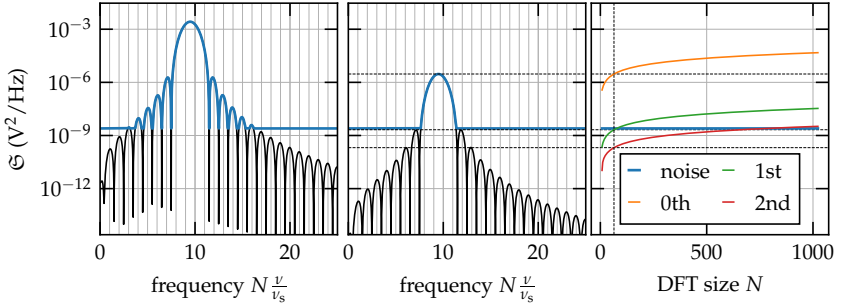


Figure 1.8: Sketch of the safety margin of the Hanning window for broadband signals ($N = 128$). As long as the side lobes of the cosine spectrum (black) stay below the noise level of the broadband signal, the spectral leakage is masked. The left and center panels show the corresponding discrete-time Fourier transform (DTFT) spectra of the periodogram of a cosine oscillation on top of a broadband background. The right panel shows the margin dependence on the discrete Fourier transform (DFT) size N .

1.3.7 Coherent Artifacts

Windows that have a rapid fall-off in their side lobes provide a kind of safety margin against coherent perturbation signals, as sketched in Fig. 1.8. When the coherent perturbation signal is low enough in amplitude so that its first side lobe lies below the noise level of the incoherent signal to be measured, then its spectral leakage is masked by the noise floor. Roughly speaking, the perturbation is contained to the frequency bins affected by the central lobe, as depicted in the center panel of Fig. 1.8. If the signal is much stronger or the window suppression is not strong enough, then side lobes rise above the noise floor and become apparent as spectral leakage (left panel). Because the coherent and incoherent signals scale differently, large spectral regions can be swamped by the perturbation signal and make measurements of the incoherent noise floor challenging. The power of the coherent perturbation expressed as a PSD scales like:

$$\frac{a_0^2}{\nu_\Delta} \propto a_0^2 \frac{N}{\nu_s},$$

that is, increasing the DFT size N makes the perturbation worse while increasing the sample rate ν_s extends the margin. The right panel of Fig. 1.8 depicts this dependence for the example from the central panel where the dashed lines indicate the equivalent PSD power levels of the first two side lobes of the artifact. Once the amplitude of the perturbation increases above a certain threshold, the spectral leakage will dominate above the noise floor. Then the source of the perturbation has to be addressed at the acquisition stage before it reaches the signal processing DFT step. That is, decreasing N or increasing ν_s cannot compensate for the quadratic term a_0^2 .

1.3.8 Mitigation of Artifacts

A not-so-obvious coherent artifact can arise from a constant offset in the input signal. Even nominally offset-free input signals passed through a direct current (DC) block can acquire an offset or even a ramp due to a non-ideal performance of the analog-to-digital converter (ADC). As the FT spectrum of a constant is a δ peak at $\nu = 0$, the DFT will correspondingly place a window response there, and this response will contaminate the low-frequency part of the spectrum. Therefore, removing the average of the input data before multiplying it by the window is advisable to mitigate this effect. If the ramp produced by the ADC is pronounced enough, it also must be removed in a process usually referred to as trend removal. There are various methods to do this that range from linear fitting to complex digital high-pass filters [86].

Of course, removing the mean and the trend has the effect that the estimate at $\nu = 0$ is no longer accurate. This is usually not a problem in NS as the information in this bin is of little interest. Besides, a constant offset voltage can be measured much more accurately using a DC voltmeter designed specifically for this purpose.

The accuracy of the highest frequency bin at $\nu = \nu_s/2$ is usually also quite poor and, provided a proper anti-aliasing filter is implemented, should be zero anyway. Therefore, both the bin at $\nu = 0$ and the bin $\nu = \nu_s/2$ can be dropped or set to an invalid (not a number) value to prevent them from accidentally being used.

1.3.9 One-Sided Spectra

The spectra presented so far have all been two-sided spectra that contain positive and negative frequencies. This is fine if only DFT spectra are considered. How-

ever, spectrometers using a frequency sweep and subsequent analog integration detect both sides of the spectrum at once. To make DFT spectra comparable to these measurements, Eq. (1.19) and Eq. (1.20) have to be altered to produce one-sided spectra that contain only positive frequencies:

$$\left. \begin{aligned} \left(\underline{\mathfrak{M}}_f\right)_k &= 2 \frac{1}{\eta_M^2} |G [fw_o]_k|^2, \\ \left(\underline{\mathfrak{S}}_f\right)_k &= 2 \frac{1}{\nu_s} \frac{1}{\eta_P} |G [fw_o]_k|^2, \end{aligned} \right\} k \in 0, \dots, N-1 \quad (1.23)$$

For example, in this convention, the MS spectrum $\underline{\mathfrak{M}}_f$ of a cosine oscillation with amplitude a_0 will yield a full power $a_0^2/2$ at the oscillation frequency ξ_0 .

1.3.10 Processing of Realistic Signals

This subsection summarizes the above sections in a step-by-step suggestion on how to process signals with the goal of NS in mind. See also [86] for a more general guide.

Analog Processing

Before starting to acquire data, the analog input signal is inspected to determine its rough frequency content and the frequency band of interest. The sampling rate ν_s is chosen so that the investigated frequency band lies below the Nyquist frequency $\nu_s/2$. A corresponding anti-aliasing low-pass filter is implemented so that the falling edge of the filtered signal at the Nyquist frequency lies at or below the expected noise floor of the acquisition system (including the combination of all the amplifiers, filters, and the digitizer or ADC). If a strong perturbation exists in the spectrum, a notch filter might be necessary. The sampling rate ν_s and the units of the measurement are noted for further processing.

Window and Size

A window w_o is selected to shape the perturbation spectrum in such a way that it has a minimal effect on the investigated broadband spectrum. The DFT size N is selected in combination with the window to yield the desired frequency resolution. For NS with moderate perturbation levels, the Hanning window is usually a

1 Basic Concepts

good starting choice. If the spectrum is free of perturbances, even using no window, i.e., the Dirichlet window, might be appropriate. The window choice and DFT size N are noted for further processing.

Digital Processing

The analog signal is digitized and converted into floating point numbers corresponding to the units of the analog signal. The mean is subtracted from the signal, and the trend is removed if the analyzer's performance allows it. The DFT of the input samples scaled by the chosen window is calculated using a FFT algorithm, and its magnitude squared $|G|^2$ is scaled to produce a one-sided periodogram estimate $\underline{\mathcal{S}}_f$ using Eq. (1.23). The periodogram is passed for further processing along with its metadata (amplifier and filter settings, low pass, ν_s , units, w_o , N). As the variance of a single periodogram is quite high, several periodograms have to be averaged. A possible averaging technique is discussed in section §2.3.

2 Power Spectral Density Estimation

A practical way to gain insight into the statistical properties of a stationary process (SP) is to estimate its PSD by a periodogram using a finite set of values sampled from one of its realizations. This chapter starts with a discussion of the properties of the periodogram estimate in section §2.1. Next, using straight-forward numerical simulation, two kinds of broadband noise sources relevant to spin noise spectroscopy (SNS) are introduced, and their properties are discussed in section §2.2. Section §2.3 presents a procedure that extends the well-established Welch method to simultaneously estimate the mean and the variance of a stream of periodograms. The need to acquire both estimates is explained in section §2.3.4.

2.1 Bias and Variance of the Periodogram

The properties of the sampled stochastic processes impose important statistical properties and limits on the PSD estimates acquired using the DFT. The PSD spectrum \mathfrak{S}_f of a stochastic signal f perfectly describes the asymptotic statistical properties of f since it has infinite knowledge of f at all times. On the other hand, the periodogram $\underline{\mathfrak{S}}_f$ only contains a finite number of samples, and its description of f or approximation of \mathfrak{S}_f highly depends on the choice of these samples. Each of the samples can be interpreted as a random variable and $\underline{\mathfrak{S}}_f$ as a weighted sum of random variables. Therefore, each frequency component of $\underline{\mathfrak{S}}_f$ itself is a random variable that is governed by some distribution that is highly dependent on the particular structure of f . The quality of the estimate can be quantified by the mean square error [82]:

$$\begin{aligned} \left\langle \left| \underline{\mathfrak{S}}_f - \mathfrak{S}_f \right|^2 \right\rangle &= \left\langle \left| \underline{\mathfrak{S}}_f - \langle \underline{\mathfrak{S}}_f \rangle + \langle \underline{\mathfrak{S}}_f \rangle - \mathfrak{S}_f \right|^2 \right\rangle \\ &= \underbrace{\left\langle \left| \underline{\mathfrak{S}}_f - \langle \underline{\mathfrak{S}}_f \rangle \right|^2 \right\rangle}_{\text{variance}} + \underbrace{\left\langle \left| \langle \underline{\mathfrak{S}}_f \rangle - \mathfrak{S}_f \right|^2 \right\rangle}_{|\text{bias}|^2}. \end{aligned}$$

2 Power Spectral Density Estimation

Therefore, as with all estimates of random variables, the performance of the estimation by a periodogram \mathfrak{S}_f is determined by its bias and variance.

The bias tells how much the expected value or mean of the estimate deviates from the true value. It can be shown that the periodogram \mathfrak{S}_f is an unbiased estimator for signals with a flat or white PSD [82]. Spectra with tall narrow peaks suffer from spectral leakage in a similar way as coherent signals considered in section §1.3.5. Only in the limit of an infinitely large DFT ($N \rightarrow \infty$) the bias vanishes for any spectrum, as this limit is equivalent to an infinitely high spectral resolution. This property is also useful for realistic experimental signals (which usually have moderate dynamic ranges) as the necessary accuracy can be achieved by increasing N . The bias of the periodogram is well-behaved as long as the spectrum can be estimated by the DFT in principle (for this restriction, see also the discussion in section §2.2.1).

On the other hand, the variance of the periodogram is not well-behaved [82]. For $N \gg 1$, it can be shown for a quite general set of signals (linearly filtered white noise signals) that the periodogram is an *inconsistent* spectral estimator. Each value of \mathfrak{S}_f fluctuates at the *same strength* regardless of the choice of N , and periodograms of independent signal sample sets are *uncorrelated*. In fact, both the mean and the standard deviation (square root of variance) of each value of \mathfrak{S}_f are equal to the value of \mathfrak{S}_f at that frequency, and this is the main relationship between the power and the variance of its estimates of the signal f :

$$\begin{aligned} \mathfrak{V}(\mathfrak{S}_f) &= \left\langle \left| \mathfrak{S}_f - \langle \mathfrak{S}_f \rangle \right|^2 \right\rangle = \mathfrak{S}_f^2, \\ \langle \mathfrak{S}_f \rangle &= \mathfrak{S}_f. \end{aligned} \tag{2.1}$$

The reason why it is impossible to get a good estimate of \mathfrak{S}_f from a single set of N samples is that at the frequency resolution given by N , the periodogram \mathfrak{S}_f fluctuates *maximally*. By repeatedly calculating \mathfrak{S}_f for L independent sets of data, the mean of the periodograms will eventually converge toward its expected value of \mathfrak{S}_f . Nevertheless, the standard error (the variance of mean) is always determined by the square root of the initial variance (i.e., the square of \mathfrak{S}_f) reduced by the number of sets L , $s_{\mathfrak{S}_f}^{(L)} = (\mathfrak{S}_f^2/L)^{1/2}$. Therefore, the total PSD of the signal to be measured is also the quantity that determines the minimum number of sets (or integration time) that are necessary to resolve spectral features in the peri-

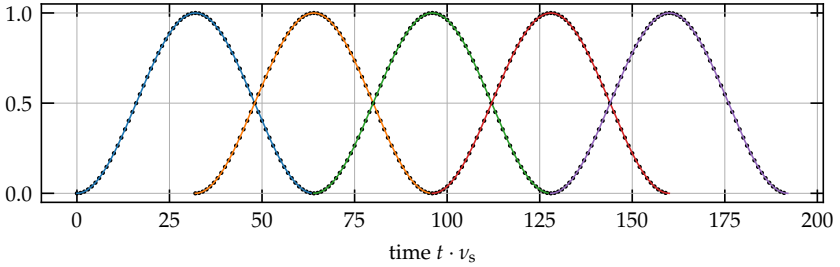


Figure 2.1: Example plot of the overlapping windows used in the Welch method for a Hanning window ($N = 64$).

odogram. An alternative interpretation can be that an accurate PSD estimate can only be acquired by reducing the frequency resolution from $\nu_s/N \cdot L$ to just ν_s/N .

The Segmented Welch Method

The reduction in the effective frequency resolution degrades the bias property of the periodogram if the PSD \mathfrak{S}_f is prone to spectral leakage. A more optimal window choice can reduce this effect to some degree, as described in section §1.3.6. However, a window introduces a different kind of complication. As the window suppresses the signal for a large portion of the window, the data in the afflicted samples is essentially thrown away. A more appropriate method could reuse these samples for the next periodogram, and its own *new* and so far unprocessed samples of low window weight would be recycled in the following DFT. This scheme, which is depicted in Fig. 2.1, is essentially the idea behind the Welch method [88].

In Fig. 2.1, the Hanning window is plotted with an overlap of 50%. This is usually a good choice for the Hanning window [86]. Making the overlap of the windows even larger is detrimental. A larger overlap increases the computational demand to produce the estimate, but there is also a less obvious consequence that concerns the quality of the estimate. The standard error reduction, as described above, is only guaranteed if the individual periodograms are not correlated. When the sample sets overlap, this is strictly no longer the case. Large overlaps alter the statistics of the averaged periodograms by creating new correlations in the data and thus artificially increase the underlying variance.

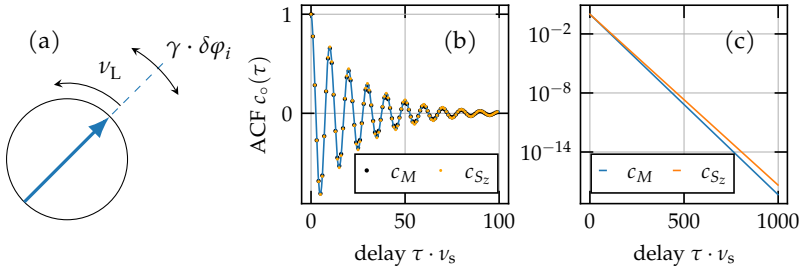


Figure 2.2: The simplified model of the polarization random walk and its deviation from the correct autocorrelation function (ACF) of spin noise (SN). Panel (a) depicts a sketch of single step of the polarization random walk. Panel (b) compares the ACF of the polarization random walk (black dots) with the physical ACF of SN (blue continuous curve). For clarity, orange dots have been plotted at the discrete steps where for results can be compared directly. Panel (c) depicts the absolute deviation of the two results for the first 1000 steps.

2.2 Broadband Spectra

It is important to consider two kinds of stochastic processes to understand the structure of experimental spin noise (SN) spectra: the thermal noise of the spin system (the actual SN) and the broadband noise background imposed by the measurement (white or colored noise). These processes can be treated mathematically rigorously using the theory of stochastic processes [83, 75]. Instead, this section chooses a less frequented, more hands-on approach using numerical simulation.

2.2.1 Simulating Spin Noise

The proper way to simulate SN is to consider the random walk of the quantum-mechanical density matrix $\hat{\rho}$. This is numerically involved and not necessary for further discussion. Any process that produces a SN-looking spectrum suffices. A classical analog to SN is a process that considers the macroscopically observable effect of a fluctuating magnetization in a sample: a “random walk” of the magnetization on a circle or sphere. Here, for simplicity, the system is assumed to be one-dimensional, as sketched in panel (a) of Fig. 2.2. The magnetization can only rotate perpendicular to the observation direction (the horizontal axis). Considering discrete incremental changes is sufficient, as the magnetization is sampled

only at discrete times. The magnetization coherently rotates by an angle $2\pi\nu_L/\nu_s$ between two samples, where $\nu_L \in [0, \nu_s/2)$ is the system's specific "Larmor" frequency. Furthermore, the magnetization angle also experiences random rotations that simulate the "loss of coherence" on the time scale γ/ν_s . If γ is very small, then the magnetization can rotate undisturbed, while for $\gamma/\nu_s \rightarrow 0.5$, the dynamics are dominated by random rotations.

Note that the similarity between the sketch in panel (a) of Fig. 2.2 and the usual representation of the spin expectation value on a Bloch sphere (like, for example, Fig. 4.2) is deceiving. The simple model considered here is a *numerical trick* that efficiently simulates a SN-looking spectrum. However, it is also very wrong, as it does not consider the evolution of the spin state $\hat{\rho}$. This is explained in more detail in section §4.2.1. See also [89] for a semi-classical treatment of spin relaxation.

With that in mind, the projection of the magnetization on the observation direction after N steps of this process can be described as follows:

$$M_N = \cos \left(\sum_{i=0}^{N-1} \left(\sqrt{\frac{2}{\pi}} \frac{\gamma}{\nu_s} \delta\varphi_i + 2\pi \frac{\nu_L}{\nu_s} \right) \right), \quad (2.2)$$

where $\delta\varphi_i$ is a random variable uniformly distributed in the interval $[-\pi; \pi)$. The process that Eq. (2.2) describes is not quite the one underlying SN, as can be seen by observing the ACF of the magnetization projection, i.e., $c_M(\tau_k) = \langle M_0 M_k \rangle$. Consecutively integrating over the probability density of the k steps $\delta\varphi_i$, the ACF at a time delay $\tau_k = k/\nu_s$ yields:

$$c_M(\tau_k) = \langle M_0 M_k \rangle = \underbrace{\left(\frac{\sin \left(\sqrt{2\pi} \frac{\gamma}{\nu_s} \right)}{\sqrt{2\pi} \frac{\gamma}{\nu_s}} \right)^k}_{\text{sinc}} \cos \left(\frac{2\pi\nu_L}{\nu_s} k \right), \quad (2.3)$$

where $M_0=1$ was assumed. On the other hand, the ACF of a fluctuating spin is [76]:

$$c_{S_z}(\tau) = \exp(-\gamma|\tau|) \cos(2\pi\nu_L\tau)$$

or, in the discrete case:

$$c_{S_z}(\tau_k) = \exp \left(-\frac{\gamma}{\nu_s} k \right) \cos \left(\frac{2\pi\nu_L}{\nu_s} k \right). \quad (2.4)$$

The sinc term in Eq. (2.3) decays slightly faster than the exponential term in the

2 Power Spectral Density Estimation

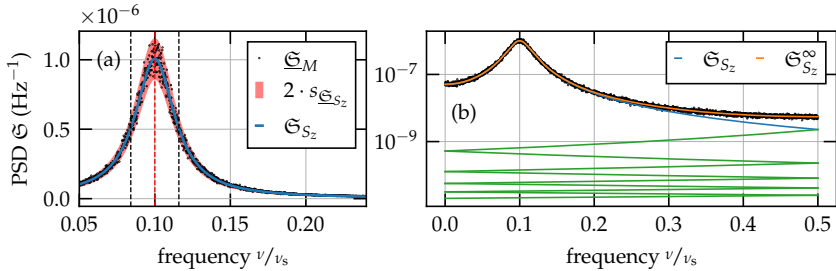


Figure 2.3: The spectrum of the corrected model and an average over 100 periodograms. Panel (a) depicts the PSD estimate using black dots. The asymptotic mean of the estimate is the underlying ACF of SN (blue curve) and the error band of two standard errors is given by two times the ACF, which is reduced by the square root of the averages. Panel (b) depicts the same result using logarithmic ordinate. For frequencies close to $\nu_s/2$ the periodogram estimate deviates from the physical ACF. It can yield only the aliased version of the ACF (orange curve) that includes the infinite sum of ever vanishing folded tail parts (green curves, only the first 9 depicted).

correct SN correlation function, as can be seen in panels (b) and (c) of Fig. 2.2. This deviation can be alleviated for numerical simulations by modifying the decay rate using the empirical formula:

$$\frac{\gamma}{\nu_s} \rightarrow \frac{\gamma}{\nu_s} \cdot \left(0.95259388 - 0.19249708 \frac{\gamma}{\nu_s} \right).$$

With this modification, the noise model can be used to simulate realistic-looking SN spectra.

An average of 100 runs of the model is depicted in Fig. 2.3. The averaged periodogram estimate \mathfrak{G}_M is depicted in panel (a) using a scatter plot of black dots. Moreover, the FT spectrum of the spin ACF \mathfrak{G}_{S_z} ,

$$\mathfrak{G}_{S_z}(\nu) = \frac{1}{2} \left(\frac{\gamma}{\gamma^2 + 4\pi^2(\nu - \nu_l)^2} + \frac{\gamma}{\gamma^2 + 4\pi^2(\nu_l + \nu)^2} \right),$$

is also plotted in blue, and the band of two standard errors for 100 averages is plotted in red around \mathfrak{G}_{S_z} . The two vertical lines designate the full width at half

maximum (FWHM) γ_{FWHM} of \mathfrak{S}_{S_z} that is equal to:

$$\gamma_{\text{FWHM}} = \frac{2\gamma}{2\pi} = \frac{\gamma}{\pi}.$$

As is the case for experimental SN spectra, the correlation rate γ of the process, as well as the Larmor frequency ν_L (red dashed line), can be directly read from the periodogram estimate.

Spectrum Periodicity

Panel (b) of Fig. 2.3 depicts all frequencies of the periodogram estimate on a logarithmic y -scale, and \mathfrak{S}_{S_z} is again plotted in blue. The \mathfrak{S}_{S_z} spectrum and the periodogram deviate for frequencies away from the Larmor frequency ν_L . This effect is quite small and is present but is not visible in panel (a). The reason for the discrepancy is that the $\underline{\mathfrak{S}}_M$ is a periodogram, and it hence suffers from the limitations of the DFT as explained in section §1.3: any spectrum produced by the DFT is of some periodic function that has no frequency content above the Nyquist frequency and is itself *periodic*. The ACF spectrum \mathfrak{S}_{S_z} does not qualify as such a spectrum; it is neither periodic nor is its frequency content limited to the allowed region. Therefore, the calculated periodogram estimate belongs not to \mathfrak{S}_{S_z} (i.e., the FT of c_{S_z}) but to the DTFT of c_{S_z} :

$$\begin{aligned} \mathfrak{S}_{S_z}^\infty(\nu) &= \frac{1}{\nu_s} \mathcal{F}_{\mathbb{Z}}[c_{S_z}](\nu) = (\mathfrak{S}_{S_z} * \text{III}_{\nu_s})(\nu) \\ &= \sum_{m \in \mathbb{Z}} \mathfrak{S}_{S_z}(\nu + m \cdot \nu_s), \end{aligned} \quad (2.5)$$

the aliased periodic version of \mathfrak{S}_{S_z} . The left panel's green superimposed curves are the first ten terms from Eq. (2.5). Alternatively, these curves can be interpreted in a way where the high-frequency content of the \mathfrak{S}_{S_z} spectrum that crosses the Nyquist frequency is aliased back to a lower frequency, and this process is repeated ten times. The \mathfrak{S}_{S_z} spectrum decays quite rapidly, and, therefore, a finite amount of terms in Eq. (2.5) yields a quite good approximation of $\mathfrak{S}_{S_z}^\infty$ that is plotted in orange.

Even though $\mathfrak{S}_{S_z}^\infty$ is the correct function to describe a SN spectrum, it is seldom used as there is no closed numerical expression for the infinite sum. Besides, (as explained in more detail below in section §3.3) realistic SN spectra are hardly ever

2 Power Spectral Density Estimation

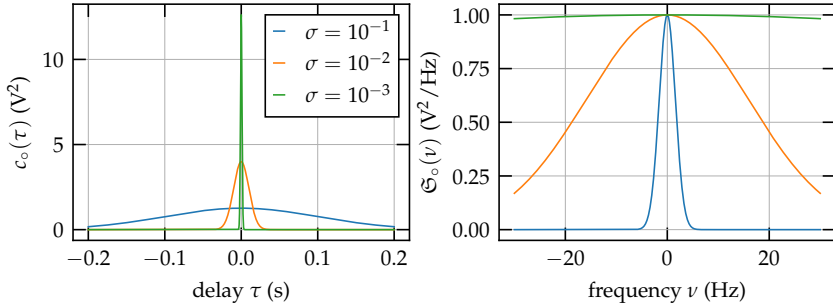


Figure 2.4: Sketch of some peak-shaped autocorrelation function (ACF) and the corresponding PSD spectrum for different peak widths σ . As the correlation peak gets increasingly narrower, its spectrum becomes increasingly flat.

dominated by the intrinsic SN variance. In such a situation, the low- and high-frequency tails visible in the right panel would drown in a much higher background noise level, and the bias error due to using \mathfrak{S}_{S_z} instead of $\mathfrak{S}_{S_z}^\infty$ would usually be lower than other sources of error.

2.2.2 White and Colored Noise

The derivation of the FT for coherent signals in section §1.1 required the math to be extended to include δ distributions to include these signals of infinite power. For the derivation of the stochastic process with a flat PSD spectrum, a similar argument must be made for the ACF and its FT. Starting from any process f that has a peak-shaped ACF c_f , it is easy to see that the narrower the peak in the correlation function becomes, the broader its corresponding spectrum (that is, \mathfrak{S}_f) reaches in the frequency domain. For example, in Fig. 2.4, the ACF is a Gaussian-bell-shaped function:

$$c_f(\tau) = \frac{1}{\sqrt{2\pi\sigma}} \exp\left(\frac{-\tau^2}{2\sigma^2}\right),$$

$$\tilde{c}_f(v) = \exp(-2(\pi v\sigma)).$$

In the limiting case where $\sigma \rightarrow 0$, the ACF c_f becomes a δ distribution, while its spectrum becomes a constant, and it does not depend in any way on the initial shape of the peak. The stochastic process that c_f belongs to is called a Gaussian or Wiener process $W(t)$. The process is usually defined in terms of its time increments dW , given by the probability function:

$$P(dW) = \frac{1}{\sqrt{2\pi dt}} \exp\left(-\frac{(dW)^2}{2dt}\right).$$

These increments are Gaussian, independent, and identical [83]; they are white noise.

As can be seen from the spectrum of ACF, this process has an infinite average power: the PSD has a value of 1 at all frequencies, and the integral over all frequencies diverges. Nevertheless, white noise is helpful, as it allows various stochastic processes to be expressed using stochastic differential equations. These differential equations can be interpreted as a kind of filter that limits the frequency content of the white noise. This property is why white noise can be used to model realistic dynamic systems that are driven by some broadband noise source. As long as the differential equations limit the frequency content below the bandwidth of the driving noise, white noise is a good approximation to real noise [83]. On the other hand, it is impossible to observe true white noise in a signal in the same way as it is impossible to observe the total power of a coherent oscillation.

A sampling of Gaussian increments with the sample rate ν_s band-limits the spectrum to $[-\nu_s/2; \nu_s/2)$ as, in this case, the DTFT is blind to anything that happens between the samples. Furthermore, taking only N values produces a periodogram of this band-limited spectrum. Therefore, a band-limited white noise source can be simulated just by a random number generator that produces numbers that are normally distributed around 0. The generator output should be scaled by $\sqrt{\eta \cdot \nu_s}$ to obtain a noise source with noise density η . Limiting the bandwidth of the white noise also makes the resulting signal a wide-sense stationary process with finite power.

Therefore, Eq. (2.1) describes the statistical properties of the corresponding periodogram. The average over 100 runs of this simulation is plotted in panel (a) of Fig. 2.5, as well as the white noise spectrum and the band of two standard errors around the mean.

A broadband noise of any shape can now be obtained by shaping the DFT of

2 Power Spectral Density Estimation

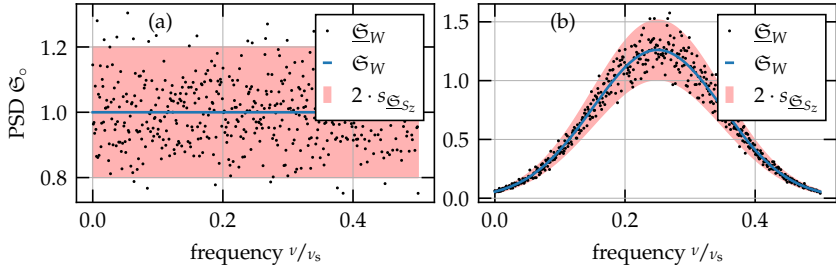


Figure 2.5: The spectrum of white and colored noise and their corresponding averages over 100 periodograms. Both panels depict the periodogram estimate using black dots and their corresponding autocorrelation functions (ACFs) using blue curves. The error band of two standard errors is given by two times the corresponding ACF, which is reduced by the square root of the averages. Panel (a) depicts the periodogram of band limited simulated white noise. Panel (b) depicts the periodogram of a white noise source that has been shaped by a Gaussian bell curve.

white noise samples and then transforming the resulting periodogram back to the time domain as done in the right panel of Fig. 2.5, where a Gaussian-shaped spectrum was generated this way. The equivalent of this operation is to apply some specially tailored filter to a white noise source. This explains why the class of linearly filtered signals is so general and why Eq. (2.1) applies to the periodograms of most realistic stochastic processes.

2.3 The Modified Welch Method

The eventual goal of SNS is to produce an approximate (asymptotic) estimator of the ACF of the underlying spin system. While the Welch method presented in section §2.1 gives an estimate for the mean PSD (the mean ACF), it does not give any information about the variance on its own. An additional variance estimate seems superfluous, as the spectral mean and spectral variance yield the same information for stochastic processes (according to Eq. (2.1)). However, realistic signals can contain a multitude of weak coherent components that can arbitrarily contaminate the broadband SN spectrum. In this section, a method is proposed that slightly alters Welch's method to be able to estimate both statistical quantities of periodograms at the same time.

Notation In the following discussion, only one frequency bin ν_i of each periodogram is considered, i.e.,

$$\left(\mathfrak{S}_f^{(k)}\right)_i = S_{k,i},$$

where the index k counts the periodograms and the index i counts the frequency bins. The described procedures have to be repeated for all available frequency bins and all periodograms to generalize the approach toward complete estimates. Furthermore, the frequency bin index i is dropped, and $S_{k,i}$ becomes S_k , and the expected value at this frequency is $\langle S \rangle = \mathfrak{S}_f(\nu_i)$.

2.3.1 Welford Summation

In principle, an estimate of the variance of the S can be determined by numerically calculating the sample mean and the Bessel corrected sample variance using the common formulas:

$$\begin{aligned}\langle S \rangle &\approx E_N := \frac{1}{N} \sum_{i=1}^N S_k, \\ \langle |S - \langle S \rangle|^2 \rangle &\approx V_N := \frac{1}{N-1} \sum_{k=1}^N (S_k - E_N)^2.\end{aligned}$$

Unfortunately, naively evaluating this formula is usually not feasible because all the periodograms recorded in a single acquisition would have to be retained in memory. Even for moderate sample rates, the amount of memory needed can quickly exceed the available memory of the digitizer. In addition to that, the intermittent instantaneous computational load during the evaluation would make simultaneous acquisition unreliable.

Welford's online algorithm for sums of squares can be used to spread the computational load and avoid retaining the periodograms [90]. Instead of using the complete data at once to arrive at the required estimates for the variance and mean, an iterative approach is taken that produces intermediate estimates and uses the sample data exactly once. This way, only the intermediate estimates have to be retained, while the incoming data can be dropped as soon as new estimates have been calculated. Effectively, instead of retaining all periodograms in memory now, only three are needed: the approximated estimates for V_{k-1} and E_{k-1} and the current periodogram S_k .

2 Power Spectral Density Estimation

The normalization needed to calculate the variance V_k in each step would make the algorithm numerically unstable. Therefore, the normalization is moved to the end of the procedure, and the unnormalized sum of squares,

$$M_k := \sum_{l=1}^k (S_l - E_k)^2,$$

is used instead. The k -th estimate of the mean E_k can be expressed as a recursive formula (see Eq. (A.1)):

$$E_k = \frac{1}{k} \sum_{l=1}^k S_l = E_{k-1} + \frac{S_k - E_{k-1}}{k} = E_{k-1} + \frac{\delta_k}{k}, \quad k > 1 \quad (2.6)$$

$$E_1 = S_1,$$

where $\delta_k := S_k - E_{k-1}$. Consequently, for the k -th estimate of the sum of squares M_k , the recursion formula is, see Eq. (A.2):

$$M_k = \sum_{l=1}^k (S_l - E_k)^2 = M_{k-1} + \delta'_k \delta_k, \quad k > 1 \quad (2.7)$$

$$M_1 = 0,$$

where the new difference is defined as $\delta'_k := S_k - E_k = \frac{k-1}{k} \delta_k$. As required, both estimates depend in each iteration only on the last estimates E_{k-1} and M_{k-1} and the new periodogram S_k . With the identities

$$\langle S \rangle \approx E_k, \quad (\text{sample mean estimator})$$

$$\langle |S - \langle S \rangle|^2 \rangle \approx \frac{1}{k-1} M_k, \quad (\text{sample variance estimator})$$

the mean, biased variance, and sample variance estimates can be determined.

2.3.2 Chan's Merging Formula

In the presence of spurious perturbation sources in the signal, it is advisable not to throw away all the intermediate periodograms at once. Sometimes a post-selection of periodogram is desired when an extrinsic perturbation from outside of the

experiment has contaminated the measurement. Therefore, a generalization of Welford's summation formulas ((2.6) and (2.7)) is necessary to merge intermediate results. The intermediate results over a set of a periodograms are designated as $\{a\}$:

$$E_{\{a\}} := E_a = \frac{1}{a} \sum_{l \in \{a\}} S_l,$$

$$M_{\{a\}} := \sum_{l \in \{a\}}^k (S_l - E_k)^2.$$

Then, for two estimates over different sets of periodograms, $\{a\}$ and $\{b\}$, a summation formula can be derived [91] that corresponds to the estimates over the union of these sets, $\{a\} \cup \{b\}$

$$\delta_{\{a\} \cup \{b\}} = E_{\{a\}} - E_{\{b\}},$$

$$E_{\{a\} \cup \{b\}} = \frac{a \cdot E_{\{a\}} + b \cdot E_{\{b\}}}{a + b},$$

$$M_{\{a\} \cup \{b\}} = M_{\{a\}} + M_{\{b\}} + \delta_{\{a\} \cup \{b\}}^2 \frac{a \cdot b}{a + b}.$$

Finally, an estimate over a set of sets $\{\{a\}\}$ can be calculated by recursively merging all estimates into a single one. In other words, pairs of sets are merged first to get new intermediate estimates. Then pairs of these new estimates are merged, and the procedure is continued in the same manner until only the total estimates for V_{total} and M_{total} remain.

2.3.3 Partial Average Statistics

Although Welford's summation described in section §2.3.1 is very useful on its own, it can still mean a performance hit if applied to each individual periodogram at very high data rates. If a decrease in the accuracy of the variance estimate is acceptable, a partial average strategy can be used instead. From elementary statistics,

2 Power Spectral Density Estimation

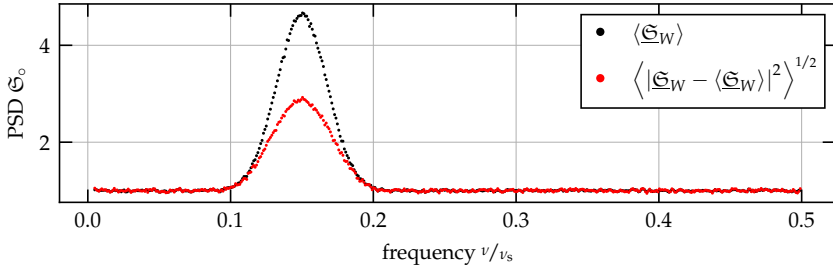


Figure 2.6: The mean and square root of the variance of 5000 periodograms for a sum of a partially coherent oscillation and a white noise background.

the following is true for the mean of n samples:

$$\begin{aligned} \langle E_n \rangle &= \langle S \rangle, \\ \langle |E_n - \langle E_n \rangle|^2 \rangle &= \frac{1}{n} \langle |S - \langle S \rangle|^2 \rangle. \end{aligned}$$

That is, the variance is scaled down by the number of samples of the partial average while the mean remains unchanged. Some of the variance information gets thrown away on the first averaging level when the partial averages $E_{\langle n \rangle}$ get used instead of individual periodograms S_l as inputs to the algorithms described in section §2.3.1 and section §2.3.2. The final result will be the correct estimate for the mean, but the variance's value will be too small and will have to be scaled up by n to recover the initial variance.

2.3.4 Variance Estimate Criterion

Having established a good estimate for the variance of a periodogram ensemble, it is now possible to tell whether or not the considered signal is artifact-free. In the example shown in Fig. 2.6, the signal consists of a white noise background to which a distribution of coherent oscillations was added. By looking just at the mean of the periodogram estimates, it is impossible to tell if the peak in the spectrum is caused by a stationary process or not. However, Eq. (2.1) fixes the expected values of the estimates for a stationary process to:

$$E_k(\nu) \approx \langle \underline{\mathfrak{S}}_f \rangle = \mathfrak{S}_f(\nu),$$

$$V_k(\nu) \approx \mathfrak{V}(\underline{\mathfrak{S}}_f) = \mathfrak{S}_f^2(\nu).$$

The square root of the variance is plotted using red dots in Fig. 2.6, and it dips below the mean, which is plotted in black. The reason is easy to understand: the oscillations are coherent, and therefore their signal is more strongly correlated than it would be for a noise source with the same spectral mean. Therefore the variance criterion for artifact-free periodogram estimates can be stated as:

$$\boxed{E_k^2 \stackrel{!}{\approx} V_k.} \quad (2.8)$$

3 Optical Noise Spectroscopy

This chapter serves as a brief summary of the theory of optical noise spectroscopy of fluctuating signals using semiconductor photodiodes and highlights the fundamental difference between quantum-mechanical, optical, and technical noise sources that can be present in an optical NS experiment.

3.1 Noise Signals in Photodetectors

Fundamentally, photodiodes are macroscopic classical detectors. They are slow devices that can resolve neither the classical electromagnetic waves' THz oscillation at optical frequencies nor individual photon events. This limits their usability to the detection of the relatively slowly changing (\lesssim GHz) mean photon flux $\Phi_D = P_D^*/h\nu_p$, where, for monochromatic light, $P_D^* = \langle P_D \rangle$ is the mean optical power on the active area of the electronically biased photodiode and $h\nu_p$ is the photon energy. Here, a convention is used, where the star * designates that P_D^* is a directly accessible statistical quantity (i.e., mean) in a real experiment. Each photon detected in this way has the probability $0 \leq \eta_Q \leq 1$ to create an electron-hole pair that contributes an elementary charge e to the photocurrent. Therefore the mean photocurrent i_D can be written as [92]:

$$i_D^* = \eta_Q e \frac{P_D^*}{h\nu_p} \equiv \eta_Q \eta_D P_D^*, \quad (3.1)$$

where $\eta_D = e/h\nu_p$ is the responsivity (A W^{-1}) of an ideal detector and $\eta_Q \eta_D$ is the sensitivity of a lossy detector. The effective bandwidth of this photocurrent is determined by the capacity of the photodiode (i.e., size) and the gain-bandwidth product of the amplifier that amplifies the tiny photocurrent. Within the bandwidth of a photodetector built in this way, the effective photocurrent can be decomposed into the mean part and the fluctuating part:

$$i_D(t) = \langle i_D \rangle + i(t), \quad (3.2)$$

3 Optical Noise Spectroscopy

where $\langle i_D \rangle = i_D^*$. The fluctuating part of the photocurrent contains the sought-after noise “signal” as well as several possible other *uncorrelated* noise contributions:

$$i = i_t + i_l + i_s, \quad (3.3)$$

where i_t denotes the fluctuation due to internal (thermal) noise sources in the detector, i_l is the fluctuation due to the used light source, i_s is the fluctuation due to the signal from the probed system, and the explicit time dependence is dropped for brevity. Because all these fluctuations are uncorrelated and average to zero ($\langle i_i \rangle = 0$ and $\langle i_i i_j \rangle = 0$ for $i \neq j$), the expected value of the photocurrent fluctuation is, *per definition*, zero as well, $\langle i \rangle = 0$.

The least exciting contribution is the thermal noise i_t which is also called electrical or technical noise. This contribution can itself consist of several components that are all usually the consequence of the finite temperature of the photodiode (dark current) and the amplification electronics (Johnson-Nyquist noise). The quantity i_t is independent of the photodetector input and uncorrelated with the other contributions. Therefore, it introduces an on-average constant component to the *variance* of i , which has important consequences, as explained below. The current fluctuation consists of a large number of contributions by individual charge carriers that are mostly uncorrelated and therefore follow an arrival times Poisson distribution. For large numbers, the Poisson distribution degenerates into a Gaussian distribution. For this reason, thermal noise i_t for an “ideal” warm and noisy circuit appears as a white noise source, as discussed in section §2.2.2. This is usually not what is observed in the experiment because the amplifier stages in the photodetector act as a filter and can shape the initial white noise into a colored noise that has a frequency-dependent PSD.

The second quantity i_l , which is induced by the light source, consists of two contributions: a quantum-mechanical part i_p and a classical part i_m , $i_l = i_p + i_m$. The quantum-mechanical part, i_p , represents fluctuations at full detector bandwidth that originate directly from the photon statistics of the incident laser light. For coherent laser light, the photons follow a Poisson distribution, and their arrival variance is given by their expected value $\mathfrak{V}(n) = \langle n \rangle \equiv P_D/h\nu_p$. As a consequence, the variance of the fluctuation i_p inherits this property and is proportional to the mean current on the diode: $\mathfrak{V}(i_p) \propto \langle i_D \rangle$. Thus, the variance per unit bandwidth

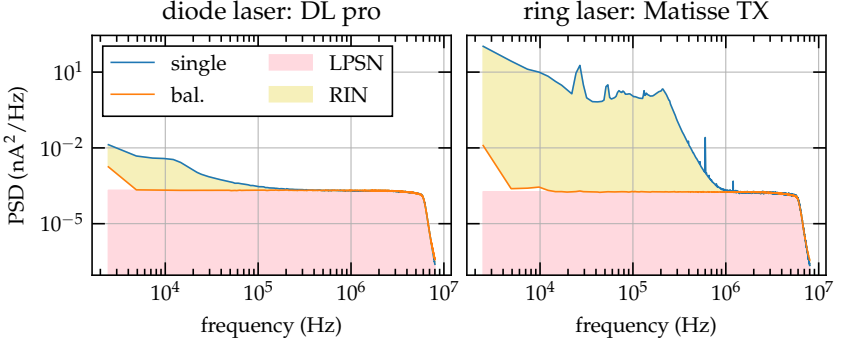


Figure 3.1: Photocurrent PSD spectra for two different laser sources (left: Toptica DL pro, right: Sirah Matisse XT) recorded using the Femto OE-300-S 08-98-006 balanced photodetector: for the upper blue curve (single), one of the diodes is blocked by a metal shield, while for the lower orange curve (balanced), both diodes receive half of the incoming laser power. The gains and beam splitter losses are compensated. Within the used bandwidth of 10 MHz, the balanced curve consists almost purely of laser photon shot noise (LPSN) while the single diode displays additional relative intensity noise (RIN).

of i_p can be written as [92]

$$\begin{aligned} \frac{\mathfrak{I}(i_p)}{\Delta\nu} &= 2e \cdot \langle i_{p,0} \rangle = 2e \cdot \eta_Q e \frac{P_D^*}{h\nu_p} = \frac{e^2}{(h\nu_p)^2} \cdot \eta_Q P_D^* \cdot 2h\nu_p \\ &= \eta_D^2 \cdot \eta_Q P_D^* \cdot 2h\nu_p. \end{aligned} \quad (3.4)$$

Again, the distribution degenerates into a Gaussian distribution, and the PSD spectrum of the i_p contribution appears white because the photon numbers are large (bright beam approximation) [93]. Nevertheless, the amplification bandwidth of a real photodetector is finite, and toward the end of the bandwidth, the spectrum stops being white. The reason is that the amplifier cannot sustain the same amplification at the highest frequencies, and the spectrum tapers out to zero.

The second part, i_m , is usually a consequence of the limited stability of the main radiating mode in laser sources [94, 95]. In particular, most semiconductor laser diodes (i.e., the absolute majority of all lasers in use) exhibit a so-called relative

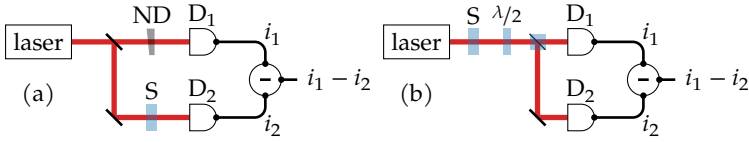


Figure 3.2: Possible balanced detection schemes (adapted from [92]). Scheme (a) measures absorption fluctuations by splitting the beam with a 50:50 splitter. The sample is placed in the beam before the second diode, while the power on the first diode is adjusted by a neutral density (ND) filter. Scheme (b) measures polarization fluctuations: the sample is placed in a linearly polarized beam that is analyzed by a $\pi/4$ -rotated polarizing beam splitter. The balancing is adjusted by a half-wave retarder. In both schemes, the balancing cancels the relative intensity noise (RIN) by only detecting the difference between the photocurrents i_1 and i_2 .

intensity noise (RIN) that results in a low-frequency photocurrent variance that can exceed the shot noise figure in Eq. (3.4) by several orders of magnitude. The fluctuations of i_m have a limited bandwidth of usually < 1 MHz as depicted in Fig. 3.1 and are in good approximation uncorrelated with i_p . For this reason, they appear as a classical fluctuation of the photon flux and produce a variance that is proportional to the average detected power:

$$\frac{\mathfrak{V}(i_m)}{\Delta\nu} \propto P_D^2.$$

Of course, the same argument is valid for *any other optical signal* on the photodetector. Therefore, the presence of the fluctuation i_m severely complicates any attempt at detecting a signal fluctuation i_s at low frequencies. The prevalence of diode lasers in modern laser systems means that even non-semiconductor-based solid-state continuous wave lasers¹ that are combined with semiconductor-based pump lasers will exhibit RIN even if they had no RIN to begin with. Therefore, the fluctuation i_m has to be addressed for low-frequency measurements, and the standard way to do so is to switch to a balanced detection scheme.

3.2 Balanced Photo-Detection

For the balanced detection scheme, the input beam is split into two equal halves by a beam splitter and detected by two diodes instead of just one. The photocurrents of the diodes are subtracted from each other, and the power on both diodes is adjusted to produce exactly zero mean difference photocurrent. Again, the difference photocurrent can be decomposed into similar contributions. *All* classical contributions cancel out by subtracting the individual photocurrents because they produce the *same photocurrent on both diodes* on average and in each instant. This is not the case for the quantum-mechanical part i_p as it results from individual photon detection events (even if the photodiode cannot resolve them) and, as far as the shot noise is concerned, the two diodes act as a single one with twice the active area. The same is also true for the thermal noise part i_t as its source is of quantum-mechanical nature as well, i.e., the conduction of charged carriers through a resistive part of the circuit or the spontaneous creation of (dark) hole-electron pairs in the photodiodes.

Now, the signal fluctuation has to be reintroduced into the measurement, as it also appears classical for the detector and got canceled as well. This can be done by placing a transparent sample into only one of the beams after the beam splitter or by using a polarizing beam splitter. As depicted in Fig. 3.2, the choice depends on the specific measurement. In both cases, the fluctuation in power introduced by the signal must be tiny compared to the detected power. Large fluctuations change the photocurrents in the photodiodes, and the “classical” contributions cannot be canceled perfectly anymore. For example, for a signal fluctuation originating from the scattering of photons inside the sample, the scattered photons are assumed to constitute a negligible fraction of all photons detected by the diodes of the detector. Therefore, the sample alters neither the initial photon statistic of the probe beam nor its mean power.

Using these assumptions, the detected fluctuation of the difference photocurrent i now consists only of the remaining terms:

$$i = i_s + i_p + i_t.$$

For a coherent laser beam, as far as the signal current i_s is concerned, the laser can be treated fully classically, as explained above. A small fluctuation characterizing

¹i.e., Titanium doped sapphire (Ti:Sa)

some aspect of the probed system, which is linear in the beam intensity, produces a photocurrent fluctuation $i_s = \eta_D \cdot \eta_Q P_D \cdot f(\nu)$, where f is the magnitude of the fluctuation. The variance per unit bandwidth of the photocurrent fluctuation is then just $\mathfrak{V}(i_s(\nu))/\Delta\nu = \eta_D^2 \cdot \eta_Q^2 P_D^{*2} \cdot \mathfrak{V}(f(\nu))$, because the mean power on the detector is just a constant.

In summary, the variance of $\mathfrak{V}(i)$ per unit bandwidth can be expressed as:

$$\frac{\mathfrak{V}(i(\nu))}{\Delta\nu} = \eta_D^2 \left(\eta_Q^2 P_D^{*2} \cdot \mathfrak{V}(f(\nu)) + \eta_Q P_D^* \cdot 2h\nu_p + \frac{\mathfrak{V}(i_t(\nu))}{\eta_D^2 \Delta\nu} \right) \quad (3.5)$$

$$\equiv \eta_D^2 (P_s^2(\nu) + P_p^2 + P_t^2(\nu)) \quad (3.6)$$

$$\equiv \eta_D^2 (\mathfrak{S}_s(\nu) + \mathfrak{S}_p(\nu) + \mathfrak{S}_t(\nu)), \quad (3.7)$$

where each quantity P_i is the noise equivalent power (NEP) density of the corresponding fluctuation in W^2/Hz and $\mathfrak{V}(f(\nu)) = \mathfrak{S}_f(\nu)$ is the PSD of the analyzed fluctuation in the sample system. Note that neither of the P_i are actual physical powers that can be measured with, i.e., a power meter. Their magnitude is only meaningful in relation to the detected power P_D^* .

3.3 PSD Estimate Variance and Limits

As defined in Eq. (3.7), the three contributions to a raw PSD spectrum $\mathfrak{S}_{\text{raw}} = \sum_i \mathfrak{S}_i$ are not correlated, and by acquiring sufficiently accurate and precise estimates where one or more components are not present, the raw estimate can be “decomposed” into its constituents. For example, the thermal contribution \mathfrak{S}_t can be acquired by recording the detector’s noise without any light on the diodes. Then the photon shot noise contribution \mathfrak{S}_p can be acquired by recording a raw spectrum where the laser on the diodes does not contain a signal and subsequently subtracting the previously acquired \mathfrak{S}_t estimate. Similarly, the signal estimate \mathfrak{S}_s can be acquired by subtracting an otherwise identical spectrum (a background spectrum) not containing the signal from a raw spectrum that contains the desired signal.

The PSD spectrum is the spectral distribution of the variance of some quantity. Taken for a unit bandwidth, the deviation of the mean of a PSD spectrum estimate, $\langle \mathfrak{S}_i(\nu) \rangle$, from the “underlying” spectrum $\mathfrak{S}_i(\nu)$ is the bias or accuracy of the estimate. The variance $\mathfrak{V}(\mathfrak{S}_i(\nu))$ of the PSD spectrum estimate per unit bandwidth

around the mean, *i.e.*, the variance of the variance density per unit bandwidth, is the precision of the estimate. In theory, the subtraction operations introduced above are accurate and arbitrarily precise. However, realistic estimates are acquired only over a finite time, and while their accuracy is preserved, their precision heavily depends on the measurement situation.

As section §2.1 explains, each contribution \mathfrak{S}_i can be modeled by a linearly filtered stationary Gaussian process. Therefore, the mean and variance of the estimates are not independent but are linked by the fundamental equation (2.1). Consequently, this equation also applies to the full raw spectrum itself. The mean $\langle \underline{\mathfrak{S}}_{\text{raw}}(\nu) \rangle$ is a variance that naturally decomposes into its constituents' individual variances $\langle \mathfrak{S}_i(\nu) \rangle$. However, the variance $\mathfrak{V}(\underline{\mathfrak{S}}_{\text{raw}}(\nu))$ allows no such decomposition: the variance always increases. For this reason, the experimental variance of any estimate derived through the subtraction of two or more raw estimates will always be given by the sum of the total variances of the individual raw spectra.

The consequences of the variance summation are illustrated in Fig. 3.3 using simulated spectra. Panel (a) depicts a raw spectrum that corresponds to the definition in Eq. (3.7). A realistic detector with an amplification bandwidth of 4.5 MHz and a pronounced thermal noise that appears roughly violet in the PSD spectrum (the noise is stronger at higher frequencies) is assumed. The “optical power” is chosen so that around 1 MHz, the thermal noise power (or variance) crosses the shot noise power level. The simulation is run $N = 1000$ times, and the resulting spectra's empirical mean $\langle \underline{\mathfrak{S}}_{\text{fg}} \rangle$ is plotted using black dots. The asymptotic value \mathfrak{S}_{fg} corresponding to the limit $N \rightarrow \infty$ can be calculated analytically by considering the individual components' theoretical shape and the detection bandwidth's low pass. The asymptotic variance of each component is given by its square (Eq. (2.1)), and, therefore, the variance of the simulated spectrum is given by the sum of these variances (panels (c) and (d)). The standard error of the foreground spectrum, $s_{\text{fg}}^{(N)}$, is the square root of the variance reduced by the number of averages:

$$s_{\text{fg}}^{(N)} = s_{\underline{\mathfrak{S}}_{\text{fg}}}^{(N)} = \frac{1}{N} \sqrt{\mathfrak{V}(\underline{\mathfrak{S}}_{\text{fg}})}.$$

A band containing two standard errors is drawn in red around \mathfrak{S}_{fg} to illustrate that the theoretical asymptotic variance indeed describes the variance at all frequencies.

The same simulation is run again without the signal part, and the difference, $\langle \underline{\mathfrak{S}}_{\text{fg-bg}} \rangle = \langle \underline{\mathfrak{S}}_{\text{fg}} \rangle - \langle \underline{\mathfrak{S}}_{\text{bg}} \rangle$, is plotted in panel (b). The asymptotic shape of the

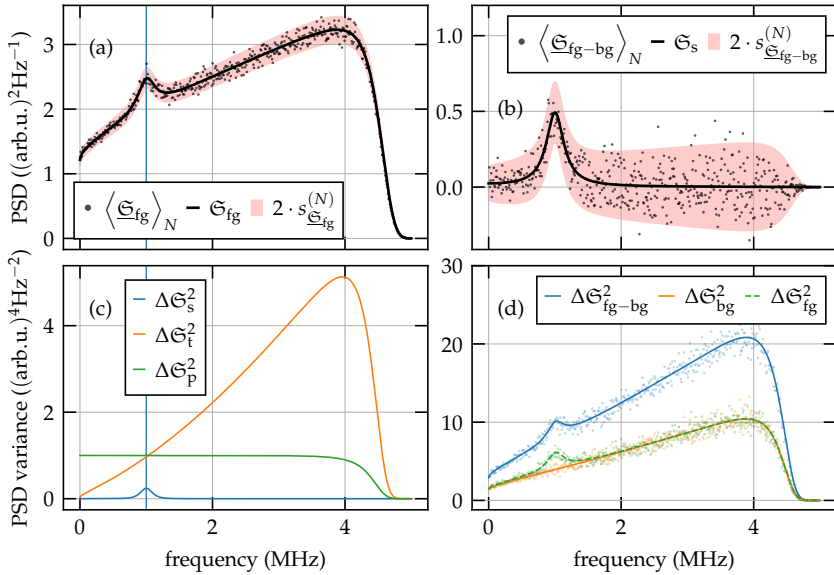


Figure 3.3: Variance and mean of various PSD estimates. Red bands designate a confidence interval of two standard errors for $N = 1000$ samples. Panel (a) depicts the mean of a simulated foreground signal $\langle \mathfrak{S}_{fg} \rangle$ and its asymptotic value \mathfrak{S}_{fg} . Panel (b) depicts the mean of a simulated difference PSD spectrum $\langle \mathfrak{S}_{fg-bg} \rangle$ as well as the asymptotic signal \mathfrak{S}_s . Panel (c) depicts the asymptotic variances of all spectral components. Panel (d) depicts the asymptotic variances of the foreground, background, and difference PSD spectra superimposed on top of their corresponding empiric variances.

spectrum is given just by the previously calculated \mathfrak{S}_s component, as all other components get canceled out on average. The variances of the involved individual raw spectra are as follows:

$$\begin{aligned}\mathfrak{V}(\underline{\mathfrak{S}}_{fg}) &= \left\langle |\underline{\mathfrak{S}}_{fg} - \mathfrak{S}_{fg}|^2 \right\rangle = (\mathfrak{S}_s + \mathfrak{S}_p + \mathfrak{S}_t)^2, \\ \mathfrak{V}(\underline{\mathfrak{S}}_{bg}) &= \left\langle |\underline{\mathfrak{S}}_{bg} - \mathfrak{S}_{bg}|^2 \right\rangle = (\mathfrak{S}_p + \mathfrak{S}_t)^2,\end{aligned}$$

and the sum of these gives the variance of the difference spectrum:

$$\boxed{\begin{aligned}\mathfrak{V}(\underline{\mathfrak{S}}_{fg-bg}) &= \mathfrak{V}(\underline{\mathfrak{S}}_{fg}) + \mathfrak{V}(\underline{\mathfrak{S}}_{bg}) \\ &= 2(\mathfrak{S}_p + \mathfrak{S}_t)^2 + \mathfrak{S}_s(\mathfrak{S}_s + 2\mathfrak{S}_p + 2\mathfrak{S}_t).\end{aligned}} \quad (3.8)$$

This form makes it easy to understand the usual shape of optical noise spectroscopy spectra. The variance of the sought-after signal $\langle \mathfrak{S}_s \rangle$ in Eq. (3.8) is hardly ever the dominating contribution compared to all other variances. Therefore, the spectrum in panel (c) of Fig. 3.3 is roughly similarly “fuzzy” at all frequencies within the amplified bandwidth as opposed to, for example, Fig. 2.3. The variance of the difference spectrum at frequencies in the vicinity and away from the signal contribution changes very little (blue curve in panel (d)). For the presented example, the variance does not stay completely constant for all frequencies because the variance of the thermal part \mathfrak{S}_t increases toward higher frequencies.

The standard deviation of the difference spectrum is:

$$\begin{aligned}\sigma_{fg-bg} &= \sigma_{\underline{\mathfrak{S}}_{fg-bg}} = \sqrt{\mathfrak{V}(\underline{\mathfrak{S}}_{fg-bg})} \\ &= \left(2(\mathfrak{S}_p + \mathfrak{S}_t)^2 + \mathfrak{S}_s(\mathfrak{S}_s + 2\mathfrak{S}_p + 2\mathfrak{S}_t) \right)^{1/2} \\ &\approx \frac{1}{\sqrt{2}}\mathfrak{S}_s + \sqrt{2}(\mathfrak{S}_p + \mathfrak{S}_t) \\ &\approx \sqrt{2}(\mathfrak{S}_p + \mathfrak{S}_t) \approx \sqrt{2}\underline{\mathfrak{S}}_{bg},\end{aligned} \quad (3.9)$$

because \mathfrak{S}_s is usually much smaller than the background contributions. Below 1 MHz, the standard deviation of the difference spectrum is mostly given by the shot noise part \mathfrak{S}_p , while above 1 MHz, the dominating term is \mathfrak{S}_t . This naturally

3 *Optical Noise Spectroscopy*

leads to the definition of the limiting noise contribution for a measurement. A noise *difference* spectrum is limited by a noise contribution \mathfrak{S}_i at frequency ν if its *background and foreground* spectra are dominated by $\mathfrak{S}_i(\nu)$.

Part II

Homodyne Spin Noise Spectroscopy on Rubidium

4 Theory

As explained in section §3.3, optical NS of weak signals is inherently limited by the noise contributions from the probe laser (shot noise) and electrical noise of the detector (thermal noise). Shot noise scales linearly with laser intensity while the signal scales quadratically. Therefore, in principle, the relative contribution of electrical noise can always be suppressed using a higher laser intensity. Unfortunately, very few physical systems of interest have a sufficiently flat intensity dependence allowing the laser intensity to be increased by such an amount in all circumstances. Consequently, most experiments require using the lowest laser intensity possible, making electrical noise the dominant limiting contribution of measurements.

Decreasing the laser intensity even further, as is, for example, necessary for single spin systems like quantum dots (QDs), imposes exploding integration times that severely limit the number of possible measurements and their temporal resolution. See chapter 11 for an example of the practical consideration involved. One way to alleviate the situation is to increase the magnitude of the signal *optically* before it reaches the detector. Such amplification would simultaneously increase the detected signal current variance and the shot noise contribution. As long as the necessary intensity stays below the saturation intensity of the photodiodes, achieving the shot-noise-limited case should always be possible. This is the idea behind homodyne spin noise spectroscopy (HSNS).

This chapter serves both as an introduction to the theoretical concepts of the detection of SN and the extension of these toward homodyne amplification. The chapter starts with a review of Jones formalism necessary to describe the state of classical light states in section §4.1. Then, section §4.2 introduces the concept of SN and how it can be measured using optical SNS. Finally, section §4.3 presents several possible extensions of SNS toward HSNS and discusses their specific properties.

4.1 Jones Formalism

This section quickly reviews the theoretical description of classical electromagnetic fields using Jones's formalism. This formalism is necessary to describe the behavior of long-time averages of the detected intensities as well as the response of the optical amplifier to classical fluctuations.

4.1.1 Classical Field Amplitudes

Classically, the laser light used to probe the sample can be approximated quite well by a solution of the wave equation with the general shape [93]:

$$\mathbf{E}_o(\mathbf{r}, t) = \mathfrak{E}_0 \cdot \left(\alpha(\mathbf{r}, t) \exp(i2\pi\nu_p t) + \alpha^*(\mathbf{r}, t) \exp(-i2\pi\nu_p t) \right) \cdot \mathbf{e}_o,$$

where \mathfrak{E}_0 is a normalization constant, α is a complex, unitless field amplitude, ν_p is the photon energy, and \mathbf{e}_o is a real or complex polarization vector $|\mathbf{e}_o|^2 = 1$ that is perpendicular to the propagation direction (i.e., the z axis). The magnitude of the complex amplitude α has the meaning of the average photon number detected in an area A_{det} over the detection time τ_{det} :

$$I_o = \epsilon_0 cn \langle |E|^2 \rangle = 2\epsilon_0 cn \mathfrak{E}_0^2 |\alpha|^2 = \frac{h\nu_o}{A_{\text{det}}\tau_{\text{det}}} |\alpha|^2, \quad \text{where} \quad \mathfrak{E}_0^2 = \frac{1}{2} \frac{h\nu_o}{\epsilon_0 cn A_{\text{det}} \tau_{\text{det}}}.$$

For a collimated, monochromatic laser beam, the complex amplitude α is usually described best by a Gaussian beam:

$$\alpha_o(\mathbf{r}, t) = \frac{i\alpha_o(t)}{q(z)} \exp\left(\frac{-ik_p r^2}{2q(z)}\right) \exp(-ik_p z), \quad (4.1)$$

where $q(z) = z + iz_R$, $z_R = \pi w_0^2/\lambda_p$ is the Rayleigh length, w_0 is the radius of the beam waist radius, $k = 2\pi/\lambda_p$ is the angular wave number, and the light propagates in the z direction. However, it is usually enough to consider just the central region of the Gaussian beam ($r \approx 0$) so that the expression can be simplified to that of a plane wave:

$$\alpha_o(z, t) = \alpha_o(t) \exp(-ik_p z).$$

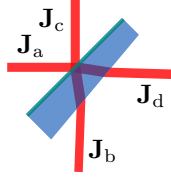


Figure 4.1: The convention for the inputs and outputs of the beam splitter matrix.

4.1.2 State Vectors

The complex amplitude $a(t)$ and the polarization vector \mathbf{e}_o together can be summarized into a Jones vector:

$$\mathbf{J}_o(t) = a(t)\mathbf{e}_o.$$

The action of most linear optical components then can be described by the multiplication with a complex 2×2 Jones matrix. For example, the effects of linear polarizers aligned to the x and y directions are described in a linear polarized basis of \mathbf{e}_x and \mathbf{e}_y by:

$$M_x = \begin{pmatrix} 1 & 0 \\ 0 & 0 \end{pmatrix} \quad \text{and} \quad M_y = \begin{pmatrix} 0 & 0 \\ 0 & 1 \end{pmatrix}.$$

Any other alignment can be achieved by transforming the Jones matrix using the rotation matrix $R(\theta)$:

$$R(\theta) = \begin{pmatrix} \cos(\theta) & \sin(\theta) \\ -\sin(\theta) & \cos(\theta) \end{pmatrix} \quad \text{and} \quad M_\theta = R(-\theta)M_xR(\theta).$$

This transformation is also valid for any other Jones matrix.

A beam splitter mixes two modes according to their polarizations and cannot be described by a simple Jones matrix. Instead, in the situation depicted in Fig. 4.1, the state vectors transform like $\tilde{\mathbf{J}}_{\text{out}} = M_{\text{BS}} \cdot \tilde{\mathbf{J}}_{\text{in}}$, where

$$M_{\text{BS}} = \begin{pmatrix} ir_x & 0 & t_x & 0 \\ 0 & ir_y & 0 & t_y \\ t_x & 0 & ir_x & 0 \\ 0 & t_y & 0 & ir_y \end{pmatrix}, \quad \tilde{\mathbf{J}}_{\text{in}} = \begin{pmatrix} J_{a,x} \\ J_{a,y} \\ J_{b,x} \\ J_{b,y} \end{pmatrix}, \quad \tilde{\mathbf{J}}_{\text{out}} = \begin{pmatrix} J_{c,x} \\ J_{c,y} \\ J_{d,x} \\ J_{d,y} \end{pmatrix},$$

and $|r_i|^2 + |t_i|^2 = 1$ for $i = x, y$. For example, a non-polarizing beam splitter is

4 Theory

realized by choosing $r_{x,y} = t_{x,y} = \sqrt{1/2}$:

$$\mathbf{J}_c = \begin{pmatrix} J_{c,x} \\ J_{c,y} \end{pmatrix} = \frac{1}{\sqrt{2}} \begin{pmatrix} iJ_{a,x} + J_{b,x} \\ iJ_{a,y} + J_{b,y} \end{pmatrix} \quad \text{and} \quad \mathbf{J}_d = \begin{pmatrix} J_{d,x} \\ J_{d,y} \end{pmatrix} = \frac{1}{\sqrt{2}} \begin{pmatrix} J_{a,x} + iJ_{b,x} \\ J_{a,y} + iJ_{b,y} \end{pmatrix}.$$

On the other hand, a polarizing beam splitter is accomplished by choosing $r_x, t_y = 0$ and $r_y, t_x = 1$:

$$\mathbf{J}_c = \begin{pmatrix} J_{c,x} \\ J_{c,y} \end{pmatrix} = \begin{pmatrix} J_{b,x} \\ iJ_{a,y} \end{pmatrix} \quad \text{and} \quad \mathbf{J}_d = \begin{pmatrix} J_{d,x} \\ J_{d,y} \end{pmatrix} = \begin{pmatrix} J_{a,x} \\ iJ_{b,y} \end{pmatrix}.$$

4.2 Spin Noise Spectroscopy

Real physical systems at a finite temperature exhibit fluctuations around their steady or equilibrium state. These fluctuations are usually perceived as an unwanted, detrimental random noise source. However, the noise of real systems is not truly random but contains information about the investigated system, as previously discussed in Part I. The particular flavor of optical noise spectroscopy considered in this thesis concerns the dynamics of charge carrier spins: spin noise spectroscopy (SNS).

Alexandrov and Zapasskii performed one of the first spin noise spectroscopy (SNS) experiments [68, 69, 70]. The experiment investigated the spin dynamics of the outer shell electron spin in sodium vapor atoms. The fluctuations of the spin system caused a fluctuation of the polarization plane of linearly polarized light transmitted through the sample cell. Radio-frequency spectral analysis of these fluctuations revealed the electron paramagnetic resonance of sodium. A theoretical interpretation of the experiment was proposed only a few years later, relating it to Raman scattering of photons at the sample [69]. Soon after, Oestreich et al. [71] transferred the technique to the solid state domain by performing an experiment on donor-bound electrons in GaAs. This experiment allowed them to extract the electron g -factor and the spin dephasing times of the bound electrons. Crooker et al. [66] transferred the technique to ensembles of charged QDs. Finally, Dahbashi et al. [72] improved the technique to work even on individual hole charges trapped in quantum dots. By now, SNS has become a well-established tool for investigating spin dynamics in even the most delicate solid-state systems.

The circumstance allowing such broad applicability of SNS stems from optical

resonances in atomic and solid-state systems. Spin polarization and the dielectric response are interlinked close to optical resonances. Spin fluctuations within the system cause a minute change in the dielectric response. This temporary optical activity imprints the spin fluctuations in the polarization state fluctuation of a laser beam interacting with the sample. In typical systems, the tails of the dielectric function are quite wide, enabling spectroscopy of the spin system with laser light far-detuned from the optical resonance. For this reason, SNS allows for continuously tuning the probing regime from a thermal equilibrium [76] to a quasi-resonantly driven regime [96] allowing this technique to be employed in very different settings.

This section starts by discussing elementary spin dynamics in section §4.2.1. These concepts are essential to understand the structure of the observed spectra. Furthermore, the quantum-mechanical framework is introduced that will be further developed in chapter 10 for describing SN of (In,Ga)As QD in a non-equilibrium regime. Section §4.2.2 discusses the general properties of SNS, and section §4.2.3 highlights the specifics of optical SNS. Finally, section §4.2.4 introduces a microscopic interpretation convenient for interference experiments.

4.2.1 Spin Dynamics

This subsection quickly introduces the quantum-mechanical description of spin dynamics and spin relaxation using the example of a single electron spin. The spin of a spin $1/2$ particle like the electron has two possible projections defined by the magnetic quantum number $m_z = \pm 1/2$. The two corresponding eigenstates are usually denoted by $|\uparrow\rangle$ and $|\downarrow\rangle$, for $m_z = +1/2$ and $m_z = -1/2$, respectively. In general, a pure spin state is defined by the superposition:

$$|\psi\rangle = \alpha |\uparrow\rangle + \beta |\downarrow\rangle,$$

where α and β are complex amplitudes. The normalization of the wave function restricts the allowed values to $|\alpha|^2 + |\beta|^2 = 1$. Up to a global phase, a spin state can be represented by [97]:

$$|\psi\rangle = \underbrace{\cos\left(\frac{\theta}{2}\right)}_{\alpha} |\uparrow\rangle + \underbrace{\exp(i\varphi) \sin\left(\frac{\theta}{2}\right)}_{\beta} |\downarrow\rangle.$$

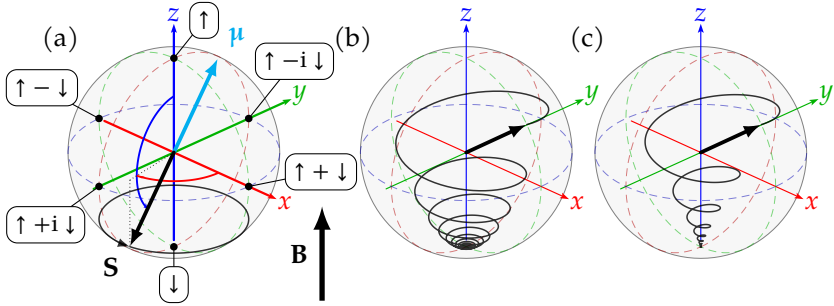


Figure 4.2: Evolution of the *electron* spin expectation value \mathbf{S} in different conditions. The panels (a), (b), and (c) depict coherent evolution, relaxation with homogeneous dephasing, and relaxation with inhomogeneous dephasing, respectively.

The pure states are a special case of the spin density matrix $\hat{\rho}$. A pure state can be converted into density matrix form using:

$$(\hat{\rho})_{i,j} = \langle i|\psi\rangle\langle\psi|j\rangle.$$

However, a conversion in the other direction is only possible if the state is pure. The spin operator $\hat{\mathbf{S}}$ determines the measurements that can be performed on the spin state $\hat{\rho}$. In the used convention, the spin operator can be defined as:

$$\hat{\mathbf{S}} = (\hat{S}_x, \hat{S}_y, \hat{S}_z), \quad \hat{S}_i = \hbar |m_z| \hat{P}_i,$$

where \hat{P}_i are the Pauli matrices¹ and the state order is $|\uparrow\rangle$ and $|\downarrow\rangle$. The expectation values of an operator are given by the trace of the operator and the density matrix, for example, $S_i = \langle \hat{S}_i \rangle = \text{tr}(\hat{S}_i \hat{\rho})$. For the spin state $|\psi\rangle$ defined above, the spin's expectation values are:

$$S_x = \frac{\hbar}{2} \sin(\theta) \cos(\varphi), \quad S_y = \frac{\hbar}{2} \sin(\theta) \sin(\varphi), \quad S_z = \frac{\hbar}{2} \cos(\theta).$$

The expectation value of the spin \mathbf{S} describes a point on a sphere. On the other hand, for a $1/2$ spin, the angles parameterizing the complex amplitudes α and β

¹ $\hat{P}_x = \begin{pmatrix} 0 & 1 \\ 1 & 0 \end{pmatrix}$, $\hat{P}_y = \begin{pmatrix} 0 & -i \\ i & 0 \end{pmatrix}$, $\hat{P}_z = \begin{pmatrix} 1 & 0 \\ 0 & -1 \end{pmatrix}$

also determine a location on a complex sphere. For pure states, this correspondence allows for mapping the amplitudes to the direction of \mathbf{S} [97], as illustrated by the black dots in panel (a) of Fig. 4.2. This mapping is called the Bloch sphere. The surface of the sphere contains the pure spin states, while inside are the partly incoherent and mixed states.

In an external magnetic field, the evolution of the spin is determined by the Zeeman Hamiltonian term [98]:

$$\mathcal{H} = -\hat{\boldsymbol{\mu}}_e \cdot \mathbf{B},$$

where $\hbar\hat{\boldsymbol{\mu}}_e = g_e\mu_B\hat{\mathbf{S}}$ is the magnetic moment of the electron, and $\mu_B = \frac{e}{2m_e}$ is Bohr's magneton. The time dependence of the state $\hat{\rho}$ is given by the Liouville-von-Neumann equation [99]:

$$\dot{\hat{\rho}} = \frac{d}{dt}\hat{\rho} = i[\hat{\rho}, \mathcal{H}] + \mathcal{L}[\hat{\rho}], \quad (4.2)$$

where the first term on the right-hand side defines the coherent part of the evolution, whereas the second term describes phenomenological relaxation or damping processes. In the absence of the second term, the solution to this system of differential equations in a magnetic field $\mathbf{B} = B_z\mathbf{e}_z$ is:

$$S_x(t) = \frac{\hbar}{2} \sin(\theta) \cos(t\omega_L + \varphi), \quad S_y(t) = \frac{\hbar}{2} \sin(\theta) \sin(t\omega_L + \varphi), \quad S_z(t) = \frac{\hbar}{2} \cos(\theta)$$

where $\omega_L = \frac{|g_e|\mu_B}{\hbar}B_z$ is the Larmor frequency. Without relaxation, the spin vector precesses around the direction of the magnetic field indefinitely without changing its azimuth angle θ .

When the spin is coupled to an environment, the coherent motion will decay and will eventually end up in a steady state that lies somewhere along the axis of the Bloch sphere between the $|\uparrow\rangle$ and $|\downarrow\rangle$ states:

$$\begin{aligned} \hat{\rho}_{ss} &= \lim_{t \rightarrow \infty} \hat{\rho} = \left(\frac{1}{2} - \frac{\bar{S}_z}{\hbar} \right) |\downarrow\rangle\langle\downarrow| + \left(\frac{1}{2} + \frac{\bar{S}_z}{\hbar} \right) |\uparrow\rangle\langle\uparrow|, \\ \dot{\hat{\rho}}_{ss} &= 0, \end{aligned}$$

where $|\bar{S}_z| \leq 1/2\hbar$ is the steady state spin polarization. The relaxation term can be concisely written using the damping superoperator for some coupling operator \hat{o} :

$$\mathcal{D}_{\hat{\rho}}[\hat{\rho}] = \frac{1}{2} (\hat{\sigma}^{\dagger} \hat{\sigma} \hat{\rho} + \hat{\rho} \hat{\sigma}^{\dagger} \hat{\sigma} - 2\hat{\sigma} \hat{\rho} \hat{\sigma}^{\dagger}).$$

For this simple example, the relaxation term can be written as:

$$\mathcal{L}[\hat{\rho}] = -\frac{\gamma}{2} (\mathcal{D}_{|\uparrow\rangle\langle\downarrow|}[\hat{\rho}] + \mathcal{D}_{|\downarrow\rangle\langle\uparrow|}[\hat{\rho}]),$$

where γ is the decay rate of the spin. Inserting the relaxation term into Eq. (4.2) yields a new differential equation. It is helpful to express the differential equation in terms of the observables S_i for a deviation of $\hat{\rho}$ from the steady state $\hat{\rho}_{ss}$, $\hat{\rho} - \hat{\rho}_{ss}$. The equations can then be stated concisely:

$$\left. \begin{aligned} \dot{S}_x(t) &= -\omega_L S_y(t) - 1/T_2 S_x(t), \\ \dot{S}_y(t) &= +\omega_L S_x(t) - 1/T_2 S_y(t), \\ \dot{S}_z(t) &= -1/T_1 (S_z(t) - \bar{S}_z), \end{aligned} \right\} \quad (4.3)$$

where $1/T_1 = \gamma$ and $1/T_2 = \frac{1}{2}\gamma$. The corresponding solution is:

$$\begin{aligned} S_x(t) &= e^{-t/T_2} (S_x(0) \cos(\omega_L t) - S_y(0) \sin(\omega_L t)), \\ S_y(t) &= e^{-t/T_2} (S_x(0) \sin(\omega_L t) + S_y(0) \cos(\omega_L t)), \\ S_z(t) &= (S_z(0) - \bar{S}_z) e^{-t/T_1} + \bar{S}_z. \end{aligned}$$

The motion of the spin describes a dampened precession around the magnetic field direction that decays toward the steady state \bar{S}_z , as depicted in panel (b) of Fig. 4.2. The $1/T_1$ rate corresponds to a dissipative force that pulls the spin's z-component toward the steady state point \bar{S}_z . Therefore, the corresponding time T_1 is called the *longitudinal relaxation* time. After T_1 seconds, the z-component has decayed to $1/e$ of its initial value toward the steady state. The $1/T_2$ rate corresponds to a force that pulls the transverse components toward the z axis. Once the spin reaches the axis, it is impossible to tell where it initially pointed. Therefore, the corresponding time T_2 is called the *transverse dephasing* or *spin coherence* time. After T_2 seconds, the magnitude of the transverse components has fallen to $1/e$. In the example above, the dephasing time is homogeneous $T_2 = 2T_1$. Generally, the relaxation processes can be more complicated, and the resulting relationship between the decay rates can be more intricate [97]. In particular, this is the case when the spin interacts with a randomly fluctuating magnetic field (or a bath of nuclear

spin). In this case, the observed dephasing is no longer limited by the spin coherence but by the statistical distribution of the fluctuations, as depicted in panel (c) of Fig. 4.2. This shorter effective dephasing time is called the inhomogeneous dephasing time $T_2^* < T_2$ [47].

4.2.2 Spin Noise

Spins systems exhibit fluctuations when the splitting E_Z between the Zeeman sub-levels is smaller than the thermal energy $k_B T$. These fluctuations temporarily drive the spin system away from its steady state $\bar{\mathbf{S}}$. The differential equations covered above govern the dynamics and decay of these excitations. Herein lies the essence of SNS: no deliberate excitation is necessary to observe the spin dynamics, as the system's temperature already provides the necessary *state preparation*. In particular, for systems close to the thermal equilibrium, the observed dynamics of thermal fluctuations correspond to the linear response of the system, as formalized by the fluctuation-dissipation theorem [78].

The dynamics can be observed through a projection of the spin. In optical SNS, the propagation direction of laser light defines this projection. The fluctuation operator $\delta\hat{S}_i = \hat{S}_i - \bar{S}_i$ describes the spin fluctuations in the introduced formalism. Here, \hat{S}_i and \bar{S}_i are the projections of the spin operator $\hat{\mathbf{S}}$ and its steady state expectation value $\bar{\mathbf{S}}$ on the observation direction. In the special case of thermal equilibrium at a high temperature, no polarization is present, and $\bar{\mathbf{S}}$ is zero. Common choices for the observation direction are the *Faraday geometry* and the *Voigt geometry*, using $\hat{S}_i = \hat{S}_z$ and $\hat{S}_i = \hat{S}_{x,y}$, respectively.

The expectation value of the fluctuation operator in the steady state corresponds to a long-time average and is zero per definition: $\langle \delta\hat{S}_i \rangle_{\text{ss}} = \langle \delta\hat{S}_i \rangle_{\infty} = 0$. However, instantaneous fluctuations $\langle \delta\hat{S}_i \rangle_{\epsilon}$ are not zero resulting in a finite variance of the observed deviation around the steady state. As the dynamics stay the same, the quantum regression theorem by Lax and Carmichael [100, 101, 102] can be used to gain insight into the statistical properties of these fluctuations. Applying the regression theorem to the Bloch equations in Eq. (4.3) yields the following expressions for the evolution of spin fluctuation correlators $c_i(\tau) = \langle \{ \delta\hat{S}_i(0), \delta\hat{S}_i(\tau) \} \rangle_{\text{ss}} / \langle \hat{S}_z^2 \rangle$:

4 Theory

$$\begin{aligned}\dot{c}_{i;x}(\tau) &= -\omega_L c_{i;y}(\tau) - 1/T_2 c_{i;x}(\tau), \\ \dot{c}_{i;y}(\tau) &= +\omega_L c_{i;x}(\tau) - 1/T_2 c_{i;y}(\tau), \\ \dot{c}_{i;z}(\tau) &= -1/T_1 c_{i;z}(\tau),\end{aligned}$$

where τ is the temporal lag, $\{\hat{a}, \hat{b}\} = \frac{1}{2}(\hat{a} \cdot \hat{b} + \hat{b} \cdot \hat{a})$, and the cross-correlators are defined as $c_{i;j}(\tau) = \langle \{\delta\hat{S}_i(0), \delta\hat{S}_j(\tau)\} \rangle_{\text{ss}} / \langle \hat{S}_z^2 \rangle$ with initial values $c_{i,j}(0) = \langle \{\delta\hat{S}_i, \delta\hat{S}_j\} \rangle_{\text{ss}} / \langle \hat{S}_z^2 \rangle$. Solving this initial value problem for the Voigt and Faraday geometries yields:

$$\begin{aligned}c_x(\tau) = c_y(\tau) &= \exp(-\tau/T_2) \cos(\omega_L \tau), \\ c_z(\tau) &= \exp(-\tau/T_1).\end{aligned}$$

The WKT links these ACFs to the statistical and spectral properties of the corresponding random process and its spectrum, as described in Part I.

The corresponding Fourier transforms of these ACFs are:

$$\begin{aligned}\tilde{c}_{x,y}(2\pi\nu) &= \frac{1/T_2}{(1/T_2)^2 + (2\pi(\nu_L + \nu))^2} + \frac{1/T_2}{(1/T_2)^2 + (2\pi(\nu_L - \nu))^2}, \\ c_y(2\pi\nu) &= 2 \frac{1/T_1}{(1/T_2)^2 + (2\pi\nu)^2}.\end{aligned}$$

In Voigt geometry, the spectrum consists of two Lorentzian peaks centered at the Larmor frequencies $\pm\nu_L = \pm\omega_L/2\pi$. The *dephasing* rate π/T_2 gives the width of the Lorentzians. Conversely, in Faraday geometry, only one peak with twice the area is present, and the *relaxation* rate gives its width π/T_1 . This feature of SNS allows for measuring both relaxation rates independently, simply by changing the magnetic field direction by $\pi/2$.

More complicated systems might consist of a spin ensemble where the Larmor precession frequencies of individual spins are not equal but are normally distributed around a mean value. In this case, $\tilde{c}_{x,y}(2\pi\nu)$ will consist of two Gaussian peaks centered at the mean frequencies $\pm\nu_L$, broadened by the corresponding width of the distribution [76, 103]. Similarly, different decay dynamics will alter the spectrum, allowing SNS to discern these different processes. Theoretical treatment of systems in the non-equilibrium regime works conceptually similarly

to the presented example and is the topic of chapter 10.

4.2.3 Optical Spin Noise Spectroscopy

The remaining piece necessary for optical SNS is a link between the instantaneous spin polarization and the optical response of the probed system. In many material systems, the optical resonances are highly sensitive to spin polarization due to strict optical dipole selection rules [104]. The rules allow a σ^\pm circularly polarized photon to be absorbed only by a transition between certain spin states. When the spin is already polarized, the probability of absorbing a photon becomes zero. Alternatively, the magnetization of the spin system can contribute additional fluctuating Zeeman splitting to (possibly otherwise unrelated) resonances. For example, the noise of nuclear spins can be revealed by a sharp optical resonance, even though the nuclear spins do not directly couple to light [103]. As explained in the supplementary of [103], the first effect leads to *state-filling*-induced dichroism, while the second effect leads to *splitting*-induced birefringence. These two effects provide the phenomenological explanation of the SNS probing process [76].

In the simplest case, the optical resonance consists of a pair of optical transitions, as would be the case for a four-level system with two allowed transitions (see chapter 9). The dielectric function for the system's red and blue Zeeman branches can be written as [105]:

$$\epsilon_{\pm}(\omega) = 1 + \frac{f_{\pm}}{\omega_{\pm}^2 - \omega^2 - i\omega\Gamma},$$

where the oscillator strengths f_{\pm} are proportional to the dipole transition matrix element and the spin polarization, ω_{\pm} are the optical transition frequencies, ω is the frequency of the probe light, and Γ is the line width of the transition. In non-magnetic systems, the square root of $\epsilon_{\pm}(\omega)$ is equal to the complex index $n_{\pm}^{\bullet}(\omega)$ that can be decomposed into real refractive and imaginary absorptive parts:

$$n_{\pm}^{\bullet}(\omega) = n_{\pm}(\omega) + i\kappa_{\pm}(\omega).$$

Linearly polarized probe light (a coherent superposition of σ^\pm light) experiences a different phase velocity and absorption for its σ^\pm components. When the light leaves the sample, it is no longer purely linearly polarized. Instead, its polarization vector describes an ellipse.

Each σ^\pm component interacts only with one of the dielectric functions. There-

4 Theory

fore, the effective dichroism and birefringence experienced by the linearly polarized light are determined by the quantities $\Delta n(\omega)$ and $\Delta\alpha(\omega)$:

$$\begin{aligned}\Delta n(\omega) &= n_-(\omega) - n_+(\omega), \\ \Delta\alpha(\omega) &= \kappa_-(\omega) - \kappa_+(\omega).\end{aligned}$$

The complex amplitude \mathbf{J} of an initially linearly polarized beam can be written as:

$$\mathbf{J}_{\text{in}} = J_{\text{h}}\mathbf{e}_{\text{h}} + J_{\text{v}}\mathbf{e}_{\text{v}} = J_{\pm}^{\bullet}\mathbf{e}_{-} + J_{\pm}^{\circ}\mathbf{e}_{+},$$

where $\mathbf{e}_{\text{h,v}}$ and \mathbf{e}_{\pm} are unit vectors in the linear and circular bases, respectively, and the circular components are $J_{\pm}^{\bullet} = \frac{1}{\sqrt{2}}(\alpha \mp i\beta)$. The circular components of the state vector acquire a different complex phase shift $\propto \exp(i n_{\pm}^{\bullet} k l)$. Finally, the state vector can be converted to a linear basis to observe the effect of the resonance. An initially vertically polarized beam with $\mathbf{J}_{\text{in}} = \mathbf{e}_{\text{v}}$ is assumed for simplicity. The components of the output state $\mathbf{J}_{\text{out}} = J_{\text{out,h}}\mathbf{e}_{\text{h}} + J_{\text{out,v}}\mathbf{e}_{\text{v}}$ read:

$$\begin{aligned}J_{\text{out,h}} &= -\frac{i}{2}(e^{i n_{+}^{\bullet} k l} - e^{i n_{-}^{\bullet} k l}), \\ J_{\text{out,v}} &= +\frac{1}{2}(e^{i n_{+}^{\bullet} k l} + e^{i n_{-}^{\bullet} k l}).\end{aligned}$$

Fig. 4.3 depicts traces of the resulting polarization ellipse at different probe frequencies for two distinct cases. Column (a) depicts a resonance with a negligible Zeeman splitting but significantly different absorption for the σ^{\pm} components. Column (b) depicts a resonance with a significant Zeeman splitting but equal absorption for the σ^{\pm} components. In both cases, on resonance (where κ_{\pm} are large), the absorption reduces the state vector amplitude and makes the polarization strongly elliptic. However, the absorption quickly drops, as visible from the lower panels. The situation is different for refractive index difference that results in a polarization rotation. Many line widths away from the resonance, the rotation is still present, even though the absorption has already become negligible, as seen from the magnitude of the state vector. In the second case, the resulting rotation far from resonance is proportional to the Zeeman splitting, known as the Faraday effect [106]. Nevertheless, for the consideration presented below, the polarization

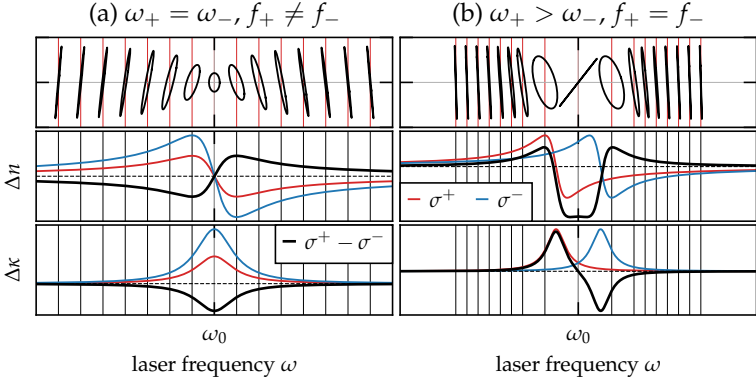


Figure 4.3: Dielectric functions of a simple four-level resonance and the corresponding ellipticity of a transmitted beam. Case (a) on the left depicts the response for a bulk dichroism at negligible Zeeman splitting. Case (b) depicts the opposite case.

plane's rotation resulting from a spin polarization fluctuation will be referred to as *Faraday rotation*, even though no bulk Faraday effect is present in case (a).

Fluctuations of the spin polarization temporarily change the oscillator strengths f_{\pm} , resulting in a fluctuation of both the ellipticity \mathcal{E} and Faraday rotation \mathfrak{F} . Therefore, the noise power of spin polarization fluctuations \mathfrak{S}_{SN} gets imprinted onto the polarization and ellipticity sidebands of the transmitted beam. Consequently, the sensitivity of the measurement is not constant but depends, instead, on the shape of the dielectric response. The variance of Faraday angle and ellipticity fluctuations is proportional to the additional change in refractive index and ellipticity:

$$\begin{aligned}\delta\mathfrak{F}^2(\omega) &\propto \mathfrak{V}(\theta_{\text{F}}(\omega)) \propto \mathfrak{V}(\Delta n(\omega)) \propto \mathfrak{S}_{\text{s}} \cdot (\delta\Delta n(\omega))^2, \\ \delta\mathcal{E}^2(\omega) &\propto \mathfrak{V}(\Delta\kappa(\omega)) \propto \mathfrak{S}_{\text{s}} \cdot (\delta\Delta\kappa(\omega))^2.\end{aligned}$$

Note that the big Δ refers to the bulk asymmetry of the dielectric response for σ^{\pm} light. In contrast, the small δ accounts only for changes of δf_{\pm} due to spin polarization fluctuations. Fig. 4.4 depicts the corresponding curves for the considered examples. The sensitivity of $\delta\mathcal{E}^2$ is maximal at $\omega = \omega_{\pm}$ (orange), while the sensitivity of $\delta\mathfrak{F}^2$ is maximal at $\omega = \omega_{\pm} \pm \Gamma/2$ (green), where the absorption is already

4 Theory

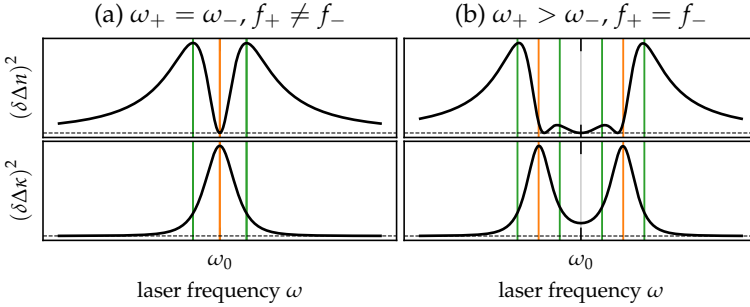


Figure 4.4: The sensitivity of SNSs is determined by the change in the dielectric response. Case (a) on the left depicts the change for a bulk dichroism at negligible Zeeman splitting. Case (b) depicts the opposite case.

significantly reduced. This fact is why SNS remains usable even far away from the resonance, allowing it to reach a quasi-nonperturbative regime. Consequently, Faraday rotation angle fluctuations $\delta\mathfrak{F}$ are the predominantly measured quantity in SNS experiments.

A polarization bridge can extract the SN sideband from the probe light by decomposing the signal beam into two mutually orthogonal polarizations and mixing them on the diodes of a balanced photodetector, as discussed in section §3.2 and below in section §4.3.1. As the laser frequency is scanned over the resonance, the bulk Faraday rotation angle changes in response to a different $\Delta n(\omega)$ (black curve in Fig. 4.3). The same is true if the external magnetic field changes, leading to a bulk Faraday effect. For the polarization bridge to work, the power on the diodes must be the same on average. This balancing is usually accomplished by biasing the bridge with a motorized half-wave retarder. The retarder compensates for the bulk rotation, aligning the input polarization to the bridge $\pi/4$ with respect to the input polarizer angles.

A properly adjusted polarization bridge is insensitive to ellipticity fluctuations \mathfrak{E} for measurements performed in transmission. However, this is generally not the case when the signal beam contains a co-propagating beam with a phase mismatch to the probe beam. This is often the case when measurements are performed in reflection geometry, as the interface between the sample and air (or vacuum) reflects part of the light back to the detector. The parasitic reflected beam interferes with the signal beam on the photodiodes and produces additional terms that depend on

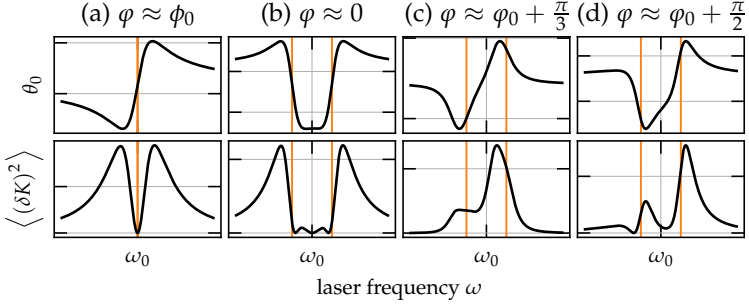


Figure 4.5: Variance of Kerr signal fluctuations for different phase mismatch. Orange lines mark the locations of the two Zeeman branches.

the phase mismatch φ between the two beams. This phase dependence is known as the *Kerr effect*. Kerr fluctuations $\delta\mathfrak{K}$ are the general case of SNS signals. They consist of a weighted sum of Faraday rotation and ellipticity fluctuations according to [107]:

$$\mathfrak{K}(\varphi, \omega) \approx \cos(\varphi) \mathfrak{F}(\omega) + \sin(\varphi) \mathfrak{E}(\omega).$$

Depending on the magnitude of the reflected beam and the phase angle, the optical frequency dependence of Kerr fluctuation variance $\langle (\delta K)^2 \rangle$ can become quite intricate, as depicted in Fig. 4.5. Here, columns (a) and (b) show the magnitude of $\langle (\delta K)^2 \rangle$ for the two examples considered so far. The phase φ has been adjusted to account for the phase shift φ_0 that the probe beam acquires. In these cases, the variance consists almost purely of Faraday fluctuations. For columns (c) and (d), the phase mismatch is increased by $\pi/3$ and $\pi/2$, respectively, making the variance curves asymmetric. In all columns, the orientation of the polarization ellipse is plotted in the upper panel. The shape of this dependence indicates if a strong phase mismatch is present in the experimental setup. For example, a Stokes polarimeter can be used to characterize the phase mismatch [108].

4.2.4 (Spin-Flip) Raman Scattering Picture

This subsection aims to present a microscopic explanation of spin noise spectroscopy SNS. Initially, this interpretation was introduced just several years after the experiment by Aleksandrov & Zapasskii [68]. Gorbovitskii & Perel suggested

4 Theory

that SNS and Raman spectroscopy shared a conceptual similarity and were governed by the same mechanism [69]. To validate this interpretation, they proposed an experiment that was successfully carried out by Kamenskii et al. [4] almost 40 years later. The underlying idea is that the formation of the polarimetric signal observed in SNS can be understood as the scattering of laser light by the sample and the spin system [69, 73, 109, 110].

The scattering of photons is subject to selection rules that determine what transitions are possible depending on the geometry of the experiment [111]. For typical material systems, it is valid that photons can transfer angular momentum to the spin system in Voigt geometry. Therefore photons scattered at the spin system can flip the spin while simultaneously changing their polarization. As the spin sub-states are split by a Zeeman energy E_Z , the scattered photons have their energy reduced by the same amount. The instantaneous spin polarization determines the probability of the scattering event, causing spin system fluctuations to manifest as a sideband ($\sim 1/T_2$) in the scattered photons.

In Faraday geometry, spin flips are typically forbidden by selection rules [111]. However, a system probed by a linearly polarized laser can take only one of the possible σ^\pm transitions for a round-trip from the ground state to an excited state and back. The scattering events change the polarization of the probe light photons, aligning it with the circular transition at which they are scattered. The photon's energy is conserved because the same transition is involved. Again, the probability of scattering at either transition is directly correlated to the instantaneous spin polarization, embedding the spin fluctuations as a sideband ($\sim 1/T_1$) of the scattered photons. Faraday and Voigt style processes are allowed when the magnetic field is tilted, and the relative amplitude depends on the tilt angle.

The resulting signal beam contains a mixture of *forward-scattered* and transmitted photons. It can be decomposed into two linear and mutually orthogonal components: $\mathbf{J}_{\text{sig}} \approx \mathbf{J}_{\text{prob}} + \mathbf{J}_{\text{scat}}$, where the \mathbf{J}_{prob} part contains photons that did not interact with the sample, and \mathbf{J}_{scat} only contains photons that got scattered. For an experiment in Voigt geometry, \mathbf{J}_{prob} and \mathbf{J}_{scat} also have different photon energy. Putting this signal through a dispersive element like a spectrometer and detecting the intensity results in a Raman spectrum with three peaks at ω_{laser} and $\omega_{\text{laser}} \pm \omega_L$. Alternatively, mixing the beams \mathbf{J}_{prob} and \mathbf{J}_{scat} in a polarization bridge lowers the spin noise sideband from the optical frequencies to radio frequencies. Recording a spectrum of the intensity fluctuations on the detector reveals two peaks of the SN sideband centered at the beat frequencies $\pm \omega_L$ [73].

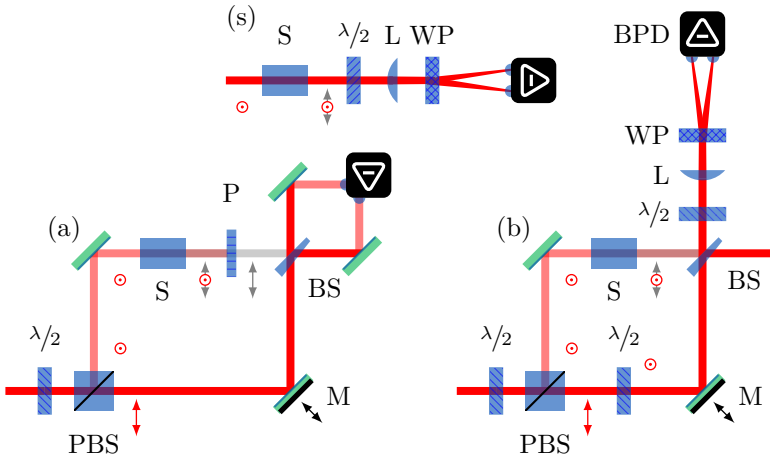


Figure 4.6: Panels (a) and (b) display two possible HSNS schemes, a balanced and an unbalanced, respectively. (BPD: Balanced photo receiver, WP: Wollaston prism, $\lambda/2$: half wave retarder, L: lens, P: linear polarizer, BS: beam splitter, PBS: polarizing beam splitter, M: piezo actuated mirror, S: sample) Panel (s) displays the standard (self-homodyne) SNS scheme.

The idea behind the experiment proposed by [69] is that the not interacting probe part J_{prob} bears no information and is therefore not necessary to detect the SN – it can be substituted by any other beam with the same frequency and phase relationship. In particular, SN should be present in photons that were scattered at an angle to the initial probe beam. The practical demonstration of a SN signature in a homodyne interference experiment between not co-axially scattered light and a separate reference beam in Ref. [4] confirms that the interpretation of Gorbovitskii & Perel is indeed a valid microscopic picture of SNS.

4.3 Homodyne Detection

The empirical view of balanced detection and the involved optical noise sources, as presented in chapter 3, is usually sufficient for regular SNS. However, a more refined approach is necessary to properly describe the optical amplification in ho-

4 Theory

modyne schemes. The optical setups presented below operate well in the linear regime and hence can be treated semi-classically. This means that the laser beams used in the setup can be represented by coherent or Glauber states. Then, using a linearization approach by Ref. [93], it is possible to show that the instantaneous detected intensity can be split into a long-term average, classical fluctuations, and an operator that describes the quantum fluctuations. As the setups are linear, the coherent and vacuum states are transported through them without experiencing a change in their variance. Consequently, the detected states are also “round” coherent states with symmetric intensity and phase quadrature variance of exactly 1.

For example, each of the photodiodes of the balanced detector in Fig. 3.2 detects a beam that has been split by a beam splitter and hence has half the initial intensity. Both beams have the same intensity quadrature variance. Therefore the quantum-mechanical part of the difference photocurrent variance is proportional to the sum of the two variances. The product of the reduced average intensity and the difference photocurrent variance due to quantum noise is equal to the product of the average intensity of the initial beam and the intensity quadrature variance of a single coherent state. That is, for the total intensity variance, it does not matter how many photodiodes detected the beam as long as all of its power was detected. Therefore, for this section, the propagation of the laser beams is described classically, and the quantum fluctuations are treated as implied. They can be recovered in the end by summing the quadrature variances of the detected states that contribute to the measured quantity and multiplying the resulting variance with the mean intensity at the detector.

4.3.1 Self-Homodyne Scheme

Before delving into the more complicated homodyne setups, it makes sense first to apply the introduced formalism to the traditional SNS scheme and recover the empirically observed shape of the Eq. (3.7). This case is depicted in panel s) of Eq. (4.6). A linearly y -polarized probe beam $\mathbf{J}_{\text{probe}} = \alpha \mathbf{e}_y$ is sent through the sample. The Faraday rotation caused by the fluctuating spin polarization in the sample S effectively slightly rotates the polarization plane by an angle θ_F . This can be expressed by applying the rotation matrix $R(\theta_F)$ to the probe beam: $\mathbf{J}_{\text{sig}} = \alpha R(\theta_F) \cdot \mathbf{e}_y$. Because the angle θ_F is very minute, it is possible to reinterpret the signal beam as a superposition of two mutually orthogonal beams. The first,

$\mathbf{J}'_{\text{prob}}$, effectively passes the sample without interacting:

$$\mathbf{J}'_{\text{prob}} = \alpha \cos(\theta_F) \mathbf{e}_y \approx \mathbf{J}_{\text{prob}}.$$

The second, \mathbf{J}_{scat} , consists purely of photons that were scattered and hence have flipped their polarization by $\pi/2$ to become \mathbf{e}_x polarized,

$$\mathbf{J}_{\text{scat}} = \alpha \sin(\theta_F) \mathbf{e}_x \approx \alpha \theta_F \mathbf{e}_x.$$

Next, the $\mathbf{J}_{\text{sig}} \approx \mathbf{J}_{\text{prob}} + \mathbf{J}_{\text{scat}}$ beam propagates further on through a half-wave retarder rotated by $\pi/8$. The retarder effectively rotates the state vector by $\pi/4$ with respect to the optical axes of the following Wollaston prism. The prism is just a polarizing beam splitter that splits the \mathbf{J}_{sig} into two mutually orthogonal beams:

$$\mathbf{J}_1 = \alpha \sin\left(\frac{\pi}{4} + \theta_F\right) \mathbf{e}_1 \quad \text{and} \quad \mathbf{J}_2 = -i\alpha \cos\left(\frac{\pi}{4} + \theta_F\right) \mathbf{e}_2 .$$

In effect, the Wollaston prism mixes the scattered part \mathbf{J}_{scat} with the transmitted beam \mathbf{J}_{prob} , whereby the \mathbf{J}_{prob} beam acts as the unaltered “reference” local oscillator. This scheme is hence designated *self-homodyne*.

Subsequently, two photodiodes measure the normalized intensities of these beams,

$$I_1 = \alpha^2 \sin^2\left(\frac{\pi}{4} + \theta_F\right) \quad \text{and} \quad I_2 = \alpha^2 \cos^2\left(\frac{\pi}{4} + \theta_F\right) ,$$

and the resulting fluctuating difference photocurrent $i = \eta_{\text{eff}} I_-$ is recorded. The intensity difference I_- is equal to

$$I_- = I_1 - I_2 = \alpha^2 \sin(2\theta_F) \approx \alpha^2 2\theta_F.$$

The SN spectrum $\mathfrak{S}_{\text{self}}$ is proportional to the variance of I_- :

$$\begin{aligned} \mathfrak{V}(I_-)_{\text{self}} &\approx \mathfrak{V}(\alpha^2 (1 + \delta c_o) 2\theta_F) = \left\langle \alpha^4 (1 + \delta c)^2 2\theta_F^2 \right\rangle \\ &= 4\alpha^4 \left\langle (1 + 2\delta c + \delta c^2) \theta_F^2 \right\rangle = 4\alpha^4 \left\langle (1 + \delta c^2) \theta_F^2 \right\rangle \\ &= 4\alpha^4 (1 + \mathfrak{V}(\delta c)) \mathfrak{V}(\theta_F) \\ &\approx 4\alpha^4 \mathfrak{V}(\theta_F) , \end{aligned} \tag{4.4}$$

where the substitution $\alpha^2 \rightarrow \alpha^2 (1 + \delta c)$ was used. The δc term is the classical in-

4 Theory

tensity variance that can originate from, for example, the RIN in the laser [112]. In this semi-classical treatment, this term is usually referred to as *wave noise* - this term generally models intensity fluctuations due to a super-Poissonian photon distribution [92]. The classical intensity variance is quite small $\mathfrak{V}(\delta c) \ll 1$. Therefore the approximation in the last line is usually a good assumption. Real detectors have just a finite ability to reject fluctuations that happen simultaneously on both photodiodes, $I_+ = I_1 + I_2$, the common mode rejection ratio η_{cm} . Consequently, the detected variance is:

$$\mathfrak{V}(I_- + \eta_{\text{cm}}I_+) = \mathfrak{V}(I_-)_{\text{self}} + \eta_{\text{cm}}^2 a^4 \mathfrak{V}(\delta c). \quad (4.5)$$

4.3.2 Mach-Zehnder Interferometer

The two schemes presented below exploit the properties of a symmetric Mach-Zehnder interferometer (MZI) as depicted in Fig. 4.6, where the investigated sample is placed in one of its arms. These schemes attempt to optimize different aspects of the experiment without sacrificing the interferometric visibility too much. The choice of this style of interferometer is not arbitrary. On the one hand, with some care, a MZI solves the problem of beam overlap. As the beams on both arms originate from the same source and travel exactly the same distance, they experience the same divergence. Beyond that, additional optical elements can be placed in the second arm to simulate any effect the sample might induce on the beam mode to improve the visibility even more. On the other hand, as the light travels only one way in a MZI (as opposed to, e.g., a Michelson interferometer), stray reflexes produced by imperfect anti-reflection coatings of optical elements and the surfaces of the sample can be easily shielded from detection.

As depicted in Fig. 4.6, starting with mostly linearly polarized light at the lower left, the first half-wave retarder “rotates” the polarization with regard to the axes of the input polarizing beam splitter. This sets the intensity ratio p between its two outputs. The beam exiting to the right does not interact with the sample and serves as a reference. This beam is called \mathbf{J}_{lo} , the local oscillator. The beam that exits on top and impinges on the sample S is called the probe beam \mathbf{J}_{prob} . As in the self-homodyne case, after traveling through the sample and acquiring a signal, it is called \mathbf{J}_{sig} . The local oscillator and the signal are recombined on the beam splitter BS, while the phase difference between \mathbf{J}_{sig} and \mathbf{J}_{lo} is adjusted by the moving of the mirror at the lower right.

4.3.3 Balanced Scheme

The scheme depicted in panel (a) of Fig. 4.6 uses both outputs of the MZI for detection by balancing their intensity to an equal level for maximum sensitivity. An additional linear polarizer oriented parallel to the polarization of the scattered beam \mathbf{J}_{scat} is placed in the signal beam to suppress the probe beam \mathbf{J}_{prob} [3]. In theory, this is unnecessary as the local oscillator \mathbf{J}_{lo} is x-polarized. Interference can only be detected between equal polarization modes. Therefore, the probe beam ought to be irrelevant. However, in practice, the bulk dielectric response of the sample leads to a slight elliptical polarization. A not suppressed $\mathbf{J}'_{\text{prob}}$ can lead to artifacts that scale with the common mode intensity fluctuations of the initial laser source. The output states behind the beam splitter are:

$$\begin{aligned}\mathbf{J}_c &= \frac{1}{\sqrt{2}} (\mathbf{J}_{\text{lo}} + i\mathbf{J}_{\text{scat}}) \approx \frac{\alpha}{\sqrt{2}} (+\sqrt{p} + e^{i\varphi} \theta_F) \mathbf{e}_x, \\ \mathbf{J}_d &= \frac{1}{\sqrt{2}} (i\mathbf{J}_{\text{lo}} + \mathbf{J}_{\text{scat}}) \approx \frac{\alpha}{\sqrt{2}} (-\sqrt{p} + ie^{i\varphi} \theta_F) \mathbf{e}_x.\end{aligned}$$

Their corresponding detected intensities are:

$$\begin{aligned}I_c &= |\mathbf{J}_c|^2 = \frac{\alpha^2}{2} (p + \theta_F^2 - 2\sqrt{p}\theta_F \sin(\varphi)), \\ I_d &= |\mathbf{J}_d|^2 = \frac{\alpha^2}{2} (p + \theta_F^2 + 2\sqrt{p}\theta_F \sin(\varphi)). \\ I_- &= I_d - I_c \approx 2\sqrt{p} \sin(\varphi) \alpha^2 \theta_F.\end{aligned}\tag{4.6}$$

In Eq. (4.6), the detected signal is maximal when the relative phase is set to $\pm\pi/2$ and scales the fluctuation value θ_F with the factor \sqrt{p} . The interference term vanishes when no signal is present, and consequently, the same intensity is present in both outputs. This scheme is therefore called the *balanced* scheme. Analogously, the average of the difference is zero, and the variance of the difference photocurrent is proportional to:

$$\mathfrak{V}(I_-)_{\text{bal}} \approx 4p \sin^2(\varphi) \alpha^4 (1 + \mathfrak{V}(\delta c)) \mathfrak{V}(\theta_F).$$

As before, the detected noise power is proportional to $\mathfrak{V}(\theta_F)$ and can be rewritten in terms of the self-homodyne expression Eq. (4.4):

$$\mathfrak{V} (I_-)_{\text{bal}} \approx p \sin^2 (\varphi) \mathfrak{V} (I_-)_{\text{self}}. \quad (4.7)$$

At $\varphi = \pi/2$, the balanced scheme optically amplifies the initial signal by a factor of p .

Considering a finite common mode rejection, the full expression has the form:

$$\mathfrak{V} (I_- + \eta_{\text{cm}} I_+)_{\text{bal}} \approx \mathfrak{V} (I_-)_{\text{bal}} + p^2 \eta_{\text{cm}}^2 \alpha^4 \mathfrak{V} (\delta c).$$

Note that this expression is not Eq. (4.5) multiplied by $p \sin^2 (\varphi)$, unlike Eq. (4.7). The common mode term scales by p^2 regardless of the phase difference. That is, the burden on the common mode rejection capability of the detector is quadratically worse in the balanced scheme.

4.3.4 Balanced Phase Stabilization

For constant amplification, the interferometer must be operated at the dark or bright fringe, that is, at $\varphi = \pm\pi/2$, respectively. Unfortunately, in a realistic interferometer, optical paths are prone to drift with day/night temperature changes, atmospheric pressure changes, or air movement in the lab. Therefore the relative phase φ has to be stabilized to a fixed value. In Eq. (4.6), the dependence on the value of φ averages to zero regardless of the value of φ . Therefore, the detected difference signal cannot be used as an error signal for phase stabilization. To still get an error signal in this scheme, an additional half-wave retarder has to be inserted between the sample and the linear polarizer [3]. The retarder is rotated slightly by the angle θ_0 to leak some of the probe beam to the recombining beam splitter. This changes the detected signal power to:

$$I_- = I_d - I_c \approx 2\sqrt{p} \sin (\varphi) \alpha^2 \theta_F + 2\sqrt{p} \sin (\varphi) \alpha^2 \theta_0, \quad (4.8)$$

where the last term $\propto \theta_0$ can be used to detect and stabilize the phase.

$$\begin{aligned} \mathfrak{V} (I_-)_{\text{stab}} &\approx \mathfrak{V} (I_-)_{\text{bal}} + 4p \sin^2 (\varphi) \alpha^4 \theta_0^2 \mathfrak{V} (\delta c) \\ &\stackrel{\varphi=\pi/2}{=} p \mathfrak{V} (I_-)_{\text{self}} + 4p \alpha^4 \theta_0^2 \mathfrak{V} (\delta c). \end{aligned} \quad (4.9)$$

Now, while the second term of Eq. (4.8) fulfills the requirements of an error function, a corresponding term appears also in the variance. Unfortunately, this new term amplifies the variance of the initial laser beam intensity $\mathfrak{V}(\delta c)$ by the amplification factor p . This term is present, even for a detector with an infinitely high common-mode rejection ratio. However, in the more realistic case of a finite rejection ratio, the \sqrt{p} dependent terms dwarf the θ_0 contribution because $\sqrt{p} \gg \theta_0$:

$$\begin{aligned} \mathfrak{V}(I_- + \eta_{\text{cm}} I_+)_{\text{stab}} = & 4p \sin^2(\varphi) \alpha^4 (1 + \mathfrak{V}(\delta c)) (\sqrt{p} + \eta_{\text{cm}} \theta_0) \mathfrak{V}(\theta_F) \\ & + p \alpha^4 (\eta_{\text{cm}} \sqrt{p} + 2\theta_0) \mathfrak{V}(\delta c). \end{aligned}$$

The intensity variance of diode lasers due to RIN is concentrated in the frequency domain around $\nu \approx 0$ Hz, as explained in section §3.1. Therefore, weak low-frequency signals in the range where the RIN dominates might be infeasible in this scheme [2].

4.3.5 Unbalanced Scheme

The scheme depicted in panel (b) of Fig. 4.6 is designed for active phase stabilization. The relative phase of the MZI is modulated, i.e., by placing an electro-optical phase modulator in one of the arms, to derive a phase-dependent error signal. This modulation causes a corresponding periodic intensity fluctuation in the interferometer outputs. For this reason, a balanced photodetector is used to suppress these intensity fluctuations, just as in the self-homodyne case. The phase modulation depth has to be very minute not to saturate the balanced photodetector's common mode rejection ratio. After all, the phase modulation gets amplified the same way as the desired signal. Additionally, in PSD estimates, such a periodic disturbance will have an artificially much higher magnitude than broad-band signals like SN. As described in section §1.3.7, this is an inherent property of the DFT and cannot be avoided. Nevertheless, a very low modulation depth can be selected using a lock-in scheme to detect the error signal, bringing this artifact down to acceptable levels.

In contrast to the balanced scheme, in the unbalanced case, a half-wave retarder (rotated by $\pi/4$) has to be placed into the local oscillator arm of the MZI to align its polarization parallel to the probe beam \mathbf{J}_{prob} . The non-polarizing beam splitter where the local oscillator \mathbf{J}_{lo} and the signal beam \mathbf{J}_{sig} recombine just superimposes

4 Theory

the two beams and does not cause interference effects for the scattered beam \mathbf{J}_{scat} . The left output of the MZI remains unused for SNS and is intended to be used for a phase stabilization scheme instead. This is a significant trade-off, as half the scattered intensity is lost, and the detected noise power will be only $\approx 1/4$ compared to the balanced scheme, all other parameters being the same. The state exiting the upper output of the beam splitter reads:

$$\begin{aligned} \mathbf{J}_c &= \frac{1}{\sqrt{2}} (\mathbf{J}_{\text{lo}} + i\mathbf{J}_{\text{sig}}) = \frac{\alpha}{\sqrt{2}} (\sqrt{p} \mathbf{e}_y + ie^{i\varphi} (\sin(\theta_F) \mathbf{e}_x + \cos(\theta_F) \mathbf{e}_y)) \\ &\approx \frac{\alpha}{\sqrt{2}} ((\sqrt{p} + ie^{i\varphi}) \mathbf{e}_y + ie^{i\varphi} \theta_F \mathbf{e}_x). \end{aligned}$$

For $\varphi = \pm\pi/2$, this state is very similar to the self-homodyne case, except that the amplitude of the component $\propto \mathbf{e}_y$ can be increased by a factor $\approx (1 + \sqrt{p})$. A polarization bridge analyzes this state as in the self-homodyne case, and the output states of the Wollaston prism read:

$$\begin{aligned} \mathbf{J}_1 &\approx \frac{\alpha}{2} (\sqrt{p} + ie^{i\varphi} (\theta_F + 1)) \mathbf{e}_1, \\ \mathbf{J}_2 &= \frac{\alpha}{2} (i\sqrt{p} + ie^{i\varphi} (\theta_F - 1)) \mathbf{e}_2. \end{aligned}$$

Again, the intensity difference on the diodes of the balanced photo receiver is dependent on the polarization fluctuation θ_F and a factor caused by interference:

$$\begin{aligned} I_1 &= |\mathbf{E}_1|^2 = \frac{\alpha^2}{4} (p + (\theta_F + 1)^2 - 2\sqrt{p} \sin(\varphi) (\theta_F + 1)), \\ I_2 &= |\mathbf{E}_2|^2 = \frac{\alpha^2}{4} (p + (\theta_F - 1)^2 - 2\sqrt{p} \sin(\varphi) (\theta_F - 1)), \\ I_- &= I_1 - I_2 \approx (1 - \sqrt{p} \sin(\varphi)) \alpha^2 \theta_F. \end{aligned} \tag{4.10}$$

Finally, the variance can again be expressed in terms of the noise power of the self-homodyne case and an amplification factor $\eta_{p,\varphi} = (1 - \sqrt{p} \sin(\varphi))^2$:

$$\begin{aligned} \mathfrak{V}(I_-)_{\text{un}} &\approx \alpha^4 (1 - \sqrt{p} \sin(\varphi))^2 (1 + \mathfrak{V}(\delta c)) \mathfrak{V}(\theta_F) \\ &= \frac{1}{4} \eta_{p,\varphi} \mathfrak{V}(I_-)_{\text{self}}. \end{aligned} \tag{4.11}$$

As opposed to the balanced scheme, the maximal amplification is achieved only on the bright fringe ($\varphi = -\pi/2$ in Eq. (4.11)), i.e., when the maximal intensity leaves the MZI from the upper output and the right output becomes darkest due to destructive interference with the probe beam. Hence this scheme is called the *unbalanced* scheme. The maximal optical amplification is around $1/4 p$ for $p \gg 1$, as expected from the initial consideration:

$$\mathfrak{V}(I_-)_{\text{un}} \stackrel{\varphi=-\pi/2}{=} \frac{1}{4} (1 + \sqrt{p})^2 \mathfrak{V}(I_-)_{\text{self}} \approx \frac{1}{4} p \mathfrak{V}(\theta_F)_{\text{self}}. \quad (4.12)$$

The noise power in Eq. (4.11) does not contain any terms independent of the polarization fluctuation, as was the case in Eq. (4.9) for the (realistic) balanced case. In addition to that, at the bright fringe operation point of $\varphi = -\pi/2$, a minute phase modulation $\delta\varphi \cos(2\pi\nu_m t)$ with a low modulation depth $\delta\varphi$ will not introduce such terms into the detected noise power.

In the second (dark) port of the interferometer, the detected intensity is:

$$I_d \approx \frac{\alpha^2 (1 + p)}{2} + \alpha^2 \sqrt{p} \sin(\varphi + \delta\varphi \cos(2\pi\nu_m t)).$$

A lock-in amplifier can demodulate the sine term deriving an error signal for phase stabilization:

$$\begin{aligned} \epsilon(\varphi) &\approx \nu_m \int_0^{1/\nu_m} (I_d - \langle I_d \rangle) \cos(2\pi\nu_m t) \\ &= \frac{1}{2} \sqrt{p} \alpha^2 \delta\varphi \cos(\varphi). \end{aligned} \quad (4.13)$$

This error signal is asymmetric around the operation point and can be used as an input of a control loop that minimizes ϵ . This sets the overall phase of the interferometer to $\pm\pi/2$. The bright and dark fringes can be distinguished by detecting the slope of ϵ . Afterward, the relative phase can be locked to the desired value of $-\pi/2$.

5 Experimental Aspects

This chapter highlights some experimental aspects of the setup used to demonstrate the superiority of homodyne spin noise spectroscopy (HSNS) over regular SNS of rubidium metal vapor. First, section §5.1 quickly introduces the sample system used for the experiment. Second, section §5.2 introduces essential parts of the setup.

5.1 The Rubidium D2 Line

For this proof-of-principle experiment, a rubidium metal vapor cell¹ served as the sample, where SNS was used to investigate the relaxation of the outer shell electron spin in rubidium atoms at room temperature. Panel (a) of Fig. 5.1 depicts a sketch of the cell that consists of an evacuated glass envelope into which a tiny quantity of artificially enriched ^{87}Rb metal was placed by the manufacturer through a side port (not depicted). Before it was welded shut, an additional helium atmosphere of ≈ 1 hPa was added. At room temperature, a fraction of the metal evaporates inside the cell due to finite vapor pressure, and the freely moving rubidium atoms become accessible to optical spectroscopy.

Panel (b) of Fig. 5.1 shows a simple absorption spectrum of a transmitted laser beam. This spectrum was recorded by scanning a power-stabilized, tunable diode laser over the resonances while simultaneously recording the transmitted power as well as the power reflected at the first cell window. The transmitted power far away from the resonances is $\approx 1 \mu\text{W}$ in a probe beam that is collimated down to a beam waist of $w_0 \approx 1.3$ mm. (This corresponds to a probe intensity of $\approx 18.8 \mu\text{W}/\text{cm}^2$.) The quotient of the transmitted power and the reflected power yields a relative transmission spectrum of the cell, and subtracting it from the residual absorption of the glass results in the depicted spectrum.

The depicted spectrum is dominated by the absorption profile of the enriched ^{87}Rb isotope. Nevertheless, the residual absorption of ^{85}Rb is still visible, as ex-

¹Triad Technology TT-RB87/He-.75T-50-Q

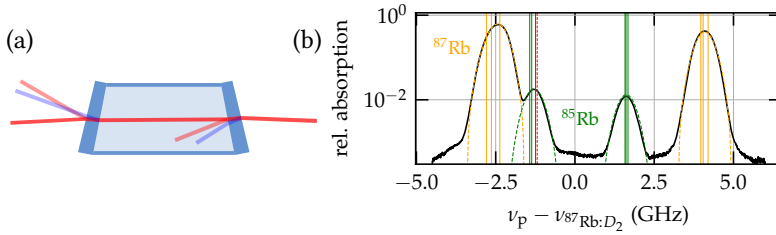


Figure 5.1: Panel (a): Schematic drawing of the probe beam (red) and its main first (weak red) and second (weak blue) surface reflections in the ^{87}Rb metal vapor cell. Panel (b): Relative transmission of the cell with clearly visible Doppler and collision broadened absorption peaks of the enriched ^{87}Rb isotope (orange) and the remaining ^{85}Rb isotope (green). Dipole-allowed underlying absorption lines are indicated by solid vertical lines. The red dashed line indicates the detuning of the probe laser during the HSNS experiment.

pected from a specified purity of $\gtrsim 98\%$. All absorption peaks consist of several underlying absorption lines that cannot be resolved using this particular sample and the simple technique employed. These absorption lines, as well as their oscillator strengths, are well-known from measurements that employ ultra-precise (Doppler-free) saturation absorption spectroscopy schemes. These values are nicely documented in, for example, the reference tables maintained by Prof. D. A. Steck in [113, 114]. The positions of the absorption lines are indicated by thin vertical lines in panel (b) of Fig. 5.1. Both isotopes have similar but distinct spectra because of a different isotope mass (isotope shift) and a different nuclear spin ($3/2$ for ^{87}Rb and $5/2$ for ^{85}Rb).

Experimentally, the only remaining free parameters are the instrument drift of the wavelength meter² and the peak widths. Both can be determined using non-linear regression. Each absorption line can be described by a Voigt profile that incorporates both the homogeneous and inhomogeneous widths. As is always the case for simple spectroscopy of a metal vapor at finite temperatures, the absorption lines are Doppler broadened due to the movement of the atoms in relation to the probe beam. Moreover, the helium buffer gas inside investigated cell leads to additional collision broadening of the resonances[115, 116] that dominates the line widths. For this reason, only a single set of inhomogeneous width parameters

²HighFinesse WSU 30 683

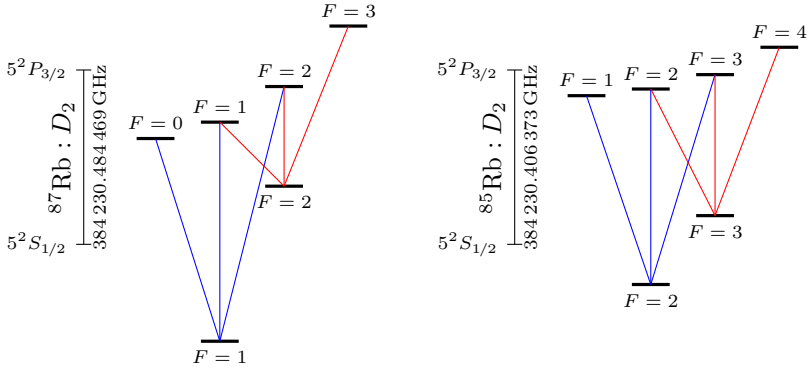


Figure 5.2: Term scheme of the hyperfine levels of the D_2 lines of the rubidium isotopes ^{87}Rb and ^{85}Rb . Data is taken from [113, 114]. The relative scale of the hyperfine manifolds is correct, the excited states are scaled up by a factor 10 to resolve the lines, while the overall transition is scaled down by the factor 50×10^{-3} .

is sufficient to describe all lines contained in the broad peaks.

The set of lines that must be considered is determined by the dipole selection rules. (Only these lines are indicated in panel b). These selection-rule-allowed transitions are between the ground-state hyper-fine manifold $5^2S_{1/2}$ and the excited-state hyper-fine manifold $5^2P_{3/2}$. For example, for the red detuned peaks, the allowed transitions for π and σ^\pm light are $F = 2 \rightarrow F' = 1, 2, 3$ for ^{87}Rb and $F = 3 \rightarrow F' = 2, 3, 4$ for ^{85}Rb , respectively, as depicted in Fig. 5.2. Note that the splitting between the ground states is much larger than the splitting between the excited states. Therefore only two peaks are resolved in the absorption spectrum, and their splitting is mostly the result of the ground state splitting.

Spin relaxation of the outer shell electron spin is usually dominated by collisions between pairs of rubidium atoms and between rubidium atoms and the walls of the cell. The helium buffer gas reduces the probability of these collisions. Most collisions happen between helium and rubidium atoms, and diffusion toward the walls is suppressed. On the other hand, because the buffer gas increases the collision probability, it also increases the likelihood of spin-destroying events resulting in a shortened spin lifetime. An in-depth investigation of rubidium spin noise at the D_2 resonances was performed, for example, in Ref. [116].

HSNS aims to amplify a very weak SN signal of a source like an individual hole spin confined in QD. The spectroscopy was performed on the weak signal of the remaining impurity (^{85}Rb isotope) at a low probe power to simulate these unfavorable conditions. For the experiment described below, the probe laser was detuned by about -1.18 GHz from the specified $^{87}\text{Rb} : D_2$ central transition frequency of $384\,230.484\,468\,5$ GHz, as indicated by the red dashed line in panel (b) of Fig. 5.1.

5.2 Proof-of-Principle Rubidium Setup

Panel (s) of Fig. 5.3 depicts a sketch of the setup that is based on the unbalanced scheme, as described in section §4.3.5. Additional elements were added for power regulation and phase stabilization. A detailed description follows in the sections below.

5.2.1 Laser Source

A temperature-stabilized self-built external cavity laser diode (ECDL) in Littrow geometry serves as the laser source. The readily available, relatively cheap, high-quality 780 nm laser diodes and the narrow resonance of rubidium make building such a laser a simple task. This laser is constructed from standard Thorlabs components. A grating mounted in a kinematic mount with additional piezo actuators provides feedback to the laser diode. The piezo actuators can scan the laser without mode-hops in a range of $\lesssim 15$ GHz. An in-house-built four-channel digital-to-analog converter³ provides the control voltages for the piezo, the laser current, and the laser temperature controllers. Furthermore, the small breadboard housing the laser diode and grating is placed in a doubly insulated box. The small breadboard is connected to a larger breadboard through several Peltier elements (thermoelectric coolers). The large breadboard serves as a sink for the thermoelectric coolers that are driven by an external computer-controlled power supply. This arrangement stabilizes the small breadboard's temperature within < 10 mK. The grating is adjusted so the emitted radiation is close to the rubidium transition. Then the main order diffracted from the grating is coupled into a polarization-maintaining fiber that transports the laser radiation to the setup and serves as a mode cleaner for the spatially inhomogeneous laser mode. An additional Faraday isolator can be placed between the grating and the fiber to prevent reflections in the setup

³provided by Ronny Hüther

from propagating back into the laser medium. One of the weaker lower orders diffracted from the grating is coupled into an auxiliary single-mode fiber. This second output is connected to a wavemeter for precise laser frequency control. In this configuration, no additional beam splitter is necessary to sample the laser for the wavemeter, which further would degrade the relatively low output power of the laser.

5.2.2 Probe Path

On the setup side, a half-wave retarder in combination with a polarizing beam splitter sets the power ratio between the transmitted local oscillator and reflected probe beam to approximately 5:1. At high splitting ratios, i.e., large deviations of the incoming polarization from $\pi/4$, the polarizing beam splitter (PBS) deviates significantly from a perfect beam splitter. While the polarization of the transmitted beam is mostly well-behaved, the reflected beam suffers *significantly*, and this fact usually has to be accounted for. In particular, the polarization plane gets rotated up to an angle of $\pi/4$ from the s plane. Furthermore, the degree of linear polarization degrades severely, and the polarization of the reflected beam becomes strongly elliptical. For this particular setup, this is not a cause of significant concern, as the goal was to arrive at a high power ratio and a very low probe power. Therefore, a linear polarizer⁴, P_{cell} , immediately before the vapor cell ensures a well-defined linear polarization at the cost of some transmitted laser power. A neutral density (ND) filter is used to further attenuate the power in the probe beam by three orders of magnitude.

The ^{87}Rb metal vapor cell consists of a hollow glass cylinder with two wedge-shaped optical windows bonded at an angle from either side. The windows lack an anti-reflective layer and produce stray reflections that are not parallel to the incoming and transmitted beams because of the geometry of the cell. Therefore, the first surface reflection on the left side (weak red reflected beam on the left side of Fig. 5.1) is used to monitor the input power by a photodiode (not depicted). The probe beam at the cell was set to $\approx 8 \mu\text{W}$. For a beam waist of $\approx 2 \text{ mm}$, resulting in an intensity of $250 \mu\text{W cm}^{-2}$. No focusing optics were present to make the intensity in the volume probed by the beam as homogeneously as possible. Also, a larger unfocused beam prevents the measured spin correlation rates from being dominated by the diffusion of rubidium atoms out of the probed volume.

⁴all linear polarizers used in the setup (P_{cell} , P_{EOM} , P_{comp}) are Thorlabs LPVIS050-MP2

In strongly focused beams, this lifetime broadening cannot be ignored even in a vapor cell where the diffusion is attenuated by collisions with a buffer gas like helium [116].

A 300 mm diameter water-cooled air-core coil was constructed and placed below the setup centered at the rubidium cell. This coil was used to provide transverse magnetic fields up to 1 mT. As the coil is much larger than the cell, the magnetic flux density inside the volume irradiated by the probe beam is homogeneous enough for the purposes of the proof-of-principle experiment. A more homogeneous configuration can be achieved by a Helmholtz coil pair complemented by even larger coils to compensate for Earth's background magnetic field. For the experiment, magnetic flux densities of $\approx 120 \mu\text{T}$ and $\approx 800 \mu\text{T}$ are used for the foreground and background fields, respectively. For ^{85}Rb , the ground states have a g -factor with an absolute value of $1/3$. Therefore these magnetic fields should result in Larmor frequencies of $\nu_{L,\text{fg}} \approx 560 \text{ kHz}$ and $\nu_{L,\text{bg}} \approx 3732 \text{ kHz}$. Because of residual hysteresis fields in steel parts of the setup and hence a slightly altered effective flux density, the observed Larmor frequencies in Fig. 6.1 are 589 kHz and 3425 kHz, respectively.

5.2.3 Local Oscillator Path

A electro-optic phase modulator (EOM)⁵ was placed in the local oscillator (LO) path to inject a very minute phase modulation. In order to get a pure phase modulation, it is crucial to align the polarization plane very precisely with the optical axis of the EOM prism. The linear polarizer P_{EOM} immediately in front of the EOM serves exactly this purpose by sacrificing a small fraction of the transmitted laser power. The modulation frequency was set to an arbitrary value of 1.111 MHz that is not an integer fraction of the sample rate to reduce the magnitude of the resulting periodic artifact (see also section §1.3.7 for details). The modulation depth is chosen as low as possible while still being detectable by a lock-in amplifier.

Bulk phase mismatches and phase drifts cannot be regulated just by the EOM because of a very limited total phase range $|\Delta\varphi_{\text{EOM}}| \lesssim 3/2\pi$. For this reason, the LO is reflected off the mirror M_1 mounted on a piezoelectric actuator resulting in an available phase adjustment range of $|\Delta\varphi_{\text{piezo}}| \approx 8\pi$.

⁵Thorlabs EO-PM-NR-C1

Note The simple mounting of the piezo mirror, as depicted in Fig. 4.6, results in a relatively high lateral beam deviation for its travel. For a displacement d of the piezo mirror, the optical path is increased by $d\sqrt{2}$, but the lateral deviation is also $d\sqrt{2}$, as depicted in panel (a) of Fig. 5.3. Depending on beam size and displacement d , this lateral deviation can decrease the mode overlap and hence the interferometric contrast. Alternatively, the configuration depicted in panel (b) can be used to reduce the lateral offset⁶. From a simple geometric consideration, it can be shown that in this configuration, the optical path is increased by $2d \cos(\zeta)$ while the lateral deviation is only $2d \sin(\zeta)$, where $0 < \zeta < \pi/4$ is the rotation angle of the piezo mirror. For example, in the provided figure a $\zeta = \pi/8$ was used, resulting in an optical path increase by $\approx 1.85d$ but a lateral shift of only $\approx 0.77d$. Because this configuration adds an additional optical surface, it raises an opportunity for additional wavefront distortion due to imperfections in the mirror. Indeed, a geometrically even better though less compact solution is to use a retro-reflector and a pick-off mirror, i.e., three additional optical surfaces.

Temperature drifts slightly change the retardance of the first half-wave plate before the PBS. Consequently, the altered retardance causes a corresponding change in the rotation of the polarization plane and the transmitted and reflected power. For the reflected beam, the power fluctuation does not pose a huge penalty because the large splitting ratio causes poor PBS performance, as described above. Consequently, the reflected power fluctuates much less than expected for a perfect PBS. On the contrary, the effect of the PBS on the transmitted beam is that of an almost perfect linear polarizer. Therefore the polarization fluctuations due to drift in the initial polarization are directly translated into fluctuations in the power ratio value p . Of course, this fluctuation in p is further worsened by any other polarization optic in the path LO, i.e., the linear polarizer before the EOM and so on. The power ratio p had to be kept stable, as the experiment's goal was to characterize the dependence of homodyne amplification performance on the power ratio. Therefore, a noise-eater circuit was implemented to stabilize the power of the LO that is impinging onto the recombining beam splitter. This circuit was built from a liquid crystal retarder that rotates the polarization plane of the LO beam and a linear polarizer P_{comp} that passes only a fraction of the power depending on the mismatch between its optical axis and the polarization plane of the beam.

⁶Initial idea by courtesy of Jens Hübner.

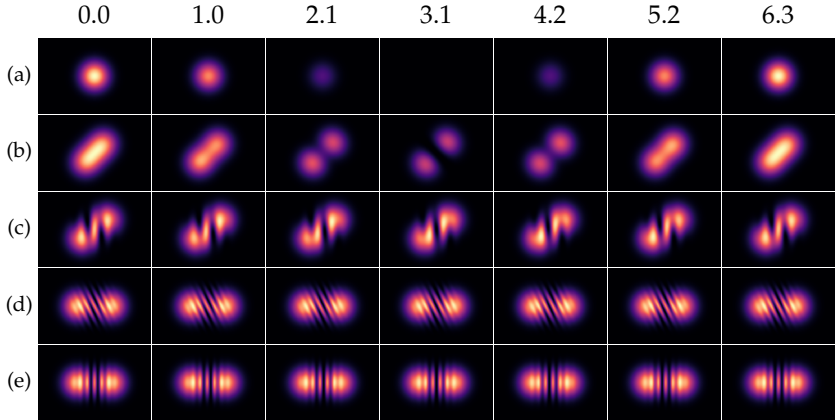


Figure 5.4: Simulation of two-beam interference patterns during interferometer alignment. The phase difference φ in rad increases from left to right, as indicated by the numbers in the first row. The rows depict: (a) perfectly coaxially aligned beams, (b) parallel but vertically and horizontally displaced beams, (c) horizontally slightly tilted beams on top of a vertical and horizontal displacement, (d) horizontally and vertically tilted beams with horizontal and vertical displacement, (e) horizontally slightly tilted beams without any vertical displacement, a slight horizontal displacement, and no vertical tilt.

5.2.4 Control Port

The right output port of the recombining beam splitter BS was used for phase stabilization and beam alignment. To this end, an auxiliary 50 : 50 beam splitter was inserted into the beam. The intensity in one of its ports was recorded by a photodetector and used as an input for phase stabilization, as described below. The other output was used for the optical alignment of the interferometer.

Optical Alignment

A digital CCD camera was used for the alignment. If the interferometer is not aligned, two slightly misaligned beams impinge on the camera sensor and produce interference patterns similar to the ones depicted in Fig. 5.4. Generally, the stronger the misalignment, the faster the intensity profile oscillates laterally. The examples in Fig. 5.4 were simulated by calculating the intensity profile of two aligned or

misaligned interfering Gaussian beams, as defined in Eq. (4.1). The simulation assumes a beam waist $w_0 = 1$ mm and a wavelength $\lambda_p = 780$ nm. The beam waist was placed $z = 300$ mm away from the camera sensor. The overall phase difference φ between the beams is varied from left to right, as indicated in the top row (a), which displays the intensity pattern of an aligned interferometer. The other rows display characteristic patterns of various misaligned cases.

In row (b), the two beams are propagating parallel to each other, but their origins are displaced horizontally and vertically. This configuration results in a phase-dependent intensity oscillation only in the areas where the beams overlap, resulting in a strongly reduced interferometric contrast.

In row (c), the two beams are displaced similarly but are also slightly tilted horizontally toward each other. This alignment causes an interference pattern between the tilted wavefronts of the beams. The lateral spatial oscillation frequency is proportional to the tilt angle and can be used as a very sensitive alignment guide. The tilt angle can be brought down to zero by steadily minimizing the spatial oscillation frequency.

In row (d), the two beams are tilted horizontally and slightly tilted vertically. They impinge at the same vertical height on the camera but are not parallel in either direction. When the interferometer is close to being aligned, deliberately tilting one of the alignment mirrors produces this pattern. Here, the horizontal mirror is tilted on purpose. Now, the fast and high contrast intensity oscillation between the beams can be used to align the tilt of the vertical axis. If the intensity oscillation pattern appears rotated, then the beams are not in the same plane. Beam walking the alignment mirrors can be used to rotate the interference bands. When the band pattern becomes vertical, like in row (e), then the beams must be parallel in the horizontal plane. Reversing the deliberate horizontal tilt aligns the interferometer, as depicted in row (a).

Phase and Power Ratio Stabilization

The second output of the auxiliary beam splitter was detected by an amplified silicon photodetector PD⁷. Its output was demodulated by a lock-in amplifier⁸ to detect the phase modulation that had been imposed onto the LO using the EOM. This effectively detects the error function defined in Eq. (4.13) that is proportional

⁷Thorlabs PDA36A-EC

⁸Stanford Research SR 844

to the overall phase difference between the LO and the signal beams. This error signal is used to steer the interferometer phase to the setpoint with an accuracy of ≈ 0.13 rad.

The photodiode also serves a second purpose. When one of the mechanical shutters S_1 or S_2 is closed, the output of the photodiode is proportional to the power in the unblocked beam. Thus, the current power ratio p between the beams can be measured by alternately closing the shutters. Using this information, the noise-eater circuit described above then steered the power ratio p to a desired value between measurement runs.

5.2.5 Measurement Port

The top output of the main beamsplitter is essentially the polarization bridge commonly used in regular SNS, as described in section §4.3.1 and section §4.3.5. A custom-built balanced detector⁹ is used to amplify the difference photocurrent produced by a matched pair of photodiodes¹⁰ that detect the power contained in the two outputs of the Wollaston prism. The typical common-mode rejection ratio of the detector is specified as 25 dB. This value corresponds to a power ratio of ≈ 17.8 . The transimpedance gain of the balanced detector is switchable between several fixed values. The gains $g_{\text{low}} = 10 \text{ kV A}^{-1}$ and $g_{\text{high}} = 100 \text{ kV A}^{-1}$ were used for the experimental results presented below. For these gains, the NEP values of the detector are $10 \text{ pW}/\sqrt{\text{Hz}}$ and $2.5 \text{ pW}/\sqrt{\text{Hz}}$, respectively. These NEP values are the dominant contribution to P_t in Eq. (3.7), regardless of the NEP of the other amplification stages.

The output of the detector was amplified electrically by the amplifier AMP¹¹ with a switchable gain. The noise floor of the amplifier is specified as $2.5 \text{ nV}/\sqrt{\text{Hz}}$. This value is negligible compared to the NEP of the detector. Therefore the amplifier can be assumed to be noise free. The purpose of the amplifier is to increase the safety margin for the input signal in relation to technical parasitic perturbations. Perturbations that appear as coherent oscillations can lead to coherent artifacts in the estimated spectra, as explained in section §1.3.7. The gain of the amplifier was selected so that the majority of the peaks were covered by the effective NEP noise floor of the detector.

⁹Femto DHPCA-S (02-49-023)

¹⁰Hamamatsu S5971

¹¹Femto DHPVA-200

5 Experimental Aspects

The amplifier was followed by a 5 MHz low pass filter¹² that served as an anti-aliasing filter. Next, the output of the filter was digitized by a PC oscilloscope card¹³ with a sampling rate of 20 MHz. The average internal noise floor of the digitizer is $\approx 80 \text{ nV}/\sqrt{\text{Hz}}$. This noise floor is also significantly lower than the effective detector NEP even without additional amplification. Nevertheless, internal perturbations from the digital circuits inside the PC enclosure (mainboard, ethernet card, etc.) contaminate the noise floor with significantly higher peaks, making the additional amplifier necessary¹⁴, as described above.

¹²Minicircuits BLP-5+

¹³Alazartech ATS9360

¹⁴A better internal shielding of the digitizer card might reject more of the perturbations and make the additional amplifier redundant.

6 Superiority and Limits of Homodyne Spin Noise Spectroscopy

In this chapter, the results of the proof-of-principle experiment are presented. First, section §6.1 illustrates the experimental spectrum of the rubidium system used for further measurements. Then, section §6.2 presents the evaluation of the homodyne experiment for two distinct different experimental configurations that yield varying levels of electrical noise. Increasing the laser power in the scenario with lower electrical noise allows for reaching the shot noise limit. Conversely, in the case of higher electrical noise, although the signal-to-noise ratio experiences a notable enhancement at maximum available amplification, the shot noise is not reached due to insufficient amplification. Finally, section §6.3 concludes this topic with a discussion of the remaining limitations of HSNS.

6.1 Spin Noise Spectrum

Fig. 6.1 depicts the underlying ^{85}Rb spectrum, which is the same for all following measurements. The plotted quantity is $\langle \underline{\mathfrak{S}}_{\theta_F} \rangle \approx \mathfrak{S}_{\theta_F} \equiv \mathfrak{S}_f$ (in rad^2/Hz) as defined in Eq. (3.7). For example, in the employed unbalanced scheme (section §4.3.5), the apparent amplified SN signal is $\mathfrak{S}_s \propto \eta_p P_{\text{sig}}^2 \mathfrak{S}_{\theta_F}$, where $\eta_p = \eta_{p,-\pi/2} = (1 + \sqrt{p})^2$ is the amplification factor. The plot depicts the averaged difference between foreground and background spectra, where the spin dynamics are shifted to distinct the foreground or background Larmor frequencies $\nu_{L,\text{fg}}$ and $\nu_{L,\text{bg}}$. For this reason, the foreground spin noise appears as a positive Lorentzian-shaped peak, while the background appears as a negative peak. For each peak at a positive Larmor frequency, there is a corresponding peak at the negative Larmor frequency. The background peaks are sufficiently separated so that in this non-logarithmic plot, the contribution of the second peak does not change the shape of the overall spectrum. The separation is not large enough for the foreground peaks (blue and cyan). Therefore, the foreground peak appears skewed. The spectrum is normal-

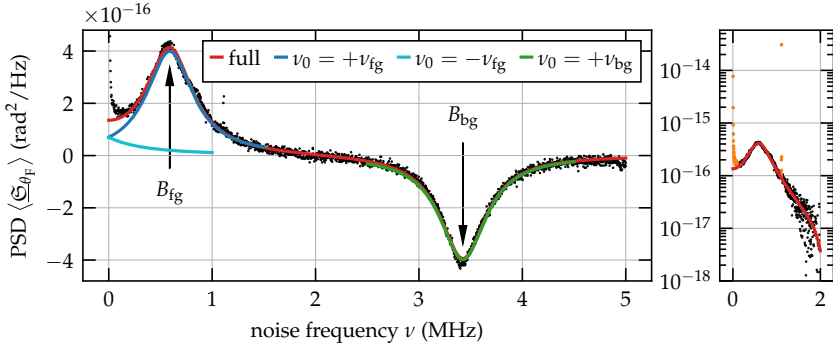


Figure 6.1: Composite spectrum of ^{85}Rb at the D_2 transition. The positive peak is the foreground and the negative peak is the background. The three individual peaks (blue $\nu_0 = \nu_{L,fg}$, green $\nu_0 = \nu_{L,bg}$, and cyan $\nu_0 = -\nu_{L,fg}$) are the dominant contributions to the full model (red). The right panel depicts the actual scale of the coherent artifact at 1.111 MHz and the remaining unsuppressed part of the RIN contribution at 0 to 100 kHz using orange dots.

ized, so it is a proper one-sided spectrum, as described in section §1.3.9.

The plot in the left panel of Fig. 6.1 is clipped to a sensible SN range to prevent it from being obscured by the coherent artifact at 1.111 MHz (see section §1.3.7), and a part of RIN from 0 to ≈ 0.1 MHz that overpowers the common mode rejection ability of the detector. For completeness, the right panel of Fig. 6.1 displays the true magnitude of these contributions on a logarithmic scale. While these contributions are unproblematic for the proof-of-principle experiment, they can become challenging when the frequency band where SN has to be measured is not arbitrary, for example, around 0 Hz, as is the case for SNS of a single quantum dot (QD).

6.2 Homodyne Amplification

The panels in Fig. 6.2 depict several examples of amplified SN spectra for different power ratios p as well as the significant other noise contributions, as defined in Eq. (3.7). The two rows depict spectra recorded for the high-speed detector configurations of $g_{\text{high}} = 100 \text{ kV A}^{-1}$ and $g_{\text{low}} = 10 \text{ kV A}^{-1}$, respectively. Each configuration has a distinct effective electrical contribution $\langle \underline{\mathcal{S}}_t \rangle$ (the dark spectrum

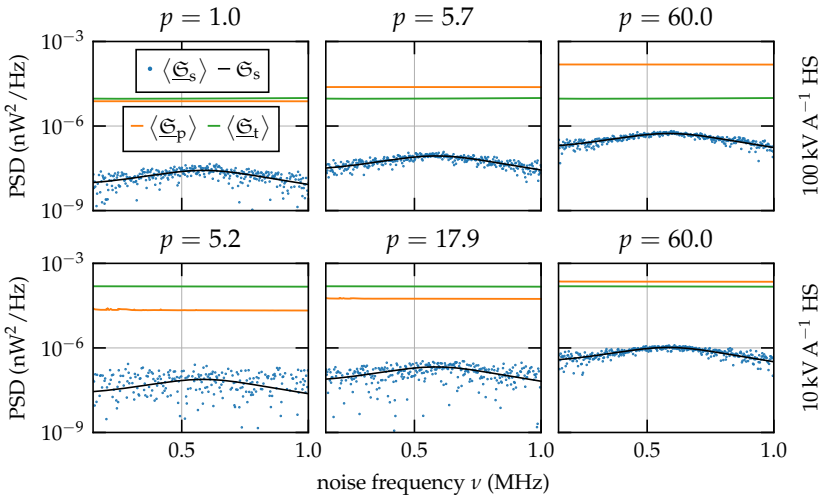


Figure 6.2: Exemplary spectra decomposed into their effective contributions: spin noise $\langle \mathfrak{S}_s \rangle$ (blue), photon shot noise $\langle \mathfrak{S}_p \rangle$ (orange), and electrical thermal noise $\langle \mathfrak{S}_t \rangle$ (green). For the top row the detector is in a configuration that has a significantly lower effective electrical contribution.

in input referring units) that stays fixed regardless of p . Both configurations start with $\langle \underline{\mathfrak{S}}_t \rangle$ as the dominating contribution at small values of p . For $\mathfrak{g}_{\text{low}}$, however, the electrical noise $\langle \underline{\mathfrak{S}}_t \rangle$ is, depending on the frequency, between 12.5 and 16.5 times larger than for $\mathfrak{g}_{\text{high}}$.

For this reason, in the $\mathfrak{g}_{\text{low}}$ case, the shot noise contribution $\langle \underline{\mathfrak{S}}_p \rangle$ becomes dominant only for the highest ratios p . On the contrary, for $\mathfrak{g}_{\text{high}}$, the spectrum is dominated by $\langle \underline{\mathfrak{S}}_p \rangle$ for almost all ratios $p > 1$. This observation gives a qualitative understanding of the amplification: the stronger the apparent electrical noise contribution, the larger p has to be chosen to yield a signal of the same quality. A more rigorous approach requires observing the scaling properties of the noise contributions $\langle \underline{\mathfrak{S}}_p \rangle$ and $\langle \underline{\mathfrak{S}}_s \rangle$.

The photon shot noise contribution $\langle \underline{\mathfrak{S}}_p \rangle$ is proportional to the actual power on the detector. In the homodyne case, it is proportional to:

$$\langle \underline{\mathfrak{S}}_p \rangle \propto \eta_Q^2 2h\nu_p \frac{1}{2} \left(\sqrt{P_{\text{sig}}^*} + \sqrt{pP_{\text{sig}}^*} \right)^2 = \eta_Q^2 2h\nu_p \left(\frac{1}{2} P_{\text{sig}}^* \eta_p \right) \equiv \eta_Q 2h\nu_p P_L^*,$$

where P_L^* is the power in the bright fringe output of the main recombining beam splitter (BS). As introduced in Eq. (3.7), the apparent SN signal $\langle \underline{\mathfrak{S}}_s \rangle$ is proportional to the square of detected power. However, in the homodyne case, from Eq. (4.11), it follows that:

$$\langle \underline{\mathfrak{S}}_s \rangle \propto 2\eta_Q^2 P_{\text{sig}}^* \left(\frac{1}{2} P_{\text{sig}}^* \eta_p \right) \langle \underline{\mathfrak{S}}_{\theta_F} \rangle = 2\eta_Q^2 P_{\text{sig}}^* P_L^* \langle \underline{\mathfrak{S}}_{\theta_F} \rangle.$$

This observation allows for defining a signal-to-noise ratio for the signal strength.

6.2.1 Signal-to-Noise Ratio

As both $\langle \underline{\mathfrak{S}}_p \rangle$ and $\langle \underline{\mathfrak{S}}_s \rangle$ are proportional to the factor P_L^* , it is possible to define a probe-power-independent signal-to-noise ratio [1]:

$$\mathcal{R}_{\text{SNR}}(\nu)|_p = \frac{1}{P_{\text{sig}}} \cdot \frac{\langle \underline{\mathfrak{S}}_s(\nu) \rangle|_p}{\langle \underline{\mathfrak{S}}_t(\nu) \rangle + \langle \underline{\mathfrak{S}}_p(\nu) \rangle|_p} = \langle \underline{\mathfrak{S}}_{\theta_F}(\nu) \rangle \cdot \frac{2\eta_Q^2 P_L^*}{\langle \underline{\mathfrak{S}}_t(\nu) \rangle + \eta_Q 2h\nu_p P_L^*}, \quad (6.1)$$

where definitions from Eq. (3.7) were substituted for the $\langle \underline{\mathfrak{S}}_p \rangle$ and $\langle \underline{\mathfrak{S}}_s \rangle$ contributions. If $\langle \underline{\mathfrak{S}}_p \rangle \gg \langle \underline{\mathfrak{S}}_t \rangle$, that is, for power ratios $p \gg 1$, this expression degenerates into the signal-to-shot-noise-ratio $\mathcal{R}_{\text{SSR}}(\nu)$:

$$\mathcal{R}_{\text{SSR}}(\nu)|_p = \frac{1}{P_{\text{sig}}} \cdot \frac{\langle \underline{\mathfrak{S}}_s(\nu) \rangle|_p}{\langle \underline{\mathfrak{S}}_p(\nu) \rangle|_p} = \frac{\eta_{\text{Q}}}{h\nu_p} \cdot \langle \underline{\mathfrak{S}}_{\theta_{\text{F}}}(\nu) \rangle. \quad (6.2)$$

This expression depends only on constants and the underlying SN spectrum. It quantifies the optimal signal-to-noise ratio achievable using classical light using homodyne amplification.

Two other ratios are useful for the following discussion. First, the relative SN amplification $\mathcal{R}_{\text{SNA}}(\nu)|_p$ is defined as

$$\mathcal{R}_{\text{SNA}}(\nu)|_p = \frac{\langle \underline{\mathfrak{S}}_s(\nu) \rangle|_p}{\langle \underline{\mathfrak{S}}_s(\nu) \rangle|_{p=1}}$$

quantifies how much the SN signal is amplified compared to the $p = 1$ case. The second quantity, the relative spin noise ratio $\mathcal{R}_{\text{SN}}(\nu)|_p$, is $\mathcal{R}_{\text{SNA}}(\nu)|_p$ divided by the amplification factor η_p :

$$\mathcal{R}_{\text{SN}}(\nu)|_p = \frac{\mathcal{R}_{\text{SNA}}(\nu)|_p}{\eta_p} \stackrel{!}{=} 1.$$

This expression quantifies how well the amplification model describes the experimental estimates, for which $\mathcal{R}_{\text{SN}}(\nu)|_p$ should be equal to exactly 1 for all values of p .

Estimates for the introduced ratios evaluated at noise frequency $\nu = \nu_{\text{L,fg}}$ are plotted in Fig. 6.3. The relative spin noise ratio \mathcal{R}_{SN} is plotted in panel (a) and stays close to the expected value of 1. This means that the amplification indeed behaves as expected and why \mathcal{R}_{SNA} in panel (b) closely follows the shape of η_p , which is plotted using a black line.

The defined signal-to-noise ratio \mathcal{R}_{SNR} can be experimentally estimated using only foreground and background estimates. At the foreground Larmor frequency, \mathcal{R}_{SNR} is equal to:

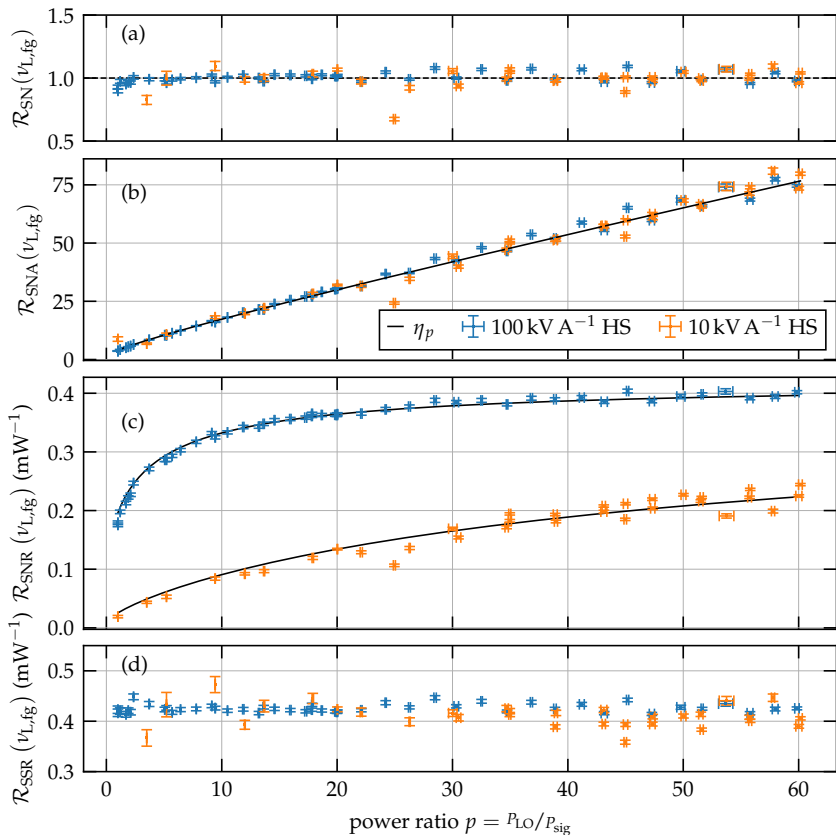


Figure 6.3: Estimates characterizing the homodyne amplification of SN at the foreground Larmor frequency $\nu_{L,\text{fg}}$ for two different electric noise floors. The panels depict: (a) apparent SN amplitude divided by the SN amplitude at $p = 1$ and the amplification factor η_p , (b) apparent SN amplitude divided just by the SN amplitude at $p = 1$, (c) probe power normalized apparent SN amplitude divided by the background along with fits of the signal-to-noise ratio model, (d) probe power normalized apparent SN amplitude divided by shot noise. The displayed error bars are regression errors, which do not account for systematic accuracy errors that are dominated by the uncertainty of the power ratio p and drifts in the electrical noise floor.

$$\mathcal{R}_{\text{SNR}}(\nu_{L,\text{fg}})|_p \approx \frac{1}{P_{\text{sig}}^*} \frac{\langle \underline{\mathfrak{S}}_{\text{fg}}(\nu_{L,\text{fg}}) \rangle|_p - \langle \underline{\mathfrak{S}}_{\text{bg}}(\nu_{L,\text{fg}}) \rangle|_p}{\langle \underline{\mathfrak{S}}_{\text{bg}}(\nu_{L,\text{fg}}) \rangle|_p}.$$

The plot in panel (c) depicts these estimates and a fit of Eq. (6.1), with the SN power as the only free parameter. As expected, the model describes the data can perfectly. For the low noise case $\mathfrak{g}_{\text{high}}$, the ratio \mathcal{R}_{SNR} quickly saturates and yields only marginal returns for an increased value of p . On the other hand, in the high noise case $\mathfrak{g}_{\text{low}}$, saturation does not happen for power ratios $p < 60$.

Finally, panel (d) depicts analogous estimates for \mathcal{R}_{SSR} , defined as:

$$\mathcal{R}_{\text{SSR}}(\nu_{L,\text{fg}})|_p = \frac{1}{P_{\text{sig}}^*} \frac{\langle \underline{\mathfrak{S}}_{\text{fg}}(\nu_{L,\text{fg}}) \rangle|_p - \langle \underline{\mathfrak{S}}_{\text{bg}}(\nu_{L,\text{fg}}) \rangle|_p}{\langle \underline{\mathfrak{S}}_{\text{bg}}(\nu_{L,\text{fg}}) \rangle|_p - \langle \underline{\mathfrak{S}}_{\text{t}}(\nu_{L,\text{fg}}) \rangle|_p}.$$

This ratio stays consistently at a constant value regardless of the value of p , as Eq. (6.2) predicted. That is, also for the experimental estimates, the ratio \mathcal{R}_{SNR} approaches the photon shot noise limited case \mathcal{R}_{SSR} for $p \gg 1$, and no further improvement is possible using classical coherent light only.

6.2.2 Shot Noise Variance Ratio

The ratios \mathcal{R}_{SNR} and \mathcal{R}_{SSR} depend on a suitable signal shape definition, but this is, in fact, not necessary. A similar criterion can be derived using just the properties of the variance of incoherent signals as defined in Eq. (2.1). As presented in Fig. 6.2, the spectra in these measurements are not dominated by SN. Therefore, according to Eq. (3.9), the variance around the mean in the difference spectra directly quantifies the strength of the two other noise contributions. A useful variance estimate can be derived using the residual distribution between the SN model function and the raw data. Any sufficiently accurate numerical estimate of the mean will also suffice if no model is available. In the left panel of Fig. 6.4, the experimental data and the model function for a portion of the foreground peak are plotted using blue dots and a black line, respectively. The light blue band around the model function is the square root of the variance of the residuals, that is, the standard deviation of the difference between the model and the experimental data. This standard deviation, σ_{peak} , is equal to the standard error of the measurement, as introduced in

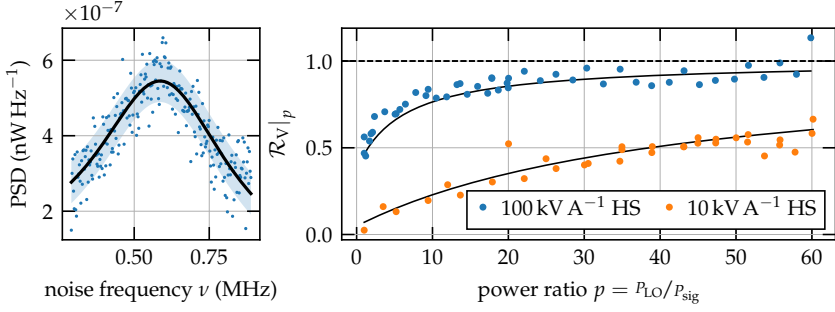


Figure 6.4: Relative variance of samples in the frequency bins around the foreground Larmor frequency $\nu_{L,\text{fg}}$ for two different electric noise floors (right panel). Plotted in black are the theoretical curves of \mathcal{R}_V for the estimated electrical noise levels. The left panel depicts the range over which the variance is calculated (blue dots are the data of the difference spectrum, black line is the model function and the light blue band designates a single standard deviation of the data).

section §3.3, and is proportional to the sum of $\langle \underline{\mathfrak{S}}_p(\nu) \rangle$ and $\langle \underline{\mathfrak{S}}_t(\nu) \rangle$. Therefore, the shot noise variance ratio \mathcal{R}_V can be defined as a quantity that tells how much the measurement is away from the shot noise limit:

$$\mathcal{R}_V|_p = \eta_{\text{red.}} \frac{\eta_Q 2h\nu_p P_L^*}{\sigma_{\text{peak}}|_p} = \frac{\eta_Q 2h\nu_p P_L^*}{\langle \underline{\mathfrak{S}}_t(\nu_{L,\text{fg}}) \rangle + \eta_Q 2h\nu_p P_L^*}, \quad \lim_{p \rightarrow \infty} \mathcal{R}_V|_p = 1,$$

where $\eta_{\text{red.}}$ is the standard error reduction factor due to averaging. The right panel of Fig. 6.4 depicts the theoretical and estimated values of \mathcal{R}_V at various power ratios p for the two detector configurations considered, using black curves and blue or orange dots, respectively. In the low electrical noise case (g_{high}) plotted using blue dots, measurements become shot noise limited around $p = 20$ and improve only marginally for larger p values. In contrast, for the high electrical noise case (g_{low}) plotted using orange dots, the shot noise limit is not approached for $p < 60$. This confirms the observation that can be made from Fig. 6.2: the high noise configuration at the highest power ratio of $p = 60$ has a similar relative variance as the low noise configuration at $p = 5$. All in all, the shape of \mathcal{R}_V reproduces \mathcal{R}_{SNR} , but this quantity has the benefit of not depending on the actual shape of the signal. The shot noise variance ratio \mathcal{R}_V will yield the same results even for a signal-free

portion of the difference spectrum within the detector bandwidth.

6.3 Conclusion

The presented proof-of-principle experiment demonstrates that optical homodyne amplification can successfully circumvent the constraints on SNS imposed by electrical noise. The proposed setup pushes the available amplification bandwidth toward much lower frequencies than the previous attempts [2, 3, 4]. The finite common mode suppression ratio of conventional balanced photodetectors poses a remaining limitation. In the low-frequency region $\lesssim 100$ kHz, the laser source's RIN is too large for the detector to compensate, contaminating the spectrum.

The same applies to any other strong modulation of the laser intensity impinging on the photodiodes, as visible from the coherent artifact in Fig. 6.1. For example, a phase averaging scheme was attempted in Refs. [117, 118] to avoid the active phase stabilization described here. The intensity modulation induced by the modulated phase resulted in a large coherent artifact that contaminated the surrounding spectrum. Unfortunately, the immense amplification of the setup reveals the smallest non-linearities in the phase modulator and imperfections in the modulation signal. The resulting artifact contains many spectral components, which a notch filter cannot filter. Moreover, even small coherent contributions overshadow the surrounding broadband spectrum because of the unfavorable scaling of coherent signals discussed in section §1.3.7. The amplification continues to work at frequencies sufficiently above the modulation frequency of ≈ 30 kHz, but the most interesting low-frequency band around $f = 0$ becomes unusable.

For the setup presented in this thesis, the influence of the RIN artifact was less severe. Nevertheless, it has to be addressed to make the technique applicable to the most fragile spin systems like single (In,Ga)As QDs. The amplification necessary for SNS of these systems is several orders of magnitude larger than for rubidium because of the low probe powers required. The saturation power of the photodetector sets a limit to the maximal optical amplification. However, the practical limit is much lower, as the amplified signal must still be strong enough to allow phase stabilization. A larger electrical amplification is therefore needed. These reasons, combined with the significant RIN of the available laser source necessary at higher wavelengths, prevented the homodyne scheme from being used in the QD experiment presented in Part IV. For future development of the technique, the following improvements could be attempted.

- Phase stabilization could be realized using a pilot beam not interacting with the sample. A pilot beam would decouple the probe power from the phase stabilization allowing much lower probe powers. Moreover, a lower electrical amplification would enable a larger amplification bandwidth and higher drift immunity. The most likely challenges for this extension are the following. For the particular experiment, the pilot laser must be prevented from interacting with the sample. Furthermore, a technique must be developed to inject and remove the pilot laser radiation with a high rejection ratio, to prevent the pilot laser from increasing the shot noise on the detector and decreasing the available amplification margin.
- The setup could be switched to a heterodyne scheme using a second laser. Most likely, this extension requires a high-finesse cavity to lock the frequency difference between the two lasers. The heterodyne interference between the signal and reference beam moves the observable SN sideband up by the difference frequency of the beams [2]. In this case, no phase stabilization is necessary. However, the sideband will be distributed around a beat note between the two lasers. For low-frequency signals to be visible, the beat note has to be sufficiently narrow to be distinguishable from the signal. Optimally, both beams should be derived from the same ultra-narrow-line-width laser source.

Part III

Measurement Infrastructure

7 Parameter Estimation

This chapter describes the universal framework that has been used in this work to provide robust histogram-like estimates for external parameters. Such reliable and verifiable estimates are necessary for noise spectroscopy of a single QD, as presented in Part IV, where this quantum mechanical system was put in a steady state defined by external parameters. Some of these parameters were imposed on the QD by its environment, e.g., the lattice temperature and the external magnetic field. Other parameters are part of the measurement process that interacts with the QD, thereby changing its state, e.g., the optical intensity and the photon energy of the laser beam that was used to probe the optical resonance. Individually varying one of these parameters and observing the changes in the resultant noise spectra provides insight into the present physical processes. By interpreting these results, the pseudo-stationary state of the QD can be estimated. While the uncertainty principle of quantum mechanics puts the lowest baseline of precision that can be achieved in principle, it is not the limiting factor for the results presented here. Instead, the estimate of the QD state is given by the precision and the accuracy of external parameters that were used to define the state. Therefore, the framework employed here provides two main features. First, given that repeated measurements of a parameter X result in a well-behaved statistical distribution $G(\mu_X, \sigma_X)$, the framework yields an accurate estimate $m_X \approx \mu_X$ and also captures the precision $s_X \approx \sigma_X$ of the measurement as well. Second, the histogram-like estimate captured by the framework contains enough information to determine whether the distribution was well-behaved.

As indicated above, a continuous physical parameter cannot be estimated with infinite precision in a single-shot measurement. Eventually, this means the parameter is known only up to a distribution. In the well-behaved case of a normal (Gaussian) distribution, the variance of the distribution is finite and is a strict sum of squares of the measurement's uncertainty and the underlying parameter's uncertainty. For other distributions, this does not have to be the case (e.g., the Cauchy distribution has an infinite variance). Even in the case of finite variance, a single

measurement can deviate more than the square root of the variance from the actual value.

Fortunately, much higher precision can be achieved when the parameter is stationary and repeated measurements can be performed. An important requirement is that the probability distribution of each measurement has a finite variance. This requirement is usually satisfied because many physical measurements are dominated by normally distributed uncertainties about a fixed mean. In this case, the central limit theorem establishes that summing over a sufficiently large number of samples will produce a normal distribution. The sample mean m_X of this distribution is the best estimate for the actual value μ_X of the measured quantity X , while its standard deviation s_X and standard error $s_{(X)}$ define prediction and confidence intervals.

Unfortunately, normal distributions are not the only situation encountered in the laboratory because sometimes quantities can shift or drift in time. Such changes in a state parameter of the system might render the measurement of the total system state meaningless, as the required number of samples to reach a normal distribution (and the associated time needed to record them) is incompatible with the available time scales.

For example, a single-mode diode laser, usually running just fine, starts to misbehave when an experimenter (named Avery) enters the laboratory. The heat emitted by the body of the experimenter introduces a temperature gradient into the structure of the laser, changing the refractive index of the gain medium, shifting the main mode in frequency as well as making it jump between two neighboring sub-modes. Had Avery not entered the laboratory, the statistics of the laser frequency would have been perfectly normally distributed. However, the statistical distribution is skewed now for timescales relevant to the experiment. Avery is unaware of their misadventure, continues the experiment, and assigns the external parameter “frequency” by noting *several* values reported by a wavelength meter and calculating the *empirical* mean and standard errors. Afterward, they throw away the raw data and continue with a different laser frequency. Only much later, when Avery evaluates the data, they realize that something *might have been off* during the measurements. However, now it is too late because the information about the *actual statistical distribution* of the raw data is lost. While neighboring points in the recorded dependence might have a relatively small deviation in their recorded statistics, the *actual* statistical distributions were vastly different. Therefore they resulted in a completely different estimate of the system state that depended on the

laser frequency.

Here, Avery made two misleading assumptions. First, Avery assumed a normal distribution of a parameter (i.e., frequency) without verifying it in some way or saving enough data to confirm that the data was indeed normally distributed for the relevant time scale. Second, they restricted the acquisition sample rate to some arbitrary value that was convenient at the time, further degrading the empirical sample set from which they derived their statistical estimates.

The main point to be made here is that the significance of the statistical distribution of raw data usually becomes apparent only at a much later stage when the complete data is not available anymore. While a total acquisition approach wherein *all* raw data is stored can definitely solve the problem, it is quite wasteful in resources like memory (for storage) and computation time (for later evaluation). So usually, the experimenter has to decide what data is *more* important than other, which, of course, cannot be predicted in advance. Furthermore, limiting the maximal available sample rate because of capacity considerations is in opposition to the requirement of the central limit theorem. Only by maximizing the number of samples taken per unit of time can an accurate estimate be derived in the shortest time possible. Therefore, a compromise is necessary that would trade a greater (preferably fixed) amount of memory needed to save the result for the ability to capture a sufficiently accurate estimate of the distribution.

The parameter estimation framework proposed here and implemented in the `plexy` module `plexy.analyzers.numeric.constant_estimator` uses a data structure that can capture an estimate of the statistical distribution of the raw data while still having a constant memory footprint: a histogram for streamed data. It is a thin wrapper around the `distogram`¹ package that implements the data structure and algorithms introduced by [119].

For the results presented in later chapters, the constant estimation framework was used for *all* measured parameters that control the state of the experiment. Parameterized cuts through the data were derived by selecting measurements with similar statistical distributions (and not only their mean value). Measurements that had significant deviations in their statistics could be successfully rejected. Later, the shape of the sampled distributions was used to investigate the source of the faults. Some faults could be eliminated, while guards were implemented for other faults that would restart the measurement in a safe state. The successful

¹<https://github.com/maki-nage/distogram> by Maki Nage, Carson Farmer, and John Belmonte

usage of the framework improved the reliability of the setup and proved the merit of using this framework. Thus, the incorporation of the framework can be highly recommended for any compatible tasks in future experiments.

7.1 The Real-Time Histogram Algorithms

This section briefly introduces the underlying data structure of a `distogram`, the main algorithm used to update this structure as new data becomes available, and auxiliary algorithms used to merge and evaluate the estimates.

The internal data structure is a sorted list h of bins, that is, tuples (p_i, m_i) where p_i is the value or position of the bin, while m_i is the magnitude. The list is kept sorted by p_i in ascending order. Compared to a regular histogram, the bins in a `distogram` are not evenly sized, and their number is kept below a threshold value N . Usually, neither the distribution nor the data limits are known in advance. Hence the data structure starts empty and is updated as new data points become available by algorithm 7.1. The maximal number of bins N must be chosen sufficiently large as it will define the resolution of the distribution's final estimate. Because the update algorithm below is lossy, the number of bins is a trade-off between storing too much data and not being able to discern individual features in the recorded estimate. For example, for peak-shaped distributions, a number of bins $N = 100$ is usually sufficient to reconstruct the distribution shape of a regular histogram to within $\approx 5\%$ accuracy [119]. In the special case when the data is normally distributed, the moments of the distribution (mean and variance) can be estimated without any loss of precision by the algorithm listed below.

The update algorithm is presented in the listing 7.1. New data points are inserted into the sorted list as individual bins with the weight 1. This continues until the threshold N is reached. From there on, the size of the structure is trimmed using the algorithm in listing 7.2. Effectively, every new data point feed to the algorithm will result in the pair of bins closest to each other being merged into a single bin with the combined weight of the individual bins. This simple algorithm captures a good estimate of any statistical distribution limited only by the resolution given by N .

For normally distributed data, the moments of this distribution can be calculated from the recorded estimate. Listing 7.3 contains the algorithm for evaluating statistical moments: for $v = 0$ and $n = 1$, this algorithm gives the mean estimator (i.e., the first moment). Using the same algorithm while assigning the first moment

Algorithm 7.1 Update

input

 a sorted list $h = \{(p_0, m_0), \dots, (p_M, m_M)\}$
 a new value p
 an upper bound N

insert $(p, 1)$ into h keeping it sorted
call the trim algorithm with h and N

Algorithm 7.2 Trim the number of bins.

input

 a sorted list $h = \{(p_0, m_0), \dots, (p_M, m_M)\}$
 an upper bound N

while $|h| > N$

 find an index i with minimal $|p_{i+1} - p_i|$
 replace $(p_i, m_i), (p_{i+1}, m_{i+1})$ with

$$\left(\frac{p_i k_i + p_{i+1} k_{i+1}}{k_i + k_{i+1}}, k_i + k_{i+1} \right)$$

end

Algorithm 7.3 Statistical moment

```

input
    a sorted list  $h = \{(p_0, m_0), \dots, (p_M, m_M)\}$ 
    a center value  $v$  and an exponent  $n$ 

foreach  $(p_i, m_i)$  in  $h$ 
    calculate  $v_i = m_i \cdot (v - p_i)^n$ 

return  $o = (\sum v_i) / (\sum m_i)$ 

```

Algorithm 7.4 Merge

```

input
    a sorted list  $h = \{(p_0, m_0), \dots, (p_M, m_M)\}$ 
    a sorted list  $h_1 = \{(q_0, n_0), \dots, (q_M, n_0)\}$ 
    an upper bound  $N$ 

foreach  $(q_i, n_i)$  in  $h_1$ 
    insert  $(q_i, n_i)$  into  $h$ 
    call the trim algorithm with  $h$  and  $N$ 

```

$v = \text{mean}(h)$ and $n = 2$ gives the variance estimator (i.e., the second moment).

The output can also be converted into a regular histogram once enough data has been sampled using the uniform algorithm found in Ref. [119] (as well as an evaluation of its accuracy for several common statistical distributions).

Statistical distributions of different data sets can be compared, and their histograms can be merged to give more precise estimates of the underlying quantities using the merge algorithm 7.4. In order to merge two estimates, the bins of the second one are inserted into the first one, followed by a trim that eliminates bins too close to each other.

In conclusion, because the algorithm is quite efficient and bounded in memory, *there is no penalty in using it for any amount of quantities, any time, every time.* There is no need to restrict the sample rate to limit the amount of data saved. Therefore, more samples can contribute to the estimate leading to more precise final results. There is no need to distinguish between more or less “important” parameters because every stationary parameter can be treated the same. In most cases, the resulting reconstructed regular histogram has enough information to assess if the

7.1 *The Real-Time Histogram Algorithms*

data it was constructed from was normally distributed. Not normally distributed data can be rejected a priori, while the usual statistical moments can be extracted for normally distributed data.

8 Cryogenic Optics Setup

This chapter is intended as a guide to the experiment that was built during this work for noise spectroscopy of single QDs. The following sections summarize the most important components that had to be constructed or implemented to perform the measurements outlined in the following Part IV.

8.1 Cryostat

The measurements presented in Part IV were carried out using a closed cycle cryostat by Cryomagnetics, Inc. This section describes some of the internal details of the cryostat's construction, as these were not or only partially provided by the manufacturer and had to be reverse-engineered. This cryogenic system is built around a refrigerator package by Cryomech that consists of a pulse tube refrigerator¹, an electrically actuated rotating valve, and a compressor package². The compressor package was placed remotely outside the laboratory in a service room to reduce noise ingress. The high-pressure helium lines are much longer than necessary for a point-to-point connection. This additional length serves as an additional buffer for the high-pressure gas. The excess length of the lines is coiled unto a rack that is anchored to a wall in the service room. One end of the high-pressure lines, along with the power supply cable from the compressor, enters the laboratory by a feed-through in the wall and directly connects to the rotating valve. The immediate ends of the high-pressure lines and the rotating valve were anchored on the concrete wall to suppress vibrations in the audio frequency range (≤ 10 kHz). Furthermore, a plastic spacer is inserted into the high-pressure feed that connects the valve output to the pulse tube, electrically insulating it from the rest of the setup.

Inside the cryostat, the two stages (40 K and 4 K) of the pulse tube refrigerator are coupled to corresponding copper stages by vibration-isolating wire-loom assemblies to reduce vibrations transmitted by the periodic pulse of the rotating

¹PT415-RM

²CPA1110

valve. A superconducting 1 T – 1 T – 7 T vector magnet assembly is mounted directly onto the second stage. It takes around 24 h to cool the second stage to a baseline of ≤ 3.6 K starting from room temperature. The actual sample chamber is realized using a variable temperature inset (VTI) with an independent Joule-Thomson (JT) circuit. Finally, the sample insert that is inserted into the sample chamber attaches to it only through a very flexible stainless steel bellows. The sample insert was suspended above the cryostat from an actively vibration-dampened optical table³ and, with the exception of the bellows, the sample insert is not touching any potentially vibrating parts of the cryostat.

8.1.1 Joule-Thomson Circuit

The cryostat incorporates a VTI implemented as an additional low-pressure JT circuit to decouple the experiment from the pulse tube, as sketched in Fig. 8.1. The external components of this JT circuit consist of a vacuum scroll pump, a helium storage tank as well as low-pressure helium lines that were mounted in the service room in a similar way as the high-pressure lines and electrically decoupled from the laboratory with plastic fittings.

Internally, the VTI consists of a gas expansion chamber, a helium evaporation chamber, and the sample chamber. The gas expansion chamber is a stainless steel tube that is welded shut at the bottom and attached to the top vacuum flange of the outer vacuum chamber (OVC) of the cryostat. It is situated mostly inside of the isolation vacuum and is protruded by the thinner stainless steel tube of the sample chamber that is approximately 30% longer than the gas expansion chamber. The flanges of both chambers are welded together at the top so that the volume of the sample chamber is isolated from the surrounding expansion chamber. This way, both chambers can be evacuated separately, and the sample chamber can be mostly decoupled from the cooling action of the cryostat for sample exchanges or high-temperature measurements. A hollow torus-like evaporation chamber is welded onto the sample chamber tube just below the end of the gas expansion chamber. The evaporation chamber is connected to a pressurized helium feed capillary through a needle valve. This capillary contains helium, which has been pre-cooled by a heat exchanger at the 40 K stage and cooled down to initially about 4 K by the regenerator of the 4 K stage and a heat exchanger at the 4 K stage. Before each heat exchanger, an activated carbon cold trap is installed that captures

³Table Stable AVI-200-XL LP with an LFS-3 sensor

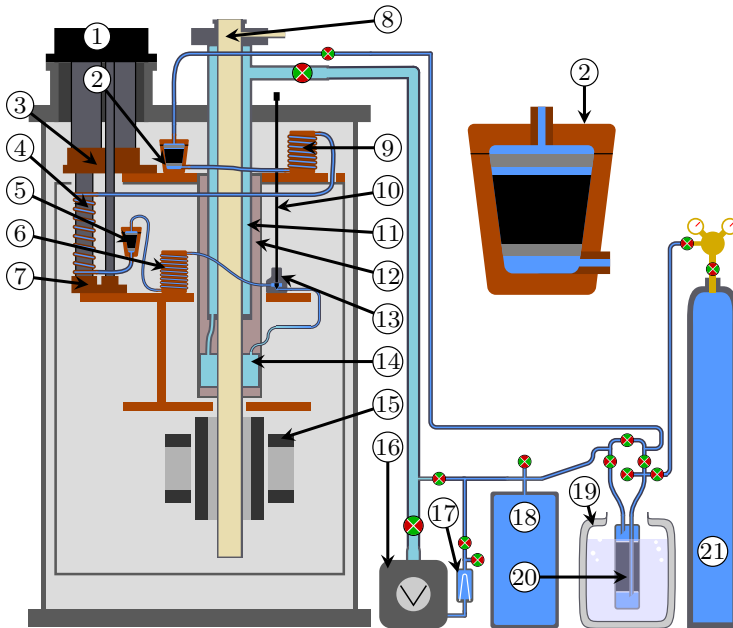


Figure 8.1: Sketch of the complete modified JT circuit. The labeled components are: (1) the pulse tube hot end of both the 4 K and 40 K stages, (2) 40 K activated charcoal cold trap (H_2O , N_2), (3) 40 K pulse tube cold end, (4) JT circuit pre-cooling coil wound on the 4 K regenerator of the pulse tube, (5) 4 K activated charcoal cold trap (N_2 , H_2), (6) JT circuit 4 K heat exchanger, (7) 4 K pulse tube cold end, (8) sample chamber with helium exchange gas, (9) JT circuit 40 K heat exchanger, (10) needle valve rod and vacuum feed-through, (11) VTI gas expansion chamber, (12) VTI radiation shield, (13) needle valve, (14) VTI evaporation chamber, (15) superconducting magnets assembly, (16) JT circuit circulation scroll pump, (17) particulate matter filter, (18) helium storage and buffer tank, (19) liquid nitrogen dewar, (20) external activated charcoal cold trap (H_2O), (21) pressurized helium cylinder. When in operation, teal and blue colored areas contain at helium < 20 hPa and 700 hPa, respectively.

residual contaminants in the helium gas. The first trap captures mostly water and nitrogen, while the second trap captures nitrogen and hydrogen. The needle valve regulates the helium flow that eventually becomes liquid due to the JT cooling effect below 40 K. The exhaust from the evaporation chamber goes into the gas expansion chamber, which is evacuated by a scroll pump through a vacuum fitting at the top flange. Then, the compressed helium from the pump is buffered in the helium storage tank. Helium from the tank recirculates back into the helium capillary to close the circuit.

Several related issues have to be considered for stable long-term operation of the JT circuit. The JT stage needs a steady helium flow with low variation, as the flow parameters directly influence the pressure and hence temperature inside the evaporation chamber. The helium has to be pure as any contaminants solid at liquid helium temperatures (i.e., most gases), as they will accumulate in the capillary and eventually clog it. When this happens, the needle valve can no longer be used to regulate the flow, and a spontaneous warm-up occurs. The two inline cold traps are quite small and have minimal capacity. Moreover, their capacity is further severely degraded by water vapor. The vapor freezes solid and glazes over the surface of the activated carbon granules in the traps, reducing their effective area that can trap other contaminants. An additional liquid nitrogen cold trap was retrofitted inline to an external section of the pressurized helium feed line to counteract this water ingress, as the manufacturer had not foreseen this problem.

To minimize water and nitrogen ingress through leaks in the pump, the manufacturer chose a special pump⁴ design. The scroll chamber of this pump is sealed by a rigid stainless steel bellows that also transmits the rotation motion to the scroll. Therefore, in this pump design, the complete scroll chamber can be sealed by just two big stationary o-rings seals. In competing designs, the scroll is moved by a shaft penetrating the scroll chamber wall and riding in a sliding seal feed-through. This sliding seal tends to leak ambient air from the outside, making these designs incompatible with the closed JT circuit.

Nevertheless, operating a scroll pump in a closed loop has a drawback in the form of abrasion dust. The two scroll parts ride on cushions of hard plastic seals. Over time, these seals abrade away, producing very fine dust in the pump exhaust. This fine dust can permanently poison the activated carbon traps by clogging the pores in the carbon granules. This is usually unacceptable, as refilling the cold

⁴Edwards nXDS 10ir

traps with fresh granules is quite complicated and error-prone. An additional particulate matter filter was inserted between the pump and the helium tank to prevent dust ingress. This filter has to be regularly inspected and replaced to avoid an eventual migration of dust particles through the filter and into the internal cold traps.

Cold Trap Maintenance and Cold Leaks

A sketch of the 40 K cold trap is depicted in the upper right corner of Fig. 8.1. The cold traps consist of a copper body that captures the activated carbon granules between two sintered metal particulate matter filters. The cryostat has to be almost completely disassembled to refill the internal cold traps, and the traps have to be disconnected from their copper-sealed fittings⁵. Then, the indium-sealed soft copper flanges of the traps must be carefully separated without marring the sealing surfaces. Finally, after refilling with fresh granules, the indium seals of the traps have to be restored to be tight for gaseous helium. The indium seal of the 4 K trap has to remain tight even for super-fluid helium below 2 K.

Afterward, the trap has to be reinstalled in the cryostat by reconnecting the fittings using *new* annealed soft copper seals⁶. Copper work hardens through elastic deformation; a tight metal-on-metal seal cannot be formed in this hardened state. Therefore, the copper seals cannot be reused and must be recycled.

Any unintended leaks will lead to helium accumulation inside the OVC. Unlike other gases, helium does not experience significant cryo-pumping as it does not freeze solid and is not efficiently trapped by cold surfaces, activated carbon coatings, and super-insulation layers inside the cryostat in appreciable quantities. Instead, it will liquefy only at the coldest parts of the cryostat. From there, it will eventually drip onto warmer surfaces and instantaneously evaporate, causing a sudden breakdown of the isolation vacuum.

A similar failure happened at the beginning of the initial measurement cycle due to an improperly brazed-on fitting that resulted in a cold leak. The vacuum breakdown was so severe and sudden that even a permanently attached high vacuum pump could not compensate for the sudden pressure increase. The whole cryostat then slowly cycled with a period of 15 min in a very characteristic way between a high-vacuum phase and a high-thermal-load phase due to a bad vacuum. No

⁵Swagelok SS-4-VCR 1/4 in series for the upper stage and SS-2-VCR 1/8 in series for the lower stage

⁶Swagelok CU-4-VCR-2 1/4 in series for the upper stage and CU-2-VCR-2 1/8 in series for the lower stage

measurements could be performed in this state, and complete disassembly and repair were needed.

Sample Chamber

A helium exchange gas filling of the sample chamber (100 to 300 hPa) was used to short-circuit the inner evaporation chamber wall with the sample insert. When evacuated, the VTI walls saturate at approximately 150 K once the cryostat is in operation, but the JT circuit is offline. Depending on the heat load exerted onto the VTI by the sample insert, a baseline of ≤ 1.7 K can be reached in $\lesssim 10$ h when starting with the VTI at the saturation temperature. Fine temperature regulation is then achieved using a heater in the sample insert and an internal heater that is attached to the outer wall of the VTI.

8.2 Cryostat Control Software

As the cryogenic system was provided without software, during the work on this thesis, a control software was developed and implemented that ensures a safe operation of the cryogenic system and its superconducting vector magnet. This section describes the high-level architecture of this software. The general idea behind the chosen architecture is to integrate all the provided devices into a unified interface. For this reason, the software is split into three parts: the control server, the logging script, the graphical user interface (GUI), and the client application programmin interface (API) for the experimenter. The server runs on an embedded, isolated miniature computer that is attached to the control and monitoring devices through Ethernet and USB interfaces. The logging script, the GUI, and the client API are realized as clients that connect to the control server from any other computer in the laboratory through a private local Ethernet network.

8.2.1 Control Server

Some of the control devices react quite sensitively to a variation in access timing and framing errors in their respective communication protocols. Worst offenders enter a non-resettable state upon receiving partial messages that can only be cleared by a hard power cycle. This is undesirable in most cases, as these devices run tight control loops that are severely disturbed by such a crude reset. For this

function	manufacturer	model	protocol
sample & VTI temperature	Cryocon	24C	SCPI like
pulse tube temperature	Cryomagnetics	612	SCPI like
OVC pressure	Leybold	PTR90NS	custom
VTI pressure controller	Pfeiffer	Center One	custom
VTI needle valve controller	Zaber	X-NMS17C	custom
VTI pump controller	Edwards	nXDS 10ir	custom
pulse tube compressor	Cryomech	CPA1110	Modbus/TCP
magnet controllers	Cryomagnetics	4G	SCPI like

Table 8.1: Devices handled by the control server and their respective communication protocols.

reason, the server is, for the most part, a minimal process that can gracefully handle failed communication while dealing with all the specific quirks of individual devices. This way, the sensitive devices are shielded from accidental programming errors that can happen during the design phase of the experiment. Moreover, the more complicated and error-prone GUI code is separated from the server and free to crash without compromising the control of the cryostat. A side benefit of this split is that the cryostat can be controlled and monitored from any computer in the laboratory.

To this end, the server⁷ was implemented in the safe system programming language Rust. Using a safe language allowed a reliable and bug-free implementation of critical communication tasks. These tasks are orchestrated to run in an asynchronous way using the `tokio` module. Employing an asynchronous architecture also allows for running hundreds of parallel tasks without overloading the limited hardware capabilities of the embedded computer. The communication protocols incorporated in the server are summarized in Tab. 8.1.

The logging script and the GUI use a common network-based API. The same API is exposed as a Python module⁸ in the `plexy` framework. For example, the API can be used to dynamically change the temperature of the sample and the current magnetic field.

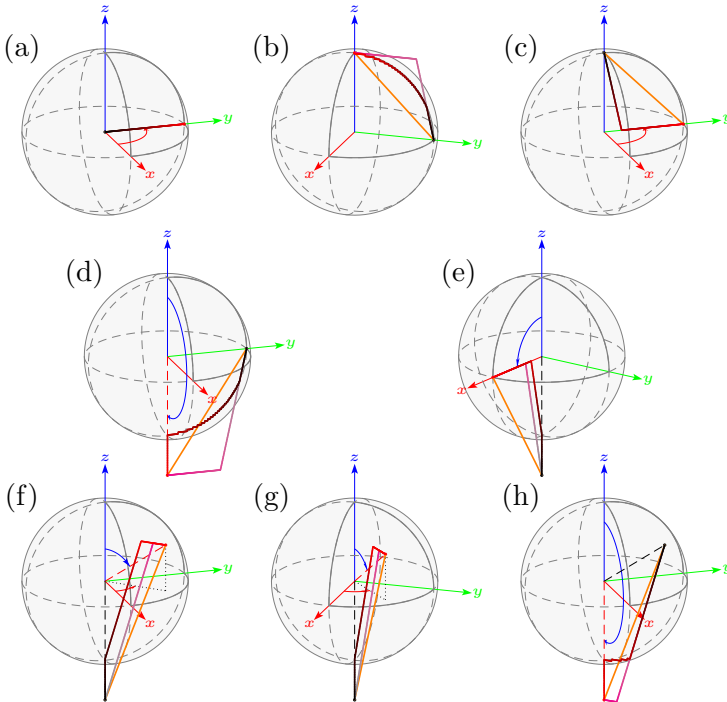


Figure 8.2: Example vector magnet sweeps: (a) $(0\ 0\ 0) \rightarrow (0\ 1\ 0)$, (b) $(0\ 1\ 0) \rightarrow (0\ 0\ 1)$, (c) $(0\ 0\ 1) \rightarrow (0\ 1\ 0)$, (d) $(0\ 1\ 0) \rightarrow (0\ 0\ -1.5)$, (e) $(0\ 0\ -1.5) \rightarrow (1\ 0\ 0)$, (f) - (g) $(0\ 0\ -1.5) \rightarrow \frac{1}{\sqrt{3}}(1\ 1\ 1)$, (h) $\frac{1}{\sqrt{3}}(1\ 1\ 1) \rightarrow (0\ 0\ -1.5)$. Thick orange line designate the shortest path with equal sweep rates. Grey-to-magenta gradient lines designate unconstrained sweeps with realistic sweep rates, while black-to-red gradient lines designate the path that does not leave the save envelope using these realistic sweep rates.

Vector Magnet Control

The superconducting magnet coils can be operated either as a vector magnet up to ≈ 1 T or as a strong z-axis magnet up to 7 T. It is very important that the transverse x, y -coils do not generate magnetic fields at all times when the z-coil is operated at fields above 1 T to prevent damage to the magnet. The magnet power supplies⁹ are completely independent - the manufacturer provided no feedback or synchronization circuits allowing a coordinated sweeping of the total field. Therefore, the next best thing was to realize the control and limiting of the allowed fields in software.

The sweep rates of the longitudinal and transverse coils are quite different. Therefore, when the magnetic field is changed, the sweep path from the initial to the final position is not always a straight line between the two values. More importantly, the sweep path might leave the safe envelope of vector magnet operation even if the initial and final fields fall within the safe zone.

An example of this scenario is depicted in panel (b) of Fig. 8.2. Here, the orange line is the shortest sweep path that is possible if all coils have equal sweep rates. Realistically, this path can only be taken by severely reducing the maximal sweep rate of the longitudinal coil. Unconditionally limiting the sweep rate degrades the average vector sweep rate of the magnet. The gray-to-magenta gradient line traces the path of an unconstrained sweep, where all coils sweep with their maximal sweep rate. This path is not allowed, as it leaves the safe envelope of ≈ 1 T for vector magnet operation. The last trace is plotted using a black-to-red gradient line. During this sweep, the sweep rate of the longitudinal coil is effectively reduced only when it leaves the safe region. Effectively, the sweep follows the outer edge of the safety region.

The actual implementation was designed around a read-check-modify loop. The panels in Fig. 8.2 depict how the following strategy handles possible sweeps. In each iteration of the loop, the current field is queried and compared with the destination field. A current setpoint change is calculated and executed depending on the absolute values *and* the field difference. The jumps visible in some traces are the simulated equivalent of realistic delays between the queries and the response of the controllers.

This strategy usually yields acceptable results. However, the corresponding control loop is somewhat handicapped by the power supply's inconsistent and over-

⁷RsCryCon (Rust Cryostat Controller)

⁸plexy-instruments-rscrycon

⁹Cryomagnetics 4G

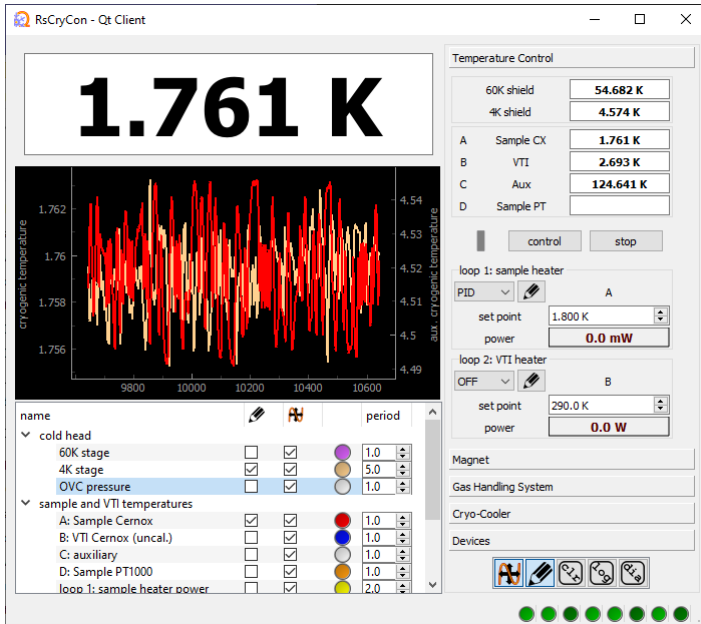


Figure 8.3: The main screen of the graphical user interface (GUI). The sample temperature is displayed in the top left. The plot view on the left can be configured using the selection tree below it to display a time trace of all the possible inputs that the server process is monitoring. The tabs on the right contain various control inputs and relevant monitored quantities sorted by topic.

all very long response times. The response times for a status query of the power supply that controls the longitudinal coil vary between 200 – 600 ms. The second power supply controls both of the transverse coils, and its response times vary between 600 – 1600 ms. For this reason, brief excursions outside of the safety region cannot always be avoided: The longitudinal limit of the sweep rate is determined by the power supply that takes the longest to reply. The implemented workaround to make the overall operation of the magnet safe is to reduce the safety region to account for the majority of these possible excursions.

8.2.2 Graphical User Interface

The GUI is depicted in Fig. 8.3 and was implemented in the Python bindings to the Qt5 framework. The interface was split into a left panel for plots and a right panel for cryostat control. On top of the left panel, the current sample temperature is displayed. Below it, a dynamic plot widget¹⁰ displays time traces of all the relevant quantities that are queried from the attached devices by the control server. In the depicted example, only the temperature of the 4 K is drawn (pencil), and the corresponding ordinate is scaled to fit the displayed data (orange waveform). The raw data is filtered by a running mean over 1 s, and the plot color is set to red. Additionally, the bottom buttons in the right control plane enable the automatic scaling and drawing, and clearing of the data in the plot widget.

The control panel on the right contains tabs that are displayed side by side in Fig. 8.4. The temperature control tab displays the measured temperatures of the internal cryostat sensors and the sample sensor. From the tab, it is possible to set up the control loops and start and stop regulation. For the usual low-temperature operation, the second loop is left offline. However, for sample exchange, the much more powerful heater of the VTI can be enabled here to reduce the time needed to warm up the sample chamber and sample insert.

The magnet control tab displays the present current and field values. A graphic representation of the magnetic fields similar to Fig. 8.2 is displayed by pressing the “set field” button, whence the server can be requested to initiate a sweep to the desired value. Both spherical and Cartesian coordinates were implemented.

The gas-handling tab displays the relevant temperatures and pressures that must be kept in mind while cooling down the sample chamber. Furthermore, the needle valve stepper motor can be controlled from here. Positive increments close the valve. The motor can be directed to an absolute (A) value using the “move” button. Alternatively, the motor can be moved an incremental amount of steps (R) using the direction buttons. Finally, the motor can be used to find the completely closed home position, and the error flags can be reset. The last group of controls contains the operation parameters of the gas-handling scroll pump. For example, the operation hours indicator should be kept track of to determine when the pump needs servicing (tip seal and bearing replacements, $\approx 1 \times 10^4$ h). The pump can be started and stopped from here, and its power level can be adjusted between 66 to 100 %. Note that if the pump was started manually by pressing the start button

¹⁰from the pyqtgraph module, <https://www.pyqtgraph.org/>

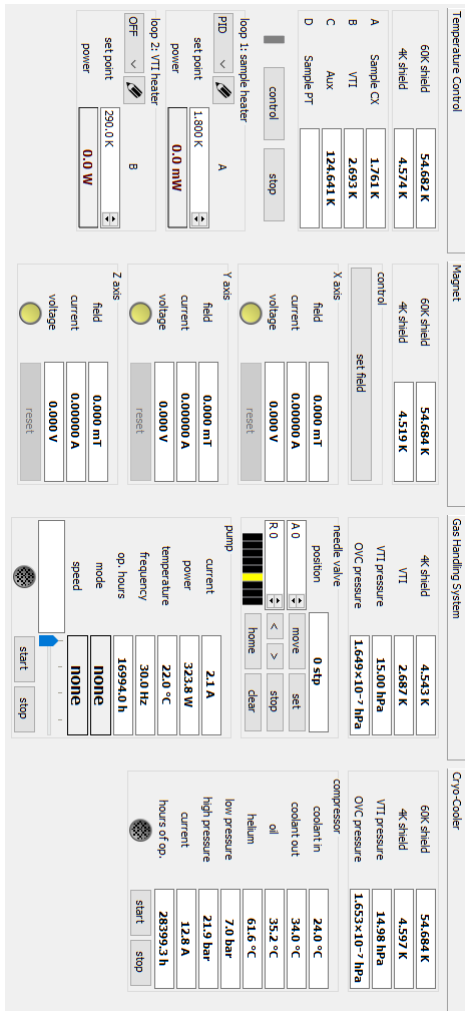


Figure 8.4: The tabs of the control panel in the cryostat control GUI.

on the pump, the start and stop buttons in the GUI will be ignored.

The cryo-cooler tab displays the operation parameters of the high-pressure helium compressor. From here, it can be ensured that the coolant, oil, and refrigerant temperature are in a valid range. The “Aeroqip” quick disconnect fittings on the high-pressure helium lines are not perfectly tight. Therefore, the low- and high-pressure readings can be used to estimate if the system lost helium and needs refilling. Finally, the operation hours indicator determines when the oil mist adsorber has to be replaced ($\approx 2 \times 10^4$ h).

8.3 Confocal Microscope and SNS Setup

8.3.1 Sample Insert

The confocal microscopy sample insert was realized as an approximately 1.4 m long custom cage system piece. Fig. 8.5 depicts a simplified technical drawing of the insert.

The cage of the insert is built from glass fiber reinforced 5 mm plastic rods (4) with a high filling ratio. Because of the high filling ratio, the thermal conductivity of the rods is mostly given by the low thermal conductivity of glass. Threaded metal caps were attached to the rods to improve mechanical stability. Commercially available rods are not perfectly straight: over the length of the sample insert, they are bent approximately 3 cm. This is not a problem, as the position of the four rods is symmetrical around the main axis of the sample insert. Therefore, during the assembly, the rods can be rotated so that they all initially point away from the main axis when they are attached only to the vacuum flange (2). Fixing them in this orientation ensures equal tension on all rods. Consequently, the whole sample insert remains straight because of the symmetric tension, even though the individual rods are bent. Furthermore, the seven intermediate stages (5, only three displayed here) stiffen the sample insert torsionally.

In the middle of the sample insert, five highly reflective radiation shields (6) are suspended between spacers (7). This level is slightly below the vacuum flange of the cryostat (8 in Fig. 8.1). These shields help reduce the thermal radiation from the room-temperature parts of the cryostat and the sample insert.

Below the thermal shields, a plastic tube (8) is loosely inserted into the round space between the stages. This tube was retrofitted into the sample insert because, over several weeks of the initial measurement cycle, the objective aperture kept

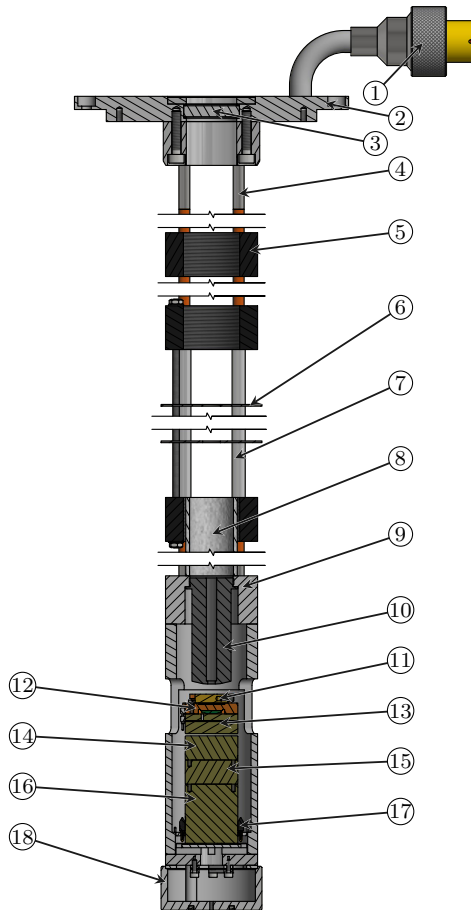


Figure 8.5: Sample insert for confocal microscopy: (1) electrical feed-through, (2) vacuum flange, (3) optical window, (4) glass fiber reinforced plastic rod with metal end caps, (5) cage plate, (6) radiation shield, (7) spacer, (8) condensation shield, (9) main body, (10) objective, (11) sample holder, (12) sample holder retainer, (13) x, y, z -piezo scanner, (14) & (15) x, y -piezo steppers, (16) z -piezo stepper, (17) electrical connections, (18) end cap and contact detection probe.

freezing up. A continuous increase of diffuse and bright stray reflections was observed during the run. An accumulation of impurities in the objective aperture is the most likely reason for the observed freezing up. The vacuum seals of the sample chamber are not perfect. Nitrogen and water impurities eventually end up in the helium exchange gas during long measurement periods. Instead of freezing on the cold outer wall of the sample chamber, some part of the impurities freezes while still freely floating in the exchange gas. This highly reflective water and nitrogen snow eventually collects in the aperture of the objective, severely degrading the objective optics. This tube serves as a condensation shield that stops the convection of frozen impurities toward the optical axis and the objective aperture. Inserting the tube reduces the effective cross-section over which the frozen impurities are collected. After the retrofit, the degradation was no longer observable in the reflected beam during the later, much longer measurement runs.

The sample insert concludes with the main body (9) that houses the objective¹¹ (10) and motorized stages¹² (13) to (16). The objective is a special cryogenic and apochromatic design by Attocube. This objective's implementation ensures consistent performance in the whole laser wavelength range of the experiment with low wavelength-dependent focus drift. This property is particularly helpful for recording wide laser photon energy detuning dependences, as it was done for the measurements presented in chapter 12.

The stack of motorized stages consists of a single longitudinal (z) and two transverse (x, y) piezo steppers. The steppers are responsible for the bulk positioning of the sample under the objective. These steppers integrate a carbon-wiper-based variable resistor used to read out the current position. The precision of the read-out is $\approx 1 \mu\text{m}$, while the accuracy at cryogenic temperatures is $\lesssim 15 \mu\text{m}$, especially when moving the stepper by more than 1 mm or changing the movement direction. An additional wide-range, flexure-based, three-axis piezo scanner was mounted on top of the stack. The transverse range of the scanner is $\approx 30 \mu\text{m}$ at cryogenic temperatures. This range combines well with the $\approx 15 \mu\text{m}$ play of the steppers, as the stepper's average deviation can be compensated by the scanner. The longitudinal scanner allows for a very precise and reproducible focus adjustment.

On top of the stack, a small copper block serves as a sample holder plates retainer. The retainer incorporates a self-calibrated low-temperature sensor¹³, a

¹¹Attocube LT-AP0/NIR/0.81

¹²Attocube ANSxyz100std/LT, ANPx102/RES/LT/HV, and ANPz102/RES/LT/HV

¹³Lakeshore Cernox CX-1050-SD-HT X148743

high-temperature sensor¹⁴, and a $50\ \Omega$ resistive heater¹⁵ that are used to sense and regulate the sample temperature. The installed sample holder plate can be removed by loosening two angled grub screws and carefully sliding it from the retainer through the window in the sample insert body. (The steppers should be positioned in a central position beforehand.) This design allows simple and quick sample exchanges.

Background Subtraction

The transverse scanners also serve a crucial function in background subtraction. A background spectrum not containing any signal is usually recorded during SNS to isolate the SN signal from other broadband contributions, as explained in section §3.3. Previously this had been done by applying a transverse magnetic field, broadening spin dynamics, and shifting them out of the analyzer bandwidth. The small superconducting coils used for the external magnetic field could provide only ≈ 31 mT but were quick to turn on and off. The large superconducting coils used in the current setup can reach much higher magnetic fields at the cost of prohibitively slow field changes. Therefore a different background subtraction scheme was implemented. Instead of shifting the spin dynamics by changing the magnetic field, a scanner axis shifts the sample, moving QD away from under the objective. Good-quality backgrounds can be acquired as long as the samples' QD density is low and there are no QDs resonant with the laser at the new position. One drawback of the new technique is that the reflected power from the sample can vary between different locations of the sample, resulting in a slightly different shot noise level. However, this effect can be easily characterized by performing a SN map akin to a photoluminescence (PL)-hyperspectral map (as explained in 9.2.1) to find an appropriate location.

Stage Stepper and Scanner Control

The scanner-stepper combination is controlled by two independent devices¹⁶ that must work in a synchronized way. Locating the exact QD position is a time-sensitive procedure, as it involves finding the QD and subsequently adjusting for piezo creep. Therefore, large involuntary excursions of the scanners should be

¹⁴Pt-1000

¹⁵Bourns CHF3523DNT500LW

¹⁶Attocube ANC350 (v4) and Thorlabs MDT693B

avoided. Furthermore, sudden jumps in voltage (such as accidentally setting the piezo to 0 V) can cause a slip of the steppers below the scanner stage, causing a gross misalignment. Finally, the scanner position should be preserved even in the event of a software crash on the experimenter's side. A server¹⁷ was implemented to fulfill these requirements that also runs on the embedded computer accessible over the laboratory network. This server saves changes to the stack's state in a database so previous movements can be tracked back and undone if necessary. The position is persistently saved over server restarts and reconnects. Additionally, the server rate limits the changes to the scanner voltage so that the saved positions remain valid. This implementation was crucial in enabling the long-term measurement performed in this thesis.

8.3.2 Optical Setup

Sample Insert Alignment Mount

The sample rod has to be suspended from the optical table into the sample chamber without actually touching it, as explained in section §8.3.1. This was achieved by the sample rod alignment mount depicted in the top right corner of Fig. 8.6. This mount is a large, purpose-built kinematic tilt mount similar to a mirror mount. The flange of the sample insert is attached to a small vacuum chamber connected to the cryostat sample chamber with the flexible stainless steel bellows. The sample insert reaches through this bellows without touching it into the sample chamber of the cryostat. This vacuum chamber attaches to the top plate of the alignment mount. When the sample chamber is evacuated, atmospheric pressure strongly compresses the bellows, and the alignment mount experiences significant forces that can change the alignment of the sample insert. For this reason, the alignment has to be done with the bellows installed and the sample chamber evacuated.

The alignment mount is attached to the optical table by four custom shallow retention screws (21) that ride on washers in oversized clearance holes. Side-to-side alignment can be ensured by loosening these screws and temporarily attaching the shifting hardware (23) to the optical table. These shifters consist of a mounting block and a micrometer screw. By fixing the alignment of the sample insert mount with four base plates¹⁸ as depicted in the figure, the mount can be shifted

¹⁷RsAttoStep

¹⁸Thorlabs BS2/M

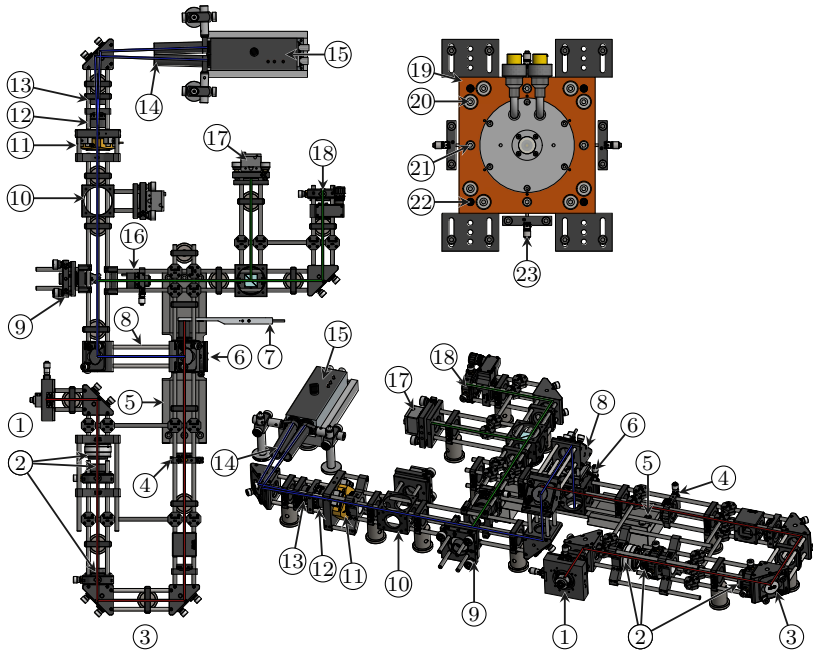


Figure 8.6: Technical drawing of the optical setup: (1) input coupler, (2) mode matching telescope, (3) probe alignment periscope, (4) probe input polarizer, (5) aluminum bridge, (6) main 10:90 beam splitter, (7) reference power meter, (8) sample alignment periscope, (9) optional PL mirror, (10) optional beam splitter for control port, (11) balancing half-wave retarder, (12) Wollaston prism, (13) focusing lens, (14) stray light shield, (15) balanced detector, (16) LCR/polarizer combination, (17) PL control port with CMOS camera, (18) PL output coupler, (19) sample rod alignment mount, (20) tensioning screws, (21) retention screws, (22) tilt alignment micrometer, (23) shift alignment micrometer. The optical paths are illustrated by thick lines: excitation (red), collection and SNS (blue), imaging and PL (green). Setup and illustration were created in collaboration with Kai Hühn and Ronny Hüther.

left-to-right by loosening the right micrometer screw while simultaneously tightening the left micrometer screw. It is advisable to place pieces of hardened steel shim stock between the tips of the micrometers and the aluminum surface of the mount to prevent the tips from scratching the surface of the mount. Similarly, the other direction can be aligned by mounting the base plates to restrict the left-to-right movement.

Four micrometer screws (22) control the sample insert's tilt. The usual procedure is to slightly loosen the tensioning screws (20) and adjust the desired tilt angle using only three of the micrometers. To this end, one of the micrometers with a flat hardened steel seat has to be retracted. The micrometers with the circular and v-groove seats have to remain under tension to ensure the mechanical alignment between the top plate and the mount. When the desired alignment is achieved, the third screw can be lowered to touch its seat, and the tensioning screws can be tightened again to increase the stiffness of the mounting.

A special, custom-built, high-impedance contact detector¹⁹ is used to help with the alignment, as the clearance between the walls of the sample insert is only ≈ 1 mm. The contact detector simultaneously registers electrical short circuits from either the thermal shields or the sample insert end cap to the sample chamber walls up to a resistance of 1 k Ω . A short through the thermal shields produces a high-pitched tone, while a short through the end cap produces a low-pitched tone. If both contacts happen at once, a superposition of the two tones will be sounded. Before alignment, it is advisable to check the calibration of the contact detector using its internal reference 1 k Ω resistor by pressing the test button of the corresponding channel. The calibration can be adjusted by internal potentiometers.

Cage System

The optical setup on top of the optical table is centered around the optical window in the sample insert's vacuum flange. It is somewhat challenging to find the initial optical alignment because of the length of the sample insert. For this reason, the optical setup is almost completely realized as a rigid cage system that can be lifted from and put back on the optical table as a single piece. Using at least three post position retainers²⁰ the optical setup can be placed on the optical table with an accuracy of less than 0.1 mm. This arrangement allows quick sample changes with

¹⁹Final Beep™ ©

²⁰Thorlabs RSPC

minimal optical alignment afterward.

The focus position of the objective of the sample insert should be adjusted beforehand at room temperature while the sample insert is still outside of the cryostat to ease the alignment even more. This is best done using an equivalent beam splitter arrangement (6) as used in the actual setup in Fig. 8.6. The sample insert can be mounted to the side of the optical table, and a bright light source can be directed from the side directly onto the sample. By imaging the surface of the sample onto a digital camera, it is very easy to find the focal plane that can then be further adjusted using a laser beam. When the focus plane and the optical setup are both adjusted, as explained above, only a minimal optimization of the beam path is necessary when the sample insert is cooled down.

Probe Path

Logically, the optical setup consists of the probe, collection, and PL paths. Fig. 8.6 depicts these paths using red, blue, and green lines, respectively. The probe path starts with the triplet collimator²¹ (1) that serves as the input coupler. The triplet collimator is a rather cost-effective way to collimate the single mode emitted by the polarization-maintaining single-mode optical fiber into an intensity distribution that comes very close to an ideal Gaussian-Hermite TEM₀₀ mode. In particular, the adjustment of the collimator is fixed at the factory and cannot drift over time. The beam waist $w_0 \approx 1.3$ mm diverges to around $w \approx 1.5$ mm because of the relatively long optical path length between the setup and the objective. This divergence is large enough to slightly clip the objective aperture and cause a visible Airy pattern. The beam waist was moved to lie right at the aperture of the objective using three lenses in a telescope configuration (2) to minimize this effect. Next, the positional alignment of the beam is set using two mirrors in a periscope configuration (3). A half-wave retarder and a polarizing beam splitter are used to set the rough probe power, and a nanoparticle polarizer²² (4) with an excellent suppression ratio is used to define the probe polarization to be parallel to the optical table. The probe beam is mostly transmitted by the 90:10 wedge beam splitter²³ (6) onto the power meter (7) that is mounted right behind it. The beam splitter was mounted in a specially designed holder (depicted in Fig. B.1) that retains the glass substrate of the beam splitter completely stress-free to prevent degradation of the

²¹Thorlabs TC12APC-850

²²Thorlabs LPVIS050-MP2

²³Thorlabs BSN11

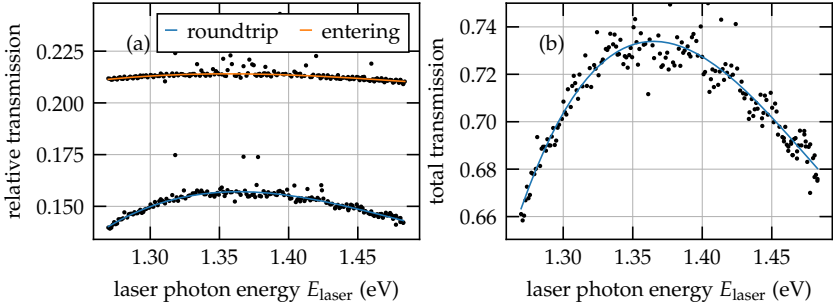


Figure 8.7: Laser photon energy dependence of power transmission curves. Panel (a) depicts the power that exits the sample insert relative to the power P_{block}^* that is measured behind the main beam splitter in orange, and the power that is reflected into the sample insert relative to P_{block}^* in blue. Panel (b) depicts the portion of the power that is reflected from the main beam splitter that exits the sample insert in blue. Smooth lines are Chebyshev polynomial fits to the raw data.

input polarization through stress-induced birefringence. This custom holder was designed to be mounted directly on the standard kinematic mount²⁴ used in (6), and for alignment purposes, it can be arbitrarily rotated without colliding with the cage rod or the cage cube.

The power detected by the power meter behind the beam splitter P_{block}^* was used as a reference for all other power measurements as well as the input to a power stabilization circuit. A lens tube was mounted flush between the cage cube and the silicon diode of the power meter to make these power measurements at low probe power levels resilient against ambient light. Before being coupled into the input fiber, the probe laser light passed a reflective, variable neutral density filter, a retarder, and a linear polarizer. Both the neutral density filter and the retarder were mounted in motorized rotational mounts²⁵. The deviation from a desired power P_{block}^* was used as an error signal. The input power was brought close to the desired value by rotating the neutral density filter. Then, the control was switched to the retarder that, together with the following polarizer, acted as a typical low-frequency “noise eater” circuit.

The curves depicted in Fig. 8.7 can be used to determine optical powers that en-

²⁴Thorlabs B4CRP/M

²⁵Newport Agilis AG-PR100

ter and leave the sample insert at various laser photon energies. The orange curve in panel (a) depicts the amount of power that enters the sample insert relative to the power P_{block}^* , which is transmitted through the main beam splitter and detected by the power meter. The blue curve depicts the amount of power that leaves the sample insert relative to the P_{block}^* , assuming a perfect mirror is placed in the focus of the objective. Panel (b) depicts the quotient of these curves: the ratio between the power that leaves and the power that enters the sample insert. For example, at 1.4 eV, the power entering the sample insert is $\approx 0.214 \cdot P_{\text{block}}^*$, and the power leaving the sample insert is $\approx 0.155 \cdot P_{\text{block}}^*$. Only $\approx 72.7\%$ of the power entering the sample insert leaves it again.

Photoluminescence Path

A small portion of the beam is reflected by the beam splitter and sent down to the sample. Then, when that beam returns back from the sample, it is almost completely transmitted by the 90:10 beam splitter. The collection periscope (8), built from three mirrors, is used to center the beam back into the cage system. Depending on whether or not the PL path is enabled by shifting the mirror (9) into the cage system, the beam goes either to the polarization bridge and SN detection part or the PL characterization and spectrometry part. The PL part starts with a liquid crystal retarder (LCR) combined with a following polarizer. The optical axes of the polarizer and LCR are fixed to each other by assembling them into a single part (16) using a short lens tube. The resulting part selectively transmits a linear polarization that can be switched between two orthogonal directions by selecting two appropriate amplitudes to drive the LCR. Furthermore, the whole part can be rotated using a rotation mount to align it to linearly polarized light emitted or reflected from the sample. For a sample emitting light at two close frequencies, which are simultaneously mutually orthogonally polarized, this configuration artificially increases the resolution of the attached spectrometer by selectively blocking one of the emitted frequencies through its polarization.

In the middle of the PL path, the light is split in two by a 50:50 beam splitter, and half of the power is sent to a sensitive monochrome CMOS digital camera²⁶. For maximal sensitivity, the camera has its manufacturer-installed near-infrared filter removed. The camera is used to image the reflected beam, which is helpful during the optical alignment steps. The probe beam starts an almost perfectly symmetrical

²⁶ iDS uEye UI-1240SE-NIR-GL

Gaussian mode, is focused by the objective, is reflected by the highly polished sample surface, and is expanded back by the objective. When the optical alignment is close to optimal, the reflected beam impinging onto the camera sensor is also almost perfectly symmetrical. Displacement and pointing deviations from optimal alignment produce asymmetric diffraction and clipping artifacts. Therefore, the alignment with an optimal circular symmetry is targeted during the alignment beam walk procedure.

The second output of the beam splitter is coupled into a polarization-maintaining single-mode optical fiber connected to a triple-stage spectrometer with a liquid-nitrogen-cooled CCD camera. The polarization-maintaining fiber was chosen over a simple single-mode fiber because of the large distance around 7 m that must be bridged between the optical setup and the spectrometer input. The fiber passes between optical tables and is influenced by ambient temperature changes by a degree that makes the output polarization of a similar plain single-mode fiber drift by more than $\pm\pi$ during the course of a day. Unfortunately, the triple stage of the spectrometer is quite sensitive to input polarization. Therefore, the more expensive polarization maintaining fiber was crucial to get consistent results during long-term measurements.

Spin Noise Spectroscopy Path

When the PL mirror (9) is retracted from the cage system, the beam can instead propagate to the SNS part of the setup. The camera can be moved from the PL part to the cage cube (10) for quick alignment optimizations. Not displayed in Fig. 8.6 is a beam splitter holder and kinematic stage that is used to direct a part of the light to the camera. This beam splitter is also a wedge that is installed in a second custom holder, as depicted in Fig. B.1. Unlike the holder initially intended by the manufacturer, the special shape of the custom holder allows both the beam splitter and the kinematic mount to be removed from the cage cube without disassembling the whole cage system. During measurements, the wedge beam splitter is removed after alignment to not sacrifice a part of the signal from the sample.

Before passing through the Wollaston prism (12), the linear polarization plane of the beam is rotated by $\pi/4$ using a zero-order half-wave retarder (11) installed in a motorized mount²⁷. The prism splits the beam into two mutually orthogonal beams propagating at a slight angle of ≈ 0.052 rad away from each other. The

²⁷Newport Agilis AG-PR100

propagation directions of the output beams are not perpendicular to the ground optical surfaces of the prism. Therefore, the output modes and the stray reflections propagate at different angles, and given enough distance from the prism, the stray reflections can be easily spatially filtered. In the far field that impinges on the photodiodes at the balanced detector²⁸ (15), the contribution of stray reflections is negligible. For this reason, a Wollaston prism can effectively achieve a better channel separation in the output beams than a regular polarizing beam splitter having an anti-reflective coating of the same quality. The two beams are then focused by the lens (13) and aligned onto the photodiodes of the balanced detector by a mirror.

The balanced detector performs best when the powers detected by the two diodes are equal. Changing the magnetic field or scanning over optical inhomogeneities in the sample strongly influences the background birefringence that is experienced by the probe beam, as explained in section §4.2.3. Additionally, temperature changes in the laboratory change the retardance of the half-wave plate. At the large transimpedance gains necessary for SNS, both effects severely impact the balancing and can easily drive the amplifier into saturation. A balancing stabilization loop to counteract these changes was implemented to prevent this from happening. The control loop steers the half-wave retarder to a position where the detected optical power on the two diodes of the detector is equal. The balanced detector exposes the output of the first amplifier stage as a low bandwidth (1 kHz) output. This voltage is proportional to slow changes in the difference photocurrent. It is amplified by an external amplifier²⁹ and used as an error signal for the balancing stabilization loop.

8.3.3 Balanced Photo-Detector

This subsection shortly summarizes some not-so-obvious experimental considerations necessary to achieve optimal performance of high-gain balanced photoreceivers. The main points concern the electrical connections, the shape and temperature sensitivity of the detector's spectral noise floor, and the spectral sensitivity.

²⁸Femto OE-300-S 08-98-006

²⁹Femto DLVPA-100-B-S

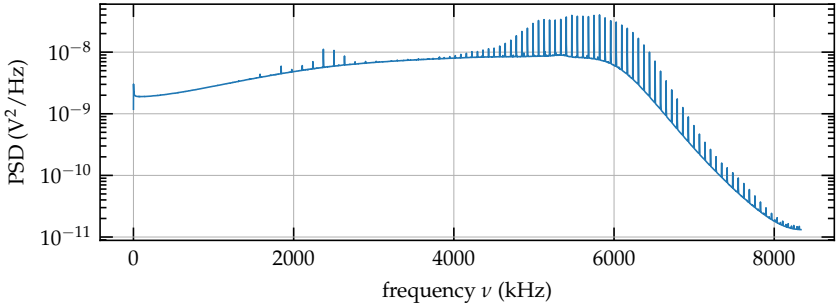


Figure 8.8: Amplified noise floor of the insufficiently grounded Femto 0E-300-S 08-98-006 balanced photo detector. Even though the effective bandwidth is only 3.5 MHz, the noise floor reached well beyond 6 MHz.

Electrical Connections

For noise spectroscopy of single QDs, a balanced photo-receiver with a relatively high trans-impedance gain of at least 1 MV A^{-1} is necessary. At such a large gain, the detector becomes very sensitive not only to the desired signal but, unfortunately, also to outside interference. In particular, switching transients from switch-mode power supplies can be capacitively and inductively coupled into the gain loop of the transimpedance amplifier of the balanced detector. While these transients are usually suppressed by the common mode rejection, they induce oscillations in the amplifier that produce visible artifacts even when no optical power is present on the diodes. Such a “dark spectrum” is depicted in Fig. 8.8 for the balanced photo-receiver³⁰ used in section §8.3.2.

Usually, these artifacts can be significantly reduced by using good quality doubly shielded coaxial cables with a matched impedance of 50Ω to connect the balanced detector, as these are more resistant to capacitive coupling than regular cables. Furthermore, a star-like grounding scheme has to be implemented, and the detector has to be grounded with a low-impedance wire to prevent common mode injection of transients through grounding loops. Moreover, it is also advisable to put the worst offenders (i.e., high-power AC inverters) on a separate circuit or to isolate them from the laboratory grid by line filters.

³⁰Femto 0E-300-S 08-98-006

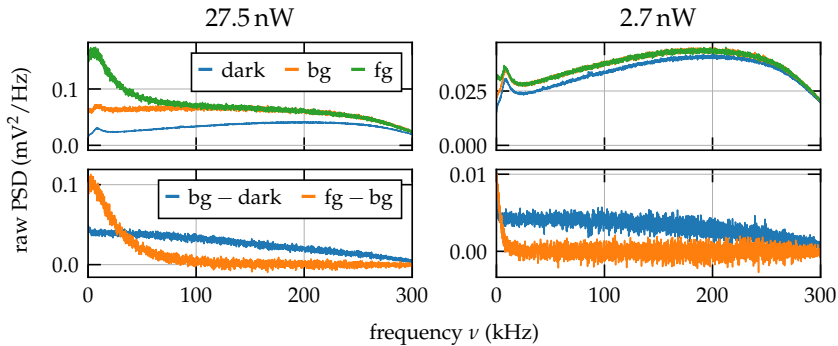


Figure 8.9: Decomposition of raw PSD difference spectrum for two probe laser powers: (dark) the electrical noise floor, (fg) foreground and (bg) background spectra. The difference (bg – dark) is the distorted estimate of the photon shot noise, while (fg – bg) is the distorted estimate of the Kerr noise signal.

Noise Floor and Sensitivity

Fig. 8.8 reveals that the shape of the noise floor does not always coincide with the amplification bandwidth of 3.5 MHz used for this example, which corresponds to the gain setting of 1 MV A^{-1} . The reason is that the amplifier’s internal noise is amplified differently than the input signals, as explained in section §3.3. Therefore, it is *very wrong* to assume that the amplification bandwidth of the detector can serve as a sufficient anti-aliasing filter. On the contrary, for the 220 kHz/ 10 MV A^{-1} setting of the detector, the excess noise will get aliased up to several times into the useful bandwidth of the detector when an improper anti-aliasing filter is used.

With light on the diodes, the detector’s spectral sensitivity determines the shape of the noise floor. The spectral sensitivity can be estimated by comparing the PSD of a known source with its experimental spectrum. For optical noise spectroscopy at frequencies from a couple of Hz to several THz, such a reference is the laser field’s frequency-independent optical photon shot noise. The electrical noise that contributes to the noise floor of the detector is not correlated to the laser shot noise, and the pure optical noise density can be extracted from raw data by subtracting the dark spectrum, as explained in section §3.3.

For a perfect detector, the resulting shot noise PSD spectrum would have, on average, the same magnitude for any frequency. In reality, experimental shot noise

spectra are usually not flat, and their envelopes roughly correspond to the amplifier bandwidth, as Fig. 8.9 depicts. This envelope defines the spectral sensitivity of the setup as any optical signal above the dark spectrum will be scaled the same way. Hence the distortion imposed by the amplifier bandwidth can be removed from the spectrum estimate by dividing a spectrum by the spectral sensitivity, as explained later in more detail in section §11.3.

Unfortunately, the detector's electrical noise floor depends on the ambient temperature. Over the course of days, even small temperature drifts in a temperature-stabilized laboratory can shift the noise floor amplitude on the order of the tiny signals of interest. This effect becomes particularly severe for the used detector at very low optical powers, i.e., below 3 nW at 900 nm. For this reason, for the majority of measurements presented in Part IV, a protocol was implemented whereby a mechanical shutter blocked the probe laser, and a dark spectrum was recorded automatically before each measurement run (i.e., a detuning of intensity dependence recorded in a single go).

The variance of the mean spectral estimates depicted in the lower panels of Fig. 8.9 appears to be constant within the majority of the detector bandwidth. This perfectly agrees with the theoretical prediction from section §3.3, as depicted, for example, in Fig. 3.3. The observed variance of the difference spectra is given by the sum of the variances of the two involved spectra. As the Kerr signal is not the major contribution at almost all frequencies, the true variance of the signal is not observable in these regions.

8.4 Other Control Servers

This section quickly mentions some of the other control servers implemented for the setup. More thorough documentation can be found in the respective project's repository.

8.4.1 Power and Balance Regulation

The setup uses several Agilis motorized stages by Newport to control the balancing or orientation of half-wave readers and other optics. The corresponding controllers can control up to two motorized stages. Unfortunately, the manufacturer did not provide a means to control the individual channels independently, so only one program could control both axes. However, in the setup, these channels

serve very different control loops that must run uninterrupted and completely independent of each other (for example, power stabilization and balancing of the detector). This was not possible in the original architecture. Besides, an improperly handled crash of the control script would leave the controller in a locked state. For this reason, a sever³¹ was implemented that abstracted over the attached controllers and the corresponding channels. This implementation allowed the control loops to reliably run decoupled from individual controllers and even computers, as the server is accessible over the laboratory network.

8.4.2 Matisse Controller: Ring Laser Control

A *Matisse* TX continuous-wave ring laser system by Sirah was used as the laser source for the setup. This incredibly well-built laser can be locked to a tunable reference cavity and can then be scanned along with the cavity for up to 60 GHz. The locking procedure is straightforward but somewhat indeterministic. A locking algorithm is implemented in the original LabView-centric software provided with the laser. However, the software did not expose the algorithm and the full scanning controls for automatized measurements.

Fortunately, the manufacturer provided the source of the LabView program. This allowed the algorithm to be reimplemented and improved in Python. The resulting program exposes a minimalist server interface that can be accessed over the laboratory network by scripts running the experiment to monitor the laser state, lock, and scan it to the desired frequency. This arrangement allowed most of the measurements to be performed automatically, maximally utilizing the precious experimental time on a closed-cycle cryostat and preventing transcription errors previously unavoidable in manual measurements.

³¹RsAgilator

Part IV

Non-equilibrium noise spectroscopy of a single QD

9 Preliminary Remarks

In this chapter, the general properties of the investigated QD material system are highlighted. First, section §9.1 serves as a review of theoretical properties. Then, section §9.2 discusses preparation measurements on the used sample and the selection and characterization process for the QD used the long-term measurements.

9.1 (In,Ga)As Quantum Dots

Indium gallium arsenide ((In,Ga)As) QDs belong to the class of self-organized hetero-structures that are composed of two III-V semiconductors with different band gaps. A tiny encapsulated island of the semiconductor with the lower band gap (indium arsenide, InAs) provides a potential well that traps free charges from the surrounding higher band gap semiconductor (gallium arsenide, GaAs). Below a specific island size, the band structure experienced by trapped charge carriers changes significantly compared to the initial bulk material. Usually, the height of the island, that is, its extent in the growth direction z , is much smaller than its width. Confining a charge carrier in one direction below its De-Broglie wavelength leaves it free to move in the perpendicular plane, but its energy in the restricted direction becomes discrete. A narrow quantum well of finite depth can model this situation. For the investigated QDs, the potential well is not very deep and can accommodate only a single energy sub-band in the growth direction [97]. Further restricting the lateral dimensions of the island results in an oblate-shaped object. The lateral confinement potential of this object can be modeled by a radially symmetric (or ellipsoid) harmonic potential with well-known solutions that have discrete energies. Effectively, the QD confinement collapses the quasi-continuous density of states of bulk charge carriers to a zero-dimensional discrete one.

9.1.1 Manufacturing

(In,Ga)As QDs are manufactured using the molecular beam epitaxy (MBE) [120] growth technique. This technique ensures a mono-crystalline growth of layers of

different semiconductors on top of each other. The growth must happen in an ultra-high vacuum chamber to prevent impurities from disturbing the process. The substrate is mounted on a heated rotation stage above heated effusion cells. From the effusion cell, individual atoms of the grown semiconductor cross the vacuum and settle on the substrate forming chemical bonds. Surface diffusion eventually leads to the formation of a homogeneous monolayer of the grown semiconductor. Usually, the growth is controlled by monitoring the intensity of a high-energy electron beam refracted by the grown surface (RHEED). The reflected intensity is maximal whenever a complete mono-crystalline layer is formed. This feedback allows the lattice to be grown with sub-monolayer accuracy [121].

The growth of QDs is performed in the so-called Stranski-Krastanov mode [122, 123] on top of a mono-crystalline GaAs layer. InAs has a $\approx 7.2\%$ larger lattice constant than GaAs. When the first InAs or InGaAs layer is grown, the mismatch between the lattice constants leads to a layer with an intermediate lattice constant. In this newly formed layer (the wetting layer), the lattice constant mismatch is translated into internal strain. Further growth above a critical thickness of $\approx 1.5 - 1.7$ monolayers results in spontaneous relaxation of this accumulated strain and formation of nm scale droplets of InAs [124]. Subsequently, a GaAs capping layer is grown on top of the InAs droplets to produce fully encapsulated InAs islands forming a potential well structure. The encapsulation also protects the QDs from further chemical reactions and the influence of surface states. Furthermore, annealing steps can be used to determine the exact size and composition of the islands through controlled diffusion of In out and Ga into the islands. These annealing steps [125] reduce the QD size and correspondingly shift the transition energies of optical resonances above 1.23 eV (below 1000 nm). The resulting lens-shaped QDs consist of $\approx 1 \times 10^5$ atoms and have a diameter of $\gtrsim 15$ nm and a height $\lesssim 5$ nm [97, 42].

9.1.2 The Quantum Dot *s*-Shell

The discrete states of a QD are constructed from continuum bulk states of the initial semiconductors and inherit the properties of these bands. For (In,Ga)As QDs, the two involved semiconductors have a direct band gap at the crystal's high symmetry Γ point, and the QD confinement potential is consequently also located at the Γ point. Therefore the discrete electron states are composed of the *s*-like conduction band, while the hole states are composed of the heavy and light hole bands

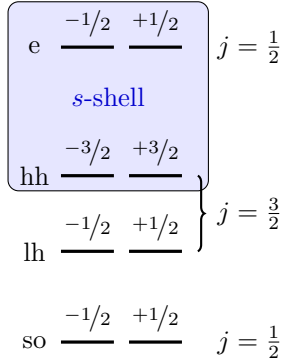


Figure 9.1: Construction of the QD s -shell. The continuum states in the shaded box are the dominant contributions to the QD electron and hole states.

and the split-off band. The split-off band is located > 300 meV below the other two bands, and its contribution is usually disregarded because of that. The p -like heavy and light hole bands are usually degenerate, but strain and the QD confinement open a gap ΔE_{LH} of up to 100 meV [126]. In particular, the confinement of the QD shifts the continuum light hole states below the heavy hole states [97]. Aside from the different effective masses, heavy hole and light hole states are characterized by their orbital angular momentum projection of $j_z^{(\text{hh})} = \pm 3/2$ and $j_z^{(\text{lh})} = \pm 1/2$, respectively. Depending on the size of the gap, the QD hole states have a varying admixture of the light hole states. For the lowest possible energy states in a radially symmetric QD, the gap is sufficiently large to assume the QD hole states as purely heavy and treat the admixture of light hole states perturbatively.

The eigenenergies of the electron and hole states in the harmonic potential can be enumerated using $m, n = 0, 1, 2, \dots$:

$$E_{m,n}^{\text{e,h}} = \hbar\omega_{\text{e,h}} (1 + m + n).$$

In analogy to atom physics, the corresponding states can be classified using the possible values for the z -component of the angular momentum $\pm(m+n)$. This classification defines the shell structure of the QD using the mapping $(m+n=0) \equiv s$, $(m+n=1) \equiv p$, and so on. The s -shell is the most important for (In,Ga)As QDs as it has the largest separation from the light hole and the continuum states. The composition of the higher shell states is more complicated, as the energetic prox-

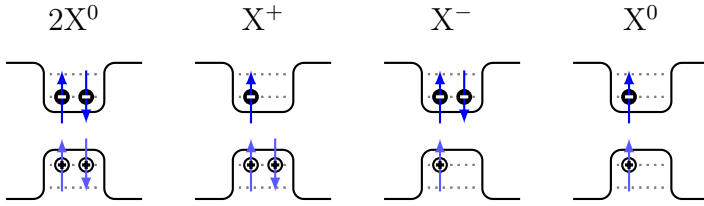


Figure 9.2: Possible exciton states in the quantum dot (QD) s -shell: biexciton $2X^0$, positive trion X^+ , negative trion X^- , and the neutral exciton X^0 .

imity to the other state makes them more sensitive to the morphology of the QD. Higher shell states usually decay toward the s -shell on ps time scales [97].

The s -shell consists of two electron and two hole states characterized by the possible z -component values of their angular momentum. For the electron, these projections correspond to the electron spin up and down states with $m_z^{(e)} = \pm 1/2$. The energy splitting between the continuum light hole states with $j_z^{(lh)} = \pm 1/2$ and the heavy hole states with $j_z^{(hh)} = \pm 3/2$ results in QD hole states that effectively behave as a particle with only two pseudo-spin states with $m_z^{(h)} = \pm 3/2$ [97, 42]. The properties of this particle and its pseudo-spin are the main targets of the experimental investigation performed in the following chapters.

9.1.3 Excitonic Resonances

The optical transition inherited from the bulk semiconductor structure allows a photon of appropriate energy to be absorbed by the QD to create an electron-hole pair inside the s -shell. The necessary transition energy is approximately given by the direct band gap reduced by the total binding energies of the charge carriers. Alternatively, free excitons, that is, electron-hole complexes bound by the Coulomb interaction, created in the bulk material by above-band-gap photons, can relax into the confinement potential of the QD. In both cases, the result is an exciton state *bound by the confinement potential* of the QD. The electron-hole pair in the s -shell can subsequently recombine, emitting a photon with an energy and a polarization characteristic to the exciton state. Therefore, resonance fluorescence (RF) spectroscopy and PL spectroscopy can be used to investigate the structure of the bound exciton states that determine the optical properties of the QD.

The possible QD exciton complexes allowed by the Pauli-exclusion within the

s -shell are sketched in Fig. 9.2. The neutral exciton X^0 and the biexciton $2X^0$ are possible for a nominally neutral QD. These configurations correspond to one or two electron-hole pairs trapped in the QD. A charge reservoir, a donator, or an acceptor atom near the QD can provide a charge carrier that permanently occupies the s -shell. In that case, the trion states X^\pm are formed from an electron-hole pair and the resident charge carrier. Moreover, non-equilibrium charge configurations during above-band-gap excitation can temporarily charge the QD and enable the trion transition. The larger binding energy the confinement provides makes these charge complexes significantly more stable than similar free trions [97].

For (In,Ga)As QDs, the charge carrier wave functions are significantly larger than the lattice constant, and their exact shapes depend on the QD morphology. The spatial overlap between these charge carrier wave functions determines the Coulomb attraction or repulsion strength between the charge carriers present in the QD s -shell. Usually, the Coulomb interaction results in a smaller correction term (≈ 10 meV [127]) than the energies given by the confinement potential (*confinement effect*). Therefore, the shape of QD and the overlap of the wave functions determine the magnitude of these correction terms. Therefore, no generally valid ordering of the transition energies of the possible exciton states can be provided [56].

9.1.4 Fine Structure of Excitons

The following investigation is performed on a sample slightly p -doped with carbon impurities (ionization energy ≈ 20 meV [129]). Therefore the most relevant excitonic resonances are the positively charged trion X^+ and the neutral exciton X^0 . These transitions are sketched in Fig. 9.3.

Neutral Excitons

The fine structure of the neutral exciton is determined by an additional electron-hole exchange interaction that couples the electron and hole spins. The possible states of the neutral exciton can be enumerated using the z component of its total angular momentum $M_z = m_z^{(e)} + m_z^{(h)}$. Of the resulting four states, the *dark* $M_z = \pm 2$ states cannot be optically addressed under normal circumstances, as photons can only transmit an angular moment equal to their helicity ± 1 . The optically addressable *bright* $M_z = \pm 1$ states depend on the QD symmetry. They are

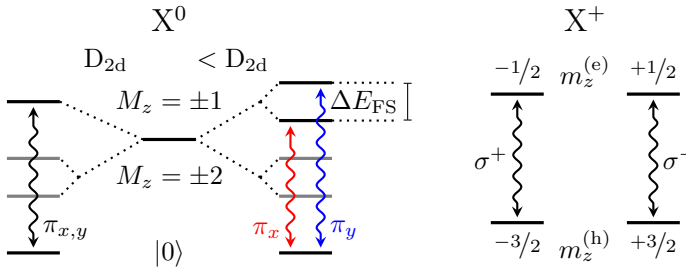


Figure 9.3: Fine structure of the QD exciton states (changed from [128]) and the possible optical transitions in absence of magnetic fields. Left panel: reduced symmetry lifts the degeneracy of the bright exciton states by the fine structure splitting ΔE_{FS} . Two linear transitions of slightly different transition energy can be observed in this case. Right panel: the trion states are a one-to-one mapping of the s -shell states and stay degenerate regardless of the QD symmetry. Two energetically indiscernible circularly polarized transitions can be observed.

given by the superpositions $\sqrt{1/2} (|M_z = +1\rangle \pm |M_z = -1\rangle)$. For a QD with a perfect D_{2d} symmetry, these states are degenerate, while lower symmetries result in a *fine structure splitting* $\Delta E_{\text{FS}} \gtrsim 10 \mu\text{eV}$ between them [128]. The two bright superposition states decay, emitting mutually orthogonally linearly polarized photons, as sketched in the left panel of Fig. 9.3. The orientation of these polarizations depends on the QD shape and does not have to coincide with high symmetry axes of the surrounding crystal lattice [130].

Trions

The trion state is particularly interesting as the s -shell is saturated for one charge carrier type. For the X^+ , this forces the hole spins to form a pseudo-singlet state with a total angular momentum of 0 [97]. The remaining electron spin states with $m_z^{(e)} = \pm 1/2$ determine the fine structure of the trion transition, as the spin does not interact with the singlet. Effectively, the charged ground states and the excited trion states provide a one-to-one mapping of the s -shell states. This mapping results in an atom-like four-level system with a twofold degenerate ground and excited states without external magnetic fields [42]. Remarkably, the ground and excited states stay degenerate even if the QD has a reduced symmetry, as the asym-

metry does not translate into an asymmetry between the spin-up and spin-down states.

Optical dipole selection rules enforcing momentum conservation apply strictly for a QD with sufficiently pure heavy hole ground states. In this situation, trions decay by emitting a circularly polarized photon. Only the vertical transitions within the four-level system are allowed, as indicated in the right panel of Fig. 9.3. When the admixture of light hole states is significant, this simple picture applies only approximately. Then $m_z^{(h)}$ is no longer a good quantum number, and normally forbidden diagonal transitions become possible. Similarly, a magnetic field misaligned with regard to the growth axis can enable diagonal transitions [131].

Magnetic Fields

Magnetic fields modify the fine structure in two ways. (The magnetic field is applied strictly parallel to the growth axis (z) for simplicity.) First, the degeneracy between spin states is lifted by a Zeeman splitting. This splitting depends on the magnitude of the magnetic field B_z and the effective exciton Landé factor $g_{\text{eff.}} = g_h + g_e \cdot \Delta E_Z = g_{\text{eff.}} \mu_B B_z$, where μ_B is the Bohr magneton. The second effect of the magnetic field is magnetic confinement, sometimes referred to as *diamagnetic squeezing* [126]. The motion of charges perpendicular to a magnetic field is restricted to circular Landau orbits. This restriction acts as an additional parabolic confinement potential with discrete energy levels (Landau levels). For the QD states, this additional effect results in correction terms proportional to the square of the magnetic field amplitude B_z^2 [132]. A large enough magnetic field can improve the radial symmetry of the QD through a stronger effective confinement potential [128]. Therefore, the diamagnetic shift observed in transition energies at large magnetic fields can be slightly different for neutral and charged excitons from the same QD if the initial confinement is not very strong [132].

9.1.5 Spin Relaxation

As explained above, for a positively charged QD, the four-level system consists of a pair of excited spin and a pair of pseudo-spin ground states. The ground state pseudo spin states behave like spin $1/2$ states, albeit with a larger angular momentum. Therefore, the electron spin and the hole pseudo-spin can be described using the Bloch formalism introduced in section §4.2.1. The empiric Bloch equations

implicitly assume an exponential decay of the spin in the two directions defined by the $1/T_1$ and $1/T_2$ rates. This assumption is not generally valid for all spin possible systems [97]. Moreover, the microscopic decay mechanisms in semiconductors can have a rich structure that these two relaxation rates alone cannot fully describe. Nevertheless, relaxation through these microscopic mechanisms usually can be reduced to approximate relaxation and dephasing rates that can be measured in an experiment [133].

The main spin relaxation channels for free charge carriers in semiconductors are the Elliott-Yafet, the D'yakonov-Perel, and the Bir-Aronov-Pikus mechanisms [133]. These relaxation mechanisms do not directly apply to the localized charges in the investigated QD system. Consequently, the spin relaxation times for charges localized in a QD can be several orders of magnitude longer than for free charge carriers. However, charge carriers provided by the environment that recharge the QD can be effectively considered free. Therefore, recharging by free carriers has an important implication for the observed (as opposed to the intrinsic) spin relaxation rate of the resident spin in the investigated QDs. At time scales relevant to the confined spin, the spins of charge carriers provided by the environment are perfectly incoherent. Therefore the observed relaxation rate of the confined spin is susceptible to tunneling or some other charge transfer between the QD and its environment. Even a minute tunneling rate between the environment and the QD will be mapped one-to-one onto an additional observed spin relaxation rate. Two possible relaxation channels are introduced below in section §9.1.6.

In particular, the spin relaxation rate is quite efficient for free holes due to the mixing of spin states from the degenerate heavy and light hole bands. This mixing usually results in relaxation times on the order of \approx ps [134]. In systems with a lifted degeneracy between the hole bands, a spin flip between the heavy hole $m_z^{(h)} = \pm 3/2$ states is only possible using higher-order processes involving three photons, for example. These processes have a very low probability and become even less likely at low temperatures [97]. This argument also applies to QD hole spins.

Hyperfine Interaction

In the absence of bulk spin relaxation mechanisms, the confined spin is left to interact with a fluctuating bath of nuclear spins of the surrounding atoms through the *hyperfine interaction*, the dominant mechanism for localized charge carriers. All

of the stable isotopes of the 1×10^5 to 1×10^6 atoms within the envelope of the QD carrier wave functions carry a nuclear spin: Ga: $3/2$, In: $9/2$, As: $3/2$. For the investigated charged QDs, the excited states exhibit an electron spin, while the ground states exhibit a hole pseudo-spin. Therefore, the interaction of both charge carrier species with the nuclear spin bath has to be considered. Such a situation where a single charge carrier spin interacts with a bath of weakly interacting nuclear spins is usually treated in the framework of the *central spin problem* [47].

The hyperfine interaction contains two main parts whose magnitude is different for electrons and holes due to their different wave functions: the *Fermi-contact interaction* and the usually an order of magnitude weaker *dipole-dipole interaction*. The Fermi-contact interaction is effective when the wave function has a significant amplitude at the locations of the nuclei, as is the case for the *s*-like wave function of QD electrons. On the contrary, holes have a *p*-like wave function that vanishes at the locations of the nuclei. Therefore, for holes, only the weaker dipole-dipole term is of significance [135]. Moreover, pure heavy hole states have their magnetic moment aligned in the growth direction *z*. This results in a strongly anisotropic “Ising”-like interaction that is not sensitive to in-plane (*xy*) components of the nuclear magnetic moments [47, 42].

Within a mean field approximation, the effect of hyperfine interaction on the charge carrier spin can be interpreted as a randomly fluctuating magnetic field \mathbf{B}_N , the Overhauser field. The *magnitude* of this field is normally distributed with a characteristic width ΔB_N . In some measurements, the fluctuations of \mathbf{B}_N can be directly observed as the nuclear spin noise [55]. The nuclear magnetic field has different effects on fast and slow time scales. On short time scales, the Overhauser field appears frozen because the dynamics of nuclei are much slower than the dynamics of the central spin. The width of the randomly distributed nuclear field results in a corresponding distribution of Larmor precession frequencies. This variation in precession frequencies results in an observable inhomogeneous *spin dephasing* rate $1/T_2^*$ for QD ensembles or repeated measurements of the same QD. The inhomogeneous spin dephasing rate $1/T_2^*$ is usually much greater than the intrinsic *spin dephasing* rate $1/T_2$ and the intrinsic *spin relaxation* rate $1/T_1$. In some contexts, the increased inhomogeneous dephasing can be considered reversible, as the intrinsic $1/T_2$ rate masked by the $1/T_2^*$ rate can be recovered by performing a Hahn spin echo experiment [136]. On longer time scales, the Overhauser field contains fluctuations $\delta \mathbf{B}_N$ that are perpendicular to \mathbf{B}_N . These slow fluctuations result in an additional relaxation that irreversibly increases the intrinsic spin relaxation

rate $1/T_1$ [137, 47].

Spin Relaxation in External Magnetic Field

For the investigated QD system, the magnitude of Overhauser field fluctuations acting on electrons, $\Delta B_N^{(e)}$, is estimated to be approximately 30 to 57 mT [135, 47]. The corresponding value for holes, $\Delta B_N^{(h)}$, can be as low as ≈ 4 mT [138]. However, the exact value depends on the purity of QD heavy hole states in each particular dot, as light hole admixture influences the anisotropy of the hyperfine interaction. Both values are quite small and can be easily overcompensated by an external magnetic field \mathbf{B}_{ext} .

In this configuration, the Zeeman splitting of the confined spin is given by the total magnetic field $\mathbf{B} = \mathbf{B}_{\text{ext}} + \mathbf{B}_N$, where the magnitude of the external field \mathbf{B}_{ext} is greater than $\Delta B_N^{(e)}$. The relative contribution of \mathbf{B}_N to the Zeeman splitting is low and acts only as a perturbation. For electrons in general and holes when $\mathbf{B}_{\text{ext}} = B_{\text{ext}} \mathbf{e}_z$, this results in a pure dephasing of the spin components transverse to \mathbf{B}_{ext} [126], as spin relaxation is *suppressed* along the direction of \mathbf{B}_{ext} [137]. In principle, pure heavy hole spins are insensitive to in-plane fluctuations of \mathbf{B}_N . It is predicted that the dephasing should be greatly reduced for such a spin when a strong in-plane magnetic field is applied [126]. However, the purity of the heavy hole state varies between different QDs due to growth imperfections. Admixture of light-hole states to the hole pseudo-spin reduces the anisotropy of the hyperfine interaction and makes it more similar to the electron case [135].

Spin-Orbit Coupling Mediated Relaxation

For pure heavy holes in an out-of-plane magnetic field, long spin relaxation times ($> 180 \mu\text{s}$) can be achieved already at fields as small as 10 mT [72]. With the dominant relaxation mechanism suppressed, other relaxation mechanisms come to the fore and can be observed. For the considered QDs, the relaxation rate is theoretically predicted to be limited by acoustic phonons [139]. Acoustic phonons cannot directly interact with the spin [140] but they can deform the QD or apply piezoelectric fields. These effects modify the spin-orbit coupling of the bands from which the QD spin states are formed. The modified spin-orbit coupling mixes bands and creates a relaxation channel for the confined QD spin [141]. Relevant contributions can be provided by bulk inversion asymmetry through a Dresselhaus coupling, by structure inversion asymmetry through Rashba coupling, or by

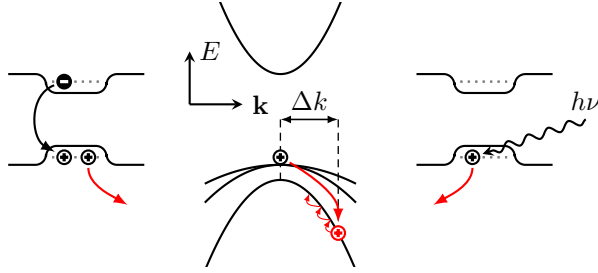


Figure 9.4: Incoherent charge loss channels: Auger recombination on the left and internal photoeffect on the right. The central panel depicts a sketch of the subsequent hot hole cool down. (adapted from [143])

coupling between the heavy and light hole states [141].

Initial modeling considered only one phonon relaxation [141]. However, these predictions are valid only at large magnetic fields above several T. At lower magnetic fields, the relaxation rate saturates at a value on the order of $\approx 100 \mu\text{s}$ instead of falling toward much lower values [142]. Therefore, the theory was extended to include a two-phonon channel that is expected to dominate the relaxation at low magnetic fields [140].

9.1.6 Incoherent Charge Dynamics

The stability of the charge state of the QD is subject to two nonradiative processes that are similar to ones in atom physics and are hence named as such: Auger recombination and internal photoeffect. Both processes are depicted in Fig. 9.4. These processes eject the resident hole¹ from the QD confinement into the surrounding continuum even if the excitation is performed using quasi-resonant below-band-gap photons. Auger recombination acts on the excited trion state, while the photoeffect acts on the ground state. In both cases, the kinetic energy of the hole is increased by an amount that is much larger than the QD confinement. The resulting hot hole subsequently cools down through multi-phonon relaxation on a time-scale of ps or faster [143]. These processes are unlikely in bulk semiconductors because energy and quasi-momentum have to be conserved, as indicated in the central panel of Fig. 9.4. Therefore, the probability of the process would depend on the availability of an additional phonon necessary to accommodate the wave vector

¹the same applies to electrons, of course

change Δk . On the contrary, the quasi-momentum is not a well-defined quantity in nanoscale objects like QDs, and these processes become possible [144, 145, 60].

While the hole remains free, its spin is subject to very efficient spin relaxation mechanisms for free charge carriers. The spin coherence is lost, even if the hole eventually returns to the QD after shedding the excess energy. Therefore, from the spin point of view, these mechanisms can be empirically considered as additional spin relaxation channels.

The coupling of the QD to a reservoir of holes in its environment determines the recovery time for the charge state. This recharging rate can be controlled by placing a highly doped layer in the proximity of the QD or by using a PIN structure with electrical contacts [60]. The thickness of the barrier between the reservoir and QD determines the tunneling rate and hence the recharging rate of the QD. While a fast recharging rate ensures that the QD stays charged, efficient tunneling simultaneously allows the hole to tunnel out and back into the QD, resulting in an additional spin relaxation mechanism [146].

Auger Recombination

Auger recombination is an alternative non-radiative decay channel for the trion. When the electron-hole pair recombines, no photon is produced. Instead, the transition energy is transferred to the residual hole, as depicted in the left panel of Fig. 9.4. An efficient Auger process can quench the optical transition, as observed in colloidal quantum dot systems [147]. For (In,Ga)As QDs, this process was long believed to be irrelevant. However, recent two-color experiments that probed both the trion and the neutral exciton resonances at once demonstrated that the Auger process is present in self-organized QDs [60, 61].

Internal Photoeffect

The emission part of the internal photoeffect is conceptually similar to Auger recombination. However, no excited state is necessary, and the hole is ejected directly from the ground state. Therefore, the photoeffect has no dependency on the photon energy as long the hole acquires enough energy to leave the QD confinement. In particular, the photoeffect can be initiated by photons with energies smaller than all optical band-to-band transitions [64]. The probability of ejecting the charge carrier depends only on the number of available photons and the

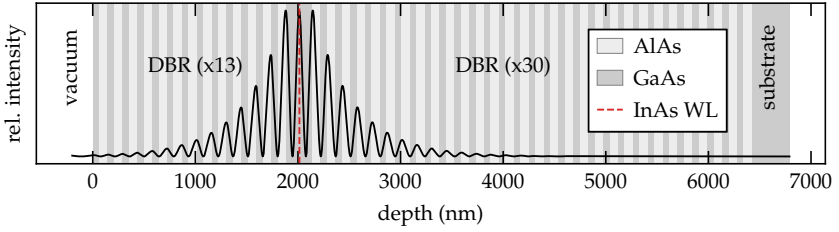


Figure 9.5: Simulated intensity distribution within the micro cavity calculated using the transfer matrix method [148]. The dashed red line indicated the location of the quantum dots (QDs) and the wetting layer (WL).

recharging rate of the QD, which results in a linear dependence on photon intensity [63].

Another consequence of the photoeffect is that it can act not only on the QD but also on the reservoir that provides the charge to the QD. Consequently, charges ejected from the reservoir can contribute to the recharging rate of the QD, causing a reappearance of the trion transition in an otherwise neutral QD [63]. Again, this cycling of the hole between QD and the reservoir results in a spin relaxation channel, as described above.

9.2 QD Sample

For the long-term experiment, the same sample² is used as previously by Dahbashi [149] and Wiegand [67], initially provided by K. Pierz (PTB Braunschweig). This MBE-grown sample contains an embedded layer of (In,Ga)As QDs. The wetting layer's thickness must be within a narrow window (see above). Below the critical point, no QDs are formed, while above the critical point, the QD density quickly becomes too large to resolve individual dots optically. For on-off samples, an alternative approach is to deposit the wetting layer without rotating the wafer. Because the effusion cell is located to the side of the wafer, the lack of rotation results in a gradient. Subsequent PL spectroscopy can then be used to determine a region with the desired QD density. The wafer piece used in this work comes from a region where the QD density transitions between ≈ 0.1 to ≈ 10 per μm^2 .

Residual carbon impurities provide a p-type doping of approximately

²P911

$1 \times 10^{14} \text{ cm}^{-3}$ in the GaAs barrier material. This low doping level is determined mainly by unavoidable hydrocarbon contamination of the MBE chamber. Samples with such low doping are usually referred to as undoped. However, this doping is sufficient to charge a significant fraction of the embedded QDs with a single hole that can be used in the experiment.

Moreover, the sample has a distributed Bragg reflector (DBR) grown below and above the GaAs barrier material containing the QD layer, as Fig. 9.5 indicates. The top (bottom) mirror consists of 13 (30) $\lambda/4$ layer pairs of GaAs and AlAs. This configuration results in a low finesse microcavity that allows measurements in reflection geometry. The microcavity is also grown with a gradient rotated $\pi/2$ relative to the QD gradient. This alignment ensures that a sweet spot exists on the sample, where the resonance frequency of the microcavity corresponds to the transition energy of the QDs. A more in-depth investigation of the optical properties of this sample can be found in Refs. [150, 149, 67] and the discussion in section §11.2.

The intensity distribution inside the microcavity can be simulated using the transfer matrix method [148]. A qualitative curve using the nominal design parameters is depicted in Fig. 9.5 for photon energies at the resonance condition. Material parameters from [151, 152] are used for this simulation. The correspondence is only qualitative for two reasons. First, the simulation does not account for absorption in the DBR layers because this sample's exact values are unknown. Second, the gradient growth results in uncertainties of the individual layer thicknesses. The exact values can be determined using, for example, energy-dispersive X-ray analysis of the cross-section of the sample. However, this method is destructive and, therefore, not viable in this case.

9.2.1 QD Selection

First, the sample is imaged using a regular microscope using an intermediate magnification, and the pictures are stitched together. A low-resolution version of the map is depicted in the background of Fig. 9.6. Imperfections and scratches on the sample surface serve as natural location markers in the resulting map. Any position on the sample can be approached using these markers with an accuracy of $\approx 10 \mu\text{m}$ given by the closed-loop steppers of the sample insert. For finer alignment, the investigated regions are scanned under above-band-gap excitation, and the resulting photoluminescence is analyzed with a single stage of the triple-stage spectrometer. The resulting luminescence hyper-spectral maps display the posi-

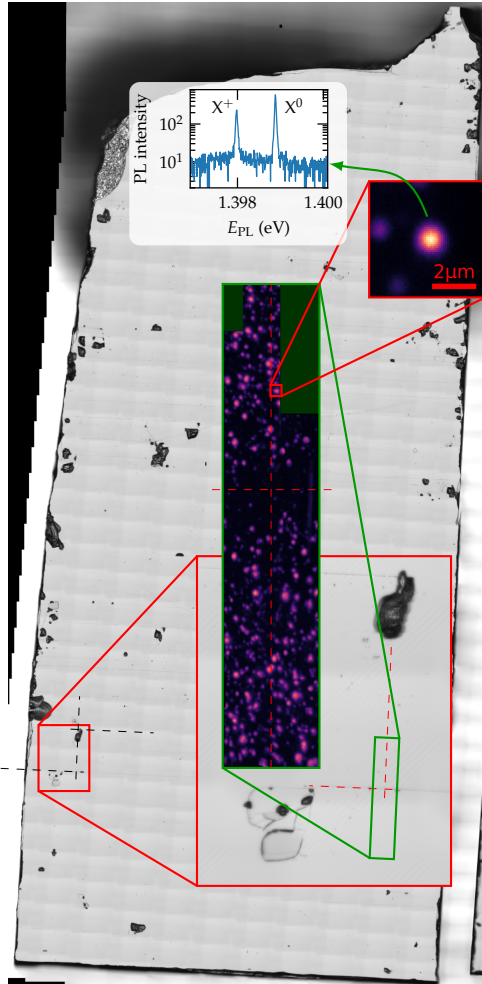


Figure 9.6: Stitched map of sample P911. The insets depict the gradual zoom in toward the investigated quantum dot (QD) by exploiting the self-organized markers (lines) and imperfections (scratches) on the sample surface. Colored maps depict photoluminescence (PL) hyper-spectral maps recorded using the scanning confocal microscope in the sample insert. The last inset depicts the PL spectrum at the QD site.

tions of the QDs and allow a specific QD to be approached with a sub μm accuracy, as demonstrated by the inset in Fig. 9.6. Note that the depicted size of the spot in this last inset is approximately two times larger than the diffraction limit of the used objective. This effect is caused by the divergence of the laser mode in the planar microcavity. The QD is approximately two orders of magnitude smaller than the laser mode. Therefore, the observed shape is almost purely given by the resolution of the confocal microscope.

A quantum dot with a large energy splitting between the neutral exciton and trion states is selected for further investigation. When the charge state of the QD fluctuates due to the Auger effect or the photoeffect, the QD alternates between these two transitions and can produce a detectable noise signal at either resonance. Therefore, a QD with a large splitting of $\approx 758 \mu\text{eV}$ between the exciton resonances is selected to separate the contributions as well as possible for magnetic fields below $\approx 4 \text{ T}$.

The second criterion is the long-term charge state stability of the QD. During the preparations for the long-term measurement, the sample was repeatedly cooled down and was allowed to warm up again. These cool-down cycles provided an opportunity to observe the stability of the charge state of QDs in several regions of the sample. The accuracy of the scanner and stepper combination, in conjunction with luminescence maps, allows repeated characterization of the same QDs in these regions. The charge state is unstable, particularly in the immediate vicinity of the sample edges, and the luminescence between different cycles changes significantly. The selected QD is located far enough away from the edge of the sample and has exhibited no changes in its charge state or luminescence spectra between the preparation cycles.

9.2.2 Photoluminescence Spectroscopy

For the selected QD, more information can be gained using photoluminescence spectroscopy by using all three stages of the spectrometer. The additional stages absorb some light and reduce the count rate of the liquid-nitrogen-cooled CCD camera. However, the increased resolution reveals the substructure of the neutral exciton resonances.

First, using the setup's polarization-resolved stage, the fine structure splitting of the neutral exciton can be determined. Fig. 9.7 depicts the recorded spectra for two orthogonal analyzer orientations. The orientation of these directions is chosen

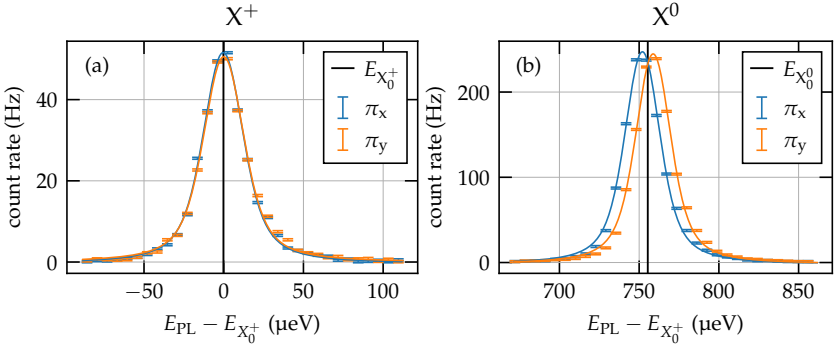


Figure 9.7: Polarization resolved photoluminescence spectroscopy of the investigated quantum dot (QD) at $B = 0$ T. Panel (a) depicts the spectra for the trion (X^+) resonance, while panel (b) depicts the spectra of the neutral exciton (X^0) resonance. In both panels fits of a Voigt model function to the experimental data are plotted using solid lines of the same color.

by maximizing the observable splitting of the peaks. This orientation of the two linear polarizations is *not* the same for QDs on the sample and has to be determined individually. This step is essential, as a resonance with its polarization axes rotated by $\pi/4$ with regard to the analyzer axes can appear to have no splitting or a splitting significantly smaller than the actual value. The results of fitting Voigt profiles to the recorded spectra are summarized Tab. 9.1.

For the lower energy resonance depicted in panel (a) of Fig. 9.7, no splitting is detectable within the resolution of the measurement. A minor splitting is detectable for the higher energy resonance depicted in panel (b). This splitting is slightly smaller than the typical $\gtrsim 10 \mu\text{eV}$, a sign of a QD with high radial symmetry. The lower and higher energy resonances can be identified as the trion and the neutral exciton resonances, respectively, using information from previous measurements performed on this sample [149, 67]. The ordering of the resonances is flipped when compared to theoretical calculations. The trion resonance is expected to have a higher transition energy. However, this discrepancy can be explained if the hole wave function is larger than the electron wave function [56].

In the second step, photoluminescence spectra are recorded while an external magnetic field along the growth direction (z) is systematically scanned from -1 T to 6 T using a long integration time for each step. Fig. 9.8 depicts a symmetric

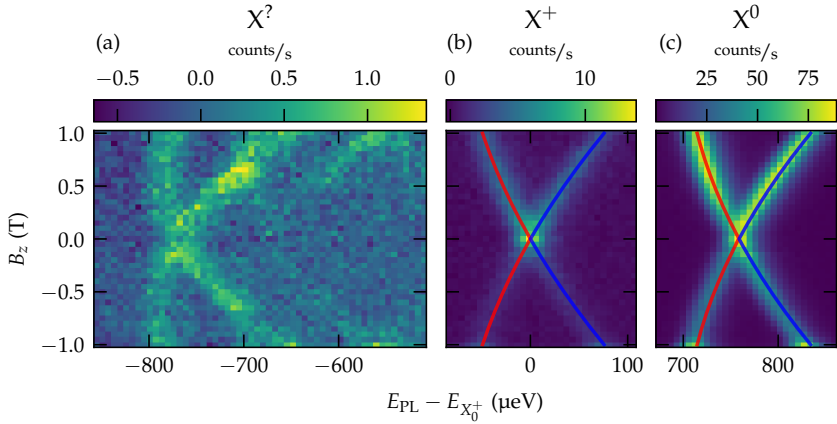


Figure 9.8: Excerpt from the recorded magneto-luminescence spectra for the investigated quantum dot (QD) at magnetic fields below $|1 \text{ T}|$. Panel (a) depicts an unassigned exciton resonance that is visible only in non-equilibrium photoluminescence spectra. Panel (b) depicts the Zeeman splitting and diamagnetic shift of the trion (X^+) resonance, while panel (c) depicts the Zeeman splitting and diamagnetic shift of the neutral exciton (X^0) resonance. Global fit curves for the assigned resonances are plotted using red and blue curves for the red-detuned and blue-detuned Zeeman branches.

quantity	units	χ^+	χ^0
ΔE_Z	$\mu\text{eV T}^{-1}$	125.0(1)	119.66(3)
$ g_{\text{eff}}^* $		2.159(2)	2.0672(5)
diamagnetic shift	$\mu\text{eV T}^{-2}$	13.28(1)	15.669(4)
center $E_{X_0^{(\pm)}}$	eV	1.397 708 3(2)	1.398 467 13(4)
ΔE_{FS}	μeV	0.3(3)	6.7(2)

Table 9.1: Zeeman splitting and fine structure splitting. The specified uncertainties are fit errors.

excerpt from these spectra in the region between ± 1 T. These spectra reveal the magnetic dependence of the Zeeman branch pairs for the identified resonances and four almost imperceptible branches of an undetermined third resonance that must belong to a higher shell state. A global regression is applied to the spectral positions of the Zeeman branches for the identified resonances. The used model function includes a linear Zeeman splitting term and a quadratic diamagnetic shift term. The results of the regression are summarized in Tab. 9.1 for each resonance. These values are very similar to ones reported in literature [132, 153, 154].

10 Theoretical Model

This chapter contains the theoretical calculations necessary to describe the optical Kerr noise spectrum of a QD partially charged by a single hole while the QD is probed by a resonant laser that drives it away from thermal equilibrium. Primarily, these calculations closely follow the approach developed by Glazov and Smirnov in [74, 96, 79, 77]. Considering the wide range of temperatures, laser photon energy detunings, and external magnetic fields in the available experimental data, some simplifying assumptions previously made in Refs. [96, 79] are not valid anymore. In particular, for most spectra, the effective Zeeman splitting $\hbar\Omega$ is larger than the line width of the optical transition. Therefore, $\hbar\Omega$ cannot be considered negligible as in Ref. [96], where only the first-order approximation was considered for the calculated noise power detuning dependences. Furthermore, for many spectra at low temperatures, $\hbar\Omega$ is also larger than the thermal energy $k_{\text{B}}T$. In this situation, thermally induced steady-state spin polarization can become significant. Such a thermally induced polarization is not handled in the previous model in Ref. [79]. This chapter expands the model and provides detailed calculation steps to facilitate future extensions and modifications of the model. In particular, the new derivation incorporates previously not addressed photoeffect-like occupancy dynamics.

The sketch in Fig. 10.1 summarizes the bird-eye view of this chapter. The overarching goal is to arrive at a theoretical expression for the autocorrelation function (ACF) of Kerr fluctuations, $c_K(\tau) = \langle \delta\hat{K}(0)\delta\hat{K}(\tau) \rangle$. Once this is achieved, the FT $\tilde{c}_K(2\pi\nu)$ can be used to predict the shape and amplitude of experimental spectra. The section §10.1 formally defines the QD model using some simplifying assumptions. Section §10.2 uses this model to derive the QD's quantum mechanical state and its temporal evolution using a corresponding density matrix $\hat{\rho}$ and its derivative $\dot{\hat{\rho}}$. The section §10.3.1 derives a quasi-steady-state solution $\hat{\rho}_{\text{qs}}$ by *separating* the fast time scale corresponding to the lifetime of the trion from slower dynamics. To do so, only terms that dominate the formation of the optical signal on very short time scales are considered for the evolution of $\hat{\rho}$. The stationary so-

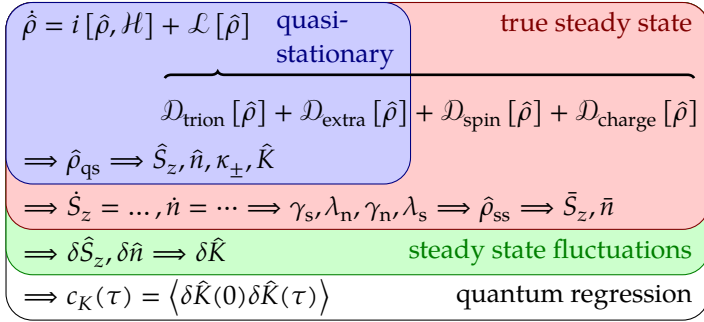


Figure 10.1: Main steps needed to derive the autocorrelation function (ACF) of Kerr fluctuations, $c_K(\tau)$.

lution $\hat{\rho}_{\text{qs}}$ is then decomposed into observables such as pseudo-spin \hat{S}_z and QD occupancy \hat{n} , which are conserved during the short trion lifetime. Additionally, line shape functions κ_{\pm} are extracted from $\hat{\rho}_{\text{qs}}$ that are roughly equivalent to the absorption of the two Zeeman branches of the optical resonance.

In section §10.3.2, the initial complete set of equations $\hat{\rho}$ is used to define a set of kinetic equations for \hat{S}_z and \hat{n} using the results derived from $\hat{\rho}_{\text{qs}}$. The coefficients of these equations $\gamma_s, \lambda_n, \gamma_n,$ and λ_s define directly or indirectly measurable quantities in the eventual noise spectroscopy. Most importantly, the effective pseudo-spin relaxation rate γ_s corresponds to the spin relaxation rate detected, for example, in bulk SNS of GaAs. The stationary solution of the kinetic equations yields the true steady-state density matrix $\hat{\rho}_{\text{ss}}$ that gives the average expectation values of pseudo-spin \bar{S}_z and occupancy \bar{n} in this equilibrium state.

In section §10.4, the observed fluctuations of the Faraday or Kerr signals are treated as deviations from steady-state equilibrium. To this end, a new set of fluctuation operators $\delta\hat{K}, \delta\hat{S}_z, \delta\hat{n}$ is introduced, and a reduced set of kinetic equations is derived for these operators. These new kinetic equations are treated in two ways. First, an approximate solution is derived by invoking the *separation of time scales* for the second time in the shape of a separation of correlator time scales (SCTS) that allows treating the contribution of different correlators to the Kerr spectrum separately. Second, the exact but more bulky solution is derived. In both cases, the quantum regression formula is used to calculate the ACF of the Kerr signal fluctuation $\delta\hat{K}$ with delayed fluctuations. Both solutions then utilize the initial values

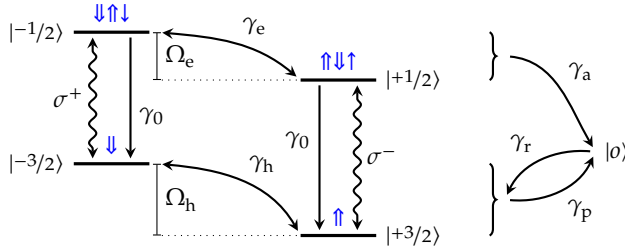


Figure 10.2: Energy level diagram for a positively charged QD.

given by the steady-state values \bar{S}_z and \bar{n} to define the ACF spectrum of the Kerr fluctuation signal $\tilde{c}_K(2\pi\nu)$.

The section §10.5 investigates parameter ranges where the SCTS approximation can be used to make qualitative and quantitative statements. The first part of the discussion highlights parameter ranges where single-spectra regressions break down, and decomposing spectra into SN and occupancy noise (ON) contributions becomes impossible. The second part isolates asymptotic regions where quantitative statements are possible and non-resonant regions where a qualitative comparison with the experiment succeeds.

Finally, section §10.6 explores experimentally observable effects caused by internal probe intensity dependence of previously fixed parameters γ_p and γ_r . Probe intensity dependence changes the overall intensity scaling of the predicted spectra. Within the qualitatively valid parameter ranges, the SCTS approximation provides experimentally testable predictions that depend on the particular shape of the internal dependence. Therefore, several parameterizations of γ_p and γ_r are considered, and corresponding predictions are formulated. These predictions are compared to experimental data in chapter 12, to discern the prevalent decay mechanisms.

10.1 Model System

The QD system can be simplified to the four-level system depicted in Fig. 10.2. This four-level system corresponds to the Zeeman-split s -shell states introduced in section §9.1.2. Higher shell states of the QD are ignored [107] under the assumption that the discarded energy levels are separated well enough from the four-level

system. Consequently, other transitions have a negligible probability of absorbing probe laser photons. This assumption implies that the QD hole states are sufficiently pure when expressed through their corresponding continuum hole states. Effectively, the QD hole states are assumed to be purely heavy holes with a negligible admixture of light-hole states, as explained in section §9.1.4. In the ground state, the QD is charged by a single hole, while in the excited trion state, the QD contains an additional electron-hole pair [42]. The ground and excited states are twofold degenerate at a vanishing external magnetic field. Under the influence of an external magnetic field, the spin states of the s -shell split. The excited state splits up with an effective Zeeman splitting of Ω_e dominated by the effective electron g_e^* factor, while the ground state splits up with an effective Zeeman splitting of Ω_h dominated by the effective heavy hole g_h^* factor [107]. Therefore, in Fig. 10.2, the excited states $|\pm 1/2\rangle$ are labeled with the z projection of the electron spin, while the ground states $|\pm 3/2\rangle$ are labeled with the z projection of the hole pseudo-spin.

The presented assumptions result in very strict selection rules. An optical transition between a ground and an excited state is only possible with σ^\pm light *if the states and the light share the same sign*. In the absence of any spin relaxation mechanisms, an excitation by a σ^\pm photon followed by an emission of a σ^\pm photon preserves the ground-state hole spin in the same state. Furthermore, because the spin relaxation rates of electron spin γ_e and hole spin γ_h are assumed to be much slower than the relaxation rate of the trion γ_0 , an excitation with linearly polarized light (that is, a coherent superposition of σ^+ and σ^- light) effectively does not change the population difference between states of the same sign in Fig. 10.2. In analogy to bulk SNS in GaAs, it is useful to introduce this difference as a conserved quantity, the pseudo-spin S_z . Accordingly, *fluctuations of this pseudo-spin give rise to a contribution to the noise spectrum*, which is determined by the variance of this quantity.

The final ingredient of the model is an outer state $|o\rangle$ that models a less-than-unity occupancy $n < 1$ of the QD by a resident hole. Here, the assumption is that on intermediate time scales ($\lesssim 100$ kHz), the QD is in a meta-stable equilibrium with its environment. After losing the resident hole by one of the following processes, the QD does not recharge immediately. Instead, the hole remains in the additional outer state before it is returned to the QD by some other process. The internal dynamics of all the possible meta-stable states outside of the QD are usually not visible in the experiment, and $|o\rangle$, therefore, serves as a simplified and incoherent blanket state where the resident hole *must* reside when the QD is neutral. All processes that eject the hole from the QD have by construction $|o\rangle$ as their

destination state. A process that ejects the hole from the excited states at a rate γ_a is analogous to Auger recombination in atomic physics [96], while a process that ejects the hole from the ground states at a rate γ_p is analogous to internal photo-effect [64]. Of course, the latter can occur in reverse by ejecting the hole from the outer state at a rate γ_r and injecting it into the ground states of the QD. Depending on background doping, this reverse emission from the outer state can be either intrinsic (i.e., thermally driven and independent of the probe intensity) [96] or extrinsically induced by the probe intensity. Either way, the actual microscopic processes responsible for the gain and loss of the charge might as well be much more complicated and depend on the exact constitution of the QD environment. However, these microscopic processes cannot be directly observed in an experiment and might only slightly alter the experimentally observed relaxation rates. Therefore, these microscopic processes are not included in the scope of this phenomenological model. All processes involving the outer state $|o\rangle$ should be incoherent and slow compared to electron spin relaxation γ_e in the excited state [96]. For processes occurring at faster rates, the occupancy n , the sum of populations of the four spin levels, is another conserved quantity. Fluctuations of the occupancy give rise to a *second contribution* to the Kerr fluctuation signal, which is determined by the variance of n .

10.2 Density Matrix

The state $\hat{\rho}$ of the combined QD-outer-state system can be defined in a quantum-mechanically sound way using the density matrix formalism, the model, and the preceding assumptions. Predictions observable in an experiment follow from the evolution of this state. The outer state has no coherent coupling to the QD by construction. Therefore, the combined density matrix of the QD and the outer state can be decomposed as:

$$\hat{\rho} = \begin{pmatrix} \hat{\rho}_{\text{QD}} & \vec{0} \\ \vec{0} & \hat{\rho}_o \end{pmatrix},$$

or explicitly in matrix form as

$$\hat{\rho} = \begin{pmatrix} \rho_{-1/2,-1/2} & \rho_{-1/2,1/2} & \rho_{-1/2,3/2} & \rho_{-1/2,-3/2} & 0 \\ \rho_{-1/2,1/2}^* & \rho_{1/2,1/2} & \rho_{1/2,3/2} & \rho_{1/2,-3/2} & 0 \\ \rho_{-1/2,3/2}^* & \rho_{1/2,3/2}^* & \rho_{3/2,3/2} & \rho_{3/2,-3/2} & 0 \\ \rho_{-1/2,-3/2}^* & \rho_{1/2,-3/2}^* & \rho_{3/2,-3/2}^* & \rho_{-3/2,-3/2} & 0 \\ 0 & 0 & 0 & 0 & \rho_o \end{pmatrix},$$

where the following ordering of the eigenstates as defined in section §10.1 is assumed:

$$(|-1/2\rangle, |+1/2\rangle, |+3/2\rangle, |-3/2\rangle, |0\rangle).$$

Here, the $\hat{\rho} = \hat{\rho}^\dagger$ property is used to define the elements below the diagonal. In this representation, the diagonal terms $\rho_{\pm 1/2, \pm 1/2}$, $\rho_{\pm 3/2, \pm 3/2}$, and ρ_o are the populations of the eigenstates, while the off-diagonal terms are the coherences. It is helpful to define a set of projector operators for later use whose expectation values are given by the diagonal terms:

$$\begin{aligned} \hat{n}_{\pm 1/2} &= |\pm 1/2\rangle \langle \pm 1/2|, & \langle \hat{n}_{\pm 1/2} \rangle_\rho &= \text{tr}(\hat{n}_{\pm 1/2} \hat{\rho}) = \rho_{\pm 1/2, \pm 1/2}, \\ \hat{n}_{\pm 3/2} &= |\pm 3/2\rangle \langle \pm 3/2|, & \langle \hat{n}_{\pm 3/2} \rangle_\rho &= \text{tr}(\hat{n}_{\pm 3/2} \hat{\rho}) = \rho_{\pm 3/2, \pm 3/2}, \\ \hat{n}_o &= |0\rangle \langle 0|, & \langle \hat{n}_o \rangle_\rho &= \text{tr}(\hat{n}_o \hat{\rho}) = \rho_o. \end{aligned}$$

Summing over a set of these projectors gives the identity operator, i.e.,

$$\langle \hat{n}_{-1/2} + \hat{n}_{+1/2} + \hat{n}_{+3/2} + \hat{n}_{-3/2} + \hat{n}_o \rangle_\rho = \text{tr}(\hat{\rho}) = 1$$

per definition of the density matrix (conservation of probability). The density matrix defines the state of the model system. The temporal evolution of this state is given by the Liouville-von-Neumann equation:

$$\dot{\hat{\rho}} = \frac{d}{dt} \hat{\rho} = i[\hat{\rho}, \mathcal{H}] + \mathcal{L}[\hat{\rho}], \quad (10.1)$$

where the first term on the right-hand side defines the coherent part of the evolution, whereas the second term describes phenomenological relaxation or damping processes. Both parts are defined next.

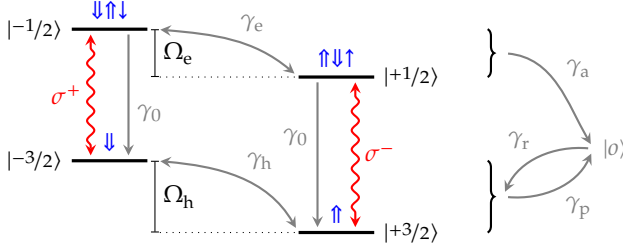


Figure 10.3: Coherent evolution of the QD states (red).

10.2.1 Coherent Part

The coherent part of the evolution is given by the commutator of the density matrix and the system Hamiltonian \mathcal{H} . In the rotating-wave approximation and in the frame that rotates with the exciting laser field, the Hamiltonian for interaction with linearly polarized light takes the form:

$$\mathcal{H} = -\Delta \hat{n}_e + \frac{\Omega_h}{2} \hat{\sigma}_h + \frac{\Omega_e}{2} \hat{\sigma}_e - \frac{\mathcal{E}}{\sqrt{2}} (\hat{d}_+ + \hat{d}_+^\dagger + \hat{d}_- + \hat{d}_-^\dagger) \quad (10.2)$$

$$= \begin{pmatrix} -\Delta - \frac{\Omega_e}{2} & 0 & 0 & \frac{\mathcal{E}}{\sqrt{2}} & 0 \\ 0 & -\Delta + \frac{\Omega_e}{2} & -\frac{\mathcal{E}}{\sqrt{2}} & 0 & 0 \\ 0 & -\frac{\mathcal{E}}{\sqrt{2}} & \frac{\Omega_h}{2} & 0 & 0 \\ \frac{\mathcal{E}}{\sqrt{2}} & 0 & 0 & -\frac{\Omega_h}{2} & 0 \\ 0 & 0 & 0 & 0 & 0 \end{pmatrix}. \quad (10.3)$$

Here, the dipole operators are defined in a circular basis,

$$\hat{d}_\pm = |\pm 3/2\rangle \langle \pm 1/2|, \quad (10.4)$$

the \hat{n}_h and \hat{n}_e operators that track the population of either the ground states or the excited states of the QD,

$$\hat{n}_h = \hat{n}_{+3/2} + \hat{n}_{-3/2}, \quad \hat{n}_e = \hat{n}_{+1/2} + \hat{n}_{-1/2}, \quad (10.5)$$

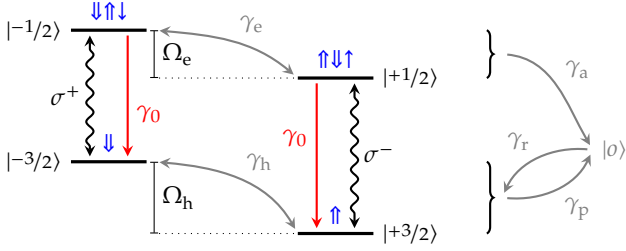


Figure 10.4: Trion decay of the excited QD states (red).

and the $\hat{\sigma}_h$ and $\hat{\sigma}_e$ operators track the polarization of either the ground-state hole pseudo-spin or the trion electron spin,

$$\hat{\sigma}_h = \hat{n}_{+3/2} - \hat{n}_{-3/2}, \quad \hat{\sigma}_e = \hat{n}_{+1/2} - \hat{n}_{-1/2}. \quad (10.6)$$

The constants introduced here are the laser detuning from the trion resonance (Δ), the Zeeman splittings for σ^\pm light of the electron (Ω_e) and the hole (Ω_h), as well as the magnitude of the optical trion transition matrix elements (\mathcal{E}). Note that the dipole operators implement the optical selection rules from the model, i.e., they preserve the sign of the spin between the states they couple.

10.2.2 Incoherent Part

The incoherent part of the evolution introduces phenomenological relaxation or damping into the otherwise unitary evolution of $\hat{\rho}$. Several processes contribute to relaxation on different time scales. This great difference between the magnitudes of damping rates is exploited later for the approximate solution by separating the time scales and treating the involved processes separately. The contributing parts can be expressed in terms of damping super¹ operators in Lindblad form. For some operator \hat{o} , the damping super operator is defined as:

$$\mathcal{D}_{\hat{o}}[\hat{\rho}] = \frac{1}{2} (\hat{o}^\dagger \hat{o} \hat{\rho} + \hat{\rho} \hat{o}^\dagger \hat{o} - 2\hat{o} \hat{\rho} \hat{o}^\dagger).$$

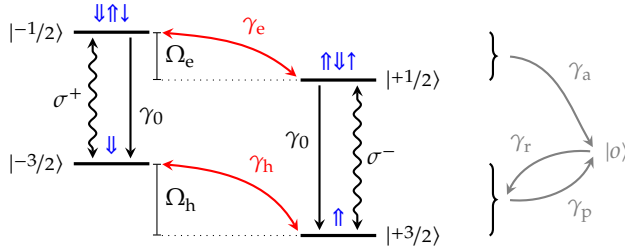


Figure 10.5: Spin relaxation of the QD states (red).

Trion Decay

The fastest relaxation mechanism is the spontaneous decay of the trion transition. This process brings the QD to the ground state by emitting a corresponding photon whenever the QD is in an excited trion state. The relaxation occurs at a characteristic rate γ_0 that determines the intrinsic line width of the trion resonance. Energy and momentum conservation during the emission of the photon means that only states with the same spin sign are coupled. This decay is implemented in terms of the dipole operators d_{\pm} :

$$\mathcal{D}_{\text{trion}}[\hat{\rho}] = -\gamma_0 \left(\mathcal{D}_{\hat{d}_+}[\hat{\rho}] + \mathcal{D}_{\hat{d}_-}[\hat{\rho}] \right). \quad (10.7)$$

Note that the defining operators appear only directly (there are no corresponding hermitian conjugate \dagger terms), i.e., the relaxation happens only one way: from the excited state to the ground state and the negative sign before the decay constant depletes the populations of the corresponding excited states.

Spin Relaxation

Optical transitions preserve the pseudo-spin $\hat{S}_z = 1/2 (\hat{\sigma}_e + \hat{\sigma}_h)$ in the QD. However, the environment causes spin relaxation on slower time scales, as described in section §9.1.5. The relaxation mechanisms couple states with opposing spin and relax any present spin polarization with a characteristic $1/T_1$ rate (γ_e for the electron and γ_h for the hole). This kind of relaxation can be implemented with a term of the following form:

¹Unlike a regular operator, these act from both sides on the density matrix.

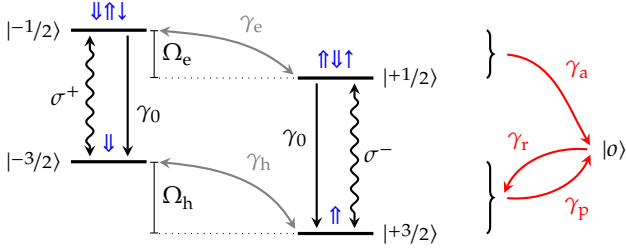


Figure 10.6: The QD charge dynamics (red).

$$\mathcal{D}_{\text{spin}}[\hat{\rho}] = -\frac{\gamma_e}{2} (\beta \mathcal{D}_{\hat{\chi}_e}[\hat{\rho}] + \mathcal{D}_{\hat{\chi}_e^\dagger}[\hat{\rho}]) - \frac{\gamma_h}{2} (\alpha \mathcal{D}_{\hat{\chi}_h}[\hat{\rho}] + \mathcal{D}_{\hat{\chi}_h^\dagger}[\hat{\rho}]). \quad (10.8)$$

Here $\hat{\chi}_e$ and $\hat{\chi}_h$ are spin-flip operators for the electron spin and the hole pseudo-spin,

$$\hat{\chi}_e = |-1/2\rangle \langle +1/2| \quad \hat{\chi}_h = |-3/2\rangle \langle +3/2|.$$

Unlike trion recombination, this process acts both ways, and a term for the operator as well as its hermitian conjugate is present. This relaxation process drives the QD toward a steady state. The included factors $0 < \alpha, \beta < 1$ in Eq. (10.8) account for a possible spin polarization in the case where the effective Zeeman splitting becomes larger than the thermal energy of the spin system: $\Omega_{e,h} > k_B T$. Note that the α and β factors are present only for one of the summands to encode that the scattering becomes directional. No energy from within the modeled system is needed to flip the spin from the high-energy state to the low-energy state. For the reverse direction, the difference in energy has to be provided by the phonon bath.

Charge Dynamics

On longer time scales, the QD and the outer state compete for the single resident hole through the two possible processes described in section §10.1. The following operators allow a concise definition of the corresponding damping terms:

$$\hat{v}_\pm = |0\rangle \langle \pm 1/2| \quad \hat{r}_\pm = |\pm 3/2\rangle \langle 0|.$$

The \hat{v}_\pm operators transfer the hole from one of the excited states to the outer state, while the \hat{r}_\pm operators transfer the hole from the outer state to one of the ground states. Both the Auger and photoeffect processes converge to a single destination state. Therefore, the damping terms have to be weighted by the corresponding rates γ_a and γ_p . There are two possible destination states for the (photo) emission from the outer state. Consequently the damping term has to be weighted by half of γ_r . The complete damping term is:

$$\begin{aligned} \mathcal{D}_{\text{charge}}[\hat{\rho}] = & -\gamma_a \left(\mathcal{D}_{\hat{v}_+}[\hat{\rho}] + \mathcal{D}_{\hat{v}_-}[\hat{\rho}] \right) \\ & -\gamma_p \left(\mathcal{D}_{\hat{r}_+}[\hat{\rho}] + \mathcal{D}_{\hat{r}_-}[\hat{\rho}] \right) \\ & -\frac{\gamma_r}{2} \left(\mathcal{D}_{\hat{r}_+}[\hat{\rho}] + \mathcal{D}_{\hat{r}_-}[\hat{\rho}] \right). \end{aligned} \quad (10.9)$$

When the hole leaves the QD, all past coherences with the eigenstates are lost. The two possible relaxation loops (through the Auger process and the photoeffect) drop the hole into one of the ground states with equal probability, i.e., the recharging does not contribute to a pseudo-spin polarization of the ground state. Therefore, each loop essentially constitutes a relaxation mechanism of the total pseudo-spin S_z , and the corresponding rates will be present in its effective relaxation rate γ_s : The Auger rate γ_a will enhance the spin relaxation only on resonance. In contrast, γ_p will contribute a detuning independent term akin to “optically induced spin relaxation”.

The intrinsic value of both γ_r and γ_p might approach 0. Accordingly, the unperturbed QD might be neutral and become charged only through the influence of the probe laser. Therefore, these two rates should generally be described by $\gamma_{p,r} = \gamma_{p,r}^\bullet + \eta_{p,r} I_{\text{probe}}$, where $\gamma_{p,r}^\bullet$ is the intrinsic part. Moreover, the magnitude of the different rates will have a strong influence on the steady-state value of the QD occupancy $\hat{n} = \hat{n}_e + \hat{n}_h$, $\bar{n} < 1$, which directly influences the magnitude of the total noise power of the Kerr fluctuations. Consequently, the power dependence of these rates should be immediately apparent in detuning dependent measurements at different probe intensity levels.

Other Dephasing Mechanisms

Separation of time scales is employed to simplify the quasi-stationary solution calculation presented below. This simplification disregards spin relaxation and

charge dynamics occurring on time scales where the quasi-stationary solution holds. However, these processes still exert some influence on the trion dephasing rate. The following universal term is included to account for this additional effect $\gamma_{\text{extra}} \geq 0$ on the total optical dephasing rate:

$$\mathcal{D}_{\text{extra}} [\hat{\rho}] = -\frac{\gamma_{\text{extra}}}{2} \left(\mathcal{D}_{\hat{d}_+} [\hat{\rho}] + \mathcal{D}_{\hat{d}_-} [\hat{\rho}] \right), \quad (10.10)$$

where \hat{d}_{\pm}' are operators acting on off-diagonal terms only,

$$\hat{d}_{\pm}' = \hat{n}_{\pm 1/2} - \hat{n}_{\pm 3/2}.$$

For instance, the damping term in Eq. (10.7) yields an effective transverse dephasing rate of $\gamma_0/2$, corresponding to homogeneous dephasing. Assuming $\alpha, \beta = 1$ the terms in Eq. (10.8) and Eq. (10.9) introduce contributions of $\gamma_e/2$, $\gamma_h/2$, and $\gamma_a/2$, respectively. Hence, it is possible to absorb all dephasing terms into γ_{extra} by defining:

$$\gamma_{\text{extra}} = \frac{1}{2} (\gamma_0 + \gamma_e + \gamma_h + \gamma_a),$$

as has been done in Ref. [96]. Alternatively, γ_{extra} can be defined to contain only the additional terms:

$$\gamma_{\text{extra}} = \frac{1}{2} (\gamma_e + \gamma_h + \gamma_a),$$

as has been done in Ref. [79]. In the presented calculation, γ_{extra} is *not explicitly defined* and just taken as an additional dephasing present in the quasi-steady-state solution. This choice is possible because, as is explained below, only the effective dephasing rate γ_d is truly necessary to describe the detuning dependence of Kerr noise spectra.

10.3 Stationary Solution

Now Eq. (10.9), Eq. (10.8), and Eq. (10.7) can be inserted into Eq. (10.1) to determine the temporal evolution of the density matrix of the system:

$$\begin{aligned} \dot{\hat{\rho}} = \frac{d}{dt} \hat{\rho} = & i [\hat{\rho}, \mathcal{H}] + \mathcal{D}_{\text{trion}} [\hat{\rho}] + \mathcal{D}_{\text{extra}} [\hat{\rho}] \\ & + \mathcal{D}_{\text{spin}} [\hat{\rho}] + \mathcal{D}_{\text{charge}} [\hat{\rho}]. \end{aligned} \quad (10.11)$$

For completeness, Eq. (10.11) can be expressed in an explicit form using operator expectation values:

$$\dot{n}_{+3/2} = -\sqrt{2}\mathcal{E}\mathcal{J}(d_+) + \gamma_0 n_{+1/2} + \frac{\gamma_r}{2} n_o - \gamma_p n_{+3/2} + \frac{\gamma_h}{2} (n_{-3/2} - \alpha n_{+3/2}), \quad (10.12)$$

$$\dot{n}_{-3/2} = +\sqrt{2}\mathcal{E}\mathcal{J}(d_-) + \gamma_0 n_{-1/2} + \frac{\gamma_r}{2} n_o - \gamma_p n_{-3/2} - \frac{\gamma_h}{2} (n_{-3/2} - \alpha n_{+3/2}), \quad (10.13)$$

$$\dot{n}_{+1/2} = +\sqrt{2}\mathcal{E}\mathcal{J}(d_+) - (\gamma_0 + \gamma_a) n_{+1/2} + \frac{1}{2}\gamma_e (n_{-1/2} - \beta n_{+1/2}), \quad (10.14)$$

$$\dot{n}_{-1/2} = -\sqrt{2}\mathcal{E}\mathcal{J}(d_-) - (\gamma_0 + \gamma_a) n_{-1/2} - \frac{1}{2}\gamma_e (n_{-1/2} - \beta n_{+1/2}), \quad (10.15)$$

$$\dot{n}_o = \gamma_a (n_{-1/2} + n_{+1/2}) + \gamma_p (n_{-3/2} + n_{+3/2}) - \gamma_r n_o, \quad (10.16)$$

$$\Re(\dot{d}_+) = -\Delta_+ \mathcal{J}(d_+) - \frac{1}{4}\Re(d_+) (2\gamma_a + 4\gamma_{\text{extra}} + 2\gamma_0 + \beta\gamma_e + \alpha\gamma_h + 2\gamma_p), \quad (10.17)$$

$$\begin{aligned} \Im(\dot{d}_+) = & +\Delta_+ \Re(d_+) - \frac{1}{4}\Im(d_+) (2\gamma_a + 4\gamma_{\text{extra}} + 2\gamma_0 + \beta\gamma_e + \alpha\gamma_h + 2\gamma_p) \\ & + \frac{\mathcal{E}}{\sqrt{2}} (n_{+3/2} - n_{+1/2}), \end{aligned} \quad (10.18)$$

$$\Re(\dot{d}_-) = -\Delta_- \mathcal{J}(d_-) - \frac{1}{4}\Re(d_-) (2\gamma_a + 4\gamma_{\text{extra}} + 2\gamma_0 + \gamma_e + \gamma_h + 2\gamma_p), \quad (10.19)$$

$$\begin{aligned} \Im(\dot{d}_-) = & +\Delta_- \Re(d_-) - \frac{1}{4}\Im(d_-) (2\gamma_a + 4\gamma_{\text{extra}} + 2\gamma_0 + \gamma_e + \gamma_h + 2\gamma_p) \\ & + \frac{\mathcal{E}}{\sqrt{2}} (n_{-1/2} - n_{-3/2}), \end{aligned} \quad (10.20)$$

where the location of the Zeeman branches Δ_{\pm} and the effective Zeeman splitting Ω are defined as:

$$\begin{aligned} \Delta_{\pm} & := \Delta \mp \frac{\Omega}{2}, \text{ and} \\ \Omega & := \Omega_e - \Omega_h. \end{aligned}$$

This set of differential equations is not very useful for noise spectroscopy, as the system's evolution usually cannot be directly observed. Instead, from these equations, a steady-state solution can be calculated that the system approaches

for very long times $t \rightarrow \infty$. Fluctuations measured in noise spectroscopy will be small deviations from this equilibrium state. Once enough time has passed, the state $\hat{\rho}(t)$ of the system not only stops depending on any initial conditions, but it also stops changing in time and it becomes stationary:

$$\begin{aligned} \hat{\rho}_{\text{ss}} &:= \lim_{t \rightarrow \infty} \hat{\rho}(t), \\ 0 = \dot{\hat{\rho}}_{\text{ss}} &= i[\hat{\rho}_{\text{ss}}, \mathcal{H}] + \mathcal{D}_{\text{trion}}[\hat{\rho}_{\text{ss}}] + \mathcal{D}_{\text{extra}}[\hat{\rho}_{\text{ss}}] \\ &\quad + \mathcal{D}_{\text{spin}}[\hat{\rho}_{\text{ss}}] + \mathcal{D}_{\text{charge}}[\hat{\rho}_{\text{ss}}], \end{aligned} \quad (10.21)$$

where $\hat{\rho}_{\text{ss}}$ is defined to be the steady-state density matrix. Note that the system of coupled *differential equations* defined by Eq. (10.11) becomes a regular system of coupled *equations* for $\hat{\rho}_{\text{ss}}$, Eq. (10.21). Therefore, a solution for Eq. (10.21) can be found by simple linear algebra.

10.3.1 Quasi-Stationary Solution

The intricate set of equations defined in Eq. (10.21) can be significantly simplified by employing the *separation of time scales*. The slow relaxation processes have a negligible effect on the QD state on the time scale relevant for optical signal formation. Hence, their corresponding quantities can be assumed to be conserved over short times. Consequently, for the rest of this subsection the effects of $\mathcal{D}_{\text{spin}}[\hat{\rho}_{\text{ss}}]$ and $\mathcal{D}_{\text{charge}}[\hat{\rho}_{\text{ss}}]$ can be disregarded. The quasi-stationary solution provides less intricate expressions for the quasi-steady-state values of these conserved quantities. These expressions facilitate finding a solution for the true steady-state later on by considering the kinetic behavior of these quantities (as defined by Eq. (10.11)).

The reduced set of equations:

$$\begin{aligned} \hat{\rho}_{\text{qs}} &:= \lim_{t \rightarrow \infty} \hat{\rho}(t), \\ 0 = \dot{\hat{\rho}}_{\text{qs}} &= i[\hat{\rho}_{\text{qs}}, \mathcal{H}] + \mathcal{D}_{\text{trion}}[\hat{\rho}_{\text{qs}}] + \mathcal{D}_{\text{extra}}[\hat{\rho}_{\text{qs}}], \end{aligned}$$

can be explicitly written in terms of operator expectation values with respect to the quasi-steady-state density matrix $\hat{\rho}_{\text{qs}}$:

$$0 = -\sqrt{2}\mathcal{E}\mathcal{J}(d_+) + \gamma_0 n_{+1/2}, \quad (10.22)$$

$$0 = \sqrt{2}\mathcal{E}\mathcal{J}(d_-) + \gamma_0 n_{-1/2}, \quad (10.23)$$

$$0 = \sqrt{2}\mathcal{E}\mathcal{J}(d_+) - \gamma_0 n_{+1/2}, \quad (10.24)$$

$$0 = -\sqrt{2}\mathcal{E}\mathcal{J}(d_-) - \gamma_0 n_{-1/2}, \quad (10.25)$$

$$0 = -\Delta_- \mathcal{J}(d_+) - \frac{1}{4} \mathfrak{R}(d_+) (4\gamma_{\text{extra}} + 2\gamma_0), \quad (10.26)$$

$$0 = \Delta_- \mathfrak{R}(d_+) - \frac{1}{4} \mathcal{J}(d_+) (4\gamma_{\text{extra}} + 2\gamma_0) + \frac{\mathcal{E}(n_{+3/2} - n_{+1/2})}{\sqrt{2}}, \quad (10.27)$$

$$0 = -\Delta_+ \mathcal{J}(d_-) - \frac{1}{4} \mathfrak{R}(d_-) (4\gamma_{\text{extra}} + 2\gamma_0), \quad (10.28)$$

$$0 = \Delta_+ \mathfrak{R}(d_-) - \frac{1}{4} \mathcal{J}(d_-) (4\gamma_{\text{extra}} + 2\gamma_0) + \frac{\mathcal{E}(n_{-1/2} - n_{-3/2})}{\sqrt{2}}. \quad (10.29)$$

Note that equations (10.22) and (10.24), as well as (10.23) and (10.25), are linearly dependent. Therefore there are effectively only six equations and only six results. The particular choice is to express the solution for $\hat{\rho}_{\text{qs}}$ as a ratio of populations,

$$\kappa_{\pm} = \frac{n_{\pm 1/2}}{n_{\pm 3/2} + n_{\pm 1/2}} = \frac{\mathcal{E}^2 \gamma_{\text{d}}}{\gamma_0 (\gamma_1^2 + \Delta_{\pm}^2)}, \quad (10.30)$$

as well as the real and imaginary parts of the dipole operators,

$$d_{\pm} = \mp \frac{\sqrt{2} \Delta_{\pm} n_{\pm 3/2} \mathcal{E}}{\gamma_1^2 + \gamma_{\text{d}}^2 + 2\Delta_{\pm}^2} \pm i \frac{\sqrt{2} \gamma_{\text{d}} n_{\pm 3/2} \mathcal{E}}{\gamma_1^2 + \gamma_{\text{d}}^2 + 2\Delta_{\pm}^2}. \quad (10.31)$$

Here, the effective dephasing rate γ_{d} and the saturation broadened line width γ_1 are defined as:

$$\gamma_{\text{d}} = \gamma_{\text{extra}} + \frac{\gamma_0}{2}, \quad (10.32)$$

$$\gamma_1 = \gamma_{\text{d}} \sqrt{1 + \frac{2\mathcal{E}^2}{\gamma_{\text{d}} \gamma_0}}. \quad (10.33)$$

As presented below, the detuning dependence of the effective pseudo-spin relaxation rate γ_s in section §10.3.2 is completely determined by the population ratios κ_{\pm} . Hence, these expressions can be called *line shape functions* because they are Lorentzian-shaped peaks centered at the Zeeman branches with a half width at half maximum (HWHM) of γ_1 .

The expressions for the dipole expectation values in Eqs. (10.31) are expressed in a circularly polarized basis. For noise spectroscopy, the probe beam is linearly polarized and is aligned (without loss of generalization) parallel to the x -axis. Therefore these solutions need to be converted to a linearly polarized basis,

$$d_x = + \frac{\mathcal{E}(\Delta_- - i\gamma_d)}{\gamma_1^2 + \gamma_d^2 + 2\Delta_-^2} n_{-3/2} + \frac{\mathcal{E}(\Delta_+ - i\gamma_d)}{\gamma_1^2 + \gamma_d^2 + 2\Delta_+^2} n_{+3/2},$$

$$d_y = - \frac{\mathcal{E}(\gamma_d + i\Delta_-)}{\gamma_1^2 + \gamma_d^2 + 2\Delta_-^2} n_{-3/2} + \frac{\mathcal{E}(\gamma_d + i\Delta_+)}{\gamma_1^2 + \gamma_d^2 + 2\Delta_+^2} n_{+3/2},$$

where the following relations are used:

$$\frac{1}{\sqrt{2}} (d_- - d_+) = d_x,$$

$$\frac{-i}{\sqrt{2}} (d_- + d_+) = d_y.$$

Now, fluctuations about the steady state of d_y are proportional to the fluctuations of the polarization angle and ellipticity of the Kerr signal [107]. More precisely, the imaginary part of d_y is proportional to fluctuations of the refractive part of the Kerr signal. On the other hand, the real part is proportional to fluctuations of the absorptive part of the Kerr signal. The evolution of $\hat{\rho}$ due to the slow damping terms can be expressed as a set of kinetic equations of the conserved quantities \hat{n} and \hat{S}_z ,

$$\hat{n} = \hat{n}_e + \hat{n}_h, \quad (10.34)$$

$$\hat{S}_z = 1/2 (\hat{\sigma}_e + \hat{\sigma}_h). \quad (10.35)$$

The dipole component d_y can be expressed in terms of expectation values of these new operators by substituting the ground-state populations $n_{\pm 3/2}$ by

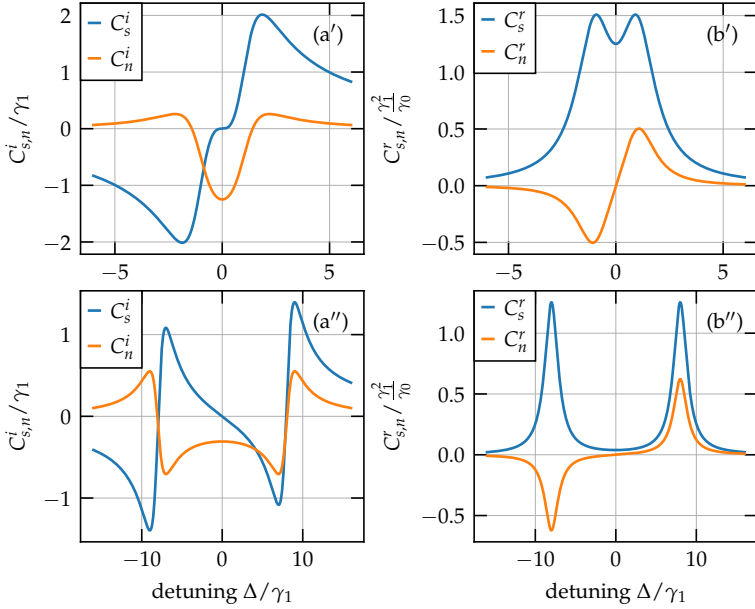


Figure 10.7: Sketch of the dipole term shape functions as defined in Eq. (10.37) and Eq. (10.39) for the quasi-stationary solution. For panels with a single prime (') the parameters were: $\Omega/\gamma_1 = 2$, $\varepsilon/\gamma_1 = 5$. For panels with a double prime (') the parameters were: $\Omega/\gamma_1 = 16$, $\varepsilon/\gamma_1 = 5$. The spin part reproduces a dielectric function built from two Lorentzian oscillators.

$$n_{\pm 3/2} = \frac{1}{2} (n \pm 2S_z) (1 - \kappa_{\pm}). \quad (10.36)$$

Consequently, the real and imaginary parts of d_y can be expressed as:

$$\Re(d_y) = C_s^r S_z + C_n^r n \quad (10.37)$$

$$\equiv \frac{\mathcal{E}\gamma_d}{2} \left(\frac{1}{\gamma_1^2 + \Delta_-^2} + \frac{1}{\gamma_1^2 + \Delta_+^2} \right) S_z - \frac{\mathcal{E}\gamma_d}{4} \left(\frac{1}{\gamma_1^2 + \Delta_-^2} - \frac{1}{\gamma_1^2 + \Delta_+^2} \right) n, \quad (10.38)$$

$$\Im(d_y) = C_s^i S_z + C_n^i n \quad (10.39)$$

$$\equiv \frac{\mathcal{E}}{2} \left(\frac{\Delta_-}{\gamma_1^2 + \Delta_-^2} + \frac{\Delta_+}{\gamma_1^2 + \Delta_+^2} \right) S_z - \frac{\mathcal{E}}{4} \left(\frac{\Delta_-}{\gamma_1^2 + \Delta_-^2} - \frac{\Delta_+}{\gamma_1^2 + \Delta_+^2} \right) n. \quad (10.40)$$

In this particular form, it becomes immediately apparent that the real part of d_y consists of two Lorentzians per observable, as expected for the absorption spectrum. In contrast, the contributions for the imaginary part of d_y correspond to the refractive part of the absorption spectrum. For the spin part, the solution reproduces the dielectric function that can be assembled from two semi-classical Lorentzian oscillators, as sketched in Fig. 10.7. On the other hand, the occupancy part yields a curve in which the sign of one Lorentzian oscillator is flipped [155].

From the theoretical treatment of the probe part of pump-probe spectroscopy [107], it is well known that $\Im(d_y)$ is proportional to the Kerr rotation angle, while $\Re(d_y)$ is proportional to the Kerr ellipticity (up to a constant factor). Therefore, from Eq. (10.37) and Eq. (10.39), the definition of the Kerr signal operator can be reconstructed to:

$$\hat{K} = \cos(\varphi) (C_s^i \hat{S}_z + C_n^i \hat{n}) + \sin(\varphi) (C_s^r \hat{S}_z + C_n^r \hat{n}). \quad (10.41)$$

Note Generally, there is no easy correspondence between the optical resonance in Fig. 10.7 and the optical noise spectrum (of the Kerr fluctuation signal). As demonstrated in the subsequent section section §10.4, the existence of multiple noise contributions can greatly alter the detuning dependence of the spectral noise power, deviating significantly from the expected form based solely on equation Eq. (10.41).

10.3.2 True Stationary Solution

Now it is time to return to the definition of the full stationary equation, Eq. (10.11). Using (10.36) from the quasi-stationary solution, the equations (10.12), (10.13),

(10.14), and (10.15) can be expressed as kinetic equations for \hat{S}_z and \hat{n} :

$$\dot{S}_z = -\gamma_s S_z + \lambda_n n, \quad (10.42)$$

$$\dot{n} = -\gamma_n n + \lambda_s S_z + \gamma_r n_o, \quad (10.43)$$

where the kinetic constants are defined by:

$$\gamma_s = \frac{\gamma_{s-}}{2} \kappa_- + \frac{\gamma_{s+}}{2} \kappa_+ + \gamma_p + \frac{\gamma_h}{2} (\alpha + 1), \quad (10.44)$$

$$\lambda_n = \frac{\gamma_{s-}}{4} \kappa_- - \frac{\gamma_{s+}}{4} \kappa_+ - \frac{\gamma_h}{4} (\alpha - 1), \quad (10.45)$$

$$\gamma_n = \frac{1}{2} (\gamma_a - \gamma_p) \kappa_- + \frac{1}{2} (\gamma_a - \gamma_p) \kappa_+ + \gamma_p, \quad (10.46)$$

$$\lambda_s = (\gamma_a - \gamma_p) \kappa_- + (\gamma_p - \gamma_a) \kappa_+, \quad (10.47)$$

$$\gamma_{s-} = \gamma_a + \gamma_e - \gamma_h - \gamma_p,$$

$$\gamma_{s+} = \gamma_a + \beta \gamma_e - \alpha \gamma_h - \gamma_p.$$

As expected, the effective pseudo-spin relaxation rate γ_s contains a detuning independent term corresponding to the intrinsic hole pseudo-spin relaxation and an effective relaxation term due to internal photoeffect. When hole spin relaxation dominates over the photoeffect, for probe laser energies significantly detuned from the Zeeman branches, a value equal to γ_h can be recovered at high temperatures ($\gamma_h \gg \gamma_p$, $k_B T > \Omega_h$, $\alpha \rightarrow 1$). At the same time, for low temperatures ($k_B T < \Omega_h$, $\alpha \rightarrow 0$), only half of γ_h remains. Close to the Zeeman branches, γ_s is dominated by the terms expressed in line shape functions κ_{\pm} . Therefore, the detuning dependence of γ_s will look like two Lorentzian-shaped peaks, each with a HWHM of γ_1 .

A surprising consequence of these kinetic equations is that the effective hole loss processes combine into a single loss rate γ_n that directly acts on the occupancy n of the QD regardless of the actual states involved. Again, for large detunings, this new rate approaches the constant photoemission value γ_p .

The system of kinetic equations defined by equations (10.42) and (10.43) is incomplete, as the dynamics of the outer state are unknown. Nevertheless, by assuming the conservation of particles [79] it follows that $1 = n + n_o$ and, therefore

$$n_o = 1 - n. \quad (10.48)$$

With this assumption, the stationary case of the kinetic equation can be solved. The average true steady-state values of the observables with respect to $\hat{\rho}_{ss}$ are:

$$\bar{S}_z = \frac{\lambda_n \gamma_r}{\gamma_s (\gamma_n + \gamma_r) - \lambda_n \lambda_s}, \quad (10.49)$$

$$\bar{n} = \frac{\gamma_r \gamma_s}{\gamma_s (\gamma_n + \gamma_r) - \lambda_n \lambda_s}, \quad (10.50)$$

$$\bar{n}_o = \frac{\gamma_r \gamma_s}{\gamma_n \gamma_s - \lambda_n \lambda_s}, \quad (10.51)$$

where the bar designates the expectation value of the operators with respect to the steady-state density matrix, that is, $\bar{n} = \langle \hat{n} \rangle_{ss} = \text{tr}(\hat{n} \hat{\rho}_{ss})$.

Note When the temperature is much higher than the effective Zeeman splitting ($k_B T \gg \Omega$), the factors α and β approach 1. Then the equations (10.44) and (10.45) can be expressed in a more familiar form [79]:

$$\gamma_s = \frac{1}{2} (\gamma_a + \gamma_e - \gamma_h - \gamma_p) (\kappa_- + \kappa_+) + \gamma_p + \gamma_h, \quad (10.52)$$

$$\lambda_n = \frac{1}{4} (\gamma_a + \gamma_e - \gamma_h - \gamma_p) (\kappa_- - \kappa_+). \quad (10.53)$$

10.4 Quantum Regression

The quantum regression formula is a very strong statement that determines the correlators of an arbitrary operator \hat{O} in terms of any complete set of system operators \hat{A}_μ . For example, for a set of system operators \hat{A}_μ , the expectation values $\langle \hat{A}_\mu(t) \rangle$ satisfy a set of coupled differential equations as determined by the Liouville-von-Neumann equation. Now, the quantum regression theorem states that the correlators $\langle \hat{O}(t) \hat{A}_\mu(t + \tau) \rangle$ must satisfy the same set of differential equations as the expectation values $\langle \hat{A}_\mu(t) \rangle$ [102]. In particular, by expressing \hat{O} in terms of \hat{A}_μ , the ACF $c_O(\tau) = \langle \hat{O}(0) \hat{O}(\tau) \rangle$ can be calculated for any operator! This section uses this property to calculate the spectrum $\tilde{c}_K(2\pi\nu)$ for the ACF of fluctuations of the Kerr signal $c_K(\tau) = \langle \delta\hat{K}(0) \delta\hat{K}(\tau) \rangle$.

10.4.1 Fluctuation Operators

The goal of noise spectroscopy is to extract useful information from fluctuations of observables with respect to some equilibrium state. So far, only actual observables have been considered. Therefore, this subsection translates the results obtained for the steady-state solutions into expressions for fluctuations with respect to $\hat{\rho}_{ss}$.

The first step is to define a general fluctuation operator. Let \hat{O} be some system operator with expectation value $\langle \hat{O} \rangle$, then the fluctuation of \hat{O} is defined as:

$$\delta\hat{O} = \hat{O} - \langle \hat{O} \rangle \equiv \hat{O} - O. \quad (10.54)$$

In particular, the expectation value of a fluctuation is zero by definition: $\langle \delta\hat{O} \rangle = \langle \hat{O} \rangle - \langle \hat{O} \rangle = 0$. The expression for the fluctuations of the Kerr signal $\delta\hat{K}$ can easily be expressed using Eq. (10.41) in terms of the fluctuations of the spin $\delta\hat{S}_z$ and the occupancy $\delta\hat{n}$:

$$\delta\hat{K} = \cos(\varphi) (C_s^i \delta\hat{S}_z + C_n^i \delta\hat{n}) + \sin(\varphi) (C_s^r \delta\hat{S}_z + C_n^r \delta\hat{n}). \quad (10.55)$$

The kinetic equations derived in section §10.3.2 give a set of coupled differential equations for \hat{S}_z and \hat{n} . Therefore, a new set of kinetic equations for $\delta\hat{S}_z$ and $\delta\hat{n}$ must be derived to meet the requirements of the quantum regression formula. This step can be done by inserting the definition of the fluctuation operators (10.54) into Eq. (10.42) and (10.43), that is:

$$\begin{aligned} \frac{d}{d\tau} \langle \hat{S}_z \rangle &= \langle -\gamma_s \hat{S}_z + \lambda_n \hat{n} \rangle \\ \Leftrightarrow \frac{d}{d\tau} \langle \delta\hat{S}_z + S \rangle &= \langle -\gamma_s (\delta\hat{S}_z + S) + \lambda_n (\delta\hat{n} + n) \rangle \\ \Leftrightarrow \frac{d}{d\tau} \langle \delta\hat{S}_z \rangle &= \langle -\gamma_s \delta\hat{S}_z + \lambda_n \delta\hat{n} \rangle + \underbrace{(-\gamma_s S + \lambda_n n - \dot{S})}_{=0} \\ \Leftrightarrow \delta\dot{S}_z(\tau) &= -\gamma_s \delta S_z(\tau) + \lambda_n \delta n(\tau), \end{aligned} \quad (10.56)$$

and similarly

$$\delta\dot{n}(\tau) = -(\gamma_n + \gamma_r) \delta n(\tau) + \lambda_s \delta S_z(\tau). \quad (10.57)$$

Now multiplying the operators inside these expectation value expressions from

the left by the steady-state fluctuation operator $\delta\hat{K} = \delta\hat{K}(0)$ yields the differential expressions for the mixed correlators ($\tau > 0$):

$$\frac{d}{d\tau} \langle \delta\hat{K}(0)\delta\hat{S}_z(\tau) \rangle_{ss} = -\gamma_s \langle \delta\hat{K}(0)\delta\hat{S}_z(\tau) \rangle_{ss} + \lambda_n \langle \delta\hat{K}(0)\delta\hat{n}(\tau) \rangle_{ss}, \quad (10.58)$$

$$\frac{d}{d\tau} \langle \delta\hat{K}(0)\delta\hat{n}(\tau) \rangle_{ss} = -(\gamma_n + \gamma_r) \langle \delta\hat{K}(0)\delta\hat{n}(\tau) \rangle_{ss} + \lambda_s \langle \delta\hat{K}(0)\delta\hat{S}_z(\tau) \rangle_{ss}. \quad (10.59)$$

This system of differential equations must be solved to get a solution for the mixed correlators. A set of initial conditions at $\tau = 0$ is necessary for a complete solution. These are by construction the expectation values of the cross-correlators with respect to the steady-state density matrix ρ_{ss} that can be easily calculated as stated below.

10.4.2 Initial Conditions

In this subsection, the steady-state correlators $\langle \delta\hat{K}\delta\hat{S}_z \rangle_{ss} = \langle \delta\hat{K}(0)\delta\hat{S}_z(0) \rangle_{ss}$ and $\langle \delta\hat{K}\delta\hat{n} \rangle_{ss} = \langle \delta\hat{K}(0)\delta\hat{n}(0) \rangle_{ss}$ are calculated, which act as initial values for Eqs. (10.58) and (10.59). The first step is to insert the definition of (10.55) and use the linearity of the trace to express these correlators in terms of fluctuation operators $\delta\hat{S}_z$ and $\delta\hat{n}$:

$$\begin{aligned} \langle \delta\hat{K}\delta\hat{S}_z \rangle_{ss} &= \cos(\varphi) \left(C_s^i \langle \delta\hat{S}_z^2 \rangle_{ss} + C_n^i \langle \delta\hat{n}\delta\hat{S}_z \rangle_{ss} \right) \\ &\quad + \sin(\varphi) \left(C_s^r \langle \delta\hat{S}_z^2 \rangle_{ss} + C_n^r \langle \delta\hat{n}\delta\hat{S}_z \rangle_{ss} \right), \end{aligned} \quad (10.60)$$

$$\begin{aligned} \langle \delta\hat{K}\delta\hat{n} \rangle_{ss} &= \cos(\varphi) \left(C_s^i \langle \delta\hat{S}_z\delta\hat{n} \rangle_{ss} + C_n^i \langle \delta\hat{n}^2 \rangle_{ss} \right) \\ &\quad + \sin(\varphi) \left(C_s^r \langle \delta\hat{S}_z\delta\hat{n} \rangle_{ss} + C_n^r \langle \delta\hat{n}^2 \rangle_{ss} \right). \end{aligned} \quad (10.61)$$

These expectation values are defined with respect to the steady-state density matrix $\hat{\rho}_{ss}$. Consequently these expectation values can be expressed in terms of the steady-state values \hat{S}_z and \hat{n} . For squares of the fluctuation operators, the results are:

$$\begin{aligned}
 \langle \delta \hat{S}_z^2 \rangle_{\text{ss}} &= \langle \delta \hat{S}_z \delta \hat{S}_z \rangle_{\text{ss}} = \left\langle \left(\hat{S}_z - \langle \hat{S}_z \rangle_{\text{ss}} \right) \cdot \left(\hat{S}_z - \langle \hat{S}_z \rangle_{\text{ss}} \right) \right\rangle_{\text{ss}} \\
 &= \left\langle \hat{S}_z \hat{S}_z - 2 \hat{S}_z \langle \hat{S}_z \rangle_{\text{ss}} + \langle \hat{S}_z \rangle_{\text{ss}} \langle \hat{S}_z \rangle_{\text{ss}} \right\rangle_{\text{ss}} \\
 &= \langle \hat{S}_z \hat{S}_z \rangle_{\text{ss}} - 2 \langle \hat{S}_z \rangle_{\text{ss}} \langle \hat{S}_z \rangle_{\text{ss}} + \langle \hat{S}_z \rangle_{\text{ss}} \langle \hat{S}_z \rangle_{\text{ss}} \\
 &= \langle \hat{S}_z \hat{S}_z \rangle_{\text{ss}} - \bar{S}_z^2 \\
 &= \frac{\bar{n}}{4} - \bar{S}_z^2, \tag{10.62}
 \end{aligned}$$

$$\begin{aligned}
 \langle \delta \hat{n}^2 \rangle_{\text{ss}} &= \langle \delta \hat{n} \delta \hat{n} \rangle_{\text{ss}} = \left\langle \left(\hat{n} - \langle \hat{n} \rangle_{\text{ss}} \right) \cdot \left(\hat{n} - \langle \hat{n} \rangle_{\text{ss}} \right) \right\rangle_{\text{ss}} \\
 &= \langle \hat{n} \hat{n} - 2 \hat{n} \langle \hat{n} \rangle_{\text{ss}} + \langle \hat{n} \rangle_{\text{ss}} \langle \hat{n} \rangle_{\text{ss}} \rangle_{\text{ss}} \\
 &= \langle \hat{n} \hat{n} \rangle_{\text{ss}} - \bar{n}^2 \\
 &= \langle \hat{n} \rangle_{\text{ss}} - \bar{n}^2 \\
 &= \bar{n} (1 - \bar{n}). \tag{10.63}
 \end{aligned}$$

Note that Eq. (10.49) and Eq. (10.50) imply $\bar{S}_z = \lambda_n / \gamma_s \bar{n}$. Therefore, $\bar{n} = 0$ implies $\bar{S}_z = 0$ and thus $\langle \delta \hat{S}_z^2 \rangle = 0$, as a permanently empty QD does not produce any SN.

For the mixed terms, the results are as follows:

$$\begin{aligned}
 \langle \delta \hat{S}_z \delta \hat{n} \rangle_{\text{ss}} &= \langle \delta \hat{n} \delta \hat{S}_z \rangle_{\text{ss}} = \left\langle \left(\hat{n} - \langle \hat{n} \rangle_{\text{ss}} \right) \cdot \left(\hat{S}_z - \langle \hat{S}_z \rangle_{\text{ss}} \right) \right\rangle_{\text{ss}} \\
 &= \left\langle \hat{n} \hat{S}_z - \hat{n} \langle \hat{S}_z \rangle_{\text{ss}} - \langle \hat{n} \rangle_{\text{ss}} \hat{S}_z + \langle \hat{n} \rangle_{\text{ss}} \langle \hat{S}_z \rangle_{\text{ss}} \right\rangle_{\text{ss}} \\
 &= \langle \hat{n} \hat{S}_z \rangle_{\text{ss}} - \langle \hat{n} \rangle_{\text{ss}} \langle \hat{S}_z \rangle_{\text{ss}} \\
 &= \langle \hat{S}_z \rangle_{\text{ss}} - \bar{n} \bar{S}_z \\
 &= \bar{S}_z (1 - \bar{n}). \tag{10.64}
 \end{aligned}$$

Now, substituting these results back into equations (10.60) and (10.61) completes the expressions of Kerr fluctuation steady-state correlators:

$$\langle \delta \hat{K} \delta \hat{S}_z \rangle_{ss} = \cos(\varphi) \left(C_n^i \bar{S}_z (1 - \bar{n}) + C_s^i \left(\frac{\bar{n}}{4} - \bar{S}_z^2 \right) \right) \quad (10.65)$$

$$+ \sin(\varphi) \left(C_n^r \bar{S}_z (1 - \bar{n}) + C_s^r \left(\frac{\bar{n}}{4} - \bar{S}_z^2 \right) \right),$$

$$\langle \delta \hat{K} \delta \hat{n} \rangle_{ss} = \cos(\varphi) (C_s^i \bar{S}_z + C_n^i \bar{n}) (1 - \bar{n}) \quad (10.66)$$

$$+ \sin(\varphi) (C_s^r \bar{S}_z + C_n^r \bar{n}) (1 - \bar{n}).$$

10.4.3 Separation of Time Scales

A direct solution of Eqs. (10.58) and (10.59) is quite bulky. Therefore, before looking at the exact solution, it is helpful to look at a possible approximation if the effective rate of change γ_n is much slower than γ_s and both decays happen on separate and independent time scales. Under these conditions, the occupancy fluctuations $\delta \hat{n}$ appear frozen in time for the much faster fluctuations of $\delta \hat{S}_z$. On the other hand, for the occupancy fluctuations $\delta \hat{n}$, the fluctuations of $\delta \hat{S}_z$ are so fast that they contribute only through their steady-state value. A similar argument applies equivalently to the correlators.

This separation of correlator time scales (SCTS) is sketched in Fig. 10.8. For short delays, the ACF is dominated by the fast decay rate γ_s , while on longer time scales, an effective rate γ_{n_1} eventually takes over. This new slow decay rate will be defined below. It incorporates the steady-state limit of Eq. (10.58) and is, in general, not equal to either γ_n or to $\gamma_n + \gamma_r$.

Pseudo-spin Fluctuation

Eq. (10.58) can be solved by assuming that the correlator follows $\langle \delta \hat{K} \delta n(\tau) \rangle$ adiabatically [79]. The solution is, of course, just an exponential decay with the decay rate γ_s :

$$\langle \delta \hat{K}(0) \delta \hat{S}_z(\tau) \rangle_{ss} = \frac{\lambda_n}{\gamma_s} \langle \delta \hat{K}(0) \delta \hat{n}(\tau) \rangle_{ss} + e^{-\tau \gamma_s} \left(\langle \delta \hat{K} \delta \hat{S}_z \rangle_{ss} - \frac{\lambda_n}{\gamma_s} \langle \delta \hat{K} \delta \hat{n} \rangle_{ss} \right) \quad (10.67)$$

$$\stackrel{\tau \rightarrow \infty}{\approx} \frac{\lambda_n}{\gamma_s} \langle \delta \hat{K}(0) \delta \hat{n}(\tau) \rangle_{ss} \quad (10.68)$$

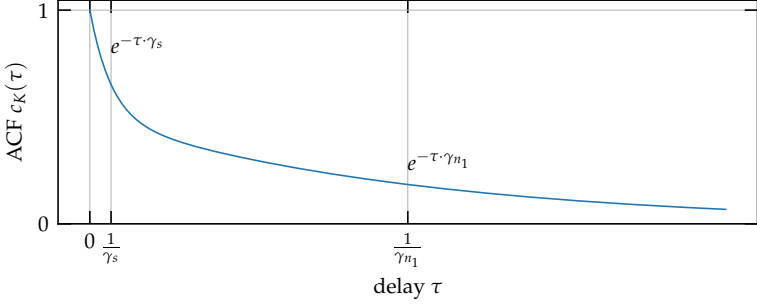


Figure 10.8: Sketch of the decay of the Kerr fluctuations auto correlation function $c_K(\tau)$. For short delays the $c_K(\tau)$ is dominated by the fast decay with the rate γ_s . For longer time scales $c_K(\tau)$ decays with the slower rate γ_{n_1} .

Note that in Eq. (10.67), the value of the correlator $\langle \delta \hat{K} \delta \hat{n}(\tau) \rangle_{ss}$ has to be replaced in the exponential term by its steady-state value $\langle \delta \hat{K} \delta \hat{n} \rangle_{ss}$ to enforce adiabatic following for long delays τ as seen in Eq. (10.68).

Occupancy Fluctuation

Next, the corresponding solution for the occupancy fluctuations can be derived using the result for the pseudo-spin fluctuations correlator. Inserting the steady-state solution (10.68) into (10.59) yields the following:

$$\frac{d}{dt} \langle \delta \hat{K}(0) \delta \hat{n}(\tau) \rangle_{ss} = -\gamma_{n_1} \langle \delta \hat{K}(0) \delta \hat{n}(\tau) \rangle_{ss},$$

with

$$\gamma_{n_1} = \gamma_n + \gamma_r - \frac{\lambda_s \lambda_n}{\gamma_s}. \quad (10.69)$$

Again, the solution is a simple exponential decay of the correlator with the newly defined decay rate γ_{n_1} :

$$\langle \delta \hat{K}(0) \delta \hat{n}(\tau) \rangle_{ss} = e^{-\tau \gamma_{n_1}} \langle \delta \hat{K} \delta \hat{n} \rangle_{ss}. \quad (10.70)$$

Kerr Fluctuation

The solutions (10.67) and (10.70) completely determine the decay of the ACF $c_K(\tau) = \langle \delta\hat{K}(0)\delta\hat{K}(\tau) \rangle_{ss}$, which can be expressed as:

$$\begin{aligned}
 c_K(\tau) &:= \langle \delta\hat{K}(0)\delta\hat{K}(\tau) \rangle_{ss} = \cos(\varphi) \left(C_s^i \langle \delta\hat{K}(0)\delta\hat{S}_z(\tau) \rangle_{ss} + C_n^i \langle \delta\hat{K}(0)\delta\hat{n}(\tau) \rangle_{ss} \right) \\
 &\quad + \sin(\varphi) \left(C_s^r \langle \delta\hat{K}(0)\delta\hat{S}_z(\tau) \rangle_{ss} + C_n^r \langle \delta\hat{K}(0)\delta\hat{n}(\tau) \rangle_{ss} \right) \\
 &= \cos(\varphi) \left(C_s^i e^{-\tau\gamma_s} \left(\langle \delta\hat{K}\delta\hat{S}_z \rangle_{ss} - \langle \delta\hat{K}\delta\hat{n} \rangle_{ss} \frac{\lambda_n}{\gamma_s} \right) \right) \\
 &\quad + \cos(\varphi) \left(\langle \delta\hat{K}\delta\hat{n} \rangle_{ss} e^{-\tau\gamma_{n_1}} \left(C_n^i + C_s^i \frac{\lambda_n}{\gamma_s} \right) \right) \\
 &\quad + \sin(\varphi) \left(C_s^r e^{\gamma_s(-t)} \left(\langle \delta\hat{K}\delta\hat{S}_z \rangle_{ss} - \langle \delta\hat{K}\delta\hat{n} \rangle_{ss} \frac{\lambda_n}{\gamma_s} \right) \right) \\
 &\quad + \sin(\varphi) \left(\langle \delta\hat{K}\delta\hat{n} \rangle_{ss} e^{-\tau\gamma_{n_1}} \left(C_n^r + C_s^r \frac{\lambda_n}{\gamma_s} \right) \right). \quad (10.71)
 \end{aligned}$$

By definition, the ACF is symmetric around $\tau = 0$, and therefore τ can be replaced by $|\tau|$. The correlation spectrum $\tilde{c}_K(\nu)$ of this ACF is then just a FT:

$$\begin{aligned}
 \tilde{c}_{K,sep}(\nu) &= A_{SN} \frac{\mathcal{E}^2 \gamma_s}{4\nu^2 \pi^2 + \gamma_s^2} + A_{ON} \frac{\mathcal{E}^2 \gamma_{n_1}}{4\nu^2 \pi^2 + \gamma_{n_1}^2}, \quad (10.72) \\
 A_{SN} &:= \frac{1}{\mathcal{E}^2} 2 \cos(\varphi) \left(C_s^i \langle \delta\hat{K}\delta\hat{S}_z \rangle_{ss} - C_s^i \frac{\lambda_n}{\gamma_s} \langle \delta\hat{K}\delta\hat{n} \rangle_{ss} \right) \\
 &\quad + \frac{1}{\mathcal{E}^2} 2 \sin(\varphi) \left(C_s^r \langle \delta\hat{K}\delta\hat{S}_z \rangle_{ss} - C_s^r \frac{\lambda_n}{\gamma_s} \langle \delta\hat{K}\delta\hat{n} \rangle_{ss} \right), \\
 A_{ON} &:= \frac{1}{\mathcal{E}^2} 2 \cos(\varphi) \left(C_n^i \langle \delta\hat{K}\delta\hat{n} \rangle_{ss} + C_s^i \frac{\lambda_n}{\gamma_s} \langle \delta\hat{K}\delta\hat{n} \rangle_{ss} \right) \\
 &\quad + \frac{1}{\mathcal{E}^2} 2 \sin(\varphi) \left(C_n^r \langle \delta\hat{K}\delta\hat{n} \rangle_{ss} + C_s^r \frac{\lambda_n}{\gamma_s} \langle \delta\hat{K}\delta\hat{n} \rangle_{ss} \right).
 \end{aligned}$$

Equation (10.72) contains two Lorentzian contributions with widths γ_s and γ_{n_1} . The first contribution is assigned to SN in analogy to bulk SNS in GaAs. The second contribution is a consequence of occupancy fluctuations and is assigned to ON. The factors A_{SN} and A_{ON} are the total noise powers of the corresponding fluctuations.

10.4.4 Exact Solution

The SCTS, as described above, is usually only valid when the ratio of the effective damping rates is sufficiently large $\gamma_s/\gamma_n \gg 1$. In general, this is not the case, and the correlation spectrum has to be derived differently. The system of differential equations given by Eqs. (10.58) and (10.59) can be expressed in vector form as:

$$\frac{d}{d\tau} \mathbf{c}(\tau) = A \cdot \mathbf{c}(\tau), \quad (10.73)$$

where $c(\tau)$ is a vector of the two correlators and A is a delay-independent matrix of the coefficients:

$$\begin{aligned} \mathbf{c}(\tau) &= \begin{pmatrix} c_s(\tau) \\ c_n(\tau) \end{pmatrix} = \begin{pmatrix} \langle \delta\hat{K}(0)\delta\hat{S}_z(\tau) \rangle_{ss} \\ \langle \delta\hat{K}(0)\delta\hat{S}_z(\tau) \rangle_{ss} \end{pmatrix}, \\ \mathbf{c}(0) &= \begin{pmatrix} c_s(0) \\ c_n(0) \end{pmatrix} = \begin{pmatrix} \langle \delta\hat{K}\delta\hat{S}_z \rangle_{ss} \\ \langle \delta\hat{K}\delta\hat{S}_z \rangle_{ss} \end{pmatrix}, \\ A &= \begin{pmatrix} -\gamma_s & \lambda_n \\ \lambda_s & -\gamma_n - \gamma_r \end{pmatrix}. \end{aligned}$$

The time domain expressions of these correlators are quite intricate. However, for the final expression $\tilde{c}_K(\omega = 2\pi\nu)$, only the Fourier-transformed versions of these correlators $\tilde{c}_s(\omega)$ and $\tilde{c}_n(\omega)$ are necessary. In the frequency domain, the expressions and the solution of the differential equation can be greatly simplified.

A general complex solution for the Fourier transformed correlators in this equation can be obtained by inverting the matrix given by $R = -(A + i\omega)$, that is:

$$\tilde{\mathbf{c}}^*(\omega) = R^{-1} \cdot \mathbf{c}(0). \quad (10.74)$$

Because this solution is complex, but the system of differential equations is real, the sought real solution is recovered by taking two times the real part of $\tilde{\mathbf{c}}^*(\omega)$:

$$\tilde{\mathbf{c}}(\omega) = 2\Re(\tilde{\mathbf{c}}^*(\omega)).$$

The inverse of R is given by the well-known formula using the determinant and adjugate of the initial matrix:

$$R^{-1} = \frac{1}{\det(R)} \text{ad}(R) = \frac{1}{\det(R)} \begin{pmatrix} \gamma_n + \gamma_r - i\omega & \lambda_n \\ \lambda_s & \gamma_s - i\omega \end{pmatrix}. \quad (10.75)$$

Here, the determinant of R has a special meaning, as the complex roots that satisfy the equation $\det(R) = 0$ can be used to express the Fourier-transformed correlators. These complex roots have the general form:

$$\gamma_{c_{\pm}} = \frac{1}{2} (\gamma_u \pm \sqrt{\lambda_u}), \quad (10.76)$$

where $\gamma_u = \gamma_s + \gamma_n + \gamma_r$ and $\lambda_u = (\gamma_n + \gamma_r - \gamma_s)^2 + 4\lambda_n\lambda_s$. Note that λ_u in Eq. (10.76) can be negative. In this case the roots acquire an imaginary component and the structure of the solution fundamentally changes, as is discussed below in section §10.4.4.

Using these roots the quotient in Eq. (10.75) can be written as.

$$1/\det(R) = \mathbf{N}_+ \mathbf{N}_-,$$

where $\mathbf{N}_{\pm} = (\gamma_{c_{\pm}} - i\omega)^{-1}$. Note that the \mathbf{N}_{\pm} expressions have the following real and imaginary parts:

$$\begin{aligned} \Re(\mathbf{N}_{\pm}) &= \frac{\Re(\gamma_{c_{\pm}})}{(\omega - \Im(\gamma_{c_{\pm}}))^2 + \Re(\gamma_{c_{\pm}})^2}, \\ \Im(\mathbf{N}_{\pm}) &= \frac{\omega - \Im(\gamma_{c_{\pm}})}{(\omega - \Im(\gamma_{c_{\pm}}))^2 + \Re(\gamma_{c_{\pm}})^2}. \end{aligned}$$

For example, the real parts of the \mathbf{N}_{\pm} expressions are Lorentzians in the frequency domain centered at $\omega = \Im(\gamma_{c_{\pm}})$ with widths of $\Re(\gamma_{c_{\pm}})$. The inverted matrix expression can then be further simplified using the identities:

$$\begin{aligned} \mathbf{N}_+ \mathbf{N}_- &= \frac{1}{\sqrt{\lambda_u}} (\mathbf{N}_- - \mathbf{N}_+), \\ i\omega \mathbf{N}_+ \mathbf{N}_- &= \frac{1}{\sqrt{\lambda_u}} (\mathbf{N}_+ \gamma_{c_+} + \mathbf{N}_- \gamma_{c_-}). \end{aligned}$$

The simplified form of the inverted matrix is then:

$$R^{-1} = \frac{1}{\sqrt{\lambda_u}} \times \begin{pmatrix} \mathbf{N}_+ (\gamma_{c_+} - \gamma_n - \gamma_r) - \mathbf{N}_- (\gamma_{c_-} - \gamma_n - \gamma_r) & \lambda_n (\mathbf{N}_- - \mathbf{N}_+) \\ \lambda_s (\mathbf{N}_- - \mathbf{N}_+) & \mathbf{N}_+ (\gamma_{c_+} - \gamma_s) - \mathbf{N}_- (\gamma_{c_-} - \gamma_s) \end{pmatrix}. \quad (10.77)$$

The solution vector can therefore be written as:

$$\tilde{c}^\bullet(\omega) = R^{-1} \cdot c(0) = \frac{1}{2} \begin{pmatrix} \Lambda_+ \mathbf{N}_+ + \Lambda_- \mathbf{N}_- \\ Y_+ \mathbf{N}_+ + Y_- \mathbf{N}_- \end{pmatrix},$$

where

$$\Lambda_\pm = \pm \frac{1}{\sqrt{\lambda_u}} 2 (c_s(0) (\gamma_{c_\pm} - \gamma_n - \gamma_r) - c_n(0) \lambda_n),$$

$$Y_\pm = \pm \frac{1}{\sqrt{\lambda_u}} 2 (c_n(0) (\gamma_{c_\pm} - \gamma_s) - c_s(0) \lambda_s).$$

Finally, the general real solution vector is acquired from the complex solution by taking two times the real part of it:

$$\begin{aligned} \tilde{c}(\omega) = & \Re(\mathbf{N}_+) \begin{pmatrix} \Re(\Lambda_+) \\ \Re(Y_+) \end{pmatrix} + \Re(\mathbf{N}_-) \begin{pmatrix} \Re(\Lambda_-) \\ \Re(Y_-) \end{pmatrix} \\ & - \Im(\mathbf{N}_+) \begin{pmatrix} \Im(\Lambda_+) \\ \Im(Y_+) \end{pmatrix} - \Im(\mathbf{N}_-) \begin{pmatrix} \Im(\Lambda_-) \\ \Im(Y_-) \end{pmatrix}. \end{aligned} \quad (10.78)$$

This spectrum is *well-defined* regardless of the parameter values, even if the roots γ_{c_\pm} and coefficients Λ_+ , Y_+ have an imaginary component. The complete Kerr spectrum is then given by:

$$\tilde{c}_K(\omega = 2\pi\nu) = \left(\cos(\varphi) \begin{pmatrix} C_s^i & C_n^i \end{pmatrix}^T + \sin(\varphi) \begin{pmatrix} C_s^r & C_n^r \end{pmatrix}^T \right) \cdot \tilde{c}(\omega). \quad (10.79)$$

Double Lorentzian Regime

An important special case is when the expression λ_u is positive. In this case, the complex roots $\gamma_{c_{\pm}}$ are purely real, and all the coefficients in Eq. (10.78) are also real. The whole expression then simplifies greatly:

$$\tilde{c}(\omega) = \Re(\mathbf{N}_+) \begin{pmatrix} \Lambda_+ \\ Y_+ \end{pmatrix} + \Re(\mathbf{N}_-) \begin{pmatrix} \Lambda_- \\ Y_- \end{pmatrix}.$$

From this simplified expression, it is readily visible that both correlators are given by two Lorentzian contributions:

$$\mathfrak{L}_{\pm}(\omega) = \Re(\mathbf{N}_{\pm}) = \frac{\gamma_{c_{\pm}}}{\omega^2 + \gamma_{c_{\pm}}^2}, \quad (10.80)$$

that are centered at $\omega = 0$ and have a width of $\gamma_{c_{\pm}}$. The powers of these contributions in the Kerr spectrum are:

$$A_{\pm} = (\cos(\varphi) C_s^i + \sin(\varphi) C_s^r) \Lambda_{\pm} + (\cos(\varphi) C_n^i + \sin(\varphi) C_n^r) Y_{\pm}. \quad (10.81)$$

Mixed Regime

When the expression λ_u is negative, the roots $\gamma_{c_{\pm}}$ are no longer completely real, and the solution vector cannot be decomposed into purely Lorentzian contributions, like in the previous case. Instead the solution has the form:

$$\begin{aligned} \tilde{c}(\omega) = & (\Re(\mathbf{N}_+) + \Re(\mathbf{N}_-)) \mathbf{c}(0) \\ & + (\Im(\mathbf{N}_+) - \Im(\mathbf{N}_-)) \begin{pmatrix} \frac{2c_n(0)\lambda_n + 2c_s(0)(\gamma_n + \gamma_r) - \gamma_u c_s(0)}{4\sqrt{\lambda_u^2}} \\ \frac{-\gamma_u c_n(0) + 2c_n(0)\gamma_s + 2c_s(0)\lambda_s}{4\sqrt{\lambda_u^2}} \end{pmatrix}. \end{aligned}$$

Both components consist of two Lorentzian and two non-Lorentzian contributions of equal amplitude centered at $\omega = \pm \frac{1}{2} \sqrt{|\lambda_u|}$.

General Regime

The general solution vector can be further simplified by forgoing the explicit form derived using the \mathbf{N}_{\pm} expressions. Then, the resulting expressions for the correla-

tors can no longer be simplified into individual contributions, but the solution is valid for all model parameters. This solution can be stated as follows:

$$\tilde{c}(\omega) = \left(\begin{array}{c} \frac{2\tilde{\xi}_1(s_0\gamma_c+n_0\lambda_n)+2\omega^2(s_0\gamma_s-n_0\lambda_n)}{\tilde{\xi}_2\omega^2+\tilde{\xi}_1^2+\omega^4} \\ \frac{2\omega^2(n_0\gamma_c-s_0\lambda_s)+2\tilde{\xi}_1(n_0\gamma_s+s_0\lambda_s)}{\tilde{\xi}_2\omega^2+\tilde{\xi}_1^2+\omega^4} \end{array} \right), \quad (10.82)$$

where the following substitutions were used for brevity:

$$\begin{aligned} \gamma_c &= \gamma_n + \gamma_r, \\ \tilde{\xi}_1 &= \gamma_c\gamma_s - \lambda_n\lambda_s, \\ \tilde{\xi}_2 &= \gamma_c^2 + 2\lambda_n\lambda_s + \gamma_s^2. \end{aligned}$$

10.4.5 Model Units and Scaling

Formulas (10.82) and (10.72) have been derived using a $\hbar = 1$ convention, and this has to be considered to calculate spectra in conventional units. Essentially, the approach is to a) express all model parameters in ratios of quantities of the same units and b) absorb all remaining units in a relative scaling factor. To this end, first, the dipole scaling factors $C_{s,n}^{i,r}$ in Eqs. (10.37) and (10.40) have to be divided by the magnitude of the dipole transition matrix \mathcal{E} . This makes the spectrum power independent by dividing it by \mathcal{E}^2 (one power scale). Second, the intrinsic trion relaxation rate γ_0 is eliminated from the model by using γ_d as a parameter instead and by substituting the ratio $2\mathcal{E}/\gamma_0\gamma_d$ with a dimensionless relative intensity parameter r in the formula (10.33) for the saturation broadened line width γ_1 . With γ_0 eliminated, the slow and fast relaxation rates appear only in ratios, and conventional units can be used for the model. Finally, PSD spectra recorded in an experiment are usually normalized single one-sided periodograms containing only positive frequencies. This convention is employed to make the spectra comparable to ones recorded by an analog integrating spectrometer. Contributions at negative frequencies are “reflected” at $\nu = 0$ and added to their corresponding contributions at positive frequencies. Therefore, the PSD spectrum has twice the amplitude of $\tilde{c}_K(2\pi\nu)$. Finally, the experimental spectrum is described by the formula:

$$\mathfrak{S}_K(\nu) = A_{\text{PSD}} \frac{2}{\bar{c}^2} \cdot \tilde{c}_K(2\pi\nu; r, \alpha, \beta, \varphi; \Omega, \Delta, \gamma_d; \gamma_e, \gamma_h, \gamma_a, \gamma_r, \gamma_p), \quad (10.83)$$

where the first four parameters are dimensionless ($r, \alpha, \beta, \varphi$), the next three parameters have the energy unit μeV (Ω, Δ, γ_d), and the remaining parameters have the frequency unit Hz. The overall scaling parameter A_{PSD} expresses the sensitivity of the experiment in the given units: multiplying the frequency scale by a factor of ζ_f scales the spectrum down by a factor of ζ_f while multiplying the energy scale by a factor of ζ_E scales the spectrum up by a factor of ζ_E^2 .

10.5 Regression Breakdown

On the surface, the SCTS solution from section §10.4.3 appears experimentally tremendously more useful than the exact solution in section §10.4.4, as the results of the former can be reasoned about more easily experimentally and on a *per-spectrum* basis. For any experimental situation, the predicted spectrum consists of two Lorentzian contributions that have a well-defined meaning of SN and ON fluctuations. The parameters describing the spectrum are exactly the four numbers predicted by the SCTS approximation from the underlying model parameters P_M :

$$P_M = (r, \alpha, \beta, \varphi, \Omega, \gamma_d, \gamma_e, \gamma_h, \gamma_a, \gamma_r, \gamma_p),$$

$$P_{\text{SCTS}}(\Delta) = P_{\text{SCTS}}(\Delta; P_M) = (A_{\text{SN}}, \gamma_s, A_{\text{ON}}, \gamma_{n_1}).$$

This simple picture works very well when the Zeeman splitting is less than the line width. However, the approach breaks down spectacularly for larger splittings, as this section demonstrates.

10.5.1 Regression Parameters

The roots $\gamma_{c_{\pm}}$ of the exact solution in Eq. (10.76) remain real for most parameter ranges. In this case, the exact spectrum decomposes into two Lorentzian components according to section §10.4.4: $\tilde{c}_K(\omega) = \sum_{\pm} \mathfrak{L}_{\pm}(\omega) A_{\pm}$. The spectrum is then determined by four numbers: $P_{\text{LL}}(\Delta) = (\gamma_{c_+}, A_+, \gamma_{c_-}, A_-)$. On the other hand, a non-linear regression of two *dissimilar* Lorentzian-shaped model func-

tions (fixed at $\nu = 0$) to an experimental spectrum yields the four fit parameters: $P_{LL}^*(\Delta) = (\gamma_{br}^*, A_{br}^*, \gamma_{nr}^*, A_{nr}^*)$, where the subscripts stand for the broad and narrow contributions, respectively. As long as the two contributions in P_{LL} are dissimilar and physical, the regression will yield estimates $P_{LL}^*(\Delta) \approx P_{LL}(\Delta)$ that closely match the exact numbers, assuming the exact spectrum describes the experimental spectrum well. When the SCTS approximation is valid, the parameters $P_{SCTS}(\Delta)$ are very close to the values of $P_{LL}(\Delta)$. Therefore the approximate mapping

$$P_{LL}^*(\Delta) \approx P_{LL}(\Delta) \approx P_{SCTS}(\Delta) \quad (10.84)$$

allows to extract the desired parameters and explains the simple assignment of noise contributions in the evaluation performed in Refs. [150, 96, 67]. Using the detuning and intensity dependences of $P_{SCTS}(\Delta)$, it is then possible to make estimates P_{M}^* of the underlying model parameters of P_M .

10.5.2 Breakdown

The mapping in Eq. (10.84) breaks down for sufficiently large Zeeman splittings, as depicted in Fig. 10.9. The upper panel depicts correlation rates, while the lower panel depicts the corresponding noise powers. The spectrum parameters $P_{SCTS}(\Delta)$ for the SCTS approximation and the parameters from the exact decomposition $P_{LL}(\Delta)$ are plotted over different detunings Δ using dashed and solid curves, respectively. Here, the parameters $P_{LL}(\Delta)$ can be considered the *optimal* result of a per-spectrum regression that enforces two Lorentzian contributions. For comparison, the black dotted curves depict the result of a single-Lorentzian regression to the exact spectrum, which simulates the quality of the gained estimate, when one spectral contribution is ignored. This figure provides several insights.

Arbitrariness of the Decomposition

The composition provided section §10.4.4 is unique. No other decomposition into two $\nu = 0$ Lorentzian contributions of different widths is possible for parameters where the decomposition is possible. However, this decomposition is somewhat arbitrary in the general case, as visible in the orange-shaded region in section §10.4.4. In this region, the “area” A_- of the second contribution becomes negative and no longer has the physical meaning of a noise power. Further on in the red band, the roots $\gamma_{c_{\pm}}$ acquire an imaginary component and lose the physical mean-

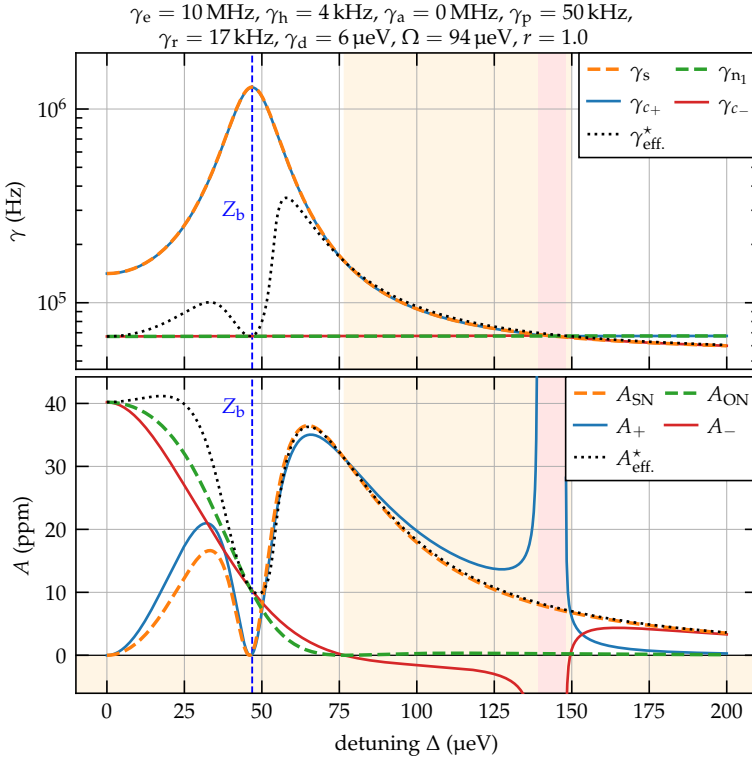


Figure 10.9: Comparison of the spectrum parameters for the SCTS approximation and the exact solution without an Auger relaxation channel. The used model parameters P_M are indicated on top of the figure. The top (bottom) panel depicts correlation rates (noise powers). The SCTS parameters $\gamma_s, \gamma_{n_1}, A_{SN}, A_{ON}$ are plotted using dashed lines. The parameters of the exact solution $\gamma_{c_+}, \gamma_{c_-}, A_+, A_-$ are plotted using solid lines. The black dotted curve is a single Lorentzian fit to the exact spectrum ($\gamma_{\text{eff}}^*, A_{\text{eff}}^*$). Inside of the orange shaded bands the decomposition of the exact solution has no physical meaning. Inside the red band, the $\gamma_{c_{\pm}}$ roots have an imaginary component and no decomposition into two Lorentzians exists.

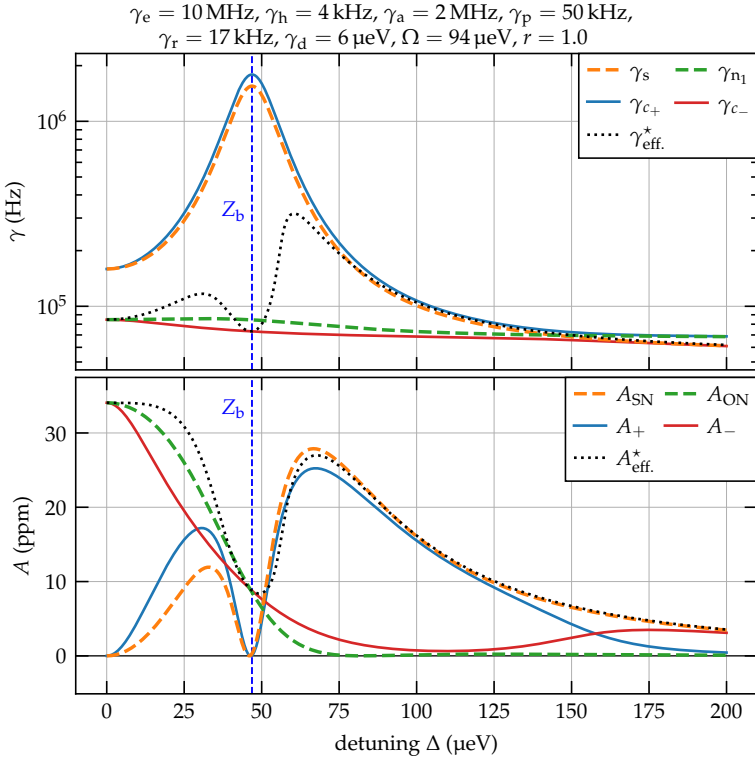


Figure 10.10: Comparison of the spectrum parameters for the SCTS approximation and the exact solution with an Auger relaxation channel. The used model parameters P_M are indicated on top of the figure. The top (bottom) panel depicts correlation rates (noise powers). The SCTS parameters $\gamma_s, \gamma_{n_1}, A_{SN}, A_{ON}$ are plotted using dashed lines. The parameters of the exact solution $\gamma_{c_+}, \gamma_{c_-}, A_+, A_-$ are plotted using solid lines. The black dotted curve is a single Lorentzian fit to the exact spectrum ($\gamma_{\text{eff}}^*, A_{\text{eff}}^*$).

ing of a correlation rate. Note that the issue is with the decomposition, not with the exact spectrum. The estimates provided by the single-Lorentzian regression enter and leave the unphysical bands without any perceptible jumps.

Extended Range of Approximation

A sufficiently large Auger rate lifts the unphysical region, as depicted in Fig. 10.10. All parameters, except for γ_a , are kept the same as in section §10.4.4. For this parameter set, the roots $\gamma_{c_{\pm}}$ stay real for all detunings, and it is easier to see the detuning dependence of individual parameters. For both simulations, the numerical values of the correlation rates predicted by the SCTS approximation are very close to the “broad” and “narrow” roots of the exact solution. Note that in the vicinity of $\gamma_s \approx \gamma_{n_1}$, the meaning of “narrow” and “broad” flips for the $\gamma_{c_{\pm}}$ roots. This correspondence is surprising for large detunings because, during the derivation of the SCTS approximation, the assumption $\gamma_s \gg \gamma_{n_1}$ has to be made. However, even for detunings where $\gamma_s \lesssim \gamma_{n_1}$, the SCTS predictions γ_s , γ_{n_1} , and A_{SN} remain good approximations. This correspondence is exploited in section §10.6 to make qualitative predictions about model parameters.

The estimates of the single-Lorentzian regression yield numerical values that are very close to the SCTS predictions of γ_s and A_{SN} for $\gamma_s \lesssim \gamma_{n_1}$. Therefore, qualitative estimates can be acquired from single-spectra regressions, ignoring the weaker spectral contribution in this region. These estimates can be compared with the SCTS predictions, but they can be interpreted as the SN contribution only if the noise power of one of the contributions is negligible.

Single-Spectra Regression Breakdown

Near of the resonance, the noise power is distributed between the two contributions of the exact solution. Both contributions bear a significant noise power that cannot be ignored. While a double-Lorentzian model function perfectly describes the spectrum, no mapping exists that could be used to decompose the noise powers of the two Lorentzians into SN and ON contributions. The single-spectrum regression *breaks down* and becomes meaningless.

Asymptotic Convergence

The single-Lorentzian regression has another valuable trait. For the asymptotic values $\Delta \rightarrow 0$ and $\Delta \rightarrow \infty$, the regression simultaneously coincides with one contribution from the SCTS prediction and the exact solution. Therefore, the asymptotic values can be used to extract some model parameters from the correlation rates. For $\Delta \approx 0$ and $|\Delta| \gg \Omega/2$, respectively, the SCTS rates γ_{n_1} and γ_s become:

$$\lim_{\Delta \rightarrow 0} \gamma_{\text{eff.}}^* = \lim_{\Delta \rightarrow 0} \gamma_{n_1} = \gamma_r + \gamma_p + \frac{r}{(r+1)} \frac{2\gamma_d^2}{4\gamma_d^2 + \Omega^2} (\gamma_a - \gamma_p), \quad (10.85)$$

$$\lim_{\Delta \rightarrow \infty} \gamma_{\text{eff.}}^* = \lim_{\Delta \rightarrow \infty} \gamma_s = \frac{(\alpha+1)}{2} \gamma_h + \gamma_p. \quad (10.86)$$

For example, the hole relaxation rate and the photoeffect coefficient γ_p/r can be extracted from the intensity dependence of the $\Delta \rightarrow \infty$ value.

Well Separated Regions

Regions, where the SCTS remains a good approximation can be found by repeating the simulation for a set of different Zeeman splittings. A comparison of SCTS predictions and the exact decomposition is depicted in Fig. 10.11 for different Zeeman splittings and otherwise the same model parameters as in Fig. 10.10. In each panel, the location of the blue Zeeman branch is plotted using a black dashed line as a guide for the eye. The color scale corresponds to the difference between the indicated components of $P_{\text{SCTS}}(\Delta)$ and $P_{\text{LL}}(\Delta)$. Here, the parameters of the exact decomposition are redefined to account for the flip in meaning between the $\gamma_{c_{\pm}}$ roots:

$$A_{\gtrless}, \gamma_{c_{\gtrless}} = \begin{cases} A_{\pm}, \gamma_{c_{\pm}} & \gamma_s > \gamma_{n_1} \\ A_{\mp}, \gamma_{c_{\mp}} & \text{else.} \end{cases}$$

(The location where the roots flip can slightly deviate from the $\gamma_s = \gamma_{n_1}$ point, but this deviation is usually very small.) The regions where $\gamma_{c_{\pm}}$ roots change their meaning (and acquire an imaginary component if γ_a is small enough) are visible as sharp bent curves on the right and top sides of the four panels. In these regions, the two solutions cannot be compared in principle, as explained above. The region enclosed by these curves is where the noise power redistributes between the A_{\pm} and deviations between $P_{\text{LL}}(\Delta)$ and $P_{\text{SCTS}}(\Delta)$ are most prominent. Within this

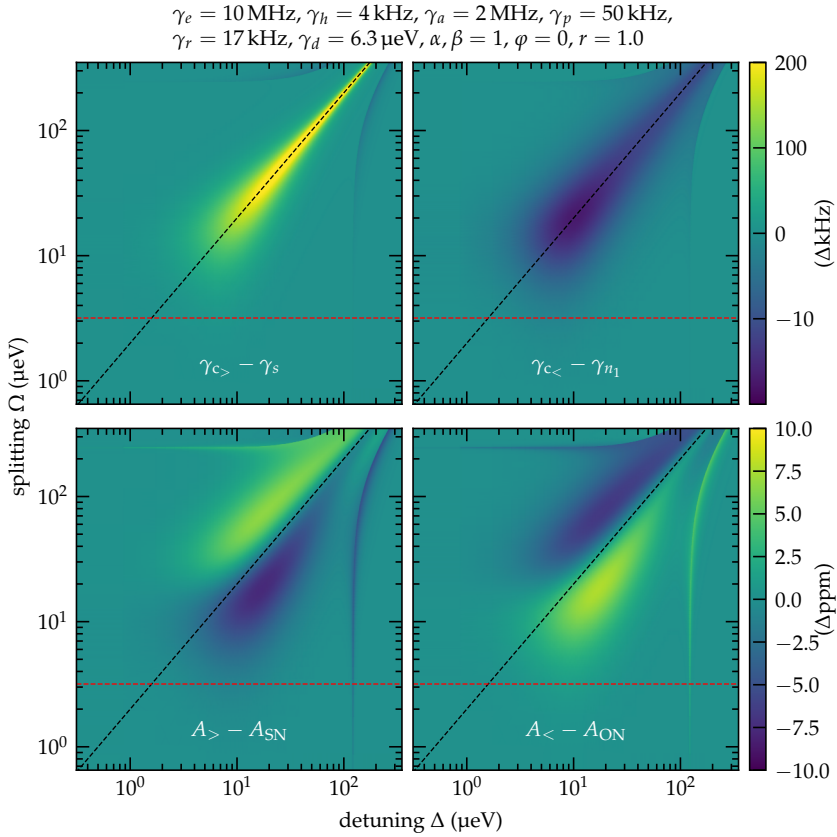


Figure 10.11: Comparison of the decomposition of the exact solution with the SCTS predictions for the specified model parameters. The position of the blue Zeeman branch Z_b of the transition is plotted using dashed black diagonal lines. The color map is shared for each row and is split for the upper panels to consistently display positive and negative deviations. The red dashed line indicates the region ($\Omega < \gamma_d/2$) where the SCTS remains a good approximation for all detunings.

	regression	SCTS	interpretation
$0 < \Delta < \Omega/2 + \gamma_d$	$\mathcal{L}\mathcal{L}$	γ_s, γ_{n_1}	qualitative
$ \Delta > \Omega/2 + \gamma_d$	\mathcal{L}	γ_s, A_{SN}	qualitative
$\Delta \rightarrow \pm\infty$	\mathcal{L}	γ_s, A_{SN}	noise power
$\Delta \rightarrow 0$	\mathcal{L}	$\gamma_{n_1}, A_{\text{ON}}$	noise power

Table 10.1: Possible single-spectra regressions and their interpretation in various detuning regions. The number of Lorentzian contributions in the model function is indicated by \mathcal{L} .

inner region, the two lower panels are approximately the inverse of each other. Here, regressions yield the exact decomposition, but the estimates cannot be compared to the SCTS predictions. For correlation rates and noise powers, this region vanishes for splittings Ω below half the homogeneous trion width ($\gamma_d/2$) as indicated by the red dashed line. This region corresponds to the parameter range where previous measurements were performed in Refs. [150, 79, 67]. Here, the SCTS approximation is valid for all detunings outside the $\gamma_s \approx \gamma_{n_1}$ region.

The deviations plotted in Fig. 10.11 confirm the trends visible in Fig. 10.10. In particular, the correlation rates are consistently overestimated (underestimated) for the SCTS parameter γ_s (γ_{n_1}), but the relative deviation is small and does not change the qualitative shape of the peak around the Zeeman branch. Moreover, the noise powers converge in the asymptotic regions $\Delta \rightarrow 0$ and $\Delta \rightarrow \infty$, and qualitatively match outside of the inner region. The information about the regions and possible regressions is summarized in Tab. 10.1.

10.5.3 General Case

When the single-spectrum regression breaks down, the general form of the exact solution in Eq. (10.82) has to be used. As explained in section §10.4.4, this general form can no longer be decomposed into individual contributions. Therefore, no information can be learned from individual spectra alone. Instead, the regression has to be applied globally on the set of all experimental spectra at once. Minimizing the direct deviation between the predicted and the experimental spectra yields an estimate P_M^* of the underlying model parameters P_M .

The set of experimental spectra has to maximize the number of available degrees of freedom for this procedure to work reliably. The exact solution has 12 model parameters and an additional overall scale factor. If the parameters have an

internal dependence like explored below in section §10.6, then the set of parameters can be even larger. Optimally, the set of experimental spectra should contain experimental data where each underlying model parameter is significantly varied. Experimentally, this is not always achievable. Therefore, some assumptions have to be made, or the values of some parameters have to be determined using complementary measurements.

10.6 Model Parameterizations

As explained in 10.5.2, the SCTS predictions remain qualitatively accurate in several regions, even when the SCTS not quantitatively correct. In particular, the qualitative predictions for the asymptotic regions $\Delta \rightarrow 0$ and $\Delta \rightarrow \pm\infty$ can be compared to single-Lorentzian regressions of experimental spectra. As introduced in section §10.1, not all parameters present in P_M are assumed to be constant for all probe intensities r . The particular form of intensity dependence assumed for individual model parameters can significantly alter the predicted detuning dependence of both correlation rates and noise powers. Therefore, this section considers several possible parameterizations of the model, whose predictions can be compared to experimental data.

For simplicity, in the models considered below, a high spin temperature regime is assumed ($\alpha, \beta = 1$). Moreover, the Kerr phase is assumed to be $\varphi = 0$ (pure Faraday rotation). In the figures corresponding to the parameterizations, the predictions of the SCTS approximation are presented. The predictions are calculated for various detunings Δ and several relative probe intensities r . The figures are organized in 2×2 grids of subplots, where the ON and SN contributions are split for clarity. For example, in Fig. 10.12, the top two panels depict the predicted correlation rates γ_{n_1} and γ_s for the ON and SN contributions, respectively. The two bottom plots display their corresponding predicted relative noise powers A_{ON} and A_{SN} . The colors of the curves correspond to the different simulated probe intensities.

10.6.1 Fixed Model

First, to highlight why a parameterization of the model is necessary, in this subsection considers a model that reproduces the assumptions previously made in Refs. [79, 67, 96]. This model assumes that the Auger-like ejection from the QD

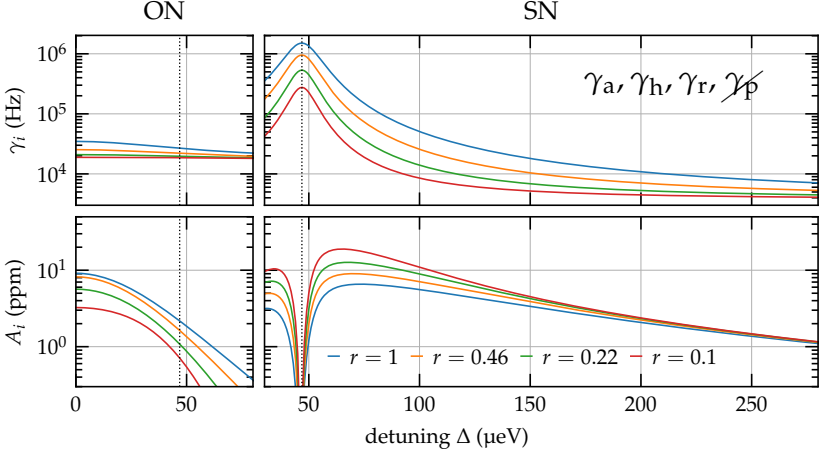


Figure 10.12: SCTS predictions for a model with fixed rates $\gamma_a = \text{const.} \neq 0$, $\gamma_r = \text{const.} \neq 0$, $\gamma_p = 0$ as assumed in Refs. [150, 72, 96, 79, 67].

causes the hole occupancy fluctuations, but it assumes no photoeffect-like process in either direction. Instead, the recharging of the QD is assumed to be purely thermal. These assumptions are equivalent to the following damping rates: $\gamma_a = \text{const.} \neq 0$, $\gamma_r = \text{const.} \neq 0$, $\gamma_p = 0$.

For this parameterization choice, the predicted spin correlation rate γ_s decays to the intrinsic hole relaxation rate γ_h for $\Delta \rightarrow \infty$ (as expected from Eq. (10.86)). The speed at which γ_s approaches depends on the probe intensity r : at a higher probe intensity, a larger detuning Δ is necessary to approach the limit than at a lower one. Nevertheless, eventually γ_h is approached for any probe intensity when the detuning becomes sufficiently large. This behavior is not present in the experimental data, as is discussed in more detail below in chapter 12. Instead, at high detunings, the spin correlation rate γ_s is a linear function of the probe intensity.

According to Eq. (10.86), in the asymptotic region ($\Delta \rightarrow \infty$) γ_s is proportional only to the “intrinsic” rates γ_h and γ_p . Therefore, an observed linear dependence can only be caused by one or both of these rates being, in fact, *not intrinsic*. The simplest possibility is that an intensity-dependent effect masks one rate. The linear dependence of γ_p is the obvious candidate, as it is constructed to behave like a photoeffect.

The experimentally observed occupancy correlation rate γ_{n_1} for $\Delta \rightarrow 0$ again

depends linearly on the probe intensity, whereas the fixed model predicts a rather minuscule change. As before, according to Eq. (10.85) for $\Delta \rightarrow 0$, such a linear dependence can only be a consequence of a corresponding inner dependence in γ_r (and, to a much lesser degree, γ_p). A linear dependence of γ_r can be explained again by a photoeffect-like process that injects the hole into a neutral QD, as explained in section §10.2.2.

Predictions of the noise powers A_{ON} and A_{SN} depend on the underlying rates in a non-trivial way. Therefore, the additional internal probe intensity dependence of the rates $\gamma_r(r)$, $\gamma_p(r)$, or $\gamma_h(r)$ can significantly change the shape and amplitude of their detuning dependence. For the best correspondence with the experimental data, A_{ON} should be primarily independent of the probe intensity, while A_{SN} should be as narrow as possible and exhibit only minimal changes in the vicinity of the resonance. Both goals are not achievable using the fixed model and, as shown below, can only be described by a model with two internal probe intensity dependences. In the fixed model, for $\Delta \rightarrow 0$, the noise power A_{ON} drops as r is reduced, while for $\Delta \rightarrow \infty$, the noise power A_{SN} still heavily depends on r .

10.6.2 Simple Intensity Dependences

Each additional internal intensity dependence significantly complicates the resulting model. In particular, additional parameters, such as the rate dependences $\eta_{x,r}$ introduced in section §10.2.2, complicate the regression of the model to the experimental data and can also reduce the predictive power of the model [156]. Therefore, this subsection considers models with a single internal intensity dependence to demonstrate that these models are insufficient to achieve the desired properties demanded in section §10.6.1.

Intensity Dependent Injection

As proposed in section §10.6.1, the most probable reason for a pronounced intensity dependence of γ_{n_1} is a photoeffect-like process that injects the hole into the QD at a rate $\gamma_r(r) = \eta_r r$. This case is depicted in the first row (i) of Fig. 10.13. For the ON part, this modification achieves the desired properties: for different probe intensities r , the detuning dependent curves of γ_{n_1} are well separated, while the magnitude of the noise power A_{ON} stays mostly unchanged around $\Delta \approx 0$. However, the SN part remains mostly unchanged compared to the fixed model.

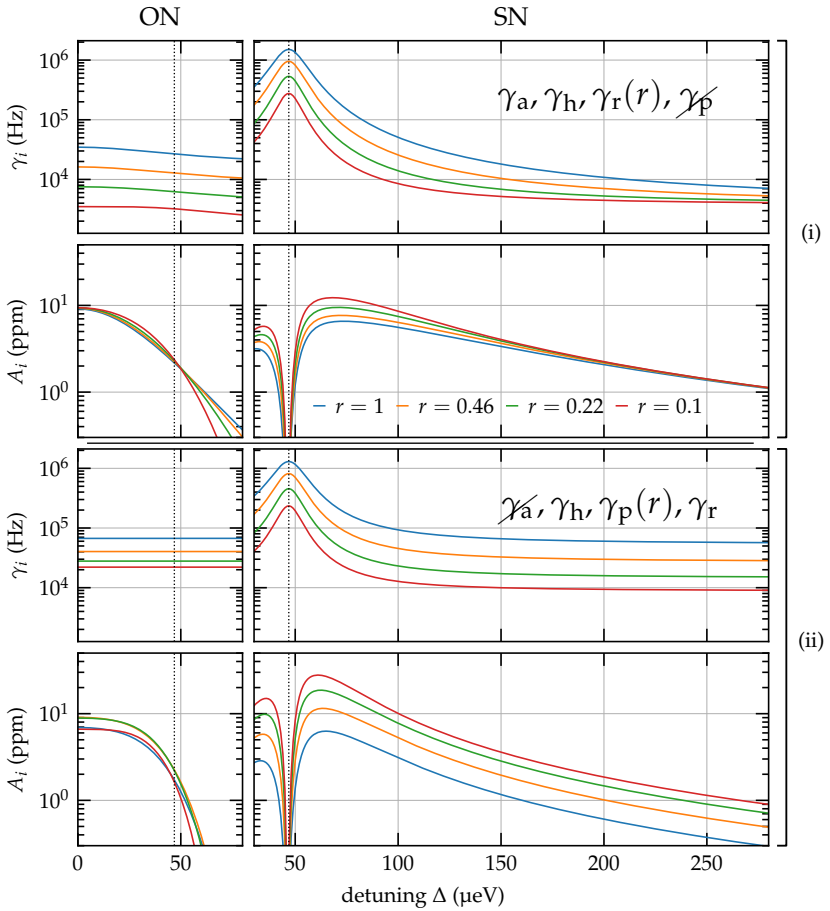


Figure 10.13: SCTS predictions for models with a single internal probe intensity dependence. Rates without an explicitly stated dependence are assumed to be fixed (i.e., γ_a). Rates with a specified r dependence (i.e., $\gamma_r(r)$) are assumed to be proportional to r without any offset.

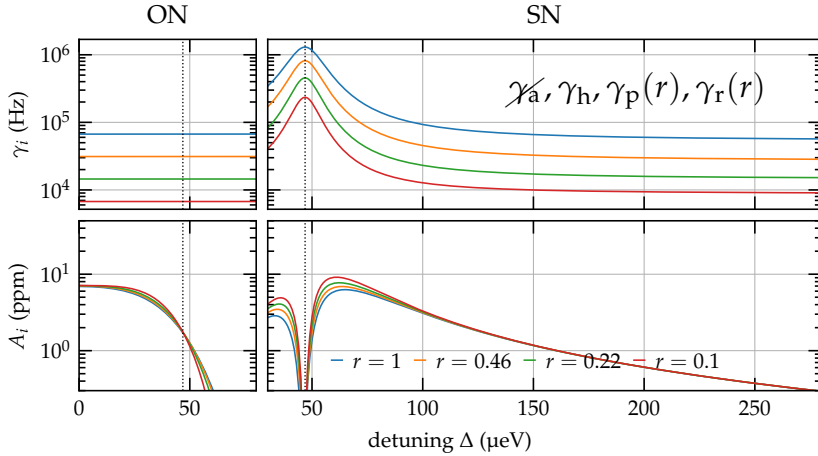


Figure 10.14: SCTS predictions for models with a dual internal probe intensity dependence. Rates without an explicitly stated dependence are assumed to be fixed (i.e., γ_a). Rates with a specified r dependence (i.e., $\gamma_r(r)$) are assumed to be proportional to r without any offset.

Intensity Dependent Ejection

The γ_p term is contained in both Eq. (10.85) and Eq. (10.86). Consequently, a photoeffect-like ejection from the QD causes the occupancy and the spin to decay. Furthermore, one occupancy loss mechanism suffices to cause fluctuations visible as the ON part, and the Auger-like process can be dropped ($\gamma_a = 0$). This case is depicted in the second row (ii) of Fig. 10.13. Again, the model yields the desired intensity scaling only for γ_s . For γ_{n_1} , the contribution through $\gamma_p(r) = \eta_p r$ is barely visible because it is mostly canceled by the third term in Eq. (10.85). Moreover, for this model, the noise power magnitudes of both contributions strongly depend on the probe intensity.

10.6.3 Dual Intensity Dependence

As section §10.6.2 explains, an internal intensity dependence of a single parameter does not produce a model with the desired intensity scaling. Therefore, this subsection considers a possible model that combines two internal dependences in a way that satisfies the requirements described in section §10.6.1.

Two-Way Photoemission

This model combines charge dynamics through photoeffect from and to the QD while dropping the Auger-like ejection ($\gamma_r(r) = \eta_r r$, $\gamma_p(r) = \eta_p r$, $\gamma_a = 0$). The model yields the required intensity scaling for the SCTS predictions. Compared to the previous models, this parameterization results in the most narrow detuning dependences for the spin noise power A_{SN} that remain of the same magnitude for all probe intensities. The reason for this is that the Auger-like ejection in the other variants simultaneously changes spin and occupancy depending on the probability of finding the QD in the excited states. For the two-way model, the first spin loss channel (γ_p) does not have a detuning dependence, while the second one (γ_e and γ_h) does not change the occupancy. This results in a relatively narrower A_{SN} detuning dependence.

11 Limitations of the Results

The reliability of the experimental results can be limited due to experimental challenges beyond the experimenter's control. Such challenges can produce artifacts in the measured data or make recorded data not comparable with similar results. For the described experiment, the greatest care was taken to ensure that all controllable parameters external to the cryostat were stabilized and traceably stayed within tight accuracy bounds. The remaining experimental uncertainties revealed during the long-term experiment are documented in section §11.1 and section §11.2 unfortunately cannot be addressed in the same manner and require changes in measurement protocol or used sample structure. The section §11.1 discusses the effect of an unavoidable slow ingress of atmospheric gases into the sample chamber on the performance of the confocal microscope. Section §11.2 discusses the effect of a less-than-ideal transmission window on the effective probe power.

The different challenge is making experimental data comparable to future experiments. When dealing with nano-scale objects like QDs, small fluctuations and drifts in probe power drastically affect the system's dynamics. In the context of noise spectroscopy, the detected noise power normalized to the square of the probe intensity is extremely sensitive to such changes in the system's dynamics, as demonstrated in section §10.6. It is, therefore, quite puzzling that the process of determining the noise power scale usually remains poorly documented. The noise power scale often ends up normalized to some auxiliary power quantity like the shot noise power, even though such a normalization does not result in a probe-power-independent quantity (see Eq. (3.7)). Other times, the power scale is specified in arbitrary units, making comparisons with similar measurements unnecessarily complicated. While some effort is necessary to derive a proper noise power scale, it is not a hard problem. Section §11.3 documents the procedure used in this work to evaluate experimental spectra as a guide for future experiments. Only when the noise power is consistently determined issues like the frost degradation of optics in section §11.1 can be addressed.

11.1 Frost Degradation of Cryogenic Optics

Measurements presented in the following chapters have been recorded during a single cool-down over a time span of almost a year. Unfortunately, toward the end of the measurement run, it became apparent that through some so far undetermined effect, the effective probe power that interacted with the QD continuously decreased in time. This decrease happened even though the power entering and leaving the cryostat was monitored and regulated to a high degree of accuracy. The most likely cause is that during the measurement run, water and nitrogen ice accumulated in the sample chamber, particularly on the sample and in the aperture of the objective. Consequently, over time the effective transmission of laser power toward the investigated QD layer dropped while the power exiting the cryostat remained constant. As presented in chapter 10, the total noise power and asymptotic correlation rates depend on the absolute probe power. Therefore, without having an independent reference for the absolute probe power, measurements taken several weeks apart cannot be reliably scaled to produce consistent results.

11.2 Degraded Microcavity Performance

A second uncertainty in the magnitude of probe power arises even for short time scales due to the non-regular shape of the cavity enhancement. Fig. 11.1 shows a trace of the reflectivity of the DBR cavity recorded in the vicinity of the investigated QD at 1.8 K. For a Fabry-Pérot cavity, the expected reflectance is [157]:

$$R_e = \frac{I_r}{I_i} = \frac{(\sqrt{R_t} - \sqrt{R_b}e^{-\alpha})^2 + 4\sqrt{R_t R_b}e^{-\alpha} \sin^2(\varphi)}{(1 - \sqrt{R_t R_b}e^{-\alpha})^2 + 4\sqrt{R_t R_b}e^{-\alpha} \sin^2(\varphi)}, \quad (11.1)$$

where R_1 and R_2 are the reflectivities of the first and second mirror, α is twice the round trip loss of optical power inside the cavity, and φ is the round trip phase gain of light passing through the cavity. In Fig. 11.1, the blue line is a fit of Eq. (11.1) to the data above 1.398 eV. As the data is not significant enough to determine the loss constant α , a loss of 0 is assumed. The fit yields $R_1 = 0.9780$ and $R_2 = 0.9988$, which corresponds to rather poorly performing mirrors strongly deviating from the theoretical values calculated in Ref. [67] (0.9893 and 0.9999, respectively). No fit is possible for laser photon energies below 1.398 eV because the decay in the reflectance cannot be described by Eq. (11.1). Consequently, for points located

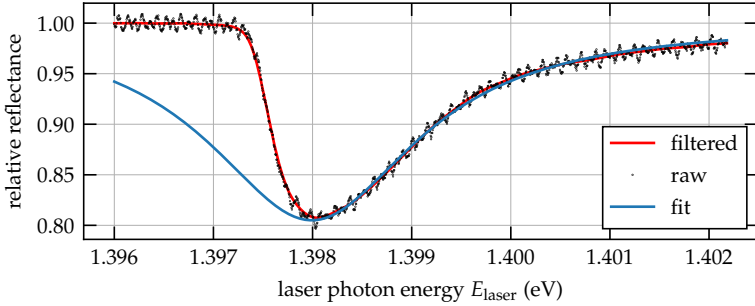


Figure 11.1: Measured cavity reflectivity at 1.8 K. For the solid red line the raw data was smoothed with a 15 bin wide Gaussian filter. The small oscillations seen in the raw data are due to etaloning caused by the coupling beam splitter. The blue line is a fit for data above 1.398 eV

along the sharp cavity slope, assessing the detuning-dependent change of the effective laser intensity in the QD layer is challenging due to the unknown magnitude of resonant cavity enhancement. The absolute scale of the probe power is either unavailable or cannot be relied upon quantitatively in this region. Measurements points located on the sharp slope have a distorted detuning dependence and can be compared to data within the central part of the cavity resonance only qualitatively.

11.3 Evaluation of Noise Spectra

Experimental noise spectra, as presented in chapter 12, below usually contain several approximately Lorentzian-shaped contributions centered around $\nu = 0$ Hz. As explained in section §10.5, these components are good estimates for the underlying fluctuation processes for probe laser detunings outside of the vicinity of the Zeeman branches. In this section, a regression strategy is presented that allows to extract the shape parameters (noise powers A_{nr}^* , A_{br}^* , and correlation rates γ_{nr}^* , γ_{br}^*) of individual contributions from such noise spectra. This strategy mainly consists of three steps: spectral distortion compensation, numerical estimation, and one or more successive nonlinear regressions using the Levenberg-Marquardt algorithm. A more detailed view of the evaluation pipeline is depicted in Fig. 11.2, and the main steps in it are described below.

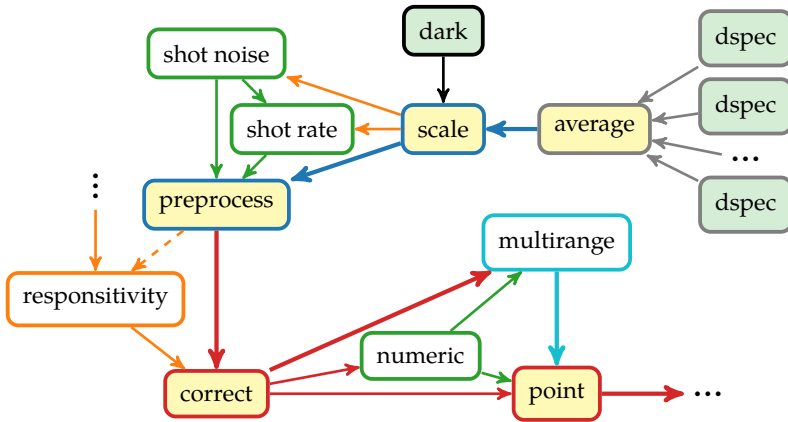


Figure 11.2: Evaluation pipeline for PSD spectra. The used colors are: **blue** for a tuple of foreground and background spectra, **green** for numeric estimates, **red** for a difference spectrum between foreground and background, **orange** for shot noise spectrum estimates and responsivity curves. The abbreviations are: *dspec* for raw spectra, *average* for averaged raw spectra, *scale* for dark noise-floor-compensated spectrum in optical power units, *shot noise* for shot noise level estimates, *shot rate* for estimates of shot noise in terms of the optical input power, *preprocess* for pre-processed uncorrected noise spectra, *correct* for noise spectra divided by the sensitivity (responsivity) curve, *numeric* for numeric peak parameter estimation, *multirange* for the nonlinear regression using a parameter dependent model, and *point* for the evaluated spectrum that is part of a dependence.

11.3.1 Preprocessing

Each final spectrum point part of a detuning or intensity dependence consists of one or more raw source nodes (designated `dspec` in Fig. 11.2). These raw source nodes consist of a tuple of background and foreground PSD spectra estimates, both acquired over an equal time span of usually 20 s. Additionally, each `dspec` contains a corresponding set of estimates for the external parameters that were acquired during the same time span, using the procedure described in chapter 7. For the PSD spectra, the summation introduced in section §2.3 is a natural merging operation in a similar way to the merge operation for the underlying `distograms` of the parameter estimates. Therefore, the `average` node in Fig. 11.2 has exactly the same form as a raw `dspec` node, but its estimates for the PSD spectra and external parameters are more precise (provided that the number of the underlying source nodes is greater than one).

The PSD spectra estimates in the `average` node are given in raw units of V^2/Hz , while the relevant experimental quantity is the optical power on the detector. Not all of the raw noise power is due to the optical power of a laser beam impinging on the detector, as explained in 8.3.3. Therefore, as a first step for constructing the `scale` node in Fig. 11.2, a separately recorded dark spectrum is subtracted from the raw spectra. Ideally, this dark spectrum has to be captured under *identical* conditions to the measurement while blocking the laser beam and all other sources of light, and its variance (given by the integration or averaging time) should optimally be of the same order or below that of the background spectrum¹. As a second step, the intermediate spectra are scaled by the total effective amplification of the acquisition system. This scale includes the initial (first feedback loop) transimpedance gain stage of the balanced detector and any amplification or attenuation from the following signal processing stages. Consequently, the resulting PSD spectra estimates contained in `scale` nodes are given in units of W^2/Hz . Assuming that the dark spectrum estimate was accurate compared to the other estimates, the background part of a `scale` node contains a pure white laser photon shot noise spectrum, while the foreground contains the desired spin noise signal on top of the shot noise spectrum.

The sensitivity curve of the acquisition system distorts both spectra contained in the `scale` node. Since the actual physical shot noise spectrum has no spectral dependency [76], the distorted shot noise estimate is instead an estimate of the

¹e.g., a dark integration time of 200 s versus a raw integration time of 20 s

spectral sensitivity that is scaled by the shot noise power $\mathfrak{S}_{\text{shot}}$, where:

$$\mathfrak{S}_{\text{shot}} = 2h\nu_{\text{laser}}P_{\text{shot}}.$$

As explained in 8.3.3, the detector noise floor is subject to drift, and the accuracy of the sensitivity curve estimate can be severely degraded for spectra that contain a low amount of shot noise, i.e., where low optical power is present on the detector. On its own, the shot noise estimate might not yield the optimal spectral sensitivity for each individual point.

Nonetheless, two other numerical estimates can be derived from the shot noise estimate in the `scale` node. First of all, usually, the spectral sensitivity contains a frequency band where it is sufficiently flat, i.e., the frequency band between 5 kHz and 30 kHz in Fig. 8.9. The average shot noise value in this band ($\mathfrak{S}_{\text{shot}}^*$) can be used as a way to measure the optical power reflected from the sample (P_{shot}^*) according to the definition of optical photon shot noise. This estimate is contained in the `shot_noise` node. The second estimate contained in the `shot_rate` node is the quotient of the optical power estimated by shot noise (P_{shot}^*) and the power that has been reflected from the coupling beam splitter (P_{block}^*). For a given laser photon energy, this ratio quantifies the “efficiency” of the experiment, and is an experimental constant.

Finally, the `preprocess` node aggregates the scaled spectral estimates, the numerical estimates derived from the shot noise part, and the initial external parameter estimates for further evaluation. These pre-processed estimates cannot be used on their own because the detector responsivity and subsequent low-pass filter distort them, and this distortion must be compensated to recover the spectral distribution of noise power.

11.3.2 Spectral Distortion Compensation

The next step is used to derive accurate estimates for the spectral sensitivity. To this end, from the set of *all preprocessed nodes*, a subset is selected that contains nodes with the highest optical input laser power, i.e., $P_{\text{block}}^* \geq 500$ nW. For these nodes, the shot noise estimate is affected the least by any variation of the analyzer noise floor. These nodes are interned by their “spectral key”² that uniquely determines the analyzer configuration (FFT size, sampling rate, and super-sampling

²See the definition of `FftAnalyzerKey` in the python module `plexy.datatools.psd`.

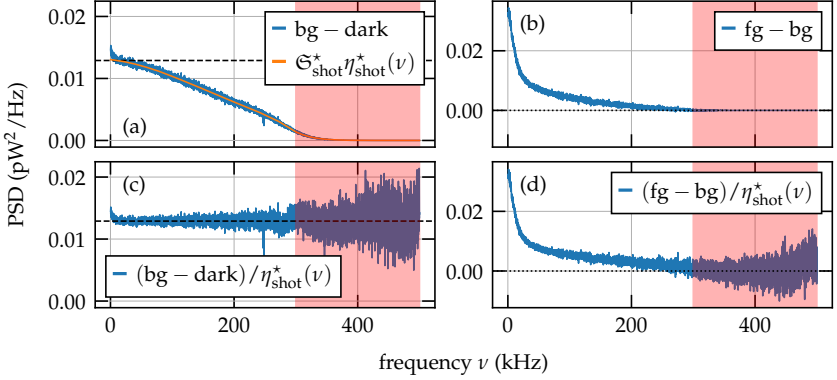


Figure 11.3: The correction step of the evaluation pipeline. Panels (a) and (b) display the uncorrected shot noise and difference (spin noise) spectra. The orange curve in panel (a) is the derived unnormalized sensitivity curve. Panels (c) and (d) display the effect of dividing the spectra in the upper panels by the sensitivity curve. The red region marks the end of the detector bandwidth.

amount) as well as the amplification and bandwidth of all involved signal processing devices. For each key, the shot noise estimates are scaled by their corresponding shot noise power estimates Ξ_{shot}^* to get a probe power invariant estimate for the spectral sensitivity. Subsequently, all spectral sensitivity curves for each key are averaged to get a *key-specific* spectral sensitivity estimate.

This estimate still has finite variance and cannot be directly used as a correction curve. Therefore, the next step is to apply a fixed-order polynomial filter. To this end, the spectrum estimate is first clipped to be strictly positive above a specified low threshold. Then, the logarithm of the spectrum is taken and subsequently filtered by a Savitzky–Golay filter, and the low-frequency bins below a cut frequency threshold are replaced by their 20 percentile value. The last step is necessary to delete the small low-frequency peak that is present in some background spectra due to either a signal from a neighboring QD or insufficient suppression of the QD under investigation. The resulting data is split into up to four overlapping ranges, and each range is fitted by a Chebyshev polynomial of a specified order. The data is then replaced by a weighted sum of the polynomials, dividing the sum by the number of overlapping polynomials in the overlapping regions. Then the curve is raised to the power of e , and the result is filtered by a Gaussian filter. The output

of this procedure is the sensitivity curve $\eta_{\text{shot}}^*(\nu)$ (i.e., the square of the normalized detector responsivity) that is represented by the `responsivity` node in Fig. 11.2. An example of the output of this procedure is depicted in panel (a) of Fig. 11.3, where the product $\mathfrak{S}_{\text{shot}}^{(\text{poly})} \eta_{\text{shot}}^*(\nu)$ is plotted in orange.

The difference between the foreground and background spectra does not change by subtracting a dark spectrum and hence has the same initial numeric value for all nodes with a blue border. For the construction of the `correct` node, this difference spectrum is divided by a sensitivity curve $\eta_{\text{shot}}^*(\nu)$ that was assigned to the corresponding spectral key to get an estimate free of the distortion imposed by the acquisition system. The consequences of this correction are visible in panels (c) and (d) of Fig. 11.3. In contrast to a spectrum produced by an ideal detector, the variance of the shot noise spectrum in panel (c) is not flat and increases toward higher frequencies even though the mean is flat. The reason is that the sensitivity curve only corrects the deviation of the mean estimate, while the mean variance just gets scaled along. Moreover, beyond the detector bandwidth, i.e., in the red band, the estimate is devoid of any physical significance and must be removed from further evaluation as even the scaled-up variance cannot account for the unphysical shape of the spectrum in panel (d). See also the note in 8.3.3 for an explanation of the observed shape of the mean variance.

11.3.3 Multi-Range Regression

The regression of individual SN spectra is performed using the nonlinear least squares Levenberg-Marquardt algorithm³, where the model function is a sum of the expected noise shapes. Initial parameters that are sufficiently close to the minimum have to be provided to ensure that the algorithm finds the global minimum of the regression. For the large number of spectra recorded during the long-term measurement run, it would be impractical to provide the initial parameters manually. Therefore, a semi-automatic strategy is implemented, which is presented in this subsection. This strategy ensures that the initial parameters are sufficiently close to the global minimum of the fit. In addition to that, this strategy also ensures that for spectra with several contributions, the parameters start close enough to their final value or, at the very least, are sufficiently different from other contributions.

³To minimize the fit, the usual Levenberg-Marquardt algorithm from `scipy.optimize` is used provided by the more convenient wrapper package `lmfit`.

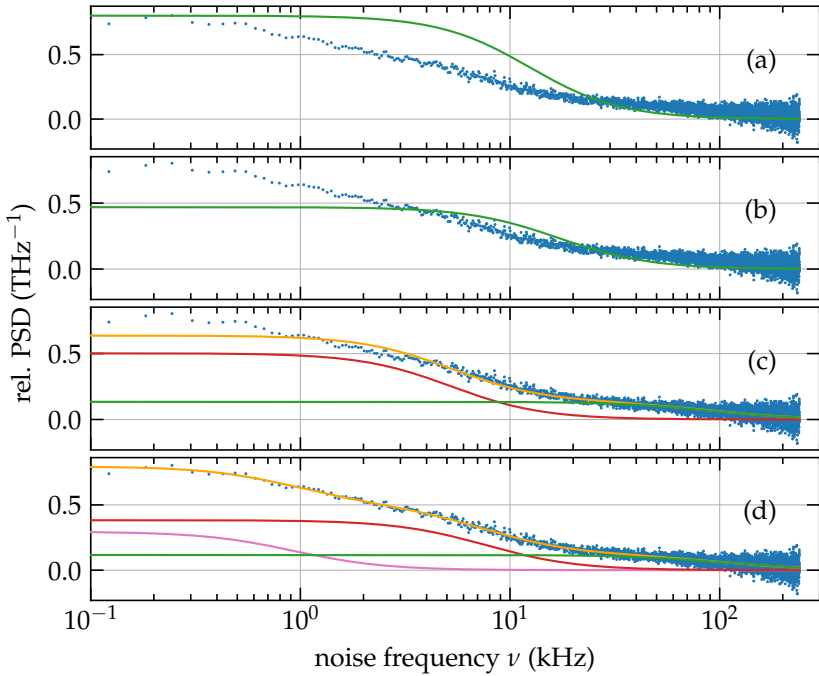


Figure 11.4: Iterations of the fitting strategy. In each panel the same PSD difference spectrum is plotted in blue. The panels show (a) the numerical estimate for a single Lorentzian shaped contribution, (b) a fitted single-Lorentzian shaped contribution, (c) a fitted double-Lorentzian model, and (d) the fitted full triple-Lorentzian model. Where it is appropriate, the sum of contributions is represented by an orange line. Furthermore, the estimated standard error of the spectrum is represented by the transparent orange shaded region.

When several similarly shaped contributions with numerically close parameters are present in a noise spectrum, the extracted parameters may become ambiguous. For example, if the auto-correlation functions of two underlying physical processes decay on a similar time scale, their contributions to the PSD spectrum will have the same width. Furthermore, as their spectra share the same shape, the relative ratio of the areas, that is, the ratio between their total noise powers, is impossible to determine. This situation is the practical equivalent of the mixed region discussed in section §10.4.4. Fortunately, the widths of the contributions in the noise spectra of the investigated QD sample usually appear well separated by approximately one order of magnitude. Therefore, provided that the noise shapes of individual contributions are known in advance, the parameters of these contributions can be determined using an iterative approach described below. Depending on the probing regime, interpreting the noise powers contained in these contributions can become challenging because of the breakdown phenomenon described in section §10.5. A regression model decomposable into independent contributions is equivalent to the decomposition of the exact solution in section §10.4.4. While the algorithm will find a global minimum for each individual spectrum, the regressed parameters might be incommensurable with predictions of SCTS approximation for a set of underlying model parameters from a global exact model regression considering all spectra at once. In particular, the contribution's noise powers might not have a one-to-one correspondence with SN and ON. See also Tab. 10.1.

To illustrate the strategy, Fig. 11.4 depicts a spectrum recorded at a magnetic field of 2 T close to the blue-shifted Zeeman branch resonance. In the first iteration, the parameters of the noise contribution with the largest expected total power are estimated numerically. The spectrum is numerically integrated to get the total noise power \tilde{S}_{tot} . For the half width at half maximum $\tilde{\sigma}_{\text{HWHM}}$, first, the height \tilde{h} of the spectrum is numerically determined. The width is then determined from a quotient of the total power and the spectrum's height: $\tilde{\sigma}_{\text{HWHM}} = \tilde{S}_{\text{tot}}/\pi\tilde{h}$. Naturally, these estimates are quite poor because the inappropriately-shaped model function averages over all present contributions; see panel (a) of Fig. 11.4. Usually, the widths and noise powers of all present contributions are proportional to these first numerical estimates. Therefore, the initial values of all present contributions are determined by weighting the numerical estimates. For example, the initial value for noise power $S_{\text{tot},i}$ of the i -th contribution is set to $w_{S,i}\tilde{S}_{\text{tot}}$. Effectively, the weights $w_{S,i}$ account for the implicit and unequal averaging of the numerical estimation. Finally, the second iteration performs a nonlinear least squares fit of

a model function that contains the sum of all expected noise contributions using the determined initial values.

Panels (b), (c), and (d) of Fig. 11.4 show different models with an increasing number of contributions. Only the last model with three Lorentzian contributions can adequately describe the measured data. The number of present contributions and their corresponding weights $W_{\text{init}} = \{(w_{S,i}, w_{\sigma_{\text{HWHM},i}}), \dots\}$ must be manually determined beforehand. The set W_{init} is a very rough and opaque description of the state of the underlying QD system. While this set is not precise enough to describe the actual state, it captures the relative scales of the observed noise contributions and can be assumed to be constant as long as the system remains at the same temperature and external magnetic field. This is the case for the laser photon energy detuning-dependent spectra presented in chapter 12.

11.3.4 Detuning Dependent Hyperspectra

The results presented in chapter 12 illustrate the evolution of parameters for multiple noise contributions in the vicinity of specific optical resonances, with a dependence on the laser photon energy. Throughout this analysis, certain lattice temperature and external magnetic field values are held constant for each detuning dependency. The laser photon energy is systematically scanned in fixed increments across a range spanning several dozens of optical line widths, symmetrically around the resonance. For each detuning dependence some particular lattice temperature and external magnetic field are kept constant. The laser photon energy is scanned in fixed increments over a range of several dozens of optical line widths symmetrically around the resonance. For low magnetic fields and large detunings from the resonance only a single contribution is present. This contribution is designated the main contribution, i.e., the spin noise of the heavy hole pseudo spin localized in the QD. However, as explained previously, a single noise contribution alone cannot account for all the spectra observed for a given detuning dependence.

The situation is depicted in Fig. 11.5 and Fig. 11.6 for specific magnetic fields examples of 250 mT and 2 T, respectively. In both figures, the sub-panels are labeled using up to three primes (') that designate the maximum permitted number of contributions for the regression. Panels labeled with (b) depict the estimated integrated noise powers of the contributions, while panels labeled with (a) depict the corresponding correlation rates. The bottom row of sub-panels that are labeled

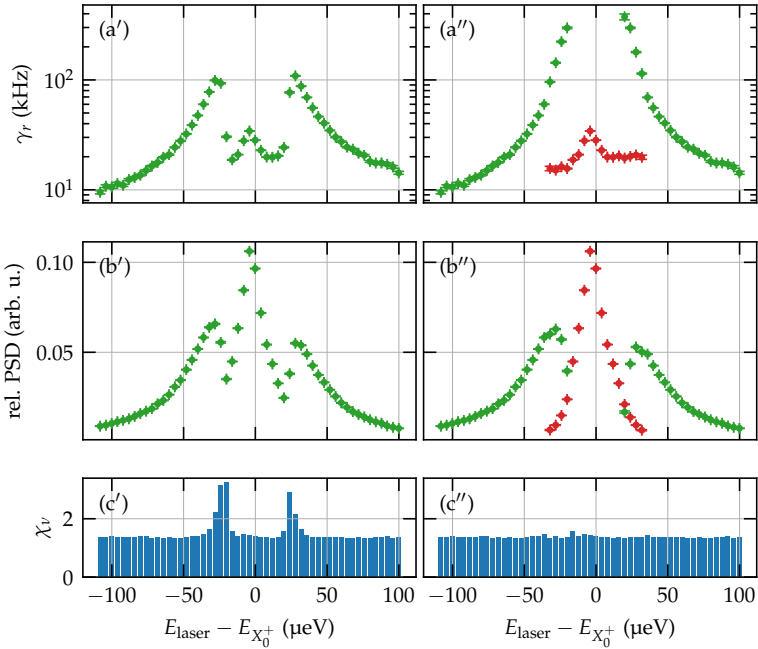


Figure 11.5: Iterations of the fitting strategy for a low magnetic field of 250 mT. Each panel shows fits of different models to the same detuning dependent spectra. Panels designated by one or two primes (') display the results for either one or two Lorentzian contributions, respectively. Each column of panels displays (a) the estimated relaxation rate of the contributions, (b) the estimated noise power of the present contributions, and (c) the reduced χ_ν for the fit of the corresponding sum model.

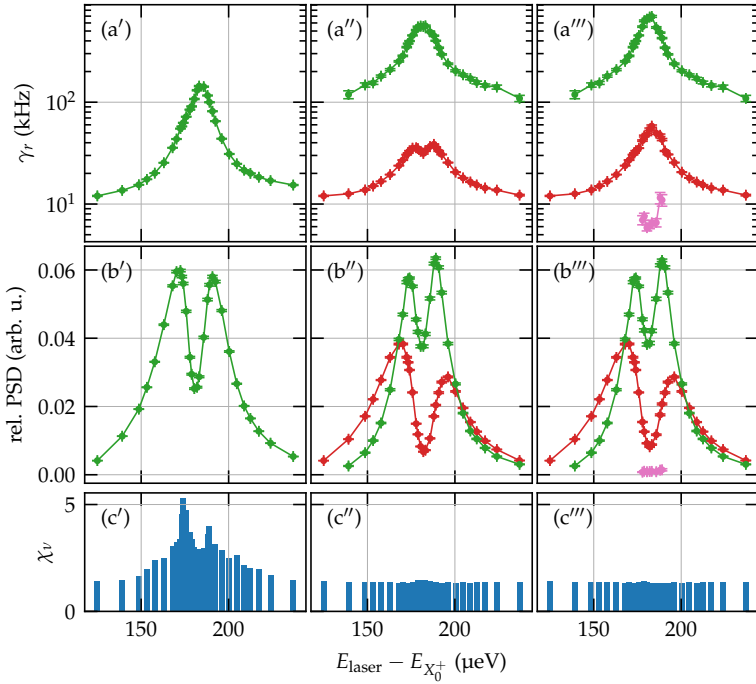


Figure 11.6: Iterations of the fitting strategy for a high magnetic field of 2 T. Each panel shows fits of different models to the same detuning dependent spectra. Panels designated by one, two or three primes (') display the results for either one, two, or three Lorentzian contributions, respectively. Each column of panels displays (a) the estimated relaxation rate of the contributions, (b) the estimated noise power of the present contributions, and (c) the reduced χ_ν for the fit of the corresponding sum model. The solid lines are a guide to the eye.

11 Limitations of the Results

with (c) depicts the reduced sum of residuals χ_ν .

The following strategy is employed to determine regions where more than one contribution is necessary. The initial fit starts with the first column. Subsequently, regions are determined where χ_ν is above the average value. For instance, in Fig. 11.5, this occurs between $\pm 50 \mu\text{eV}$. The fit in this region is repeated using a model with two contributions. Next, the shape of χ_ν is reevaluated, and smaller regions are selected, where χ_ν has features that lie above the average. For example, in Fig. 11.6, the newly identified region is $\approx 180 \pm 10 \mu\text{eV}$. The final fit is performed in this region using a model incorporating three contributions. Effectively, this procedure determines an experimental counterpart to Tab. 10.1. Similar to the simulated case, reducing the number of components improves qualitative agreement at the expense of numerical accuracy.

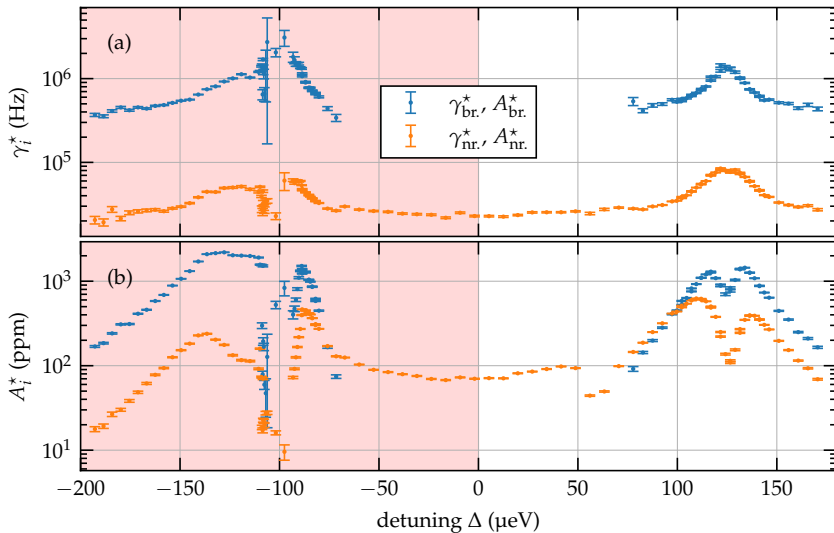


Figure 11.7: Extracted correlation rates and noise powers for two contributions at $B_z = 2 \text{ T}$, $T = 5 \text{ K}$. The transparent red band indicates the spectral region at negative detunings that is excluded from the evaluation due to the ambiguous effects of the cavity.

Finally, at large magnetic fields above 1.5 T , the detuning hyperspectra begin to display increasing asymmetry and distortion in the region of the red Zeeman

branch, as illustrated in Fig. 11.7. Slightly elevated temperatures above 2K exacerbate this phenomenon. The underlying root cause is likely linked to the micro-cavity's asymmetric and quite steep transmission profile, as depicted in Fig. 11.1. Moreover, at even higher magnetic fields of 3.5T, the detuning hyperspectra acquire a scanning-direction-dependent hysteresis around the red Zeeman branch, potentially indicating optically induced nuclear polarization [47]. Conversely, the blue Zeeman branch exhibits *no* hysteresis or strong deviations from a smooth resonance shape across all applied magnetic fields. Consequently, in the following chapter, spectra from the red Zeeman branch at laser photon energies corresponding to negative detunings are excluded from the evaluation, as indicated by the transparent red band in Fig. 11.7.

Regardless of the limitations, these following results were made possible by several improvements of the measurement scheme as explained in chapter 8 and therefore represent the best known long-term record of noise spectroscopy of a charged In(Ga)As QD in a low finesse DBR micro-cavity. In particular, the increased data density allows for gaining new insight into an effect previously overlooked in Refs. [96, 67] due to its low visibility: the charge dynamics of the QD *non-resonantly* induced by the probe laser power.

12 Quasi-Resonant Regime

This chapter presents the results gathered from detuning hyperspectra recorded for laser photon energies in the quasi-resonant regime around the blue Zeeman branch of the QD trion transition at a temperature of 1.8 K and magnetic fields of 30 mT, 125 mT, 250 mT, 500 mT, 750 mT, 1 T, 1.5 T, 2 T, and 2.5 T. Most of these hyperspectra are depicted in the appendix C, while the following sections mostly use the hyperspectrum at 750 mT as an example to illustrate the findings. For the following evaluation, the effect of thermally induced polarization is neglected ($\alpha = \beta = 1$). The Zeeman splitting is not large enough at low magnetic fields to cause a significant polarization. However, the polarization must be low even at the highest magnetic fields because the measurement-induced spin relaxation channel continuously recharges the QD with a hot spin. The effect should eventually become visible at very low powers, where the recharging rate is significantly lower than the intrinsic spin relaxation rate. For the experimental data presented here, the influence is insignificant, and the penalty of including additional model parameters is worse than the potential insights gained. Furthermore, for the investigated QD sample, the noise spectrum contains only a negligible contribution of ellipticity noise, as previously demonstrated in Ref. [67]. This circumstance eliminates the Kerr phase ($\varphi = 0$).

This chapter starts with an evaluation in the spirit of [67] using the qualitative correspondence of single-spectra regressions to the SCTS approximation. First, in section §12.1, single-spectrum regression estimates for the correlation rates of the SN and ON contributions are used to extract some of the underlying model parameters of the QD system. The linear intensity dependence of the non-resonant hole-loss and reoccupation rates is used to demonstrate the need for a model parameterization, as introduced in section §10.6. In section §12.2, the parameters extracted from the single-spectra estimates are used to define a global model that uses the exact solution from Eq. (10.82). This global model is then used to estimate the remaining parameters of the model. Afterward, this model is directly compared to the raw experimental spectra. Finally, section §12.3 discusses the highest mag-

netic fields in the data set. The spectra at these large magnetic fields exhibit more complicated dynamics and require a more sophisticated model.

12.1 Non-Resonant Dynamics

For this section, a regression was performed on individual spectra of the detuning hyperspectrum, as described in section §11.3. This procedure yields a set of detuning-dependent estimates $P_{LL}^*(\Delta)$. The star * emphasizes experimentally extracted values in the employed convention. According to section §10.5.2, the extracted correlation rates qualitatively match the SCTS approximation. Therefore the correlation rates of the narrow and broad contributions were assigned to corresponding correlation rates of the ON and SN contributions within the SCTS approximation ($\gamma_{nr}^* \approx \gamma_{n_1}^*, \gamma_{br}^* \approx \gamma_s^*$). Fig. 12.1 illustrates the results for a magnetic field of $B_z = 750$ mT. For clarity, the assigned correlation rates are plotted in panels (a) and (b), respectively. The γ_s^* estimates are expected to describe the system well for larger detunings, while they are expected to be less reliable in the immediate vicinity of the Zeeman branch. Therefore, γ_s^* estimates in this region are excluded for further evaluation, as indicated by the transparent red band in Fig. 12.1.

12.1.1 Baseline Dependence

A striking result immediately visible in panel (b) of Fig. 12.1 is that the baselines of the correlation rates γ_s^* are dependent on probe power. In light of the discussion in section §10.6, this dependence strongly indicates at least one measurement-induced spin relaxation mechanism. For each probe power, the correlation rates in panel (b) can be fitted remarkably well by a Lorentzian curve on top of a variable baseline γ_s^\bullet . Only the line width, the area, and the baseline were left as free parameters for these regressions, while the resonance position and Zeeman splitting between the branches were left fixed. The results are plotted using black lines. Additionally, the baselines are indicated by dotted lines. Similarly, the correlation rates $\gamma_{n_1}^*$ of the ON component seen between the Zeeman branches can be described just by a constant baseline $\gamma_{n_1}^\bullet$.

The power dependence of γ_s^\bullet implies that the value of the effective spin relaxation rate γ_s^* at the highest probe power can never reach the same value as γ_s^* at a lower probe power and similar detuning. The estimates of the highest probe power (blue dots in panel (b) of Fig. 12.1) saturate for high detunings. This obser-

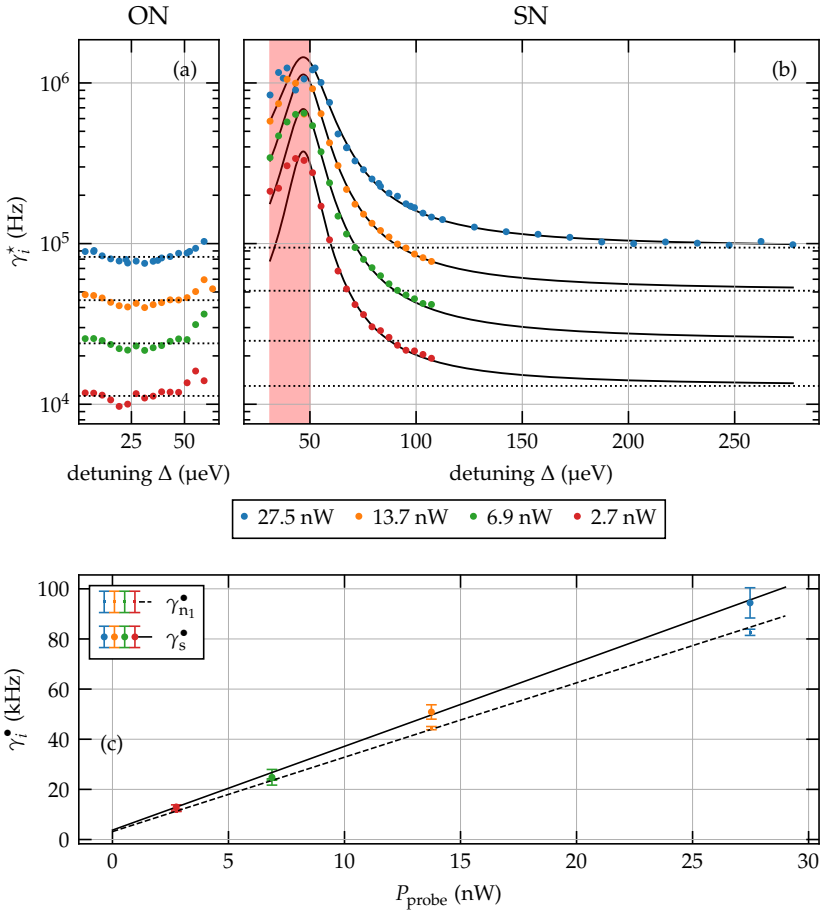


Figure 12.1: Extracted correlation rates and noise powers according to the separation of correlator time scales (SCTS) approximation at $B_z = 750$ mT, $T = 1.8$ K, and different probe powers. The transparent red band indicates the spectral region that is excluded from the evaluation. The panels depict the regression values of: (a) the correlation rate $\gamma_{n_1}^*$ of occupancy noise (ON), (b) the correlation rate γ_s^* of spin noise (SN), (c) the estimated baselines $\gamma_{n_1}^*$ and γ_s^* for both ON and SN, respectively.

vation contradicts a long-standing assumption from, e.g., [67] that the observed spin relaxation rates for very small probe laser powers at intermediate detunings should be similar to corresponding rates at high probe laser powers and large detunings. However, the observed asymptotic value *cannot reach the intrinsic hole pseudo-spin relaxation rate* $\gamma_h \approx \lim_{P_{\text{probe}}^* \rightarrow 0} \gamma_s^*$ for any detuning and finite probe power $P_{\text{probe}}^* > 0$. Panel (c) of Fig. 12.1 summarizes the results of this simple evaluation. Both baselines display a well-visible *linear* dependence on the probe power P_{probe}^* . This dual dependence can only be explained using the two-way photoeffect model for the non-equilibrium charge dynamics described in section §10.6.3.

In the two-way photoeffect model, the slope and intercept of the γ_s^* baseline dependence have simple interpretations. The slope corresponds to the photoeffect rate coefficient η_p . The intercept value γ_h^* corresponds to the extrapolated case of vanishing probe power equal to the upper bound of the intrinsic hole pseudo-spin relaxation rate $\gamma_h^* \approx \gamma_h^\bullet$. A similar consideration is also true for the $\gamma_{n_1}^*$ baseline. The intercept γ_r^* has an interpretation as the upper bound of the intrinsic thermal reoccupation rate γ_r^* . Unfortunately, the mixed term in Eq. (10.85) prevents a simple interpretation of the slope η_{n_1} of $\gamma_{n_1}^*$. For simplicity, both baseline dependences are assumed linear for this simple evaluation:

$$\gamma_{n_1}^* \left(P_{\text{probe}}^* \right) \approx \gamma_r^* + \eta_{n_1} P_{\text{probe}}^* \quad (12.1)$$

$$\gamma_s^* \left(P_{\text{probe}}^* \right) \approx \gamma_h^* + \eta_p P_{\text{probe}}^* \quad (12.2)$$

Of course, the same evaluation can be performed for all other magnetic field values B_z , as depicted in the additional figures in appendix C. The results of this evaluation are summarized in Tab. 12.1. The same results are plotted over external longitudinal magnetic fields in Fig. 12.2.

For magnetic fields below 500 mT, unconstrained regressions yield γ_h^* values that are very close to zero or even slightly negative. Therefore, in the presented results, these values are fixed at zero to reduce the estimation error for the slope. The effective *systematic error* for all intercept values is usually slightly larger than the specified fit errors and is on the order of ≈ 1 kHz. Therefore, the value for γ_h^* became too small to be resolved within the accuracy of the measurement. These small values imply intrinsic relaxation rates $\gamma_h^* \ll 1$ kHz ($1/\gamma_h^* \gg 1$ ms).

In this regard, it is remarkable that for *all* magnetic fields, the values of γ_h^* are up to two orders of magnitude smaller than those reported previously ($T_1^{(h)} \approx$

B_z	$\gamma_{n_1}^\bullet \approx \gamma_r^\bullet + \eta_{n_1} P_{\text{probe}}^*$		$\gamma_s^\bullet \approx \gamma_h^\bullet + \eta_p P_{\text{probe}}^*$		$T_1^{(h)} \approx 1/\gamma_h^\bullet$ μs
	η_{n_1}	γ_r^\bullet	η_p	γ_h^\bullet	
	kHz nW^{-1}	kHz	kHz nW^{-1}	kHz	
30 mT	27(4)	94.6(334)	7.1(2)	≈ 0	> 1000
125 mT	8.4(9)	15(5)	3.81(10)	≈ 0	> 1000
250 mT	6.3(3)	4.6(8)	2.5(1)	≈ 0	> 1000
500 mT	3.7(1)	2.9(5)	3.19(6)	0.7(3)	1448.78(55158)
750 mT	2.97(6)	3.2(3)	3.34(10)	3.8(6)	266.4(418)
1 T	2.54(7)	4.3(6)	3.12(2)	4.9(2)	203(10)
1.5 T	2.30(8)	13(1)	3.0(2)	44(3)	23(2)
2 T	2.2(2)	8(2)	2.5(4)	132(5)	7.6(3)
2.5 T	2.9(2)	4(1)	7(4)	188.5(609)	5(2)

Table 12.1: Linear dependence of separation of correlator time scales (SCTS) correlation rate baselines on probe power. The specified uncertainties are fit errors. The systematic error for the intercept values is ≈ 1 kHz.

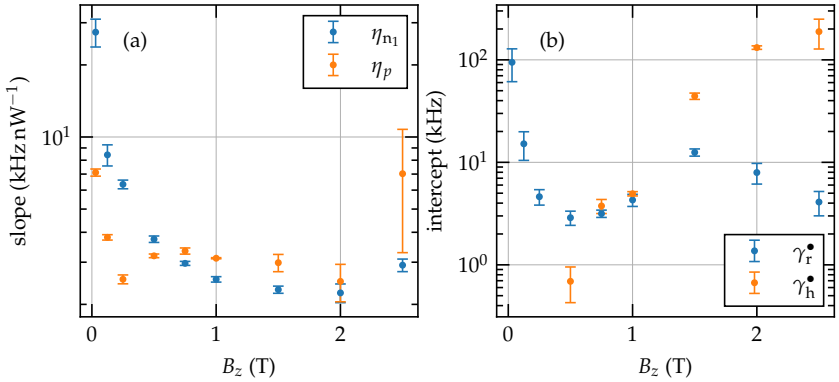


Figure 12.2: Coefficients of the linear dependence on probe power for correlation rate baselines γ_s^\bullet and $\gamma_{n_1}^\bullet$. Panel (a) depicts the slopes, while panel (b) depicts the intercepts.

2.5 μs , $1/T_1^{(h)} \approx 400$ kHz) in Ref. [96] for a different QD from this sample. For most magnetic fields, the rate is also below the lowest rate reported in Ref. [72] recorded for very low intensities.

This discrepancy cannot be explained just by the larger magnetic fields used here. For this sample, the magnitude of Overhauser field fluctuations experienced by holes was estimated to be ≈ 6 mT in Ref. [150]. Therefore, relaxation through nuclear field fluctuations should be strongly suppressed for the previously used magnet field of ≈ 30 mT and all magnetic fields used here. However, even at the largest magnetic fields used here, where a different relaxation mechanism clearly takes over, the intrinsic relaxation rate is about 50% lower than the previously reported value of $1/T_1^{(h)} \approx 400$ kHz. Assuming that the QDs in both studies were comparable, there are two possible explanations for the discrepancy. First, the intrinsic hole relaxation might have been obscured by the unresolved dynamics of the photoeffect. Second, the QD used in this work possesses a superior radial symmetry, resulting in more efficient protection of the hole spin from relaxation processes caused by band mixing.

The trend of intrinsic hole pseudo-spin relaxation rates γ_h^\bullet in panel (b) of Fig. 12.2 displays a saturation for high magnetic fields. Moreover, for low magnetic fields, there is also a potential plateau visible. The significance of the data at low magnetic fields is insufficient due to slow correlation rates. Qualitatively, the shape of $\gamma_h^\bullet(B_z)$ is similar to the theoretical prediction by Ref. [140]. The saturation at high magnetic fields could correspond to on-phonon limited relaxation, while the plateau at low magnetic fields could correspond to the two-phonon limit. A more thorough investigation of this dependence is warranted, as a quantitative evaluation is impossible using the presented data. To this end, additional intensity-dependent hyperspectra have also been recorded in the *non-resonant regime* during the same measurement run on this QD. The evaluation and discussion of the results will be included in the thesis by the second collaborator on this project in Ref. [158].

12.1.2 Line Shape

At magnetic fields larger than 500 mT, the Zeeman branches are well separated. This separation allows the line width of the optical transition to be estimated from the Lorentzian regression performed in, for example, Fig. 12.1. The results of these regressions are depicted in panel (a) of Fig. 12.3 for all magnetic fields

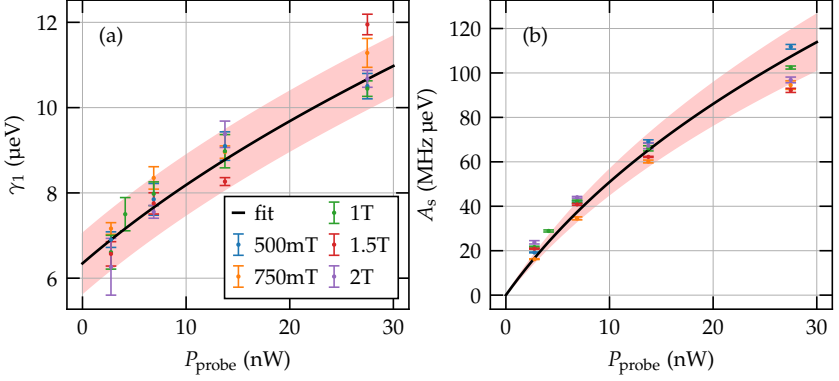


Figure 12.3: Saturation broadened line width (a) and area (b) probe power dependence for various magnetic fields.

quantity	γ_d^*	$P_{\text{sat.}}^*$	$P_{\text{block,sat}}$	γ_e^*	$1/\gamma_e^* \approx T_1^{(e)}$
unit	μeV	nW	nW	MHz	ns
value	6.3(2)	15(2)	274.1	9.9(2)	101(2)

Table 12.2: Line shape parameters. The specified uncertainties are fit errors. The $P_{\text{block,sat}}$ value is the equivalent saturation power value measured by the reference power meter, as described in section §8.3.2.

where the regression yields consistent values. Note that the estimated saturation broadened line width value γ_1^* slightly depends on the choice of the excluded region (transparent red band in Fig. 12.1). Therefore, the effective systematic error is around $0.7 \mu\text{eV}$. No visible magnetic field dependence of the saturation broadening curve is visible in panel (a) within this error margin. Therefore, a regression of Eq. (10.33) is performed, incorporating data from all displayed magnetic fields. The used model function is:

$$\gamma_1^* = \gamma_d^* \sqrt{1 + \frac{P_{\text{probe}}^*}{P_{\text{sat.}}^*}}. \quad (12.3)$$

This evaluation yields both the saturation power $P_{\text{sat.}}^*$ and the effective homogeneous width γ_d^* , as listed in Tab. 12.2.

The electron spin relaxation rate is much faster than all other relaxation rates. Therefore, a rough estimate of γ_e^* can be extracted from the area dependence of the

12 Quasi-Resonant Regime

Lorentzian regression performed before. Assuming $\gamma_e \gg \gamma_h, \gamma_r, \gamma_p, \gamma_a$, Eq. (10.52) for γ_s simplifies to:

$$\gamma_s(\Delta) \approx \frac{1}{2} \gamma_e (\kappa_-(\Delta) + \kappa_+(\Delta)). \quad (12.4)$$

The integral of this expression is:

$$A_s(r) = \frac{\pi}{2} \frac{r}{\sqrt{1+r}} \gamma_d \gamma_e. \quad (12.5)$$

Note that $A_s(r)$ is proportional to the area of both peaks κ_{\pm} , but Fig. 12.1 depicts only one peak. Therefore the area visible in the plot corresponds only to half of $A_s(r)$. The areas for all evaluated magnetic fields are depicted in panel (b) of Fig. 12.3. Again, the dependence does not change between the magnetic fields within the specified error margin given by the accuracy of the γ_d^* estimate. Consequently, the regression using Eq. (12.5) as a model function was performed for the combined data of all fields. The corresponding curve is plotted using a black line, and the resulting estimate for the electron relaxation rate is listed in Tab. 12.2. This value is three times smaller than the 30.4 MHz reported in Ref. [79]. All of the magnetic fields in Fig. 12.3 are significantly larger than the estimated value of 30 to 57 mT [135, 47] for the effective Overhauser fluctuations experienced by the electron spin. Therefore, the Overhauser field fluctuations should have a reduced impact on the total relaxation rate, and a constant electron spin relaxation rate γ_e^* is not surprising.

12.1.3 Noise Powers

Noise power estimates extracted from single-spectrum regressions potentially suffer a significant bias relative to the SCTS predictions, as discussed in section §10.5. Nevertheless, the intensity scaling properties of the detuning hyperspectra are qualitatively represented in these estimates. In Fig. 12.4, the top panels (a) and (b) are reproduced one-to-one from Fig. 12.1 for comparison. Panels (c) and (d) depict the noise power estimates for ON and SN, respectively. Note that the noise powers are plotted normalized to the square of the probe power. The quadratic dependence of spin noise power on the optical power is a purely extrinsic measurement detail. See also Eq. (3.7). Here only the intrinsic scaling is of interest. The corresponding SCTS predictions are plotted for each probe power using solid lines of the same color. The underlying model parameters P_M are determined by:

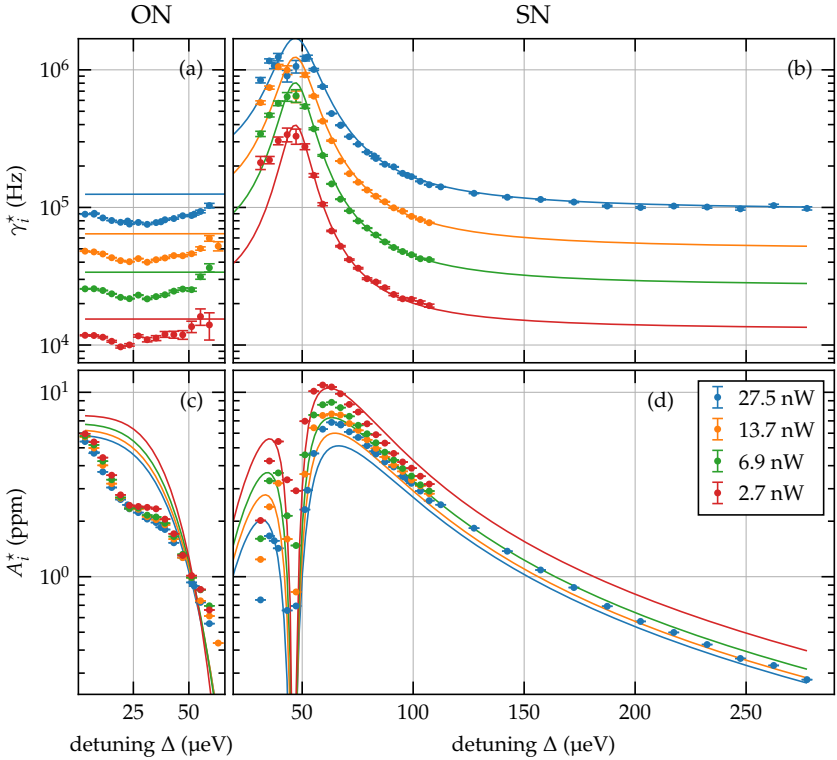


Figure 12.4: Results of single spectrum regression of detuning hyper-spectra at 1.8 K, 750 mT, and different probe powers. Panels (a) and (c) display the extracted parameters for correlation rate and relative noise power of the narrow contribution attributed to ON. Panels (b) and (d) show the respective parameters for the broad contribution attributed to SN. Solid lines are corresponding separation of correlator time scales (SCTS) approximations of globally fitted exact model.

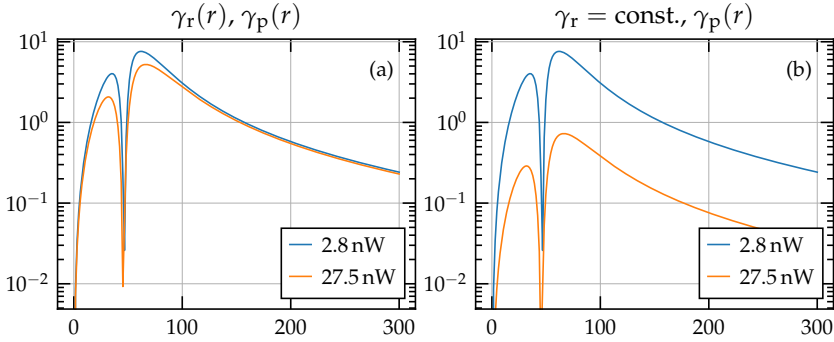


Figure 12.5: Spin noise power dependence models for two different probe powers. Panel (a) depicts the same model as used in Fig. 12.4 with $\gamma_r = \gamma_r^* + \eta_{n_1} P_{\text{probe}}^*$ and $\gamma_p = \eta_p P_{\text{probe}}^*$. Panel (b) depicts a model with $\gamma_r = \text{const.}$ that is tuned to coincide with panel (a) at the lower probe power.

$$P_M = \left\{ \begin{array}{llll} r = \frac{P_{\text{probe}}^*}{P_{\text{sat}}^*} & \alpha = 1 & \beta = 1 & \varphi = 0 \\ \Omega = \Omega_{\text{PL}} & \gamma_d = \gamma_d^* & \gamma_e = \gamma_e^* & \gamma_h = \gamma_h^* \\ \gamma_a = 0 & \gamma_r = \gamma_r^* + \boxed{\eta_r} P_{\text{probe}}^* & \gamma_p = \eta_p P_{\text{probe}}^* & \boxed{A_{\text{PSD}}} \end{array} \right\}.$$

The quantities surrounded by a box are extracted through a global regression of the exact solution to the experimental spectra at all probe powers simultaneously, while the other parameters are taken from the previous evaluation.

Surprisingly, the implications of the linear dependency of the *occupancy-related* reoccupation rate γ_r on the noise power of the SN component are even more profound and revealing than for the noise power of the ON contribution. A simplified version of the graphs from the discussion in section §10.6 is depicted only for the noise power of the SN component in Fig. 12.5. Panel (a) depicts the model used above in this subsection. Panel (b) depicts an alternative model with a constant reoccupation rate γ_r fixed so that both models coincide for the lower of the presented probe powers. The fixed model suffers a significant loss in SN power by increasing the probe power by a factor of ten, while the variable model sees only a slight reduction. The latter case is necessary to reproduce the probe power dependence in the experimental data. Thus, the linear dependence of γ_r is strictly necessary

even without any prior knowledge of the dependence of the correlation rate $\gamma_{n_1}^*$ of the ON contribution. This observation confirms that the experimentally observed dependence of the baseline $\gamma_{n_1}^\bullet$ indeed is enhanced by a linear dependence of the underlying reoccupation rate.

The explanation of this dependence can be understood as follows. The value of γ_r directly influences the steady state occupancy of the QD (Eq. (10.50)). The occupancy, in turn, determines the detected noise power. An increased probe power is more likely to eject the hole from the QD (for example, through the photoeffect). Therefore, the higher power reduces the steady-state occupancy of the QD and hence the detected noise power. A model with a variable γ_r can partially compensate for the lost occupancy via a mechanism that returns the hole back into the QD, making the loss in noise power less severe.

12.2 Qualitative Correspondence

A direct comparison between the experimental data and the developed model is depicted in Fig. 12.6. The figure is subdivided into several rows for each recorded probe power. In each row, in the left panel, the available data of the recorded hyperspectrum is depicted. A corresponding rendering of the exact model is plotted in the right panel. The set of model parameters P_M is determined using quantities extracted from single-spectra regressions and a subsequent global fit of the remaining parameters, as described above. These model parameters P_M are shared among all renderings, and only the relative probe intensity $r = P_{\text{probe}}^*/P_{\text{sat}}^*$ is changed accordingly. Additionally, white equipotential curves highlight more of the structure of the presented hyperspectra and renderings.

The presented model describes experimental data qualitatively well for detunings greater than the blue branch of the resonance. Quantitatively, the model's predictive power is limited, as the model parameters derived from single spectrum-regression estimates are potentially error-prone. Unfortunately, the model also cannot be fitted directly to the data. Leaving all model parameters in P_M free to vary leads to various over-fitting artifacts. Moreover, the spectra are increasingly concentrated at lower frequencies as the probe power is reduced. This changing spectral distribution makes proper weighting of the contributions from the different data sets somewhat challenging.

The model does not describe the experimental data well for detuning that fall into the region between $\Delta = 0$ and the center of the Zeeman branch. In this region,

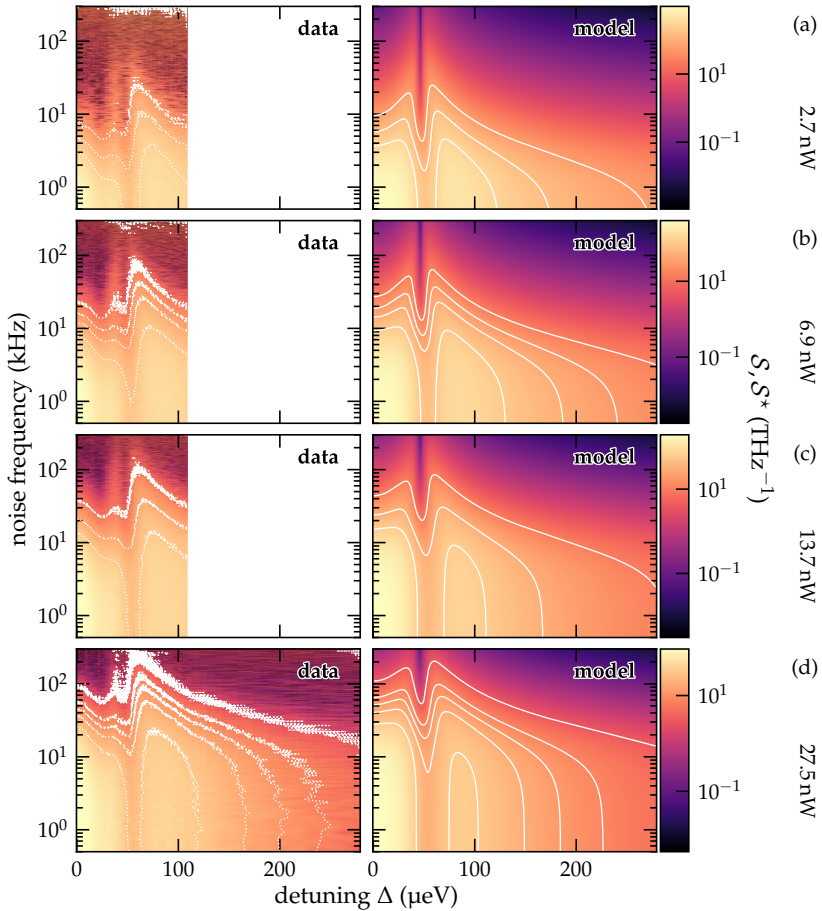


Figure 12.6: Comparison of experimental detuning hyperspectra and the exact model at 1.8 K, 750 mT, and various probe powers. Each row depicts the experimental data in the left panel and a rendering of the exact model in the right panel. The *same* model parameters P_M are shared among all rows. For ease of comparison, equipotential curves are plotted in white.

B_z	η_r
	kHz nW^{-1}
125 mT	5.96(4)
250 mT	2.233(9)
500 mT	2.043(4)
750 mT	1.132(2)
1 T	1.804(3)
1.5 T	2.63(3)

Table 12.3: Results of the global regression of the remaining model parameter using the exact model. The specified uncertainties are fit errors.

the expected magnitude of occupancy fluctuations is the strongest. For the derivation of the model, in Eq. (10.9), the dynamics of the outer state are assumed to be governed by a rather simplistic exponential decay. As even the “exact” model cannot describe the resonance’s internal region, this assumption might need to be revisited for a more refined model.

The results of similar evaluations for the other magnetic fields are listed in Tab. 12.3. Here, only magnetic fields that yield a mostly Gaussian distribution of the residuals without major artifacts are included. Unfortunately, the extracted parameters do not reveal any particular trend, which suggests that the underlying effective systematic errors are several orders of magnitude greater than the listed fit errors. The most likely source of these errors is the incomplete description of the QD dynamics and the potentially large uncertainty of the model parameters extracted from single-spectra regressions.

12.3 High Longitudinal Magnetic Fields

At magnetic fields above 1.5 T, the structure of the hyperspectra markedly changes when compared to the hyperspectra at lower magnetic field values. For example, the hyperspectra of the 2.5 T detuning dependence are plotted in Fig. 12.7. Comparing the highest probe power in panel (d) with the lowest probe power in panel (a) reveals a striking change in the spectra’s shape in the resonance’s immediate vicinity. At high probe powers, the spin noise power (broad contribution) dips in the immediate vicinity of the resonance. The observed dip does not go to zero completely, as expected for a perfectly homogeneous line, but the reduced noise power is nevertheless clearly visible. Conversely, the spin noise power stays al-

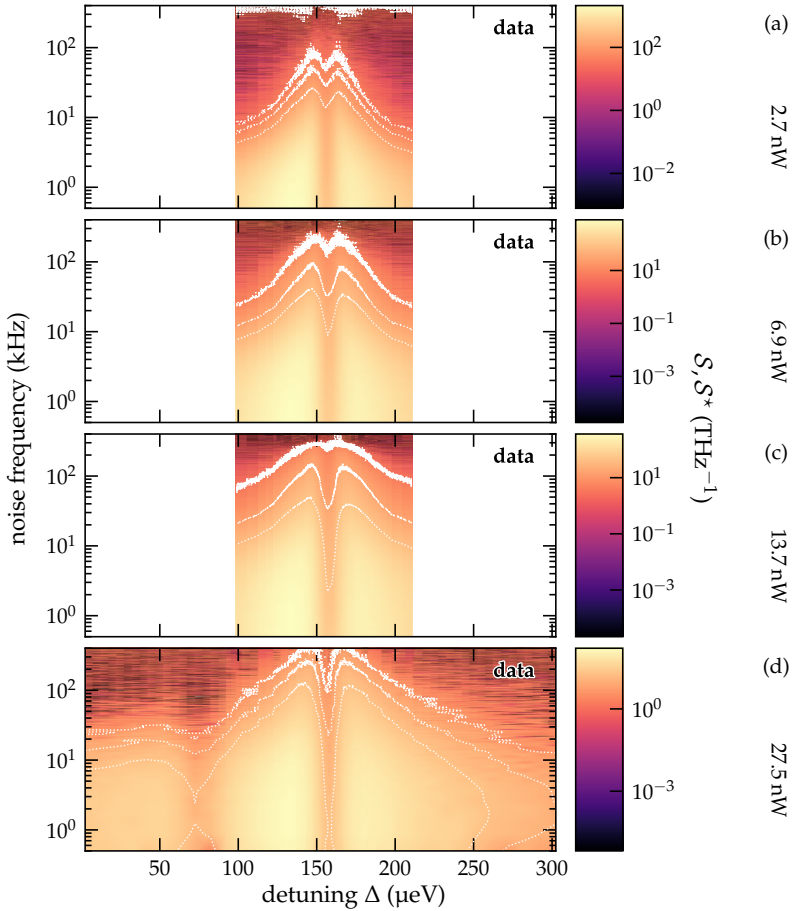


Figure 12.7: Experimental detuning hyperspectra at 1.8 K, 2.5 T, and different probe powers. Equipotential curves are plotted in white.

most constant at low probe powers, as can be assessed from the outer band above the top equipotential line in panel (a).

The magnitude of the individual contributions present in the hyperspectrum can be estimated from single-spectrum regressions if the underlying contributions are sufficiently separated, as in the SCTS approximation. The result of these regressions is depicted in Fig. 12.8. Note that the same caveats discussed in section §10.5 apply here, and the presented estimates might contain significant skews due to a mismatch between the SCTS approximation and forced decomposition of the spectrum. The correlation rates and noise powers of the contributions presented in section §10.5 are estimated using the procedure described in section §11.3.4. The top row of panels contains the estimated correlation rates, while the bottom row contains the noise powers.

The spectrally broadest contribution assigned to SN is plotted in panel (f). Here, the detuning dependence of the noise power clearly depicts that the dip around the Zeeman branch vanishes almost completely as the probe power is reduced. Additionally, the corresponding correlation rates plotted in panel (c) exhibit no change in the observed line width γ_1^* , which stays at a value of $\approx 6(1) \mu\text{eV}$. A possible explanation of this behavior is that the observed line of the Zeeman branch is no longer homogeneously broadened. Instead, the broadening is provided by some other mechanism in the environment that dominates the line width at the used probe powers. A Voigt or Gaussian profile is usually expected when the effective inhomogeneous broadening exceeds the underlying line width, as would be the case here. Rather surprisingly, a Lorentzian describes the line shape surprisingly well for all probe powers shown in Fig. C.9.

A possible explanation of the vanishing dip is that strong magnetic fields localize residual free and hopping charges in the QD environment [159]. As the charges are not free to move, the electric fields of dopants are not effectively shielded. Consequently, the Stark effect from these electric fields shifts the trion transition energy. Excitation by the probe laser can create free charges that get eventually localized, which entails a redistribution of charge in the QD environment. As the electrical fields in the environment are not effectively shielded, this causes a corresponding change in the Stark shift and the resonance frequency. When these charge fluctuations happen quicker than the measurement rate, the resulting measurement averages over all possible charge configurations weighted by the corresponding prevalence. Conversely, at greater probe powers, sufficient free charges would be produced to shield the electric field of the donors, which would make

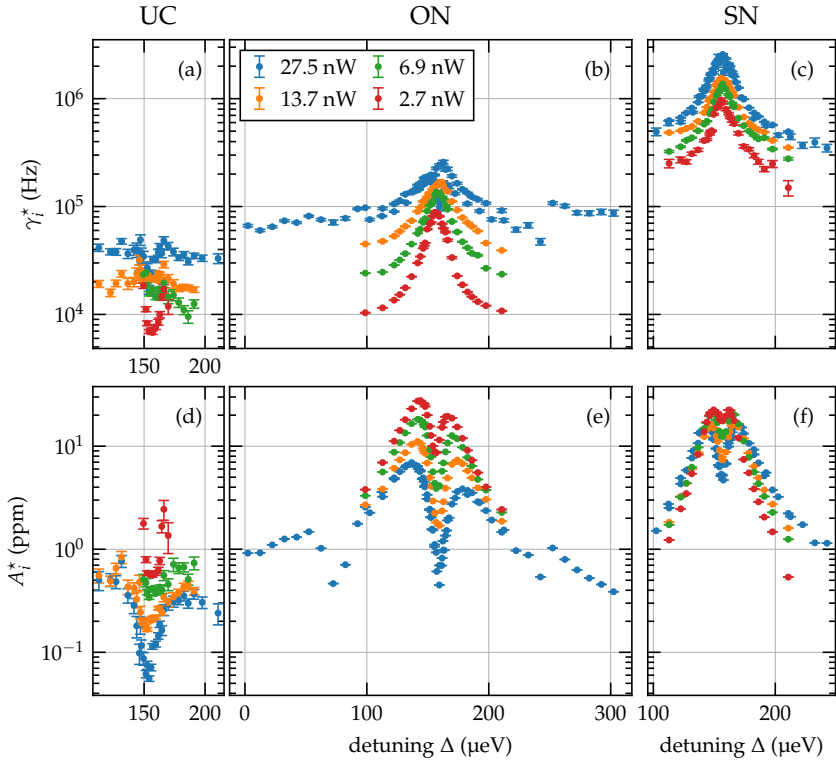


Figure 12.8: Results of single spectrum regression of detuning hyper-spectra at 1.8K, 2.5 T, and different probe powers. Panels (b) and (e) display the extracted parameters for correlation rate and relative noise power of the narrow contribution attributed to ON. Panels (c) and (f) show the respective parameters for the broad contribution attributed to SN. Panels (a) and (d) show the respective parameters for the potential third contribution.

individual localization events affect the transition frequency less severely. A good test of this supposition would be to measure the same detuning dependence under an additional illumination by non-resonant light with photon energies lower than the energy of the trion optical transition [160].

The noise power of the narrower contribution assigned to ON has a shape that can be qualitatively described by A_{ON} from section §10.4.3. However, the relative magnitude of A_{ON} is too large to align with SCTS approximation even qualitatively. Moreover, the peak observed in the correlation rates of this component in panel (b) of Fig. 12.8 can be reproduced only by a model with a rather fast Auger rate. Such a fast Auger rate would deform the detuning dependence of A_{ON} and A_{SN} in a way that is qualitatively very different from the shapes depicted in Fig. 12.8. Therefore, unfortunately, the model developed in chapter 10 cannot be applied to experimental spectra recorded at the largest magnetic fields above 1.5 T.

Finally, the single-spectra regressions indicate the existence of a third so far unassigned contribution, “UC”. This contribution’s correlation rates and noise powers are plotted in panels (a) and (d), respectively. This contribution has no equivalent component in the SCTS approximation. Such a third contribution implies an additional state in the environment of the quantum dot QD. Close to the resonance, spectral contributions can redistribute the noise power, as discussed in section §10.5. It is, therefore, conceivable that the untypical detuning dependence visible in Fig. 12.8 is a direct consequence of a further redistribution due to an additional spectral contribution. Therefore, the model developed in chapter 10 would need to be extended to model this new state’s dynamics properly. For low magnetic fields, a similar model was developed in Ref. [79].

13 Conclusion and Outlook

Summary

This thesis presented an in-depth, long-term study of non-equilibrium hole spin and charge dynamics of an individual quantum dot (QD) at high magnetic fields up to 2.5 T. For the experimental study, the technique of spin noise spectroscopy (SNS) was used to resolve fluctuations of the hole spin and occupancy in polarization fluctuations imprinted on a laser beam due to a scattering of light by the QD system. Very long intrinsic hole spin relaxation times were observed exceeding $T_1^{(h)} \gg 1$ ms for external longitudinal magnetic fields below 500 mT. These relaxation times values are slightly longer than those reported by Dabhshi et al. in [72] for this sample and significantly longer than the values reported by Wiegang et al. in [96, 67]. The discrepancy with Ref. [72] is most probably caused by a superior radial symmetry of the QD used for this thesis. Higher symmetry results in a cleaner heavy hole state and hence better protection from relaxation through Overhauser field fluctuations. The discrepancy with Refs. [96, 67] is most likely due to an unaccounted contribution of the photoeffect to the correlation rate and the subsequent previously commonly made incorrect equation of the effective correlation rate at large detunings with the intrinsic hole relaxation rate.

The presented data demonstrates that a relation between the asymptotic effective correlation rate $\gamma_s^\bullet = \lim_{\Delta \rightarrow \pm\infty} \gamma_s$ and the intrinsic hole relaxation rate γ_h cannot be made when a non-resonant charge loss channel like the photoeffect is present in the system. This is the most striking result of this thesis, as the photoeffect was usually considered negligible in (In,Ga)As QDs. The model for spin and occupancy dynamics developed in this thesis gives a *qualitatively* excellent description of observed spin noise spectra, requiring only one globally fitted parameter in addition to an overall constant describing the sensitivity of the setup. Furthermore, the model highlights detuning regions where a *quantitative* evaluation of the correlation rates yields accurate estimates of the underlying dynamics.

Failing to recognize the photoeffect is in no way a fault of the previous studies.

A previously not available cryogenic system capable of delivering stable low temperatures and large longitudinal magnetic fields over long times was essential for the measurements performed for this thesis. At low magnetic fields, QD trion resonance's dielectric response squeezes the detuning dependence of spin noise (SN) spectra into a narrow band. In this narrow band, most of the structure is not resolved. As shown in the theoretical part of this thesis, the dynamics of spin and occupancy can only be uniquely distinguished when multiple line widths separate the resonance's Zeeman branches. Once this separation is attainable, the discovery of the photoeffect becomes inevitable. Furthermore, the large magnetic fields enable the effective g -factor of the resonance to be measured with high accuracy to the value of $2.159(2)$ or $125.0(1) \mu\text{eV T}^{-1}$, eliminating it as a free parameter from the model.

The line shape parameters of the trion transition were extracted similarly as in Ref. [67], accounting for the photoeffect. A homogeneous width of $6.3(2) \mu\text{eV}$, a saturation power (intensity) of $15(2) \text{ nW}$ ($4.8(7) \text{ nW } \mu\text{m}^{-2}$), and the electron spin relaxation rate $1/T_1^{(e)}$ of $9.9(2) \text{ MHz}$ or $101(2) \text{ ns}$ describe the intensity and detuning dependence of the two Zeeman branches quite well. In contrast to Ref. [67], no Auger rate was necessary to describe the spectra because the effect is either quenched at larger magnetic fields or because the photoeffect was falsely misinterpreted as the Auger effect.

Two distinct photoeffect rates were observed for the used QD system. The first photoeffect non-resonantly ejects the hole along with its spin from the QD, quenching the QD trion resonance and destroying the spin state. The second photoeffect repopulates an empty QD with a hole carrying an unpolarized, hot spin. The first effect's rate was extracted from the intensity dependence of the asymptotic spin correlation rate γ_s^* and was, on average, equal to $4(2) \text{ kHz nW}^{-1}$ or $12(7) \text{ kHz } \mu\text{m}^2 \text{ nW}^{-1}$. The second rate was extracted using a global fit of the theoretical model and is, on average, equal $2.0(6) \text{ kHz nW}^{-1}$ or $6(2) \text{ kHz } \mu\text{m}^2 \text{ nW}^{-1}$. For both rates, a trend in the magnetic field dependence exists. Therefore, these values are only rough estimates.

Conclusion

The photoeffect observed in this thesis limits the usability of (In,Ga)As QDs as spin-photonic interfaces. Even the most symmetric QD with negligible spin relaxation rate cannot be used reliably if the readout process has a significant proba-

bility of destroying the spin by simply ejecting the hole into the solid-state continuum. Quenching of the resonance is prevented by providing a reservoir that recharges the QD. However, this configuration potentially only worsens the hole relaxation rate, as the hole could temporarily leak out of the QD in such a device, relaxing its spin in the process.

At least to some degree, the internal photoeffect in a semiconductor must be determined by energy and quasi-momentum conservation. Therefore, it might be possible to confine the QD in a heterostructure that decreases the probability of the photoeffect. For this to happen, the underlying microscopic mechanism of the photoeffect must be understood. As demonstrated in this thesis, SNS can detect the presence of the photoeffect and determine its effective rates. Other complementary techniques based on single-photon detection and counting can potentially provide a microscopic explanation of the mechanisms behind the photoeffect.

Outlook

The model and data evaluation steps described in this thesis allow for qualitative modeling of the detuning and intensity dependence of SN spectra in a self-consistent way. The width, area (power), and general shape dependences are reproduced, and no ad-hock renormalization [96] or empirical weighting [161] is necessary. The modeling remains excellent for large detunings but degrades somewhat in the region between the Zeeman branches. Two possible explanations are possible. For one, the model collapses all charge states outside of the QD to a single “outer” state and assigns this state an exponential decay rate back into the QD. This assumption simplifies the model but might fail to capture some charge dynamics. The accuracy of this assumption can be tested by deliberately modifying the charge dynamics (for example, in a gated sample) while observing the resulting spectral detuning dependences.

Another explanation is that the QD resonance and the sample structure modify the Kerr phase nontrivially. No asymmetry characteristic of a constant Kerr phase was observed for the detunings described in this thesis. The remaining observed asymmetry between the Zeeman branches was consistent with the asymmetry of the microcavity cavity surrounding the QD layer in this sample. For this reason, the Kerr phase mismatch is assumed to be zero, and ellipticity noise is absent from the evaluation. However, the remaining discrepancy between the model and the experimental spectra could be explained by a detuning-dependent Kerr phase that

is an odd function around the resonance. Fortunately, this assumption is very easy to test, for example, using a Stokes polarimeter to detect the full polarization state of the reflected light while scanning the laser photon energy over the resonance. Therefore, such an experimental step should be added to future preliminary measurements on QDs.

Summary of Performed Work

Improvements to the Setup

For this thesis, the original QD setup of Dahbashi et al. [149] and Wiegand et al. [67] was improved and extended in several ways. The new setup was built around a new cryogenic, apochromatic objective that enabled a consistent performance over wide laser wavelength ranges, which have not been attainable previously in the simple single-lens design. Incorporating a precise three-axis piezo scanner beside the already present piezo steppers further enhanced the setup. This combination allowed reproducible sample positioning, enabling comparative measurements on the same QDs between several cool-downs. This way, it was possible to select QD that exhibited the most stable charge state and the desired spectral properties. Several of the closed-cycle refrigerator's shortcomings were addressed to allow for uninterrupted operation for more than six months. An improved balanced detector generation was commissioned and manufactured, increasing the experiment's sensitivity by two orders of magnitude. The improved sensitivity of the setup combined with the almost unlimited operation time of the closed-cycle refrigerator enabled an overwhelming breadth of intensity and detuning dependences to be recorded that is almost an order of magnitude larger than possible before in earlier measurements. All these improvements enabled the longest-term study of spin and occupancy dynamics performed on a single QD, demonstrating the advantages and drawbacks of this materials system.

Improvements to the Measurement

A new background subtraction scheme was implemented by moving the sample on a μm scale in front of the objective to facilitate SNS measurements in a constant external magnetic field. Furthermore, a unified external parameter estimation framework was developed and employed to prevent drifts and skews in measurements. Unlike in previous iterations, all externally accessible parameters like

probe laser power, laser photon energy, sample temperature, magnetic field, or balancing of the photodetector were regulated within tight tolerances by several control loops. The scanning of the laser source was automated, allowing the experiment to run and record data almost completely automated around the clock for the whole measurement run.

Improvements to the Model

The model for the theoretical description of QD SN spectra initially developed by Wiegand et al. in [96, 79] was extended to allow arbitrary longitudinal magnetic fields. Previously missing Kerr signal terms were added to the model. Furthermore, the handling of thermally induced hole and electron spin polarization present at very high magnetic fields was added to the model. A numerical package with a Python interface was written that efficiently calculates the quantities predicted by the model. Several parameterizations for the non-equilibrium charge dynamics in a QD were added to the model allowing predictions for an experiment to be formulated. The photoeffect mechanism that was not accounted for so far was included in the model. Finally, the model's derivation steps were documented in a detailed way to facilitate the ease of future extensions.

Part V

Appendix

A Derivations

A.1 Mathematical derivations

A.1.1 Welford's sum of squares

The k -th approximation of the mean E_k can be expressed as a recursive formula:

$$\begin{aligned} E_k &= \frac{1}{k} \sum_{l=1}^k S_l \\ &= \frac{1}{k} \left(\sum_{l=1}^{k-1} S_l + S_k \right) \\ &= \frac{(k-1)E_{k-1} + S_k}{k} \\ &= E_{k-1} + \frac{S_k - E_{k-1}}{k} =: E_{k-1} + \frac{\delta_1^{(k)}}{k} \end{aligned} \tag{A.1}$$

Furthermore, the following identities are valid for all $l < k, \delta_1^{(k)} = S_k - E_{k-1}$:

$$S_l - E_k = S_l - E_{k-1} - \frac{\delta_k}{k},$$

$$\delta_k' := S_k - E_k = \frac{k-1}{k} \delta_k$$

Then for the sum of squares the recursion below follows:

$$\begin{aligned}
M_k &= \sum_{l=1}^k (S_l - E_k)^2 \\
&= \sum_{l=1}^{k-1} (S_l - E_k)^2 + (S_k - E_k)^2 \\
&= \sum_{l=1}^{k-1} \left(S_l - E_{k-1} - \frac{\delta_1^{(k)}}{k} \right)^2 + \delta_k'^2 \\
&= \sum_{l=1}^{k-1} (S_l - E_{k-1})^2 + \sum_{l=1}^{k-1} \left(\frac{2\delta_1^{(k)}}{k} (E_{k-1} - S_l) + \frac{\delta_1^{(k)}}{k^2} \right) + \delta_k'^2 \\
&= M_{k-1} + \frac{(k-1)2\delta_1^{(k)}}{k} (E_{k-1} - E_{k-1}) + (k-1) \frac{\delta_1^{(k)}}{k^2} + \delta_k'^2 \\
&= M_{k-1} + \left(\frac{k-1}{k^2} + \frac{(k-1)^2}{k^2} \right) \delta_k^2 \\
&= M_{k-1} + \frac{k-1}{k} \delta_k^2 \\
&= M_{k-1} + \delta_k' \delta_k
\end{aligned} \tag{A.2}$$

B Technical Drawings

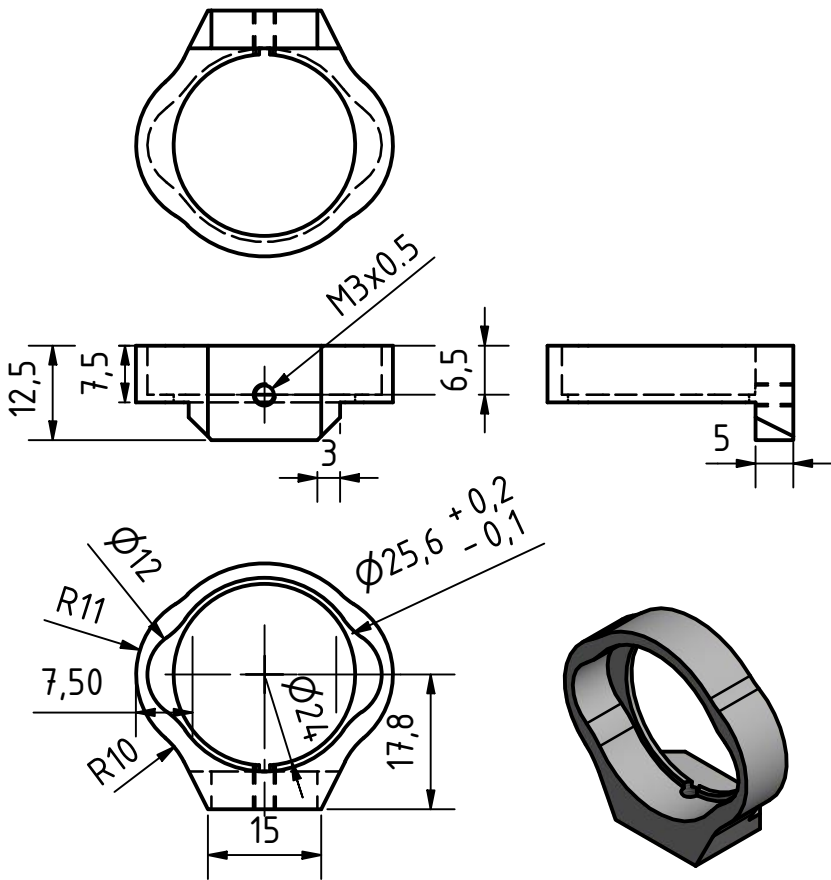


Figure B.1: Technical drawing of the strain free wedge beam splitter holder.

C Additional Figures

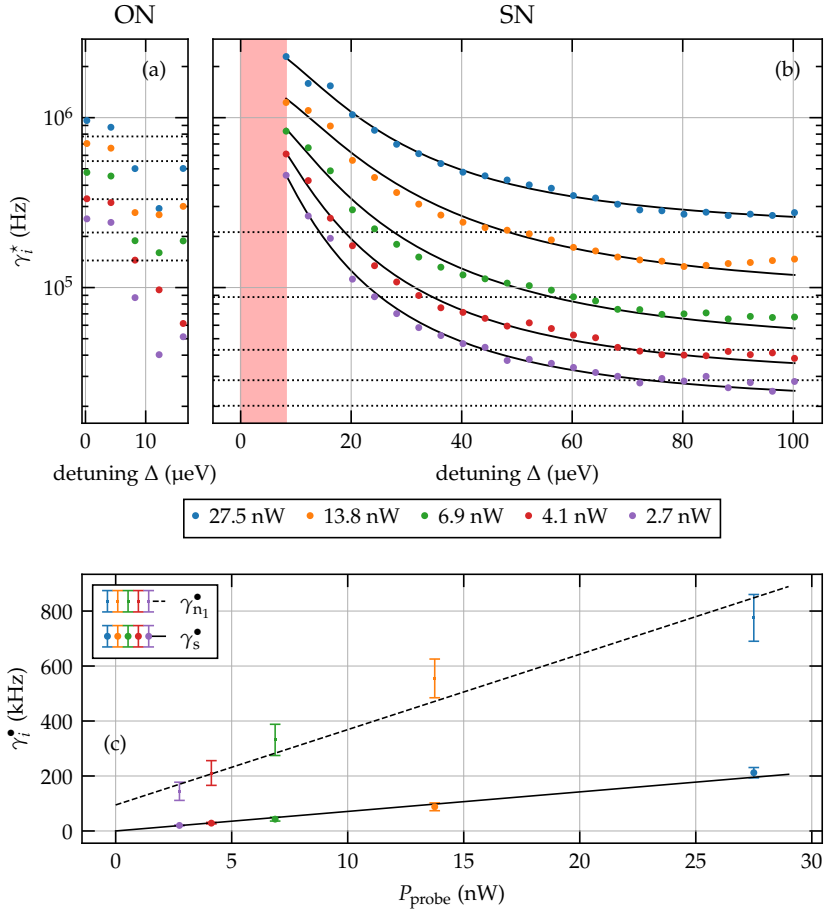


Figure C.1: Extracted single spectrum correlation rates according to the separation of correlator time scales (SCTS) approximation at $B_z = 30$ mT, $T = 1.8$ K, and different probe powers. The transparent red band indicates the spectral region that is excluded from the evaluation. The panels depict the regression values of: (a) the correlation rate $\gamma_{n_1}^*$ of occupancy noise (ON), (b) the correlation rate γ_s^* of spin noise (SN), (c) the estimated baselines γ_s^\bullet and $\gamma_{n_1}^\bullet$ for both ON and SN, respectively.

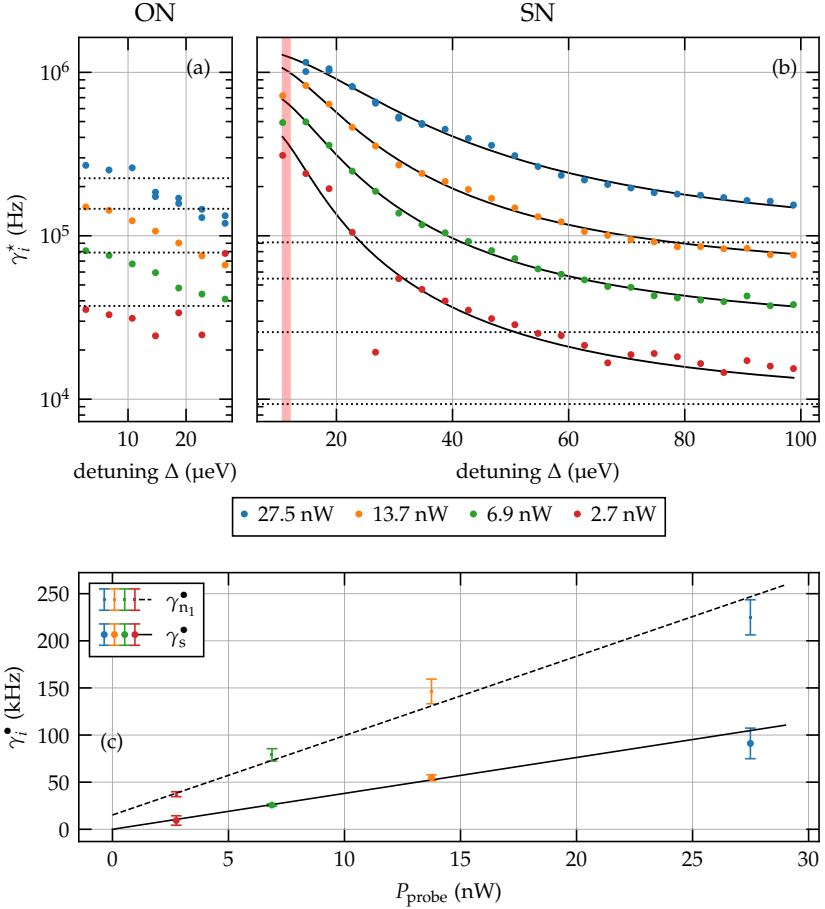


Figure C.2: Extracted single spectrum correlation rates according to the separation of correlator time scales (SCTS) approximation at $B_z = 125$ mT, $T = 1.8$ K, and different probe powers. The transparent red band indicates the spectral region that is excluded from the evaluation. The panels depict the regression values of: (a) the correlation rate $\gamma_{n_1}^*$ of occupancy noise (ON), (b) the correlation rate γ_s^* of spin noise (SN), (c) the estimated baselines γ_s^\bullet and $\gamma_{n_1}^\bullet$ for both ON and SN, respectively.

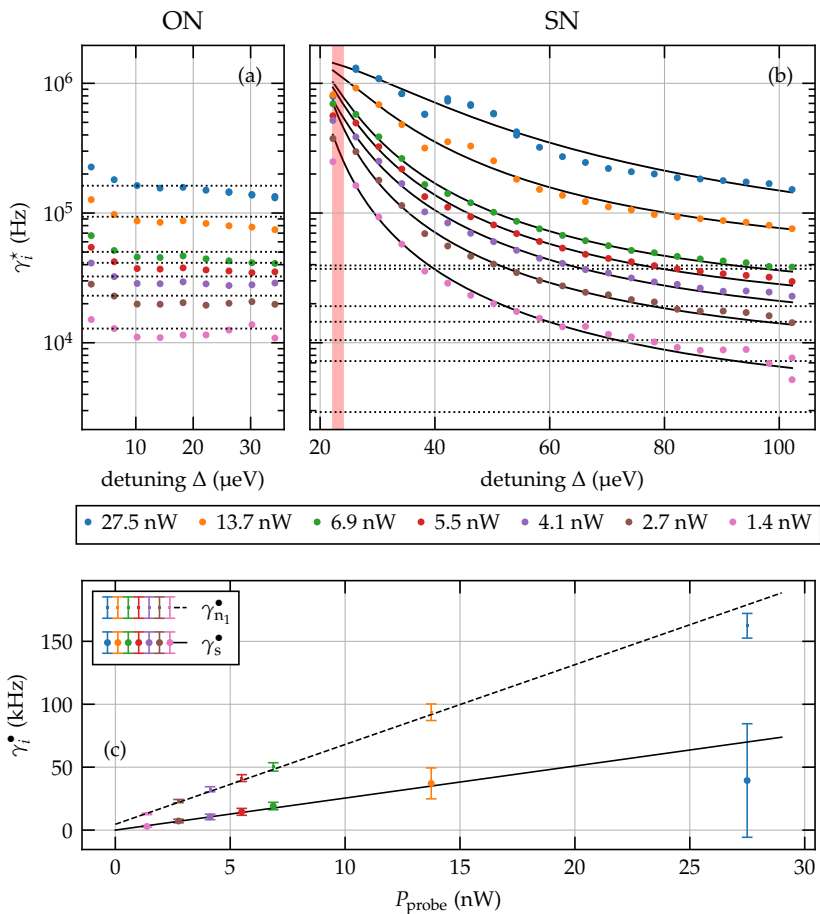


Figure C.3: Extracted single spectrum correlation rates according to the separation of correlator time scales (SCTS) approximation at $B_z = 250$ mT, $T = 1.8$ K, and different probe powers. The transparent red band indicates the spectral region that is excluded from the evaluation. The panels depict the regression values of: (a) the correlation rate $\gamma_{n_1}^*$ of occupancy noise (ON), (b) the correlation rate γ_s^* of spin noise (SN), (c) the estimated baselines γ_s^\bullet and $\gamma_{n_1}^\bullet$ for both ON and SN, respectively.

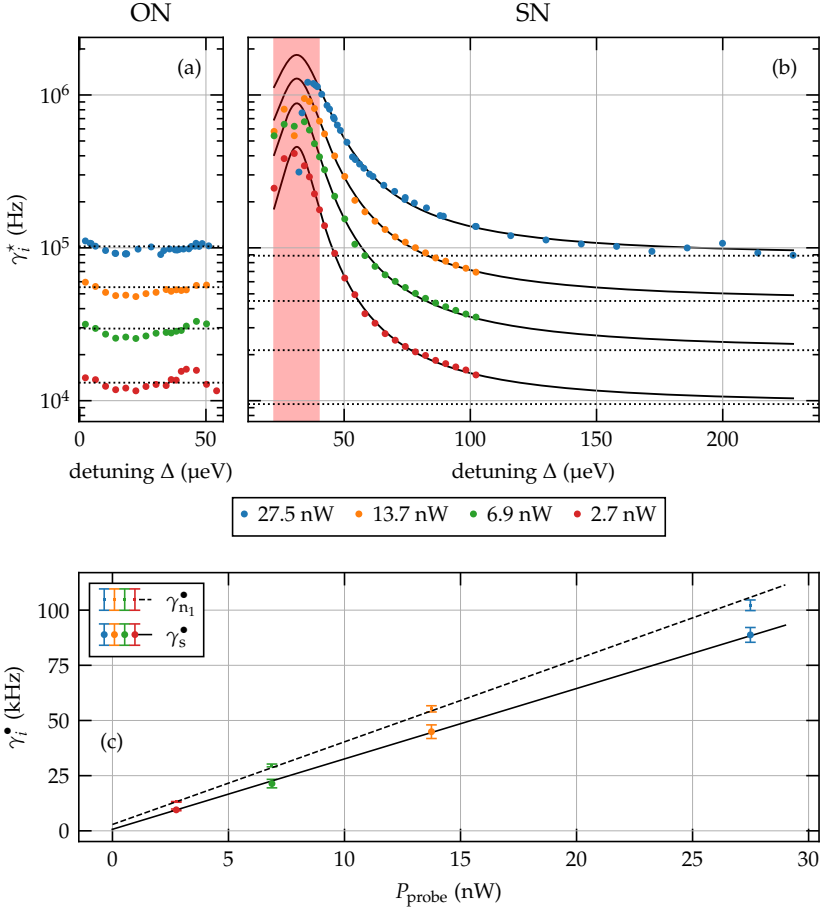


Figure C.4: Extracted single spectrum correlation rates according to the separation of correlator time scales (SCTS) approximation at $B_z = 500$ mT, $T = 1.8$ K, and different probe powers. The transparent red band indicates the spectral region that is excluded from the evaluation. The panels depict the regression values of: (a) the correlation rate $\gamma_{n_1}^*$ of occupancy noise (ON), (b) the correlation rate γ_s^* of spin noise (SN), (c) the estimated baselines γ_s^\bullet and $\gamma_{n_1}^\bullet$ for both ON and SN, respectively.

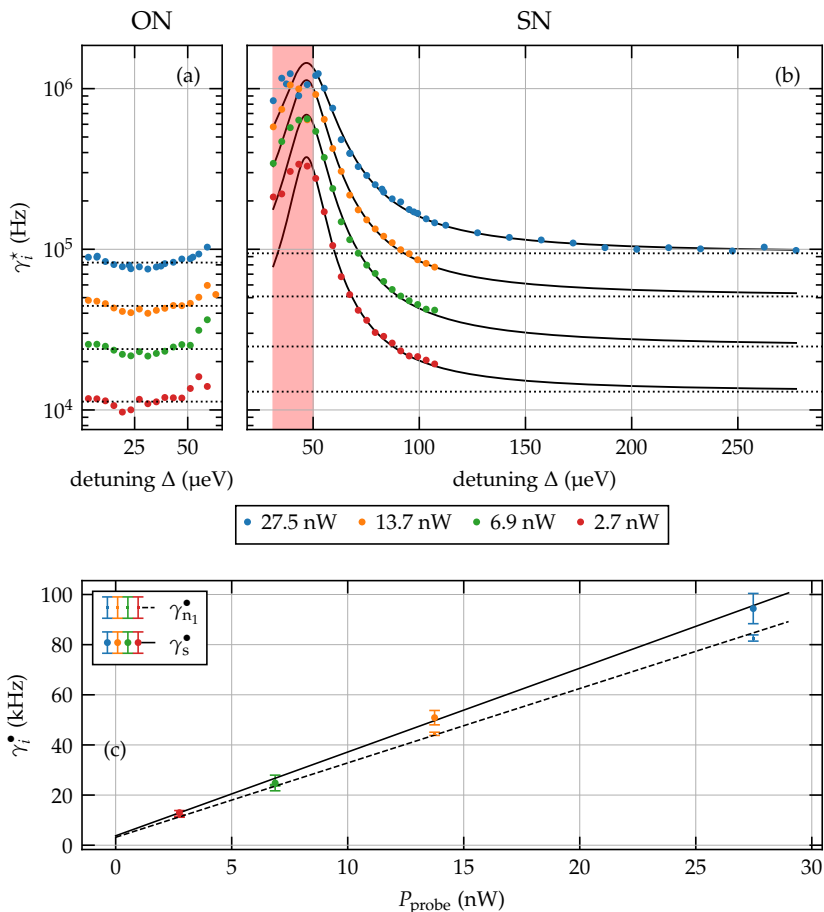


Figure C.5: Extracted single spectrum correlation rates according to the separation of correlator time scales (SCTS) approximation at $B_z = 750$ mT, $T = 1.8$ K, and different probe powers. The transparent red band indicates the spectral region that is excluded from the evaluation. The panels depict the regression values of: (a) the correlation rate $\gamma_{n_1}^*$ of occupancy noise (ON), (b) the correlation rate γ_s^* of spin noise (SN), (c) the estimated baselines γ_s^\bullet and $\gamma_{n_1}^\bullet$ for both ON and SN, respectively.

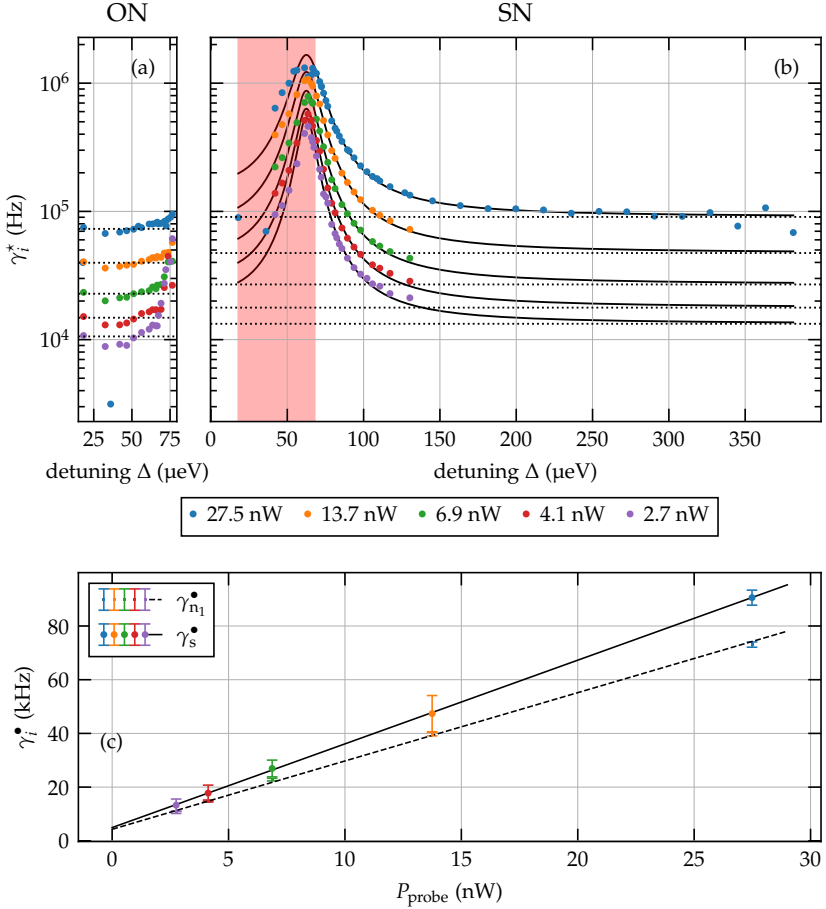


Figure C.6: Extracted single spectrum correlation rates according to the separation of correlator time scales (SCTS) approximation at $B_z = 1\text{ T}$, $T = 1.8\text{ K}$, and different probe powers. The transparent red band indicates the spectral region that is excluded from the evaluation. The panels depict the regression values of: (a) the correlation rate $\gamma_{n_1}^*$ of occupancy noise (ON), (b) the correlation rate γ_s^* of spin noise (SN), (c) the estimated baselines γ_s^\bullet and $\gamma_{n_1}^\bullet$ for both ON and SN, respectively.

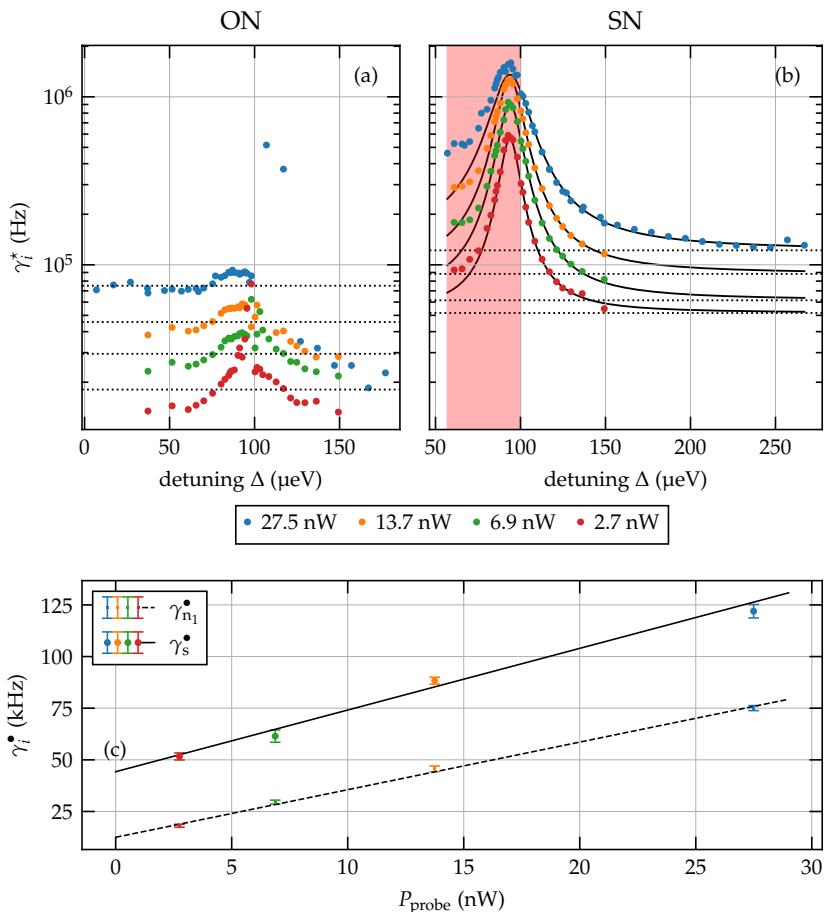


Figure C.7: Extracted single spectrum correlation rates according to the separation of correlator time scales (SCTS) approximation at $B_z = 1.5$ T, $T = 1.8$ K, and different probe powers. The transparent red band indicates the spectral region that is excluded from the evaluation. The panels depict the regression values of: (a) the correlation rate $\gamma_{n_1}^*$ of occupancy noise (ON), (b) the correlation rate γ_s^* of spin noise (SN), (c) the estimated baselines γ_s^\bullet and $\gamma_{n_1}^\bullet$ for both ON and SN, respectively.

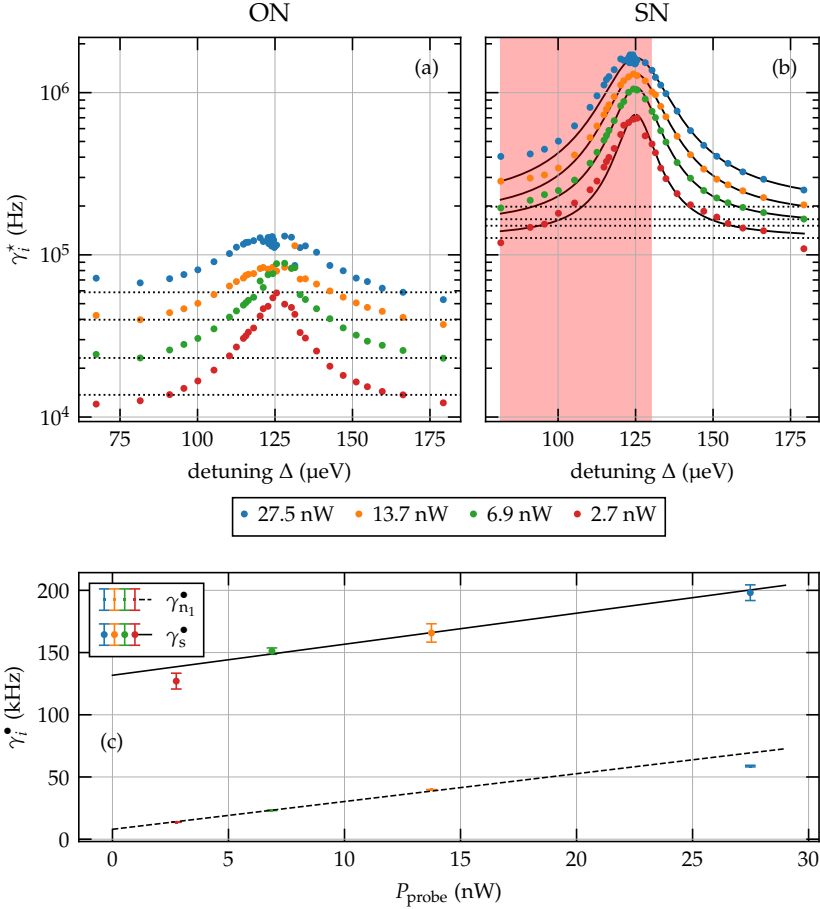


Figure C.8: Extracted single spectrum correlation rates according to the separation of correlator time scales (SCTS) approximation at $B_z = 2\text{ T}$, $T = 1.8\text{ K}$, and different probe powers. The transparent red band indicates the spectral region that is excluded from the evaluation. The panels depict the regression values of: (a) the correlation rate $\gamma_{n_1}^*$ of occupancy noise (ON), (b) the correlation rate γ_s^* of spin noise (SN), (c) the estimated baselines γ_s^\bullet and $\gamma_{n_1}^\bullet$ for both ON and SN, respectively.

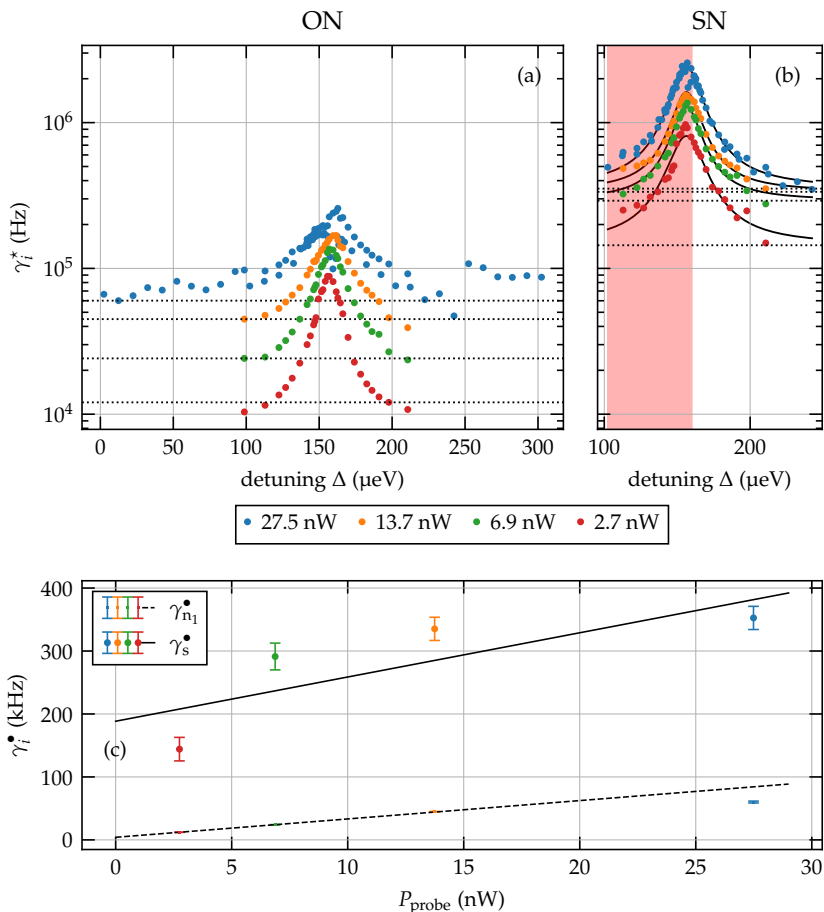


Figure C.9: Extracted single spectrum correlation rates according to the separation of correlator time scales (SCTS) approximation at $B_z = 2.5$ T, $T = 1.8$ K, and different probe powers. The transparent red band indicates the spectral region that is excluded from the evaluation. The panels depict the regression values of: (a) the correlation rate $\gamma_{n_1}^*$ of occupancy noise (ON), (b) the correlation rate γ_s^* of spin noise (SN), (c) the estimated baselines γ_s^\bullet and $\gamma_{n_1}^\bullet$ for both ON and SN, respectively.

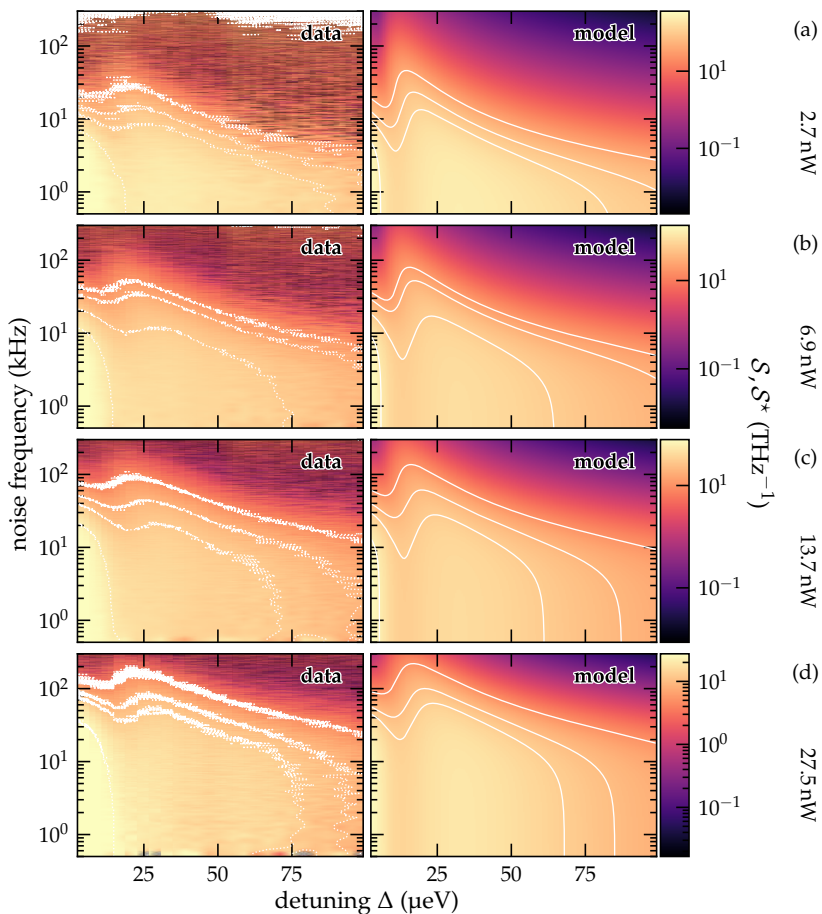


Figure C.10: Comparison of experimental detuning hyperspectra and the exact model at 1.8 K, 125 mT, and various probe powers. Each row depicts the experimental data in the left panel and a rendering of the exact model in the right panel. The *same* model parameters P_M except the relative power r are shared among all rows. For ease of comparison, equipotential curves are plotted in white.

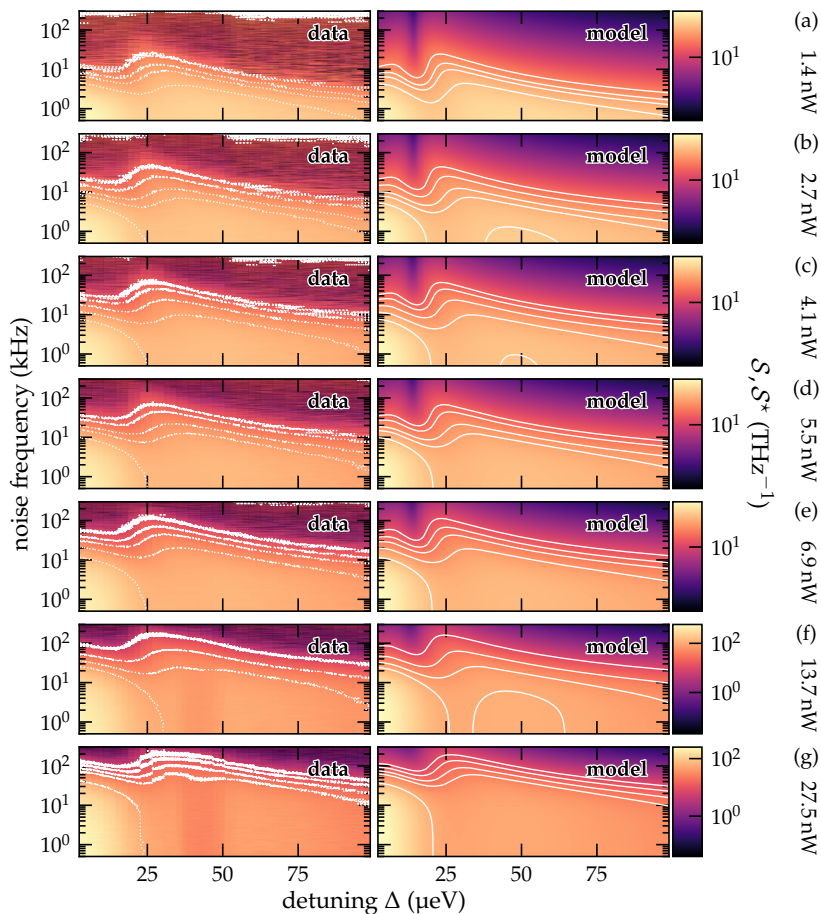


Figure C.11: Comparison of experimental detuning hyperspectra and the exact model at 1.8 K, 250 mT, and various probe powers. Each row depicts the experimental data in the left panel and a rendering of the exact model in the right panel. The *same* model parameters P_M except the relative power r are shared among all rows. For ease of comparison, equipotential curves are plotted in white.

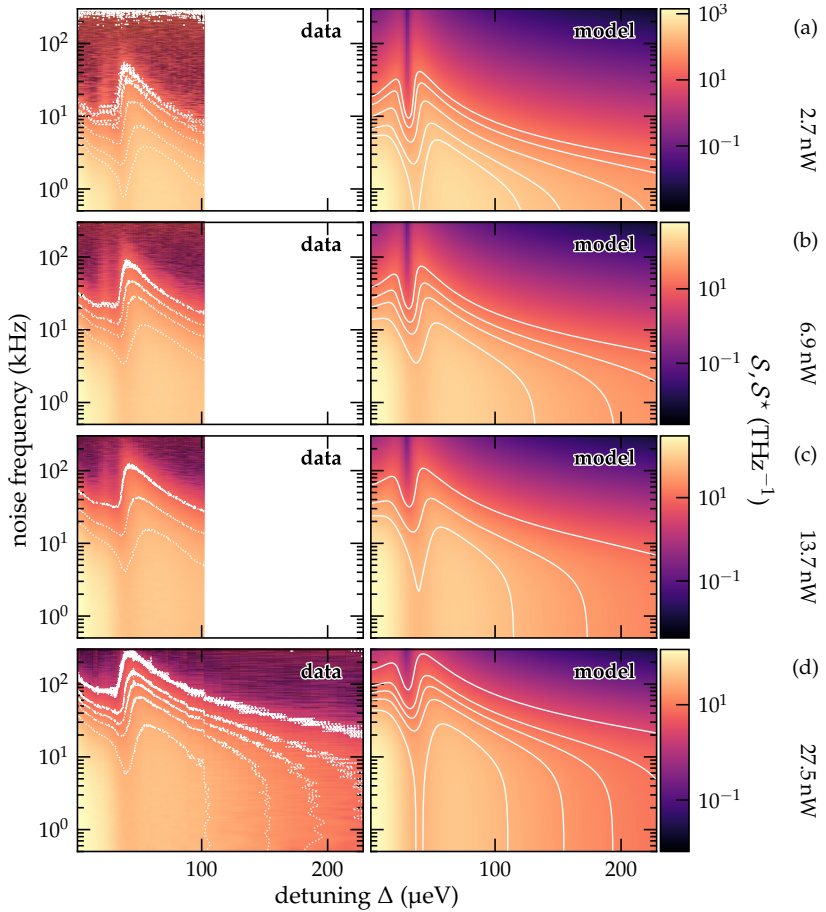


Figure C.12: Comparison of experimental detuning hyperspectra and the exact model at 1.8 K, 500 mT, and various probe powers. Each row depicts the experimental data in the left panel and a rendering of the exact model in the right panel. The *same* model parameters P_M except the relative power r are shared among all rows. For ease of comparison, equipotential curves are plotted in white.

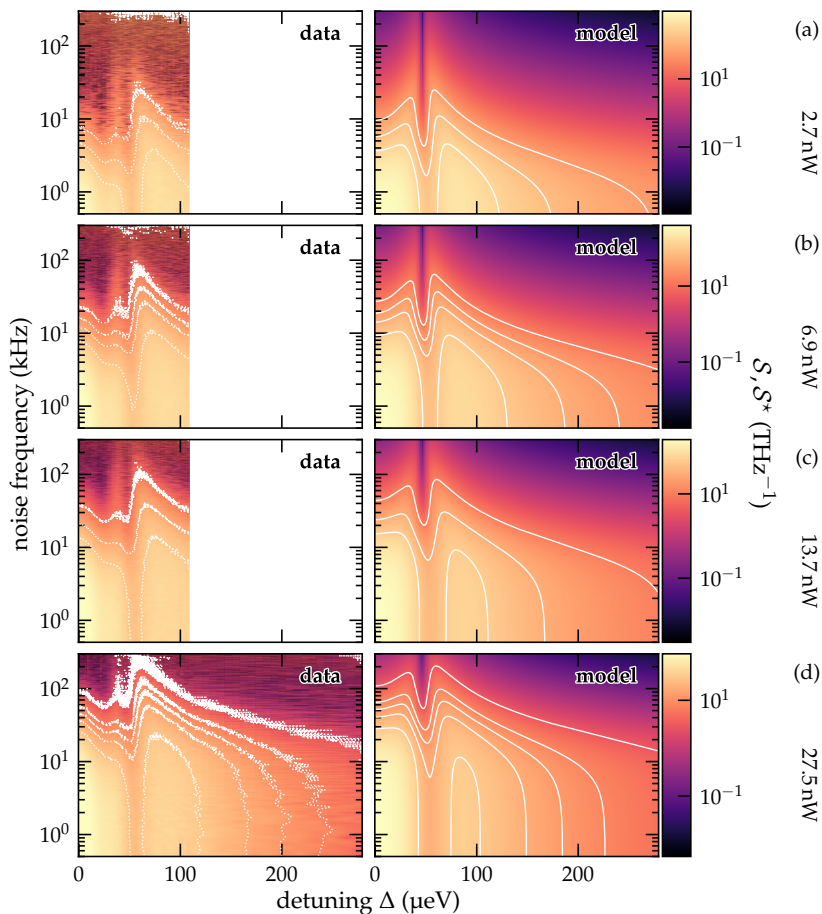


Figure C.13: Comparison of experimental detuning hyperspectra and the exact model at 1.8 K, 750 mT, and various probe powers. Each row depicts the experimental data in the left panel and a rendering of the exact model in the right panel. The *same* model parameters P_M except the relative power r are shared among all rows. For ease of comparison, equipotential curves are plotted in white.

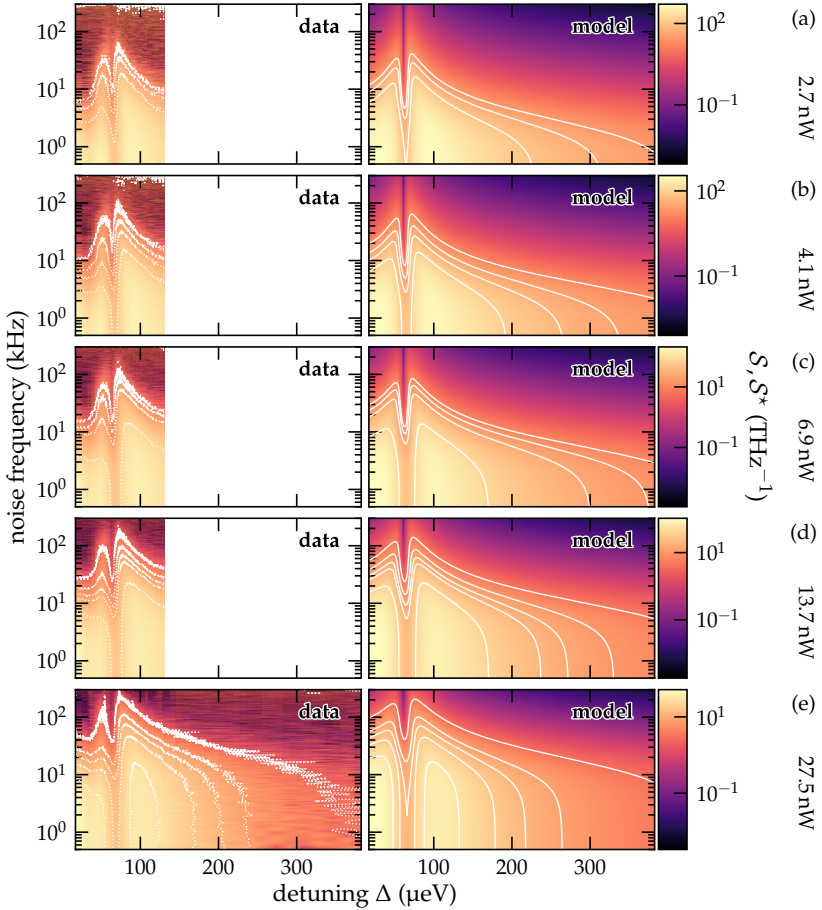


Figure C.14: Comparison of experimental detuning hyperspectra and the exact model at 1.8 K, 1 T, and various probe powers. Each row depicts the experimental data in the left panel and a rendering of the exact model in the right panel. The *same* model parameters P_M except the relative power r are shared among all rows. For ease of comparison, equipotential curves are plotted in white.

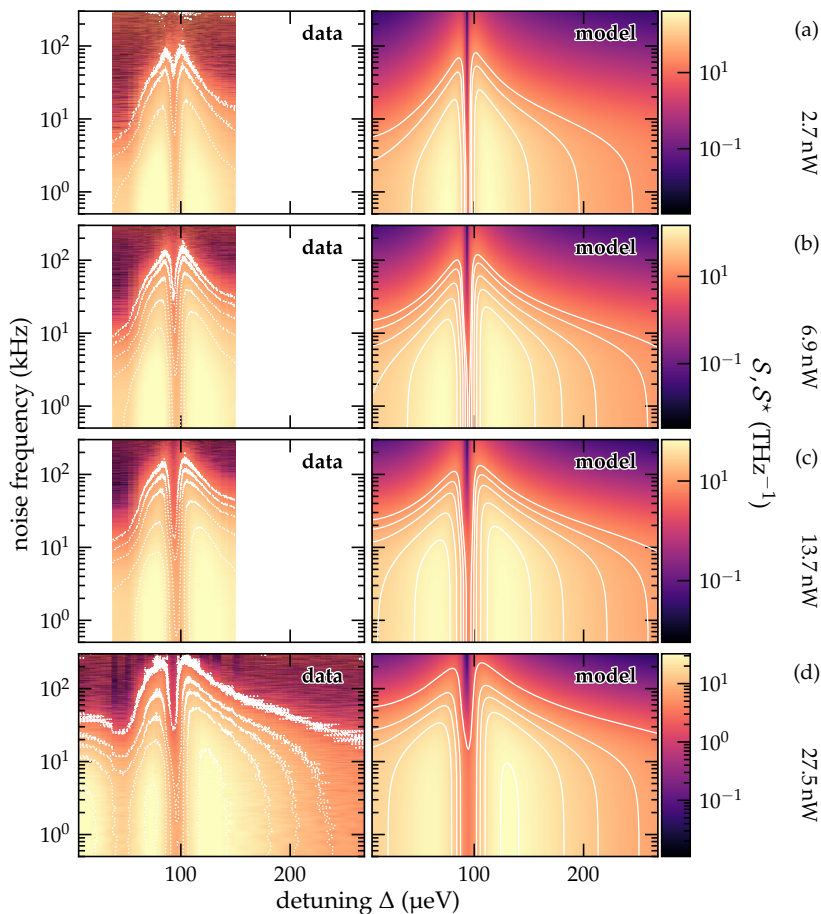


Figure C.15: Comparison of experimental detuning hyperspectra and the exact model at 1.8 K, 1.5 T, and various probe powers. Each row depicts the experimental data in the left panel and a rendering of the exact model in the right panel. The *same* model parameters P_M except the relative power r are shared among all rows. For ease of comparison, equipotential curves are plotted in white.

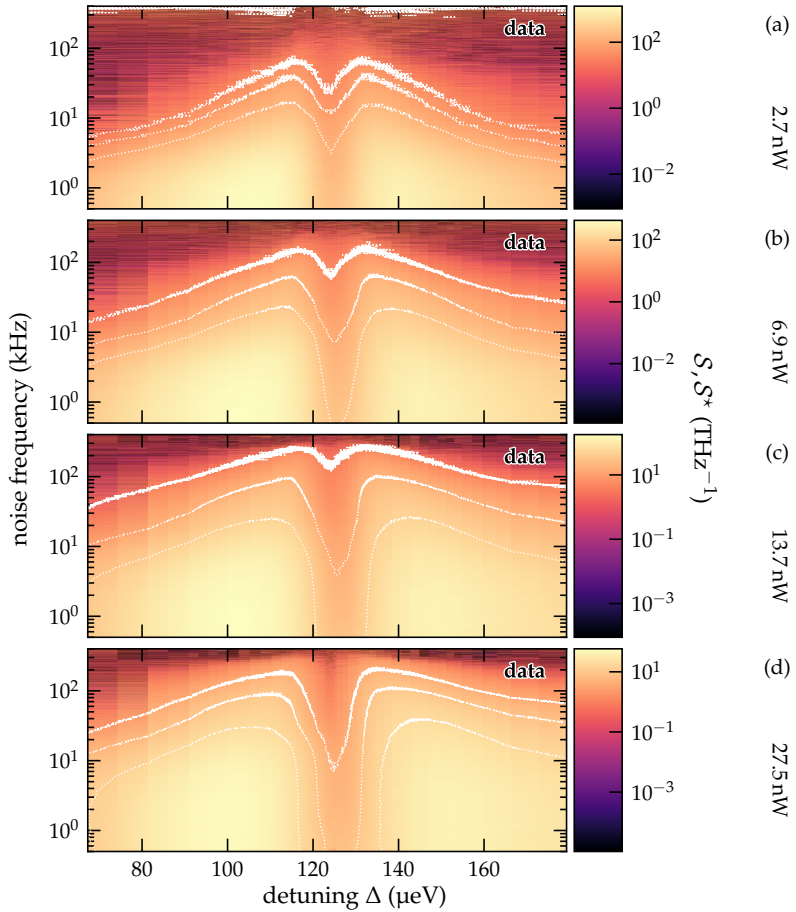


Figure C.16: Experimental detuning hyperspectra at 1.8 K, 2 T, and different probe powers. Equipotential curves are plotted in white.

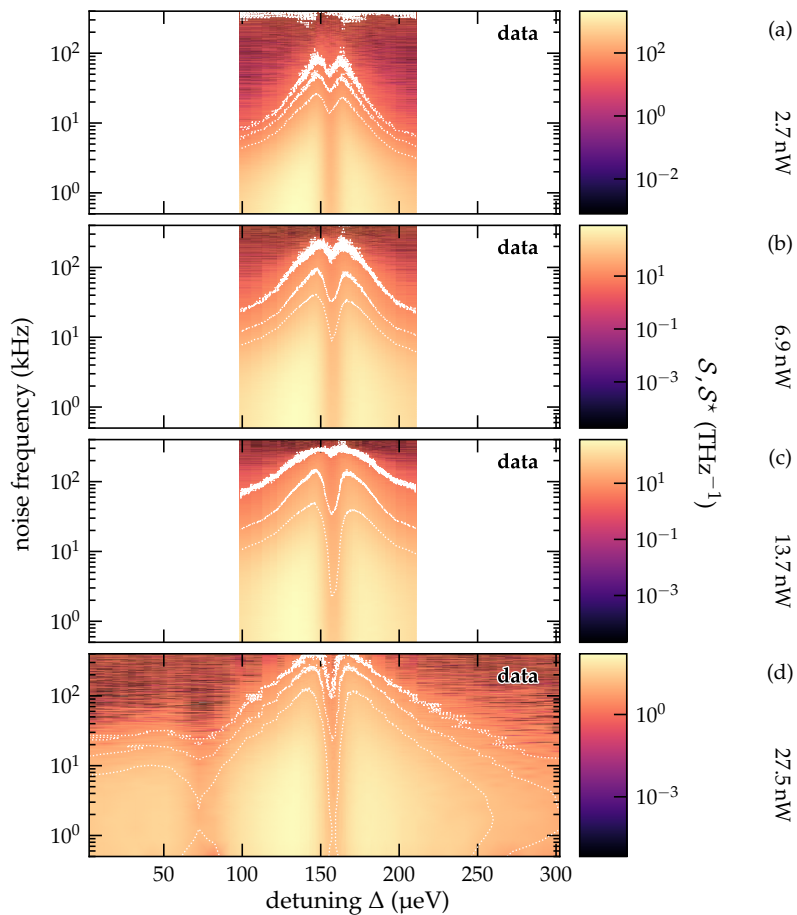


Figure C.17: Experimental detuning hyperspectra at 1.8K, 2.5T, and different probe powers. Equipotential curves are plotted in white.

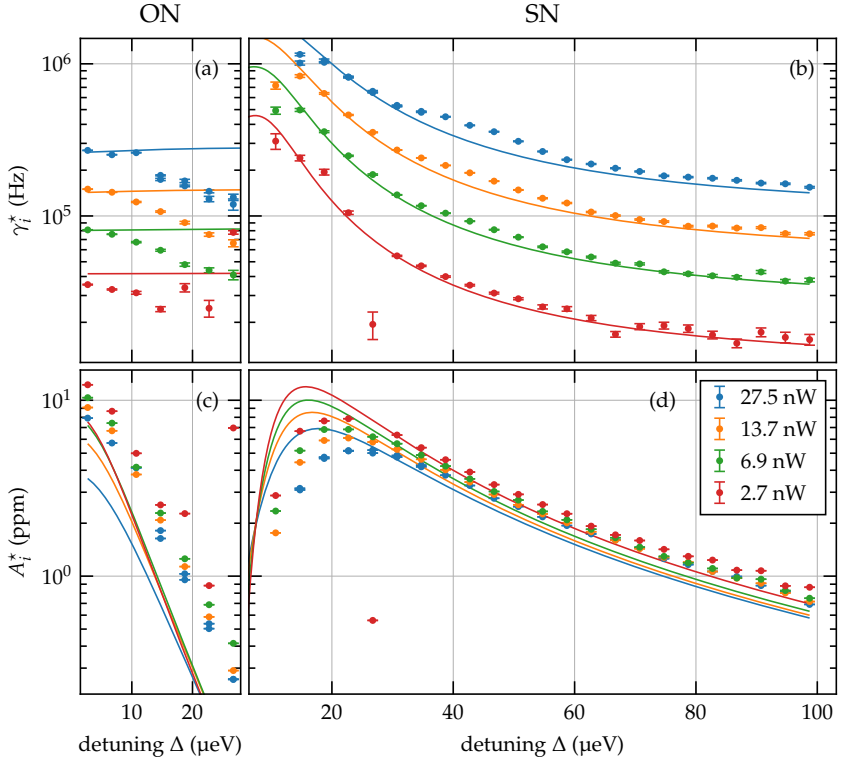


Figure C.18: Results of single spectrum regression of detuning hyper-spectra at 1.8 K, 125 mT, and different probe powers. Panels (a) and (c) display the extracted parameters for correlation rate and relative noise power of the narrow contribution attributed to ON. Panels (b) and (d) show the respective parameters for the broad contribution attributed to SN. Solid lines are corresponding separation of correlator time scales (SCTS) approximations of globally fitted exact model.

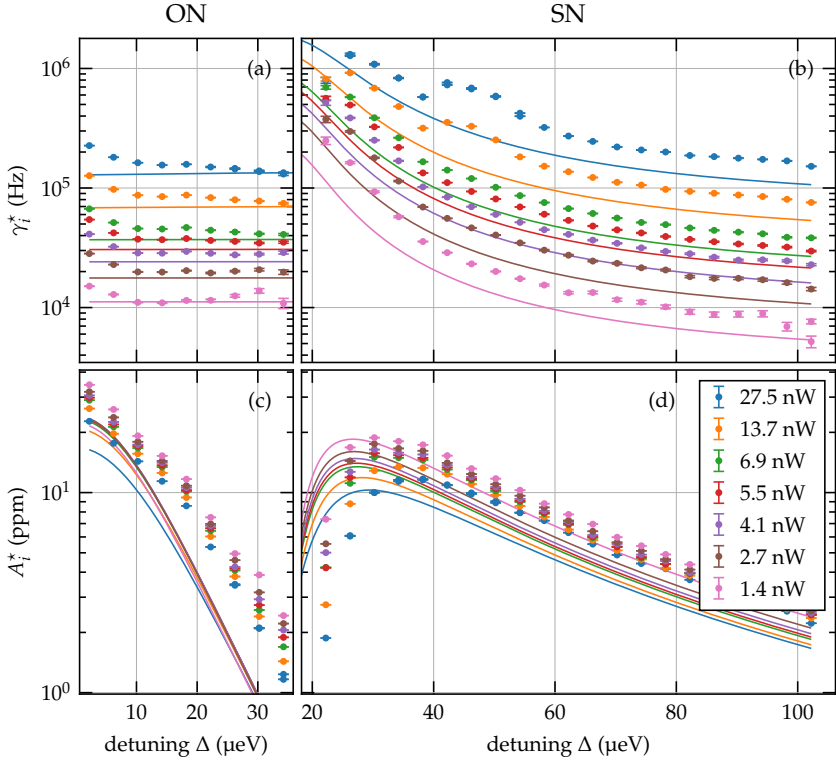


Figure C.19: Results of single spectrum regression of detuning hyper-spectra at 1.8 K, 250 mT, and different probe powers. Panels (a) and (c) display the extracted parameters for correlation rate and relative noise power of the narrow contribution attributed to ON. Panels (b) and (d) show the respective parameters for the broad contribution attributed to SN. Solid lines are corresponding separation of correlator time scales (SCTS) approximations of globally fitted exact model.

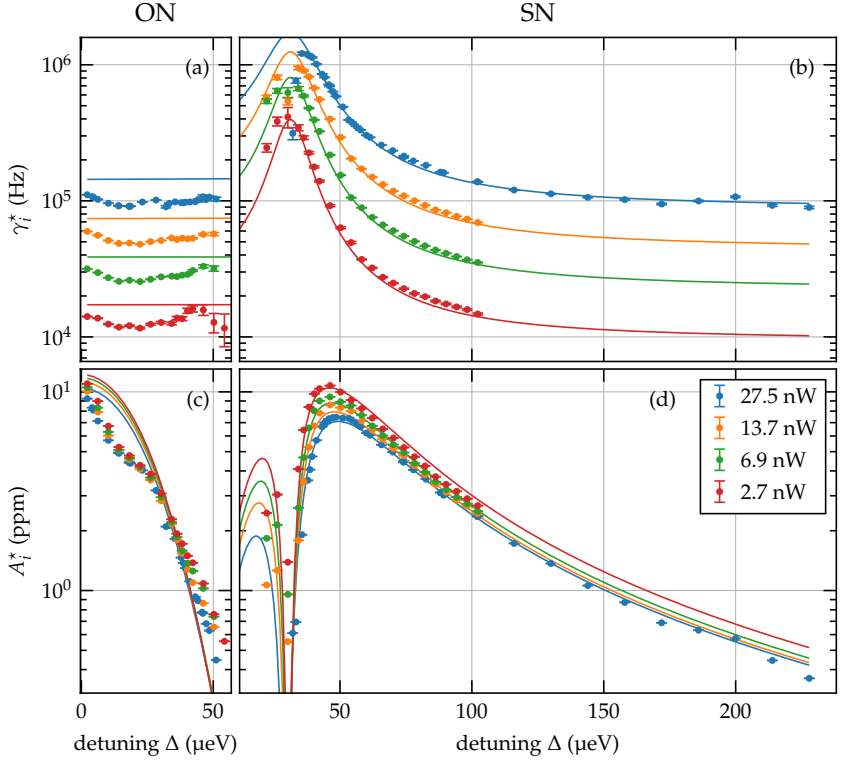


Figure C.20: Results of single spectrum regression of detuning hyper-spectra at 1.8 K, 500 mT, and different probe powers. Panels (a) and (c) display the extracted parameters for correlation rate and relative noise power of the narrow contribution attributed to ON. Panels (b) and (d) show the respective parameters for the broad contribution attributed to SN. Solid lines are corresponding separation of correlator time scales (SCTS) approximations of globally fitted exact model.

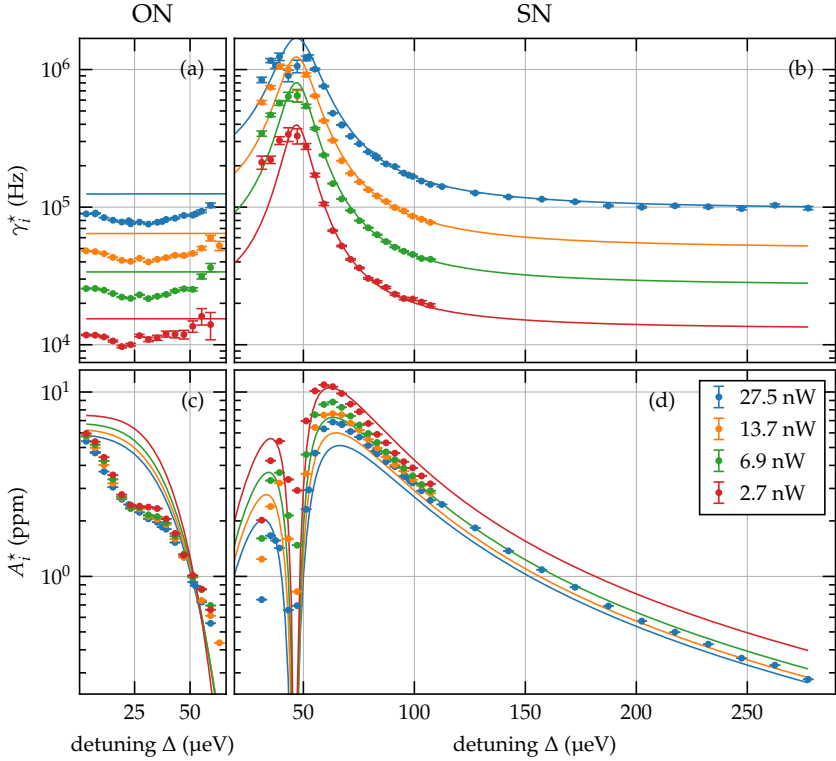


Figure C.21: Results of single spectrum regression of detuning hyper-spectra at 1.8 K, 750 mT, and different probe powers. Panels (a) and (c) display the extracted parameters for correlation rate and relative noise power of the narrow contribution attributed to ON. Panels (b) and (d) show the respective parameters for the broad contribution attributed to SN. Solid lines are corresponding separation of correlator time scales (SCTS) approximations of globally fitted exact model.

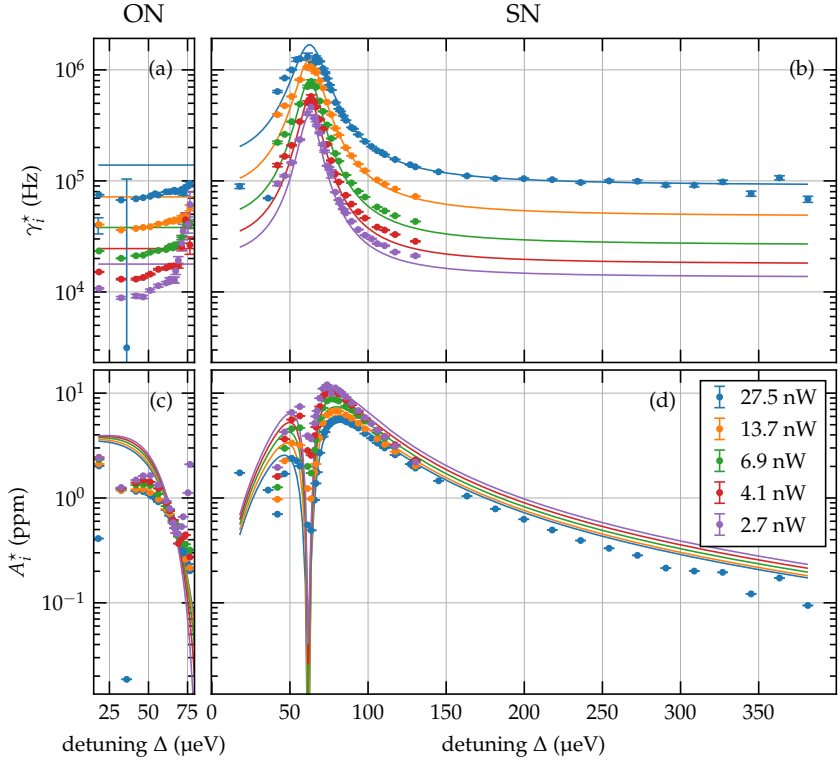


Figure C.22: Results of single spectrum regression of detuning hyper-spectra at 1.8 K, 1 T, and different probe powers. Panels (a) and (c) display the extracted parameters for correlation rate and relative noise power of the narrow contribution attributed to ON. Panels (b) and (d) show the respective parameters for the broad contribution attributed to SN. Solid lines are corresponding separation of correlator time scales (SCTS) approximations of globally fitted exact model.

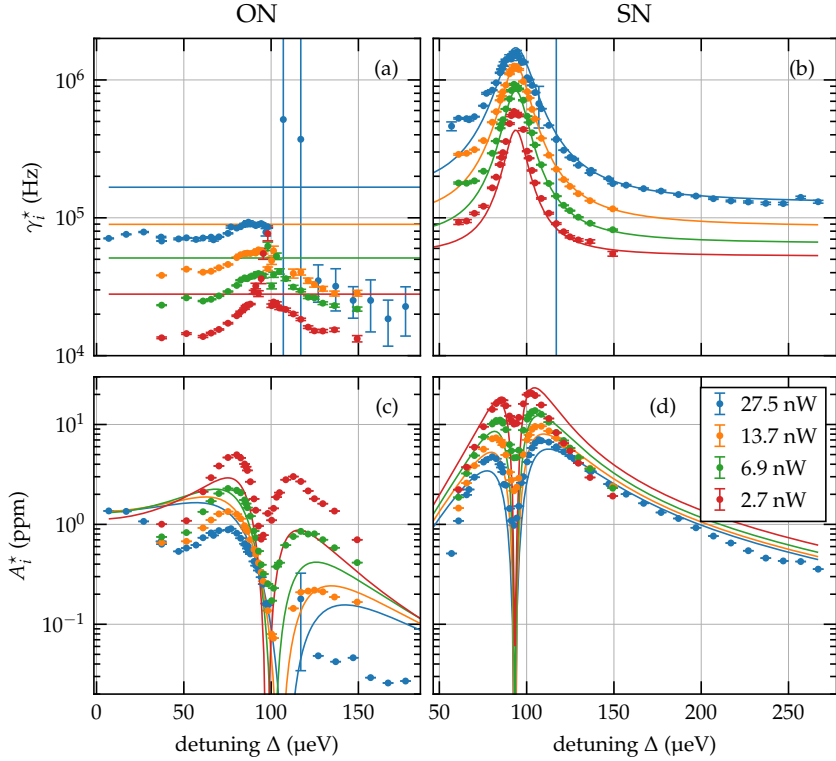


Figure C.23: Results of single spectrum regression of detuning hyper-spectra at 1.8 K, 1.5 T, and different probe powers. Panels (a) and (c) display the extracted parameters for correlation rate and relative noise power of the narrow contribution attributed to ON. Panels (b) and (d) show the respective parameters for the broad contribution attributed to SN. Solid lines are corresponding separation of correlator time scales (SCTS) approximations of globally fitted exact model.

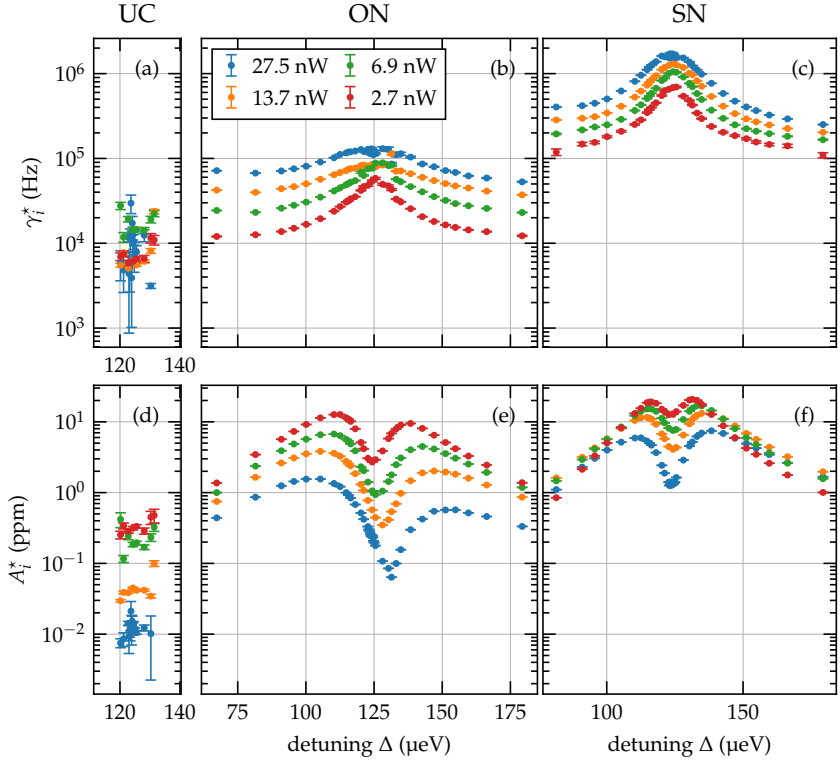


Figure C.24: Results of single spectrum regression of detuning hyper-spectra at 1.8 K, 2 T, and different probe powers. Panels (b) and (e) display the extracted parameters for correlation rate and relative noise power of the narrow contribution attributed to ON. Panels (c) and (f) show the respective parameters for the broad contribution attributed to SN. Panels (a) and (d) show the respective parameters for the potential third contribution.

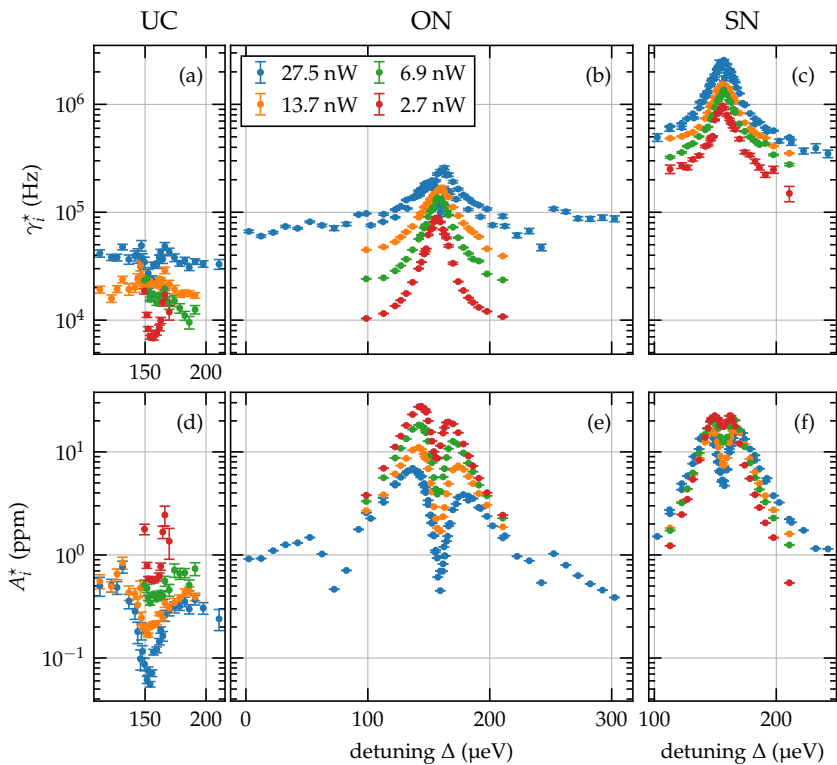


Figure C.25: Results of single spectrum regression of detuning hyper-spectra at 1.8 K, 2.5 T, and different probe powers. Panels (b) and (e) display the extracted parameters for correlation rate and relative noise power of the narrow contribution attributed to ON. Panels (c) and (f) show the respective parameters for the broad contribution attributed to SN. Panels (a) and (d) show the respective parameters for the potential third contribution.

Bibliography

- [1] P. Sterin, J. Wiegand, J. Hübner, and M. Oestreich, "Optical Amplification of Spin Noise Spectroscopy via Homodyne Detection", *Physical Review Applied* **9**, 034003 (2018), doi:10.1103/PhysRevApplied.9.034003.
- [2] S. Cronenberger and D. Scalbert, "Quantum limited heterodyne detection of spin noise", *Review of Scientific Instruments* **87**, 093111 (2016), doi:10.1063/1.4962863.
- [3] M. Y. Petrov, A. N. Kamenskii, V. S. Zapasskii, M. Bayer, and A. Greulich, "Increased sensitivity of spin noise spectroscopy using homodyne detection in n-doped GaAs", *Physical Review B* **97**, 125202 (2018), doi:10.1103/PhysRevB.97.125202.
- [4] A. N. Kamenskii, M. Y. Petrov, G. G. Kozlov, V. S. Zapasskii, S. E. Scholz, C. Sgroi, A. Ludwig, A. D. Wieck, M. Bayer, and A. Greulich, "Detection and amplification of spin noise using scattered laser light in a quantum-dot microcavity", *Physical Review B* **101**, 041401 (2020), doi:10.1103/PhysRevB.101.041401.
- [5] L. Abaspour, P. Sterin, E. P. Rugeramigabo, J. Hübner, and M. Oestreich, "Doping and temperature dependence of nuclear spin relaxation in n-type GaAs", *Physical Review B* **102**, 235205 (2020), doi:10.1103/PhysRevB.102.235205.
- [6] T.-J. Sun, P. Sterin, L. Lengert, C. Nawrath, M. Jetter, P. Michler, Y. Ji, J. Hübner, and M. Oestreich, "Non-equilibrium spin noise spectroscopy of a single quantum dot operating at fiber telecommunication wavelengths", *Journal of Applied Physics* **131**, 065703 (2022), doi:10.1063/5.0078910.
- [7] P. Sterin, L. Abaspour, J. G. Lonnemann, E. P. Rugeramigabo, J. Hübner, and M. Oestreich, "Temperature-dependent electron spin relaxation at the

- metal-to-insulator transition in n-type GaAs”, *Physical Review B* **106**, 125202 (2022), doi:10.1103/PhysRevB.106.125202.
- [8] P. Sterin, K. Hühn, M. M. Glazov, J. Hübner, and M. Oestreich, “Two-way photoeffect-like occupancy dynamics in a single (InGa)As quantum dot”, *Physical Review B* **108**, 125301 (2023), doi:10.1103/PhysRevB.108.125301.
- [9] P. Sterin, J. Hübner, and M. Oestreich, “Interferometrically Enhanced Spin Noise Spectroscopy of ^{87}Rb ”, 2016, Talk, International Workshop of the School for Contacts in Nanosystems.
- [10] P. Sterin, J. Hübner, and M. Oestreich, “Interferometrically Enhanced Spin Noise Spectroscopy of Rubidium”, 2017, Poster, Workshop of the School for Contacts in Nanosystems.
- [11] P. Sterin, J. Wiegand, J. Hübner, and M. Oestreich, “Optical amplification of spin noise spectroscopy via homodyne detection”, 2019, Poster, DPG Spring Meeting of the Condensed Matter Section in Regensburg.
- [12] P. Sterin, J. Wiegand, J. Hübner, and M. Oestreich, “Beating the Electric Limit: Homodyne Detection for Spin Noise Spectroscopy”, 2017, Talk, International Workshop of the School for Contacts in Nanosystems.
- [13] P. Sterin, J. Wiegand, J. Hübner, and M. Oestreich, “Optical amplification of spin noise spectroscopy via homodyne detection”, 2018, Talk/Poster, Workshop of the School for Contacts in Nanosystems.
- [14] L. Abaspour, P. Sterin, J. G. Lonnemann, E.-P. Rugeramigabo, J. Hübner, and M. Oestreich, “Towards a Complete Model of Spin Relaxation in n-GaAs”, 2018, Talk, Workshop of the School for Contacts in Nanosystems.
- [15] P. Sterin, M. Baron, J. Wiegand, J. Hübner, and M. Oestreich, “Spin Noise Spectroscopy via Phase Modulated Homodyne Detection”, 2019, Talk, International Workshop of the School for Contacts in Nanosystems.
- [16] P. Sterin, J. Hübner, and M. Oestreich, “Interferometrically Enhanced Spin Noise Spectroscopy of Rubidium”, 2017, Poster, DPG Spring Meeting of the Condensed Matter Section in Dresden.

- [17] J. R. Schaibley, A. P. Burgers, G. A. McCracken, L.-M. Duan, P. R. Berman, D. G. Steel, A. S. Bracker, D. Gammon, and L. J. Sham, “Demonstration of Quantum Entanglement between a Single Electron Spin Confined to an InAs Quantum Dot and a Photon”, *Physical Review Letters* **110**, 167401 (2013), doi:10.1103/PhysRevLett.110.167401.
- [18] T. Guerreiro, A. Martin, B. Sanguinetti, J. Pelc, C. Langrock, M. Fejer, N. Gisin, H. Zbinden, N. Sangouard, and R. Thew, “Nonlinear Interaction between Single Photons”, *Physical Review Letters* **113**, 173601 (2014), doi:10.1103/PhysRevLett.113.173601.
- [19] P. O. Schmidt, T. Rosenband, C. Langer, W. M. Itano, J. C. Bergquist, and D. J. Wineland, “Spectroscopy Using Quantum Logic”, *Science* **309**, 749 (2005), doi:10.1126/science.1114375.
- [20] C. H. Bennett and G. Brassard, “Quantum cryptography: Public key distribution and coin tossing”, *Theoretical Computer Science* **560**, 7 (2014), doi:10.1016/j.tcs.2014.05.025.
- [21] H. Bernien, S. Schwartz, A. Keesling, H. Levine, A. Omran, H. Pichler, S. Choi, A. S. Zibrov, M. Endres, M. Greiner, V. Vuletić, and M. D. Lukin, “Probing many-body dynamics on a 51-atom quantum simulator”, *Nature* **551**, 579 (2017), doi:10.1038/nature24622.
- [22] M. Kroutvar, Y. Ducommun, D. Heiss, M. Bichler, D. Schuh, G. Abstreiter, and J. J. Finley, “Optically programmable electron spin memory using semiconductor quantum dots”, *Nature* **432**, 81 (2004), doi:10.1038/nature03008.
- [23] M. Atatüre, J. Dreiser, A. Badolato, A. Högele, K. Karrai, and A. Imamoglu, “Quantum-Dot Spin-State Preparation with Near-Unity Fidelity”, *Science* **312**, 551 (2006), doi:10.1126/science.1126074.
- [24] X. Xu, Y. Wu, B. Sun, Q. Huang, J. Cheng, D. G. Steel, A. S. Bracker, D. Gammon, C. Emary, and L. J. Sham, “Fast Spin State Initialization in a Singly Charged InAs-GaAs Quantum Dot by Optical Cooling”, *Physical Review Letters* **99**, 097401 (2007), doi:10.1103/PhysRevLett.99.097401.

- [25] B. D. Gerardot, D. Brunner, P. A. Dalgarno, P. Öhberg, S. Seidl, M. Kroner, K. Karrai, N. G. Stoltz, P. M. Petroff, and R. J. Warburton, “Optical pumping of a single hole spin in a quantum dot”, *Nature* **451**, 441 (2008), doi:10.1038/nature06472.
- [26] T. M. Godden, J. H. Quilter, A. J. Ramsay, Y. Wu, P. Brereton, I. J. Luxmoore, J. Puebla, A. M. Fox, and M. S. Skolnick, “Fast preparation of a single-hole spin in an InAs/GaAs quantum dot in a Voigt-geometry magnetic field”, *Physical Review B* **85**, 155310 (2012), doi:10.1103/PhysRevB.85.155310.
- [27] D. Brunner, B. D. Gerardot, P. A. Dalgarno, G. Wüst, K. Karrai, N. G. Stoltz, P. M. Petroff, and R. J. Warburton, “A Coherent Single-Hole Spin in a Semiconductor”, *Science* **325**, 70 (2009), doi:10.1126/science.1173684.
- [28] A. Imamog̃lu, D. D. Awschalom, G. Burkard, D. P. DiVincenzo, D. Loss, M. Sherwin, and A. Small, “Quantum Information Processing Using Quantum Dot Spins and Cavity QED”, *Physical Review Letters* **83**, 4204 (1999), doi:10.1103/PhysRevLett.83.4204.
- [29] D. Press, T. D. Ladd, B. Zhang, and Y. Yamamoto, “Complete quantum control of a single quantum dot spin using ultrafast optical pulses”, *Nature* **456**, 218 (2008), doi:10.1038/nature07530.
- [30] A. Greilich, S. E. Economou, S. Spatzek, D. R. Yakovlev, D. Reuter, A. D. Wieck, T. L. Reinecke, and M. Bayer, “Ultrafast optical rotations of electron spins in quantum dots”, *Nature Physics* **5**, 262 (2009), doi:10.1038/nphys1226.
- [31] K. De Greve, P. L. McMahon, D. Press, T. D. Ladd, D. Bisping, C. Schneider, M. Kamp, L. Worschech, S. Höfling, A. Forchel, and Y. Yamamoto, “Ultrafast coherent control and suppressed nuclear feedback of a single quantum dot hole qubit”, *Nature Physics* **7**, 872 (2011), doi:10.1038/nphys2078.
- [32] T. M. Godden, J. H. Quilter, A. J. Ramsay, Y. Wu, P. Brereton, S. J. Boyle, I. J. Luxmoore, J. Puebla-Nunez, A. M. Fox, and M. S. Skolnick, “Coherent Optical Control of the Spin of a Single Hole in an InAs/GaAs Quantum Dot”, *Physical Review Letters* **108**, 017402 (2012), doi:10.1103/PhysRevLett.108.017402.

- [33] M. Atatüre, J. Dreiser, A. Badolato, and A. Imamoglu, “Observation of Faraday rotation from a single confined spin”, *Nature Physics* **3**, 101 (2007), doi:10.1038/nphys521.
- [34] J. Berezovsky, O. Gywat, F. Meier, D. Battaglia, X. Peng, and D. D. Awschalom, “Initialization and read-out of spins in coupled core-shell quantum dots”, *Nature Physics* **2**, 831 (2006), doi:10.1038/nphys458.
- [35] M. W. Wu, J. H. Jiang, and M. Q. Weng, “Spin dynamics in semiconductors”, *Physics Reports* **493**, 61 (2010), doi:10.1016/j.physrep.2010.04.002.
- [36] S. Ritter, C. Nölleke, C. Hahn, A. Reiserer, A. Neuzner, M. Uphoff, M. Mücke, E. Figueroa, J. Bochmann, and G. Rempe, “An elementary quantum network of single atoms in optical cavities”, *Nature* **484**, 195 (2012), doi:10.1038/nature11023.
- [37] M. Saffman, “Quantum computing with atomic qubits and Rydberg interactions: progress and challenges”, *Journal of Physics B: Atomic, Molecular and Optical Physics* **49**, 202001 (2016), doi:10.1088/0953-4075/49/20/202001.
- [38] S. Debnath, N. M. Linke, C. Figgatt, K. A. Landsman, K. Wright, and C. Monroe, “Demonstration of a small programmable quantum computer with atomic qubits”, *Nature* **536**, 63 (2016), doi:10.1038/nature18648.
- [39] E. A. Martinez, C. A. Muschik, P. Schindler, D. Nigg, A. Erhard, M. Heyl, P. Hauke, M. Dalmonte, T. Monz, P. Zoller, and R. Blatt, “Real-time dynamics of lattice gauge theories with a few-qubit quantum computer”, *Nature* **534**, 516 (2016), doi:10.1038/nature18318.
- [40] L. Henriet, L. Beguin, A. Signoles, T. Lahaye, A. Browaeys, G.-O. Reymond, and C. Jurczak, “Quantum computing with neutral atoms”, *Quantum* **4**, 327 (2020), doi:10.22331/q-2020-09-21-327.
- [41] M. Bayer, “Happier for longer”, *Nature Physics* **7**, 103 (2011), doi:10.1038/nphys1922.
- [42] R. J. Warburton, “Single spins in self-assembled quantum dots”, *Nature Materials* **12**, 483 (2013), doi:10.1038/nmat3585.

- [43] G. M. Müller, M. Römer, D. Schuh, W. Wegscheider, J. Hübner, and M. Oestreich, "Spin Noise Spectroscopy in GaAs (110) Quantum Wells: Access to Intrinsic Spin Lifetimes and Equilibrium Electron Dynamics", *Physical Review Letters* **101**, 206601 (2008), doi:10.1103/PhysRevLett.101.206601.
- [44] D. J. English, J. Hübner, P. S. Eldridge, D. Taylor, M. Henini, R. T. Harley, and M. Oestreich, "Effect of symmetry reduction on the spin dynamics of (001)-oriented GaAs quantum wells", *Physical Review B* **87**, 075304 (2013), doi:10.1103/PhysRevB.87.075304.
- [45] D. H. Feng, I. A. Akimov, and F. Henneberger, "Nonequilibrium Nuclear-Electron Spin Dynamics in Semiconductor Quantum Dots", *Physical Review Letters* **99**, 036604 (2007), doi:10.1103/PhysRevLett.99.036604.
- [46] A. Bechtold, D. Rauch, F. Li, T. Simmet, P.-L. Ardelit, A. Regler, K. Müller, N. A. Sinitsyn, and J. J. Finley, "Three-stage decoherence dynamics of an electron spin qubit in an optically active quantum dot", *Nature Physics* **11**, 1005 (2015), doi:10.1038/nphys3470.
- [47] B. Urbaszek, X. Marie, T. Amand, O. Krebs, P. Voisin, P. Maletinsky, A. Högele, and A. Imamoglu, "Nuclear spin physics in quantum dots: An optical investigation", *Reviews of Modern Physics* **85**, 79 (2013), doi:10.1103/RevModPhys.85.79.
- [48] J. H. Prechtel, A. V. Kuhlmann, J. Houel, A. Ludwig, S. R. Valentin, A. D. Wieck, and R. J. Warburton, "Decoupling a hole spin qubit from the nuclear spins", *Nature Materials* **15**, 981 (2016), doi:10.1038/nmat4704.
- [49] V. Zwiller, H. Blom, P. Jonsson, N. Panev, S. Jeppesen, T. Tsegaye, E. Goobar, M.-E. Pistol, L. Samuelson, and G. Björk, "Single quantum dots emit single photons at a time: Antibunching experiments", *Applied Physics Letters* **78**, 2476 (2001), doi:10.1063/1.1366367.
- [50] A. J. Shields, "Semiconductor quantum light sources", *Nature Photonics* **1**, 215 (2007), doi:10.1038/nphoton.2007.46.
- [51] H. Kamada, H. Gotoh, J. Temmyo, T. Takagahara, and H. Ando, "Exciton Rabi Oscillation in a Single Quantum Dot", *Physical Review Letters* **87**, 246401 (2001), doi:10.1103/PhysRevLett.87.246401.

- [52] X. Xu, B. Sun, P. R. Berman, D. G. Steel, A. S. Bracker, D. Gammon, and L. J. Sham, "Coherent Optical Spectroscopy of a Strongly Driven Quantum Dot", *Science* **317**, 929 (2007), doi:10.1126/science.1142979.
- [53] E. B. Flagg, A. Muller, J. W. Robertson, S. Founta, D. G. Deppe, M. Xiao, W. Ma, G. J. Salamo, and C. K. Shih, "Resonantly driven coherent oscillations in a solid-state quantum emitter", *Nature Physics* **5**, 203 (2009), doi:10.1038/nphys1184.
- [54] C. Schimpf, M. Reindl, F. Basso Basset, K. D. Jöns, R. Trotta, and A. Rastelli, "Quantum dots as potential sources of strongly entangled photons: Perspectives and challenges for applications in quantum networks", *Applied Physics Letters* **118** (2021), doi:10.1063/5.0038729.
- [55] A. V. Kuhlmann, J. Houel, A. Ludwig, L. Greuter, D. Reuter, A. D. Wieck, M. Poggio, and R. J. Warburton, "Charge noise and spin noise in a semiconductor quantum device", *Nature Physics* **9**, 570 (2013), doi:10.1038/nphys2688.
- [56] A. Schliwa, M. Winkelkemper, and D. Bimberg, "Few-particle energies versus geometry and composition of $\text{In}(x)\text{Ga}(1-x)\text{As}/\text{GaAs}$ self-organized quantum dots", *Physical Review B* **79**, 075443 (2009), doi:10.1103/PhysRevB.79.075443.
- [57] J. Martín-Sánchez, R. Trotta, A. Mariscal, R. Serna, G. Piredda, S. Stroj, J. Edlinger, C. Schimpf, J. Aberl, T. Lettner, J. Wildmann, H. Huang, X. Yuan, D. Ziss, J. Stangl, and A. Rastelli, "Strain-tuning of the optical properties of semiconductor nanomaterials by integration onto piezoelectric actuators", *Semiconductor Science and Technology* **33**, 013001 (2017), doi:10.1088/1361-6641/aa9b53.
- [58] W. Ou, X. Wang, W. Wei, T. Jin, Y. Zhu, T. Wang, J. Zhang, X. Ou, and J. Zhang, "Strain Tuning Self-Assembled Quantum Dots for Energy-Tunable Entangled-Photon Sources Using a Photolithographically Fabricated Micro-electromechanical System", *ACS Photonics* **9**, 3421 (2022), doi:10.1021/acsp Photonics.2c01033.
- [59] M. Settnes, P. Kaer, A. Moelbjerg, and J. Mork, "Auger Processes Mediating the Nonresonant Optical Emission from a Semiconductor Quantum Dot

- Embedded Inside an Optical Cavity”, *Physical Review Letters* **111**, 067403 (2013), doi:10.1103/PhysRevLett.111.067403.
- [60] A. Kurzman, A. Ludwig, A. D. Wieck, A. Lorke, and M. Geller, “Auger Recombination in Self-Assembled Quantum Dots: Quenching and Broadening of the Charged Exciton Transition”, *Nano Letters* **16**, 3367 (2016), doi:10.1021/acs.nanolett.6b01082.
- [61] P. Lochner, A. Kurzman, J. Kerski, P. Stegmann, J. König, A. D. Wieck, A. Ludwig, A. Lorke, and M. Geller, “Real-Time Detection of Single Auger Recombination Events in a Self-Assembled Quantum Dot”, *Nano Letters* **20**, 1631 (2020), doi:10.1021/acs.nanolett.9b04650.
- [62] H. Mannel, J. Kerski, P. Lochner, M. Zöllner, A. D. Wieck, A. Ludwig, A. Lorke, and M. Geller, “Auger and spin dynamics in a self-assembled quantum dot”, arXiv:2110.12213 [cond-mat] (2021).
- [63] A. Kurzman, A. Ludwig, A. D. Wieck, A. Lorke, and M. Geller, “Photoelectron generation and capture in the resonance fluorescence of a quantum dot”, *Applied Physics Letters* **108**, 263108 (2016), doi:10.1063/1.4954944.
- [64] P. Lochner, J. Kerski, A. Kurzman, A. D. Wieck, A. Ludwig, M. Geller, and A. Lorke, “Internal photoeffect from a single quantum emitter”, *Physical Review B* **103**, 075426 (2021), doi:10.1103/PhysRevB.103.075426.
- [65] D. S. Smirnov, P. Glasenapp, M. Bergen, M. M. Glazov, D. Reuter, A. D. Wieck, M. Bayer, and A. Greilich, “Nonequilibrium spin noise in a quantum dot ensemble”, *Physical Review B* **95**, 241408 (2017), doi:10.1103/PhysRevB.95.241408.
- [66] S. A. Crooker, J. Brandt, C. Sandfort, A. Greilich, D. R. Yakovlev, D. Reuter, A. D. Wieck, and M. Bayer, “Spin Noise of Electrons and Holes in Self-Assembled Quantum Dots”, *Physical Review Letters* **104**, 036601 (2010), doi:10.1103/PhysRevLett.104.036601.
- [67] M. J. S. Wiegand, “Nonequilibrium Spin Noise Spectroscopy on Single Quantum Dots”, PhD Thesis, Leibniz Universität Hannover, 2019.

- [68] E. B. Aleksandrov and V. S. Zapasskil, "Magnetic resonance in the Faraday-rotation noise spectrum", *Zhurnal Eksperimentalnoi I Teoreticheskoi Fiziki* **81**, 132 (1981).
- [69] B. M. Gorbovitskii and V. I. Perel, "Aleksandrov and Zapasskii experiment and the Raman effect", *Optics and Spectroscopy* **54**, 229 (1983), ADS Bibcode: 1983OptSp..54..229G.
- [70] S. A. Crooker, D. G. Rickel, A. V. Balatsky, and D. L. Smith, "Spectroscopy of spontaneous spin noise as a probe of spin dynamics and magnetic resonance", *Nature* **431**, 49 (2004), doi:10.1038/nature02804.
- [71] M. Oestreich, M. Römer, R. J. Haug, and D. Hägele, "Spin Noise Spectroscopy in GaAs", *Physical Review Letters* **95**, 216603 (2005), doi:10.1103/PhysRevLett.95.216603.
- [72] R. Dahbashi, J. Hübner, F. Berski, K. Pierz, and M. Oestreich, "Optical Spin Noise of a Single Hole Spin Localized in an (InGa)As Quantum Dot", *Physical Review Letters* **112** (2014), doi:10.1103/PhysRevLett.112.156601.
- [73] M. M. Glazov and V. S. Zapasskii, "Linear optics, Raman scattering, and spin noise spectroscopy", *Optics Express* **23**, 11713 (2015), doi:10.1364/OE.23.011713.
- [74] M. M. Glazov, "Spin fluctuations of nonequilibrium electrons and excitons in semiconductors", *Journal of Experimental and Theoretical Physics* **122**, 472 (2016), doi:10.1134/S1063776116030067.
- [75] N. A. Sinitsyn and Y. V. Pershin, "The theory of spin noise spectroscopy: a review", *Reports on Progress in Physics* **79**, 106501 (2016), doi:10.1088/0034-4885/79/10/106501.
- [76] J. Hübner, F. Berski, R. Dahbashi, and M. Oestreich, "The rise of spin noise spectroscopy in semiconductors: From acoustic to GHz frequencies: The rise of spin noise spectroscopy in semiconductors", *physica status solidi (b)* **251**, 1824 (2014), doi:10.1002/pssb.201350291.
- [77] D. S. Smirnov, V. N. Mantsevich, and M. M. Glazov, "Theory of optically detected spin noise in nanosystems", *Uspekhi Fizicheskikh Nauk* **191**, 973 (2021), doi:10.3367/UFNr.2020.10.038861.

- [78] R. Kubo, "The fluctuation-dissipation theorem", *Reports on Progress in Physics* **29**, 255 (1966), doi:10.1088/0034-4885/29/1/306.
- [79] J. Wiegand, D. S. Smirnov, J. Osberghaus, L. Abaspour, J. Hübner, and M. Oestreich, "Hole-capture competition between a single quantum dot and an ionized acceptor", *Physical Review B* **98**, 125426 (2018), doi:10.1103/PhysRevB.98.125426.
- [80] J. M. LaForge and G. M. Steeves, "Noninvasive optical amplification and detection of Faraday rotation", *Applied Physics Letters* **91**, 121115 (2007), doi:10.1063/1.2785111.
- [81] J. M. LaForge and G. M. Steeves, "A Mach-Zehnder interferometer for the detection and noninvasive optical amplification of polarization rotation", *Review of Scientific Instruments* **79**, 063106 (2008), doi:10.1063/1.2948309.
- [82] P. Stoica and R. L. Moses, *Spectral analysis of signals*, Pearson/Prentice Hall, Upper Saddle River, New Jersey, 2005.
- [83] K. Jacobs, *Stochastic Processes for Physicists: Understanding Noisy Systems*, Cambridge University Press, 2010.
- [84] F. Harris, "On the use of windows for harmonic analysis with the discrete Fourier transform", *Proceedings of the IEEE* **66**, 51 (1978), doi:10.1109/PROC.1978.10837.
- [85] B. Mulgrew, P. Grant, and J. Thompson, *Digital Signal Processing*, Macmillan Education UK, London, 1999, doi:10.1007/978-1-349-14944-5.
- [86] G. Heinzel, A. Rüdiger, and R. Schilling, "Spectrum and spectral density estimation by the Discrete Fourier transform (DFT), including a comprehensive list of window functions and some new at-top windows", 2002, URL: https://pure.mpg.de/pubman/faces/ViewItemOverviewPage.jsp?itemId=item_152164.
- [87] S. Starosielec and D. Hägele, "Discrete-time windows with minimal RMS bandwidth for given RMS temporal width", *Signal Processing* **102**, 240 (2014), doi:10.1016/j.sigpro.2014.03.033.

- [88] P. Welch, "The use of fast Fourier transform for the estimation of power spectra: A method based on time averaging over short, modified periodograms", *IEEE Transactions on Audio and Electroacoustics* **15**, 70 (1967), doi:10.1109/TAU.1967.1161901.
- [89] D. Pines and C. P. Slichter, "Relaxation Times in Magnetic Resonance", *Physical Review* **100**, 1014 (1955), doi:10.1103/PhysRev.100.1014.
- [90] B. P. Welford, "Note on a Method for Calculating Corrected Sums of Squares and Products", *Technometrics* **4**, 419 (1962), doi:10.1080/00401706.1962.10490022.
- [91] T. F. Chan, G. H. Golub, and R. J. LeVeque, "Updating Formulae and a Pairwise Algorithm for Computing Sample Variances", in *COMPSTAT 1982 5th Symposium held at Toulouse 1982*, edited by H. Caussinus, P. Ettinger, and R. Tomassone, pages 30–41, Physica-Verlag HD, Heidelberg, 1982, doi:10.1007/978-3-642-51461-6_3.
- [92] M. Fox and M. Fox, *Quantum Optics: An Introduction*, Oxford Master Series in Physics, Oxford University Press, Oxford, New York, 2006.
- [93] H. Bachor and T. C. Ralph, *A Guide to Experiments in Quantum Optics*, Wiley, 1 edition, 2019, doi:10.1002/9783527695805.
- [94] F. Martin Ciurana, G. Colangelo, R. J. Sewell, and M. W. Mitchell, "Real-time shot-noise-limited differential photodetection for atomic quantum control", *Optics Letters* **41**, 2946 (2016), doi:10.1364/OL.41.002946.
- [95] eagleyard Photonics GmbH, "Relative Intensity Noise of Distributed Feedback Laser", Application Note,, URL: https://www.toptica-eagleyard.com/fileadmin/downloads/documents/eyP_App_Note_RIN__1-6.pdf.
- [96] J. Wiegand, D. S. Smirnov, J. Hübner, M. M. Glazov, and M. Oestreich, "Spin and reoccupation noise in a single quantum dot beyond the fluctuation-dissipation theorem", *Physical Review B* **97**, 081403 (2018), doi:10.1103/PhysRevB.97.081403.
- [97] O. Gywat, H. J. Krenner, and J. Berezovsky, *Spins in Optically Active Quantum Dots: Concepts and Methods*, Wiley-VCH Verlag GmbH & Co. KGaA, Weinheim, Germany, 2009, doi:10.1002/9783527628988.

- [98] J. M. Brown, R. J. Buenker, A. Carrington, C. Di Lauro, R. N. Dixon, R. W. Field, J. T. Hougen, W. Hüttner, K. Kuchitsu, M. Mehring, A. J. Merer, T. A. Miller, M. Quack, D. A. Ramsay, L. Veseth, and R. N. Zare, “Remarks on the signs of g factors in atomic and molecular Zeeman spectroscopy”, *Molecular Physics* **98**, 1597 (2000), doi:10.1080/00268970009483366.
- [99] H. J. Carmichael, *Statistical Methods in Quantum Optics 1*, Springer Berlin Heidelberg, Berlin, Heidelberg, 1999, doi:10.1007/978-3-662-03875-8.
- [100] M. Lax, “Formal Theory of Quantum Fluctuations from a Driven State”, *Physical Review* **129**, 2342 (1963), doi:10.1103/PhysRev.129.2342.
- [101] M. Lax, “Quantum Noise. X. Density-Matrix Treatment of Field and Population-Difference Fluctuations”, *Physical Review* **157**, 213 (1967), doi:10.1103/PhysRev.157.213.
- [102] H. J. Carmichael, *An open systems approach to quantum optics: lectures presented at the Université libre de Bruxelles, October 28 to November 4, 1991*, Number m 18 in Lecture notes in physics, Springer-Verlag, 1993.
- [103] F. Berski, J. Hübner, M. Oestreich, A. Ludwig, A. Wieck, and M. Glazov, “Interplay of Electron and Nuclear Spin Noise in n-Type GaAs”, *Physical Review Letters* **115**, 176601 (2015), doi:10.1103/PhysRevLett.115.176601.
- [104] F. Meier and B. P. Zakharchenya, editors, *Optical orientation*, North-Holland, 1984.
- [105] R. Gross and A. Marx, *Festkörperphysik*, De Gruyter Oldenbourg, 2014, doi:10.1524/9783110358704.
- [106] A. K. Zvezdin and V. A. Kotov, *Modern Magneto-optics and Magneto-optical Materials*, CRC Press, 1997.
- [107] I. A. Yugova, M. M. Glazov, E. L. Ivchenko, and A. L. Efros, “Pump-probe Faraday rotation and ellipticity in an ensemble of singly charged quantum dots”, *Physical Review B* **80**, 104436 (2009), doi:10.1103/PhysRevB.80.104436.
- [108] P. Sterin, “Präzise Stokes-Polarimetrie von magneto-optischen Effekten zweiter Ordnung in Galliumarsenid”, Master’s thesis, Leibniz Universität Hannover, 2016.

- [109] G. G. Kozlov, I. I. Ryzhov, and V. S. Zapasskii, "Light scattering in a medium with fluctuating gyrotropy: Application to spin-noise spectroscopy", *Physical Review A* **95**, 043810 (2017), doi:10.1103/PhysRevA.95.043810.
- [110] G. G. Kozlov, A. A. Fomin, M. Y. Petrov, I. I. Ryzhov, I. I. Ryzhov, and V. S. Zapasskii, "Raman scattering model of the spin noise", *Optics Express* **29**, 4770 (2021), doi:10.1364/OE.415034.
- [111] E. L. Ivčenko, *Optical spectroscopy of semiconductor nanostructures*, Alpha Science, Harrow, UK, 2005.
- [112] J. W. Goodman, *Statistical optics*, Wiley series in pure and applied optics, Wiley, Hoboken, New Jersey, second edition edition, 2015.
- [113] D. A. Steck, "Rubidium 87 D Line Data", Technical report, Oregon Center for Optics, Department of Physics, University of Oregon, 2015.
- [114] D. A. Steck, "Rubidium 85 D Line Data", Technical report, Oregon Center for Optics, Department of Physics, University of Oregon, 2013.
- [115] J. Ma, P. Shi, X. Qian, Y. Shang, and Y. Ji, "Optical spin noise spectra of Rb atomic gas with homogeneous and inhomogeneous broadening", *Scientific Reports* **7**, 10238 (2017), doi:10.1038/s41598-017-08759-4.
- [116] H. Horn, G. M. Müller, E. M. Rasel, L. Santos, J. Hübner, and M. Oestreich, "Spin-noise spectroscopy under resonant optical probing conditions: Coherent and nonlinear effects", *Physical Review A* **84**, 043851 (2011), doi:10.1103/PhysRevA.84.043851.
- [117] M. L. F. Baron, "Ultrasensitive Spinrauschspektroskopie mittels phasenmodulierter homodyner Detektion", Bachelor's thesis, Leibniz Universität Hannover, 2020.
- [118] M. L. Hesse, "Investigation of phasemodulated homodyne detection in Spin Noise Spectroscopy", Bachelor's thesis, Leibniz Universität Hannover, 2022.
- [119] Y. Ben-Haim and E. Tom-Tov, "A Streaming Parallel Decision Tree Algorithm", *Journal of Machine Learning Research* **11**, 849 (2010).

- [120] P. M. Petroff and S. P. DenBaars, "MBE and MOCVD growth and properties of self-assembling quantum dot arrays in III-V semiconductor structures", *Superlattices and Microstructures* **15**, 15 (1994), doi : 10.1006/spmi.1994.1004.
- [121] H. A. Atwater, C. C. Ahn, S. S. Wong, G. He, H. Yoshino, and S. Nikzad, "Energy-filtered rheed and reels for in situ real time analysis during film growth", *Surface Review and Letters* **04**, 525 (1997), doi:10.1142/S0218625X9700050X.
- [122] I. N. Stranski and L. Krastanow, "Zur Theorie der orientierten Ausscheidung von Ionenkristallen aufeinander", *Monatshefte für Chemie und verwandte Teile anderer Wissenschaften* **71**, 351 (1937), doi : 10.1007/BF01798103.
- [123] D. Leonard, M. Krishnamurthy, C. M. Reaves, S. P. Denbaars, and P. M. Petroff, "Direct formation of quantum-sized dots from uniform coherent islands of InGaAs on GaAs surfaces", *Applied Physics Letters* **63**, 3203 (1993), doi : 10.1063/1.110199.
- [124] D. Leonard, K. Pond, and P. M. Petroff, "Critical layer thickness for self-assembled InAs islands on GaAs", *Physical Review B* **50**, 11687 (1994), doi : 10.1103/PhysRevB.50.11687.
- [125] J. M. García, G. Medeiros-Ribeiro, K. Schmidt, T. Ngo, J. L. Feng, A. Lorke, J. Kotthaus, and P. M. Petroff, "Intermixing and shape changes during the formation of InAs self-assembled quantum dots", *Applied Physics Letters* **71**, 2014 (1997), doi:10.1063/1.119772.
- [126] J. Fischer, W. A. Coish, D. V. Bulaev, and D. Loss, "Spin decoherence of a heavy hole coupled to nuclear spins in a quantum dot", *Physical Review B* **78**, 155329 (2008), doi:10.1103/PhysRevB.78.155329.
- [127] O. Stier, M. Grundmann, and D. Bimberg, "Electronic and optical properties of strained quantum dots modeled by 8-band $k \cdot p$ theory", *Physical Review B* **59**, 5688 (1999), doi : 10.1103/PhysRevB.59.5688.
- [128] M. Bayer, G. Ortner, O. Stern, A. Kuther, A. A. Gorbunov, A. Forchel, P. Hawrylak, S. Fafard, K. Hinzer, T. L. Reinecke, S. N. Walck, J. P. Reithmaier, F. Klopff, and F. Schäfer, "Fine structure of neutral and charged

- excitons in self-assembled In(Ga)As/(Al)GaAs quantum dots”, *Physical Review B* **65**, 195315 (2002), doi:10.1103/PhysRevB.65.195315.
- [129] R. Heilman and G. Oelgart, “Ionization energy of the carbon acceptor in $\text{Al}_x\text{Ga}_{1-x}\text{As}$ ”, *Semiconductor Science and Technology* **5**, 1040 (1990), doi:10.1088/0268-1242/5/10/006.
- [130] R. Seguin, A. Schliwa, S. Rodt, K. Pötschke, U. W. Pohl, and D. Bimberg, “Size-Dependent Fine-Structure Splitting in Self-Organized InAs/GaAs Quantum Dots”, *Physical Review Letters* **95**, 257402 (2005), doi:10.1103/PhysRevLett.95.257402.
- [131] J. Debus, V. F. Sapega, D. Dunker, D. R. Yakovlev, D. Reuter, A. D. Wieck, and M. Bayer, “Spin-flip Raman scattering of the resident electron in singly charged (In,Ga)As/GaAs quantum dot ensembles”, *Physical Review B* **90**, 235404 (2014), doi:10.1103/PhysRevB.90.235404.
- [132] C. Schulhauser, D. Haft, R. J. Warburton, K. Karrai, A. O. Govorov, A. V. Kalameitsev, A. Chaplik, W. Schoenfeld, J. M. Garcia, and P. M. Petroff, “Magneto-optical properties of charged excitons in quantum dots”, *Physical Review B* **66**, 193303 (2002), doi:10.1103/PhysRevB.66.193303.
- [133] I. Žutić, J. Fabian, and S. Das Sarma, “Spintronics: Fundamentals and applications”, *Reviews of Modern Physics* **76**, 323 (2004), doi:10.1103/RevModPhys.76.323.
- [134] K. Shen and M. W. Wu, “Hole spin relaxation in intrinsic and p-type bulk GaAs”, *Physical Review B* **82**, 115205 (2010), doi:10.1103/PhysRevB.82.115205.
- [135] C. Testelin, F. Bernardot, B. Eble, and M. Chamarro, “Hole–spin dephasing time associated with hyperfine interaction in quantum dots”, *Physical Review B* **79**, 195440 (2009), doi:10.1103/PhysRevB.79.195440.
- [136] D. Press, K. De Greve, P. L. McMahon, T. D. Ladd, B. Friess, C. Schneider, M. Kamp, S. Höfling, A. Forchel, and Y. Yamamoto, “Ultrafast optical spin echo in a single quantum dot”, *Nature Photonics* **4**, 367 (2010), doi:10.1038/nphoton.2010.83.

- [137] I. A. Merkulov, A. L. Efros, and M. Rosen, "Electron spin relaxation by nuclei in semiconductor quantum dots", *Physical Review B* **65**, 205309 (2002), doi:10.1103/PhysRevB.65.205309.
- [138] B. Eble, C. Testelin, P. Desfonds, F. Bernardot, A. Balocchi, T. Amand, A. Mirard, A. Lemaître, X. Marie, and M. Chamarro, "Hole-Nuclear Spin Interaction in Quantum Dots", *Physical Review Letters* **102**, 146601 (2009), doi:10.1103/PhysRevLett.102.146601.
- [139] T. Calarco, A. Datta, P. Fedichev, E. Pazy, and P. Zoller, "Spin-based all-optical quantum computation with quantum dots: Understanding and suppressing decoherence", *Physical Review A* **68**, 012310 (2003), doi:10.1103/PhysRevA.68.012310.
- [140] M. Trif, P. Simon, and D. Loss, "Relaxation of Hole Spins in Quantum Dots via Two-Phonon Processes", *Physical Review Letters* **103**, 106601 (2009), doi:10.1103/PhysRevLett.103.106601.
- [141] D. V. Bulaev and D. Loss, "Spin Relaxation and Decoherence of Holes in Quantum Dots", *Physical Review Letters* **95**, 076805 (2005), doi:10.1103/PhysRevLett.95.076805.
- [142] D. Heiss, S. Schaeck, H. Huebl, M. Bichler, G. Abstreiter, J. J. Finley, D. V. Bulaev, and D. Loss, "Observation of extremely slow hole spin relaxation in self-assembled quantum dots", *Physical Review B* **76**, 241306 (2007), doi:10.1103/PhysRevB.76.241306.
- [143] I. Pelant and J. Valenta, *Luminescence Spectroscopy of Semiconductors*, Oxford University Press Oxford, 1 edition, 2012, doi:10.1093/acprof:oso/9780199588336.001.0001.
- [144] J. M. Pietryga, K. K. Zhuravlev, M. Whitehead, V. I. Klimov, and R. D. Schaller, "Evidence for Barrierless Auger Recombination in PbSe Nanocrystals: A Pressure-Dependent Study of Transient Optical Absorption", *Physical Review Letters* **101**, 217401 (2008), doi:10.1103/PhysRevLett.101.217401.
- [145] I. Robel, R. Gresback, U. Kortshagen, R. D. Schaller, and V. I. Klimov, "Universal Size-Dependent Trend in Auger Recombination in Direct-Gap and

- Indirect-Gap Semiconductor Nanocrystals”, *Physical Review Letters* **102**, 177404 (2009), doi:10.1103/PhysRevLett.102.177404.
- [146] J. Dreiser, M. Atatüre, C. Galland, T. Müller, A. Badolato, and A. Imamoglu, “Optical investigations of quantum dot spin dynamics as a function of external electric and magnetic fields”, *Physical Review B* **77**, 075317 (2008), doi:10.1103/PhysRevB.77.075317.
- [147] P. P. Jha and P. Guyot-Sionnest, “Trion Decay in Colloidal Quantum Dots”, *ACS Nano* **3**, 1011 (2009), doi:10.1021/nn9001177.
- [148] C. C. Katsidis and D. I. Siapkas, “General transfer-matrix method for optical multilayer systems with coherent, partially coherent, and incoherent interference”, *Applied Optics* **41**, 3978 (2002), doi:10.1364/AO.41.003978.
- [149] R. Dabhashi, “Spinrauschen in nulldimensionalen Strukturen”, PhD Thesis, Leibniz Universität Hannover, 2015.
- [150] R. Dabhashi, J. Hübner, F. Berski, J. Wiegand, X. Marie, K. Pierz, H. W. Schumacher, and M. Oestreich, “Measurement of heavy-hole spin dephasing in (InGa)As quantum dots”, *Applied Physics Letters* **100**, 031906 (2012), doi:10.1063/1.3678182.
- [151] S. Gehrsitz, F. K. Reinhart, C. Gourgon, N. Herres, A. Vonlanthen, and H. Sigg, “The refractive index of $\text{Al}_x\text{Ga}_{1-x}\text{As}$ below the band gap: Accurate determination and empirical modeling”, *Journal of Applied Physics* **87**, 7825 (2000), doi:10.1063/1.373462.
- [152] S. Koseki, “Monolithic Waveguide Coupled GaAs Microdisk Microcavity Containing InGaAs Quantum Dots”, PhD thesis, Stanford University, 2008.
- [153] Y. J. Fu, S. D. Lin, M. F. Tsai, H. Lin, C. H. Lin, H. Y. Chou, S. J. Cheng, and W. H. Chang, “Anomalous diamagnetic shift for negative trions in single semiconductor quantum dots”, *Physical Review B* **81**, 113307 (2010), doi:10.1103/PhysRevB.81.113307.
- [154] H. M. G. A. Tholen, J. S. Wildmann, A. Rastelli, R. Trotta, C. E. Pryor, E. Zallo, O. G. Schmidt, P. M. Koenraad, and A. Y. Silov, “Active tuning of the g-tensor in InGaAs/GaAs quantum dots via strain”, *Physical Review B* **99**, 195305 (2019), doi:10.1103/PhysRevB.99.195305.

- [155] V. S. Zapasskii, A. Grelich, S. A. Crooker, Y. Li, G. G. Kozlov, D. R. Yakovlev, D. Reuter, A. D. Wieck, and M. Bayer, "Optical Spectroscopy of Spin Noise", *Physical Review Letters* **110**, 176601 (2013), doi:10.1103/PhysRevLett.110.176601.
- [156] A. Puy, P. Beneventano, S. A. Levin, S. Lo Piano, T. Portaluri, and A. Saltelli, "Models with higher effective dimensions tend to produce more uncertain estimates", *Science Advances* **8**, eabn9450 (2022), doi:10.1126/sciadv.abn9450.
- [157] M. Pollnau and M. Eichhorn, "Spectral coherence, Part I: Passive-resonator linewidth, fundamental laser linewidth, and Schawlow-Townes approximation", *Progress in Quantum Electronics* **72**, 100255 (2020), doi:10.1016/j.pquantelec.2020.100255.
- [158] K. Hühn, "N. N.", Unpublished doctoral dissertation, Leibniz Universität Hannover.
- [159] E. S. Moskalenko, L. A. Larsson, M. Larsson, P. O. Holtz, W. V. Schoenfeld, and P. M. Petroff, "Effective tuning of the charge state of a single InAs/GaAs quantum dot by an external magnetic field", *Physical Review B* **78**, 075306 (2008), doi:10.1103/PhysRevB.78.075306.
- [160] E. S. Moskalenko, M. Larsson, K. F. Karlsson, P. O. Holtz, B. Monemar, W. V. Schoenfeld, and P. M. Petroff, "Enhancement of the Luminescence Intensity of InAs/GaAs Quantum Dots Induced by an External Electric Field", *Nano Letters* **7**, 188 (2007), doi:10.1021/nl062417u.
- [161] Z. Sun, A. Delteil, S. Faelt, and A. Imamoğlu, "Measurement of spin coherence using Raman scattering", *Physical Review B* **93**, 241302 (2016), doi:10.1103/PhysRevB.93.241302.
- [162] L. Lengert, "Spindynamik in n-dotierten Halbleitern", Bachelor's thesis, Leibniz Universität Hannover, 2018.
- [163] N. Meinck, "Spektralanalyse eines aktiven Schwingungsisolierungssystem für einen optischen Tisch", Bachelor's thesis, Leibniz Universität Hannover, 2018.

- [164] L. Rötz, "Installation eines Tieftemperaturmessplatzes für zeitaufgelöste Photolumineszenz-Spektroskopie an GaAs", Bachelor's thesis, Leibniz Universität Hannover, 2020.
- [165] E. Dunkel, "Vergleichende Spektroskopie an In(Ga)As-Quantenpunkten", Bachelor's thesis, Leibniz Universität Hannover, 2022.
- [166] F. Lange, "Spinrauschspektroskopie an einzelnen (InGa)As-Quantenpunkten", Master's thesis, Leibniz Universität Hannover, 2022.

Curriculum Vitae

Pavel Sterin,

born on February 22nd, 1989 in Gomel, Belarus

November 2018 - today	Employment as a research assistant at the Institute of Solid State Physics at the Leibniz university of Hanover (LUH)
March 2016 - August 2023	Work on the PhD project "Interaction of few-spin Systems with their Environment" at the Institute of Solid State Physics at the LUH, supervised by Prof. Dr. Michael Oestreich
October 2015 - September 2018	Scholarship as a fellow of the NTH School for Contacs in Nanostructures
March 2016	MSc degree in physics at the LUH: "Präzise Stokes-Polarimetrie von magnetooptischen Effekten zweiter Ordnung in Galliumarsenid" supervised by Prof. Dr. Michael Oestreich
December 2012	BSc degree in physics at the LUH: "Quantenwalks in fastperiodischen Strukturen" supervised by Prof. Dr. Reinhard F. Werner
2009-2016	Study of physics at the LUH
June 2009	Abitur at the Bismarckschule in Hanover
2000-2009	School education in Germany
1996-1999	School education in Belarus

Mentored Bachelor and Master Projects

- L. Lengert, "Spindynamik in n-dotierten Halbleitern", Bachelor's thesis, Leibniz Universität Hannover, 2018.
- N. Meinck, "Spektralanalyse eines aktiven Schwingungsisolationssystem für einen optischen Tisch", Bachelor's thesis, Leibniz Universität Hannover, 2018.
- M. L. F. Baron, "Ultrasensitive Spinrauschspektroskopie mittels phasenmodulierter homodyner Detektion", Bachelor's thesis, Leibniz Universität Hannover, 2020.
- L. Rötz, "Installation eines Tieftemperaturmessplatzes für zeitaufgelöste Photolumineszenz-Spektroskopie an GaAs", Bachelor's thesis, Leibniz Universität Hannover, 2020.
- E. Dunkel, "Vergleichende Spektroskopie an In(Ga)As-Quantenpunkten", Bachelor's thesis, Leibniz Universität Hannover, 2022.
- M. L. Hesse, "Investigation of phasemodulated homodyne detection in Spin Noise Spectroscopy", Bachelor's thesis, Leibniz Universität Hannover, 2022.
- F. Lange, "Spinrauschspektroskopie an einzelnen (InGa)As-Quantenpunkten", Master's thesis, Leibniz Universität Hannover, 2022.

Acknowledgements

Science is a team effort. Therefore, I want to thank everybody who made this thesis possible.

First, I would like to thank my supervisor Prof. Dr. Michael Oestreich for bringing me into his group, captivating me with many different research topics, and allowing me to work on them to my fullest ability. You gave me the opportunity and encouraged me to acquire knowledge and experience in many different domains, not only physics. Your supervision and guidance allowed me to explore all these topics that I attempted to include in this thesis. Thank you very much for allowing me to do it!

I also thank our trusty second commander-in-chief, PD Dr. Jens Hübner. Not only do your hands do literal wonders in the lab when the laser straight out refuses to lase – you are also an extremely valuable adviser, always ready to talk about any topic required. You encouraged me to stop using the old unmaintainable LabView code by starting the mighty plexy framework in Python. The switch to a real programming language allowed us to create a robust, documented, extensible control software usable by experimentalists in our group and beyond. I also thank you for proofreading parts of my thesis.

I thank Prof. Dr. Ilja Gerhardt for agreeing to be my second referee. When I first met you at a conference in Bad Honnef, I was immediately amazed at the breadth of topics you work on. As a Ph.D. student, I tried to emulate your example and attempt to master as many topics as possible. I feel honored to have you as a referee.

I thank Prof. Dr. Daniel Hägele for agreeing to be my third referee. The talks you gave visiting our institute were inspirational when I worked on the theory part of the thesis.

I thank Prof. Dr. Klemens Hammerer for heading the examination committee.

I thank Prof. Dr. Mikhail M. Glazov for providing invaluable help with the theoretical model and the publication. Thank you for tirelessly answering all my questions and allowing me to gain a glimpse of an understanding of quantum mechanics.

I thank Kai Hühn, my collaborator on the project, for enduring my pedanticism and attention to detail for so long, even though it must have sometimes been hard. We have built a great setup that will serve you and future generations well.

I thank Ronny Hüther, our technical assistant, and resident engineer. Without your technical expertise and helpful discussions, this project would have been impossibly harder to realize. Your combined knowledge in cryogenics, electronics, and mechanical engineering is truly remarkable, and you were always ready to share your knowledge with me. I also thank you for teaching me how to run the small CNC robot in our workshop and allowing me to use it for making small parts needed in the laboratory – this was one of the best experiences I had during my time in the institute. I also thank our team from the mechanical workshop for meticulously building all of the crazy contraptions I made them do. Thank you, Matthias Rabe, Uwe Grothof, Andreas Wittig, and Jens Wiegmann. I also thank our secretaries, Yvonne Griep and Anna Braun, for shielding me from a great part of the bureaucracy, hence allowing me to concentrate on doing science.

I thank Prof. Dr. Rolf J. Haug for organizing the NTH School for Contacts in Nanosystems, which supported me with a scholarship during the first three years of my Ph.D. project.

I thank Dr. Lina Bockhorn for the scientific and non-scientific discussions we had and for proofreading parts of my thesis.

I thank the Femtos for all these memorable moments we had: Fabian Berski, Jennifer Haack, Hendrik Kuhn, Ramin Dahbashi, Julia Wiegand, Michael Beck, Jan-Gerrit Lonnemann, Lida Abaspour, Magnus Neumann, Eduard Sauter, André Frauendorf, Tianjiao (Fiona) Sun, Kevin Rempel.

I thank my students for patiently enduring my teachings: Brandon Walker, Nico Meinck, Liza Lengert, Maximilian Baron, Lennard Rötze, Erik Dunkel, Florian Lange, Martin Hesse, and Nico Eggeling. Explaining these topics to you really helped me understand them better myself.

I thank Marvin Dzinnik for sharing the burden of IT administration with me. Furthermore, I thank all the other Nanos and anyone I forgot to mention for the great times we had at the institute.

Finally, I want to thank my mother, who was my greatest supporter during all this time, for never losing faith in me to finish what I started. Мама, большое тебе спасибо!